

Fundamental Applications of Nanopores: Controlled DNA Translocations to Nanofluidics

Présentée le 9 octobre 2020

à la Faculté des sciences et techniques de l'ingénieur
Laboratoire de biologie à l'échelle nanométrique
Programme doctoral en physique

pour l'obtention du grade de Docteur ès Sciences

par

Sebastian James DAVIS

Acceptée sur proposition du jury

Prof. F. Mila, président du jury
Prof. A. Radenovic, S. Marion, directeurs de thèse
Prof. V. Tabbarð-Cossa, rapporteur
Prof. A. Siria, rapporteur
Prof. M. Dal Peraro, rapporteur

A certain type of perfection can only be realised
through a limitless accumulation of the imperfect.

— Haruki Murakami

To S.

Abstract

Nanopores are nanometer sized openings that are the connection between two electrolyte filled reservoirs. The measurement of the ion transport flowing through such a pore allows to probe physically or biologically interesting phenomena. These range from the passage of biological molecules, to the modulation of current due to multiple physical effects when the nanopore undergoes mechanical strain or pressure induced flow. Many types of nanopores exist: biological protein pores engineered to be able to sequence DNA, glass nanocapillaries easily interfaced with optical tools, or silicon nitride membrane pores which are a standard tool of recent nanotechnology.

This thesis is split into two parts. The first focuses on the use of glass nanocapillaries which allow the facile combination of nanopore experiments with optical tweezers. Optical tweezers are a well established single molecule tool that allow precise force measurement on biologically relevant scales. They are used here for the control of DNA passing through the nanopore. Their ability to measure small scale forces allows the detailed investigation of DNA binding proteins, and attempts to measure the force of DNA passage through biological pores. Extensions of these experiments to the elastic behaviour of DNA during its passage through a nanopore reveal the effects of flow generated by the charged surface of nanopores themselves. This motivates attempts to control such flows as well as the second part of the thesis.

The second part of the thesis focuses on nanofluidics, the role of fluid flow and ion transport at the nanoscale. Using a setup combining pressure with nanopores it is possible to probe, via precise measurements of the conduction of the nanopore, the wetting state of the pore. Contamination phenomena are shown to be abundant with such small systems and a description of their effects on standard measurements such as direct current current-voltage curves is given. Following this, pressure is applied to perfectly filled pores and, thanks to a new alternating current detection method, is shown to be able to discern the effect of pressure induced strain at the pore as well as the coupling of hydraulic flow with electrical properties of the pore. Finally, extensions beyond aqueous solvents are explored in both nanocapillaries and silicon nitride pores. For this, room-temperature ionic liquids are used. These liquids are known from previous studies to behave differently at surfaces and in nano-confinement. The nanopore system both with and without added pressure is shown to be a good tool for investigating such phenomena.

Keywords: Nanopore, nanocapillary, optical tweezers, DNA translocation, DNA-protein complex, DNA dynamics, electroosmotic flow, ionic current rectification, protein nanopores, room-temperature ionic liquids, hydrostatic pressure, mechano-sensitivity.

Résumé

Les nanopores sont des ouvertures de taille nanométrique qui sont la seule connexion entre deux réservoirs de liquide. La mesure du courant électrique à travers le nanopore permet de mesurer des phénomènes physiques et biologiques variés. Parmi ceux-ci on compte la translocation de molécules biologiques, ou la modulation du courant dû à de multiples effets tels que la mise en contrainte mécanique du pore ou les effets de flux de liquide à travers le pore. Plusieurs variétés de nanopores existent, entre autres les nanopores biologiques dont la plupart sont des protéines trans-membranaires modifiées pour le séquençage d'ADN, des nanocapillaires de verre facilement associés aux mesures optiques, ou les nanopores dans des membranes de nitrure de silicium qui sont le standard du domaine. Cette thèse est divisée en deux parties. La première se concentre sur l'utilisation de nanocapillaires en verre en combinaison avec des pinces optiques. Les pinces optiques sont un outil de biophysique uni-moléculaire puissant qui a récemment reçu un prix Nobel. Cet outil est utilisé comme un contrôle mécanique sur la translocation d'ADN. La possibilité de cet outil de mesurer la force s'appliquant à l'ADN permet de détecter et de caractériser des protéines liées. Des extensions de cette technique à la mesure de la dynamique élastique de l'ADN durant la translocation révèlent l'importance des effets de flux de liquide dans ces systèmes. Ces flux peuvent être dus à la charge de surface intrinsèque des nanopores ou à une pression externe.

La deuxième partie de la thèse concerne la nanofluidique, la physique des flux de liquide à l'échelle nanométrique. En utilisant un nouveau montage combinant la pression et les nanopores il est possible, en mesurant précisément la conduction électrique du nanopore, de déterminer l'état de mouillage du pore. Des phénomènes de contamination sont présentés comme étant abondant dans ce genre de système et une description des effets de la contamination sur la caractéristique électrique des pores est décrite. Il est ensuite possible de mesurer des pores complètement remplis qui montre que la mise en contrainte mécanique des nanopores, via l'application d'une pression, est mesurable dans la conduction électrique du pore. Il est également possible de quantifier l'effet du couplage entre la pression et les caractéristiques électriques du pore. Finalement, une extension au-delà des électrolytes aqueux est tentée tant pour des nanocapillaires de verres que pour des nanopores en nitrure de silicium. Pour ceci des liquides ioniques à température ambiante sont utilisés qui sont connus pour avoir des propriétés différentes proche de surfaces ou en confinement nanométrique. L'outil du nanopore avec ou sans l'addition de pression se montre être un système utile pour la description de ces liquides et leurs propriétés.

Keywords : Nanopore, nanocapillaire, pinces optiques, translocation d'ADN, protéines liées, dynamique d'ADN, flux électro-osmotique, rectification du courant ionique, nanopore biologique, liquide ionique à température ambiante, pression hydrostatique, sensibilité mécanique.



Declaration

I declare that the work in this thesis was carried out in accordance with the requirements of the University's Regulations and Code of Practice for Research Degree Programmes and that it has not been submitted for any other academic award. Except where indicated by specific reference in the text, the work is the candidate's own work. Work done in collaboration with, or with the assistance of, others, is indicated as such. Any views expressed in the thesis are those of the author.

Sebastian Davis

Acknowledgements

This thesis has been a long and arduous journey, and I could not have made it to the end without the help and support of many people[1]. I would like to thank some of them here[2].

First I would like to thank the members of my PhD committee: Frédéric Mila, Vincent Tabard-Cossa, Alessandro Siria, and Matteo Dal Peraro. Thank you all for providing critical feedback to the content of the thesis and for extremely interesting discussions during the defence.

Next to my supervisors Aleksandra Radenovic and Sanjin Marion. Thank you Aleksandra for accepting me as a PhD student all those years ago and providing support and guidance. A big thanks to Sanjin for taking me under your wing when arriving in the lab and coming up with crazy and (some) wonderful ideas for us to knock our heads against during these years[3]. Your mentorship has allowed me to progress as a scientist and as a person.

My thanks to Roman, AKA the dude, who was my first mentor at LBEN and taught me all he knew on capillaries and optical tweezers. The other famous capillary guy: Po-Ling. Thank you for always being so kind to me whether helping me in the lab, the enormous parcels of goodies I regularly get from you, or by sharing your famous cooking. Next all the members of LBEN, the old guard whether still here or moved on to other pastures: Gedis, Hendrik, Martina, Michael, Lely, Ke, and Jiandong. And the new: Michal, Arielle, Jochem, Kristin, Vytautas, Mukesh, Simon, Alessio, Adrien, Evgenii, Andrey, Miao, Jean. Thank you all for making LBEN a fun place to be with trips to sat, bbqs by the lake or our group retreats. Thanks also to our visiting collaborators Jens and Andrew who brought not only MspA to the lab but loads of laughs and good times[4].

I would like to thank the members of two other labs who trained me and taught me the basics of performing experimental science before arriving at LBEN. Firstly to members of ex-LCB. Josiane, Chiara, Céline, Franck thank you for instilling in me a sense of rigour and discipline in scientific work that I carry with me to this very day. I have not forgotten the lessons in cell culture, PDMS, or microscopy work and our lunches together on campus have always been a welcome break to talk about life and most importantly laugh. Next to the members of the Small Biosystems lab in Barcelona: Joan, Anna, Mark, Alvaro, Javi, and all the others, my time with you was short however you made me feel at home despite my lack of speaking Catalan.

Next to the boys at LUC Rugby who are too many to name. Being able to share the pitch every Tuesday and Thursday with all of you has been a godsend. However stressed or anxious I have been it manages to evaporate while running (and cursing Jimmy's name[5]) or throwing the ball around with you all. I would like to mention Arnold who I have known since my start at ERRL many seasons ago. You were always present with a reassuring word before a tough match, a consoling arm (and beer) after a loss, and a great smile (and beer) after a victory. Thank you for all of it you will be sorely missed.

Acknowledgements

To my friends: Cédric, Maud, Kilian, Chloé, Bastien and his wonderful family. Our group has been together since our bachelor and master days struggling to grasp our basic courses[6]. Thank you all for always being there to go on a much needed trip to Japan, Bristol, Italy, Israel or others. Or more simply just to go out and have a beer[7] and a meal.

Finally to my family. Thank you so much Mum and Dad for always pushing me to do what I loved. I will always remember how you have nurtured my love for science and discovery ever since drawing the solar system on my bedroom wall in St-Cierges, observing growing tadpoles, or growing salt crystals. I cannot express how much your support has meant to me over the years, whether professional[8], sporting[9], or personal[10], and I feel eternally privileged to be your son. Beav thanks to you for your unfailing sense of humour you can always draw a smile with your dry wit whatever the occasion[11]. Our trip to Japan[12] together with Cédric has most definitely been a highlight of the recent years and I've always loved seeing your natural talent released on stage to well deserved applause[13]. Last but not least to S.. Words are not enough to express how much your love, caring, and support have helped me over the past years. Every struggle however big or small is magically[14] lessened just by seeing, and talking to you.

Lausanne, October 1, 2020

S.J. D.

Contents

Abstract (English/Français)	i
Declaration	v
Acknowledgements	vii
List of Figures	xiii
List of Tables	xv
List of Publications and Conferences	xvii
1 Introduction	1
1.1 Nanopores	1
1.2 Motivation	6
1.3 Thesis Layout	7
I Controlled Translocations	9
2 Nanocapillaries combined with optical tweezers	11
2.1 Glass nanocapillaries as nanopores	11
2.2 Fabrication and characterisation of nanocapillary devices	13
2.2.1 Laser assisted pulling	13
2.2.2 Scanning electron microscopy characterisation and shrinking	14
2.2.3 Mounting into fluidic cells	16
2.3 Optical tweezers	17
2.3.1 Principle and calibration	18
2.3.2 Optical tweezer setup	20
2.4 Combination of nanocapillaries with optical tweezers	20
3 Localisation and discrimination of DNA-protein complexes	23
3.1 Introduction to DNA-protein complex detection	23
3.2 Using nanocapillaries combined with optical tweezers	25
3.2.1 Localisation of DNA-protein complexes	26
3.2.2 Discrimination of DNA-protein complexes	32
3.3 Conclusion	35
4 DNA retraction measured with optical tweezers	37
4.1 Introduction to DNA elasticity for taut relaxation	37
	ix

Contents

4.2	Experimental description	41
4.3	Measuring DNA retraction with nanocapillaries combined with optical tweezers	42
4.3.1	Deconvolution from the effects of the colloidal bead	43
4.3.2	Force decay exponent analysis	44
4.3.3	Length dependence	45
4.4	Controlled translocations and the role of electroosmotic flow: Conclusions	47
4.5	Polymer coating of nanocapillaries	48
4.5.1	Electroosmotic flow and ionic current rectification in nanopores	48
4.5.2	Measuring and reducing effects of electroosmotic flow	50
4.5.3	Conclusion	57
5	Combining protein pores with optical tweezers: SPRNT calibration	59
5.1	Introduction to protein nanopores	59
5.2	Combination of protein pores with nanocapillaries	62
5.3	Combination of glass capillaries, optical tweezers, and the MspA system	64
5.3.1	Lipid bilayer formation on glass microcapillaries	64
5.3.2	MspA insertion and free translocation confirmation	65
5.3.3	Locating and optimisation of lipid bilayer position	68
5.3.4	Optimising stability of lipid bilayers on capillaries	70
5.4	Conclusion	72
II	Confinement and Nanofluidics	73
6	Confinement of room-temperature ionic liquids	75
6.1	Introduction to room-temperature ionic liquids	75
6.2	Measuring room-temperature ionic liquids in confinement	78
6.3	Temperature dependent measurements of room-temperature ionic liquids	80
6.4	Conclusion	83
7	Pressure effects on wetting of nanopores	85
7.1	Introduction to wetting of nanopores	85
7.2	Hydrostatic pressure system	88
7.3	Wetting of nanopores	90
7.3.1	Wetting of hydrophilic pores	90
7.3.2	Wetting of hydrophobic pores	95
7.4	Conclusion	96
8	Nanofluidics	97
8.1	Introduction to nanofluidics	97
8.2	Pressure induced strain enlargement measured via pore resistance	100
8.3	Pressure induced ionic current rectification in symmetric nanopores	103
8.4	DC pressure dependent measurements and FEM extensions	107
8.5	Pressure phenomena in aqueous solutions: Conclusions	109
8.6	Applying hydrostatic pressure to room-temperature ionic liquid filled pores	110
8.6.1	First measurements of pressure dependent phenomena in non-aqueous electrolyte	110
8.6.2	Resistance of room-temperature ionic liquids in silicon nitride nanopore confinement	112
8.6.3	Zeta potential of room-temperature ionic liquids in nanopore confinement	113

8.6.4	Arrays of nanopores for signal to noise enhancement in streaming measurements	115
8.7	Conclusions	117
9	General conclusions and outlook	119
9.1	General conclusions	119
9.1.1	Conclusions: Controlled translocations	119
9.1.2	Conclusions: Confinement and nanofluidics	120
9.2	Outlook	120
	Bibliography	123
	Curriculum Vitae	145

List of Figures

1.1	Nanopore sensing scheme.	2
1.2	Zeta potential definition.	5
2.1	Glass nanocapillaries as nanopores.	12
2.2	Nanocapillary fabrication and SEM imaging.	15
2.3	Mounting and filling glass nanocapillaries.	17
2.4	Principle and calibration of an optical trap.	19
2.5	Optical trap setup.	21
3.1	Measuring DNA-protein interactions.	24
3.2	Schematic of the OT-nanopore setup and example of raw data traces.	27
3.3	Forwards or backwards localisation and work.	28
3.4	Distinguishing non-specific binding via statistical analysis.	29
3.5	Localisation of DNA-protein complexes.	30
3.6	Localisation shift and correction.	31
3.7	Discrimination of DNA-protein complexes.	34
4.1	DNA tension propagation models and their relevance during a translocation event.	38
4.2	First measurements of DNA elasticity.	40
4.3	Experimental setup and detected signals during taut relaxation of DNA.	41
4.4	Dependence of DNA relaxation on optical trap stiffness and contribution due to convolution with bead dynamics.	44
4.5	Extraction of exponent for long time-scales and comparison to simulation.	45
4.6	Length dependence of taut DNA dynamics.	46
4.7	Electroosmotic flow and ionic current rectification in nanopores.	49
4.8	Liquid AFM measurements on polymer coated silicon nitride chips.	52
4.9	Electrical characterisation of polymer coated nanocapillaries.	54
4.10	Conductance and ionic current rectification spread in small glass nanocapillaries.	55
4.11	Free translocations of DNA as a marker for electroosmotic flow reduction.	56
4.12	Comparison of force measured in the optical tweezers setup.	57
5.1	Most common biological nanopore structures.	60
5.2	SPRNT technique and its application.	61
5.3	Methods for forming lipid bilayers and combining with glass capillaries.	63
5.4	Schematic of electrophoretic force measurements in MspA nanopore system with optical tweezers.	64
5.5	Lipid bilayer formation over glass nanocapillaries.	66
5.6	Current voltage curve characterising MspA biological pores.	67

List of Figures

5.7	Free translocations of λ -DNA through MspA biological pores.	68
5.8	Conformation of lipid bilayer position on glass nanocapillaries.	69
5.9	Parylene C coating and micro-structuring on glass capillaries.	71
6.1	Ionic liquid structural properties at surfaces and in confinement.	77
6.2	Probing nanoconfinement of room-temperature ionic liquids.	79
6.3	Room-temperature ionic liquids behave as glassy liquids with temperature.	81
6.4	Size dependence of room-temperature ionic liquid glass temperature.	82
6.5	Platinum coated nanocapillaries.	83
7.1	Wetting of nanopores.	87
7.2	Nanofluidics chamber and pressure application system.	89
7.3	Capacitance under pressure: a measure of membrane wetting.	91
7.4	Wetting artifacts in hydrophilic pores.	93
7.5	Finite element modelling of obstructed pores.	95
8.1	Combinations of nanopores and nanoscale materials with pressure.	98
8.2	Application of pressure to perfectly filled solid state nanopores.	100
8.3	Elastic response of membranes under pressure: strain induced enlargement.	102
8.4	Compression pressure behaviour and elastic membrane phenomena.	103
8.5	Pressure induced ionic current rectification in symmetric solid state nanopores.	104
8.6	Spatial asymmetry in ion concentrations for positive and negative bias.	106
8.7	DC pressure curves: merging phenomena.	108
8.8	Effects of varying salt concentration and pore size for ICR pressure behaviour.	109
8.9	Pressure application setup for use with RTIL.	111
8.10	Temperature dependent resistance of RTIL in silicon nitride pores.	112
8.11	Pressure dependent characteristics of RTIL filled pores.	113
8.12	Streaming measurements of RTIL confined in single pores.	114
8.13	Signal increase in square nanopore arrays.	115
8.14	Nanopore arrays filled with RTIL.	116

List of Tables

2.1	Example pipette puller parameters for quartz nanocapillaries.	13
2.2	Example pipette puller parameters for small silica nanocapillaries.	14
2.3	Example pipette puller parameters for silica microcapillaries.	14

List of Publications and Conferences

List of publications in peer reviewed journals:

- R. Bulushev*, S. Marion*, E. Petrova*, **S. J. Davis***, S. Maerkl, and A. Radenovic, Single Molecule Localization and Discrimination of DNA-Protein Complexes by Controlled Translocation Through Nanocapillaries, *Nano Letters*, 2016, 16, 12, 7882-7890
- S. Marion, **S. J. Davis**, Z.-Q. Wu, and A. Radenovic, Nanocapillary confinement of imidazolium based ionic liquids, *Nanoscale*, 2020, 12, 8867-8874
- V. Navikas, S. M. Leitao, S. Marion, **S. J. Davis**, B. Drake, G. E. Fantner, and A. Radenovic, High-throughput, nanocapillary filling method based on microwave radiation, *ACS Applied NanoMaterials*, 2020, 3, 8, 7829-7834
- S. Awasthi, P. Sriboonpeng, C. Ying, J. Houghtaling, I. Shorubalko, S. Marion, **S. J. Davis**, L. Sola, M. Chiari, A. Radenovic, and M. Mayer, Polymer coatings to minimize protein adsorption in solid-state nanopores, *Small Methods*, 2020, 2000177
- **S. J. Davis**, M. Macha, A. Chernev, D. M. Huang, A. Radenovic, and S. Marion, Hydrostatic pressure induced enlargement and ionic current rectification in symmetric nanopores. *Nano Letters*, 2020
- S. Marion, M. Macha, **S. J. Davis**, A. Chernev, and A. Radenovic, Wetting of nanopores probed with pressure, submitted to *Science Advances*, 2020

List of conference contributions:

- Swiss NanoConvention, *Basel Switzerland*, 2016.
- 13th Greta Pifat Mrzljak International School of Biophysics, *Croatia*, 2016. Poster contribution on DNA-protein complex localisation and discrimination in nanocapillaries combined with optical tweezers.
- Biology for Physics: Is there new Physics in living matter?, *Barcelona Spain*, 2017. Poster contribution on DNA-protein complex localisation and discrimination in nanocapillaries combined with optical tweezers.
- On the trail of Nanopores, *Bremen Germany*, 2017. Poster contribution on DNA-protein complex localisation and discrimination in nanocapillaries combined with optical tweezers.
- From Solid State to Biophysics IX, *Cavtat Croatia*, 2018. Poster contribution on DNA-protein complex localisation and discrimination in nanocapillaries combined with optical tweezers. Collaborators presented posters on nanocapillary confinement of imidazolium ionic liquids and polymer coating of glass nanocapillaries for electro-osmotic flow reduction.
- Dead Sea Water 2019 Workshop: Nanomaterials at the water-energy nexus, *Ein Gedi Israel*, 2019. Poster contribution on nanocapillary confinement of imidazolium based ionic liquids.

1 Introduction

Ever since Richard Feynman's famous invitation to study the physics of the very small in his seminar "There's plenty of room at the bottom"[15], scientists from all fields of physics, biology, chemistry, computer science, and material science have investigated nanoscale phenomena. This new field of nanotechnology surfaced from the concerted efforts to develop tools and devices to be able to probe the smallest length scales. This has resulted in the emergence of scanning tunnelling microscopy[16], nanoscale transistors[17], optical tweezers[18], or atomic force microscopy[19], to cite but a few. New systems were also discovered, the most famous of which may be the carbon based fullerenes[20], nanotubes[21], and graphene[22] that now make up a whole research field unto themselves. These discoveries have not only allowed an unprecedented description of the nanoscale but have allowed the discovery of physical properties hitherto unknown[23]. These range from effects in fluid flows where molecular slippage or surface dominant effects can be key[24], electro-chemistry at nanoscale electrodes[25], magnetism at the nanoscale in otherwise non-magnetic materials[23], or nanoscale superconductivity[26].

The widening of nanoscience to bio-nanotechnology is of key interest as it allows the expansion of these powerful tools to the biological world. Indeed, applications of nanotechnology have seen great breakthroughs with a plethora of medically related products containing or utilising nanomaterials[27]. This ranges from drug delivery, to diagnosis, to molecular imaging at the nanoscale with great potential in cancer therapy[28; 29; 30]. This is the start of what Feynman had predicted as "swallowing the doctor" and will only grow in importance with the following decades' push towards more personalised medicine[31].

1.1 Nanopores

Nanopores fit squarely within this field of bio-nanotechnology and have, over the past decades, shown the power to sequence DNA[32], and detect the passage of proteins[33]. They have also been applied to other areas of import including desalination[34], ion-pumps[35], and as tools to harvest the energy of mixing salt solutions[36]. The prevailing tool used throughout this thesis is the nanopore device. In order to introduce this topic, a broad overview of nanopores, their sensing principle, and their applications is given here. For more specific introductions to types of nanopores such as biological or solid state pores, as well as certain interesting characteristics such as electroosmotic flow, the chapters pertaining to each specific case will contain a detailed introduction to the phenomena and relevant literature.

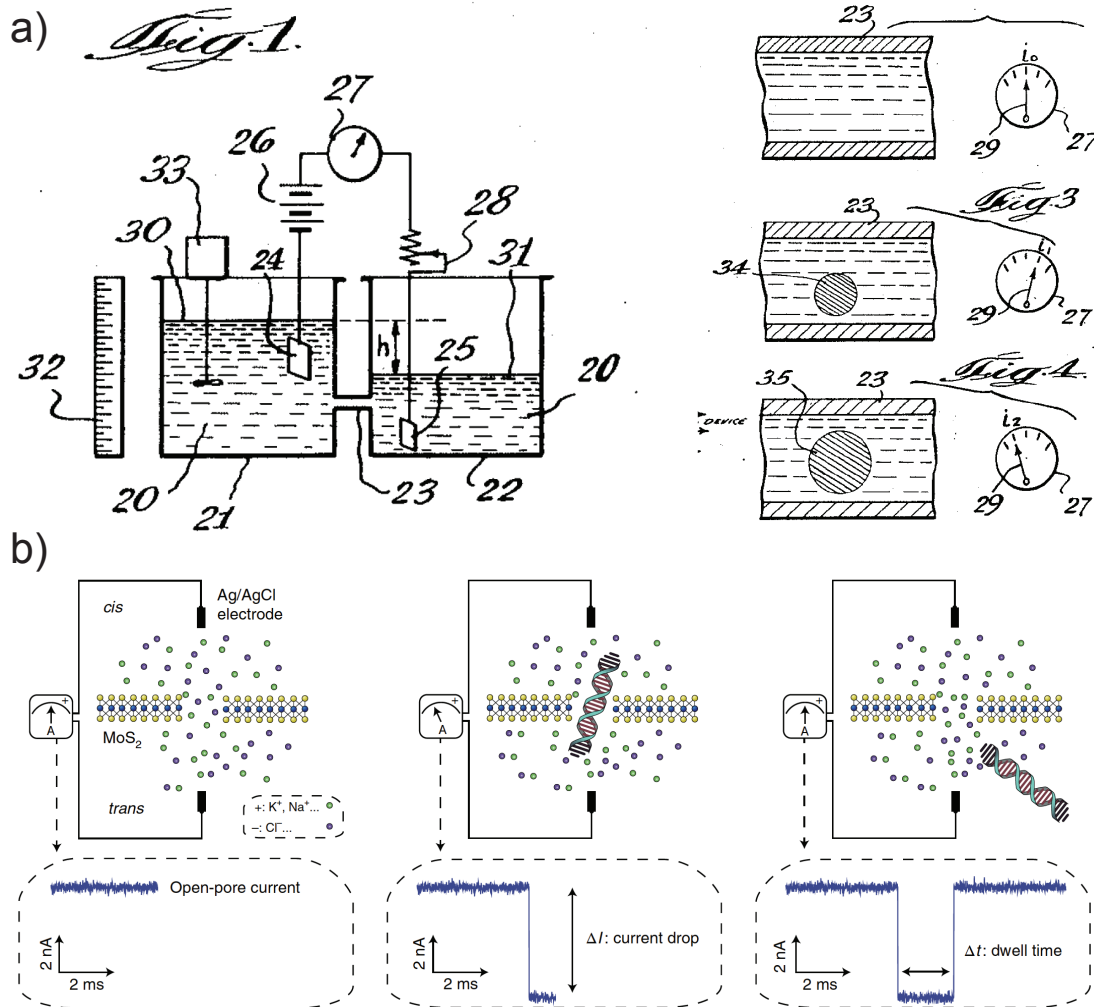


Figure 1.1 – Nanopore sensing scheme. a) Images from the original patent of the Coulter counter from 1953. This sensing scheme known as resistive pulse sensing was applied to the counting of erythrocytes. The same resistive pulse sensing method is behind the nanopore sensing mechanism, albeit on a smaller scale. Image is adapted from ref. [37]. **b)** Example of the resistive pulse sensing technique in nanopores, in this case a quasi-2D MoS₂ membrane. The insulating membrane separates the two electrolyte filled reservoirs and the nanopore is the only connection leading to an open pore current dependent on the membrane and pore characteristics. When an analyte such as DNA translocates through the pore the open pore current is reduced by a value ΔI for a duration Δt characterizing the translocating molecule. Image is adapted from ref. [38].

By definition a nanopore is a nanometer sized hole that acts as the sole connection between two chambers filled with electrolyte solution. They can be divided into two distinct categories: biological nanopores, and solid state nanopores. Most biological nanopores used for DNA sequencing are ion channels extracted from bacterial cell membranes such as *Mycobacterium smegmatis*. These have been engineered by amino acid mutations to have charge properties desirable for the translocation of DNA[39] and have been the first nanopores to robustly show the possibility of DNA sequencing[32]. Solid-state nanopores show at least as much variety as their biological cousins. Indeed, pores can be engineered in many materials at different length scales (0.2-100s nm): from flat silicon nitride

membranes, atomically thin membranes such as molybdenum disulfide (MoS_2)[38] or graphene[40], to glass nanocapillaries with their conical geometry[41]. A third category could be described as a hybrid of these biological and solid state nanopores: synthetic nanopores made from DNA origami[42; 43]. In this case the pore is created by engineered strands of DNA that fold into a 3D pore structure and can be interfaced with either a solid state supporting pore, or a lipid bilayer. However, this thesis will not deal with such origami nanopores.

Whatever the nanopore of choice though, their sensing mechanism is the same (Figure (1.1)). Similar to the Coulter counter principle, when an electric field is applied across the nanopore this induces charged ions to move through the small restriction of the pore thus generating a current. By current measurements with an amplifier the conductance of the pore, and how this conductance changes when an analyte moves through the pore constriction yields information about the nanopore and the analyte. The conductance of solid state nanopores is described by the addition of one term due solely to the cylindrical pore itself and a second term due to the two access regions at each pore entrance[44; 45]. These access resistances are due to the fact that the bulk electrolyte converges sharply at the pore mouth to the confined region of the pore. The conductance is thus modelled as:

$$G_{np} = \sigma_B \left(\frac{4L}{\pi d^2} + \frac{1}{2d} \right)^{-1}, \quad (1.1a)$$

$$G_{nc} = \sigma_B \left(\frac{4t}{\pi dD} + \frac{1}{2d} + \frac{1}{2D} \right)^{-1}. \quad (1.1b)$$

The first equation[45] is given for a flat nanopore geometry with L the thickness of the membrane, d the diameter of the pore, and σ_B the bulk conductance of the electrolyte solution. The second equation[41] is a modification of the first to take into account an asymmetric pore shape with d the small pore radius, D the large pore radius, and t the taper length. This is the equation that governs the conductance of glass nanocapillaries discussed in the first part of the thesis. As is represented on figure (1.1b) translocations of analytes through nanopores yield two main quantities, the dwell time Δt and the current drop ΔI (equivalently the conductance drop $\Delta G = \Delta I / V$). Almost all the measurements with nanopores base themselves on conductance measurements and how the conductance may change in conditions such as a salt gradient[46], laser illumination of the pore surrounding[47], or when hydrostatic pressure is applied to one side[48].

The electric field in nanopores is spatially restricted to the area of largest resistance. In silicon nitride pores this is mostly dominated by the pore volume itself with an additional contribution from access regions. In quasi-2D pores the thickness of the membrane being so small the field contribution comes mostly from the access regions. Tapered nanocapillaries on the other hand behave slightly differently. Due to their elongated geometry the electric field is extended as compared to membrane based nanopores[49]. This extension in electric field will be discussed in more detail in chapter (3).

Due to the extensive range of length scales that solid state pores can span, different physical effects may be relevant. Some useful length-scales to keep in mind throughout the thesis and discussions on nanopores are given here. The first are the Debye length and Gouy-Chapman length. These are related to the surface charge of the membrane material. Any charged surface in liquid will induce the build up of an electrical double layer (EDL). This EDL is due to counter ions in the solution drawn by Coulomb forces close to the charged surface which has the effect of screening the surface charge in the

bulk electrolyte[50].

The electrical double layer, as its name suggests, is assumed to be made up of two distinct phases: the Stern or immobile layer, and the diffuse layer. The Stern layer is the layer of ions that are at the closest approach distance to the surface and are considered to be immobile compared to it due to adsorption and Coulomb interactions being strong. In contrast to the Stern layer, the ions within the diffuse layer are mobile compared to the surface. Electro-neutrality of the solution is broken in the EDL due to a surplus of counter-ions. This breaking of electro-neutrality is important since when under a bias potential the EDL diffuse region will feel a body force due to the electric field. This will in turn generate a macroscopic liquid flow termed electroosmotic flow (EOF).

EOF is an important factor when membrane thickness is large, surface charge is high, or when asymmetry in the nanopore geometry is present in which case it can cause ionic current rectification. These effects will be discussed further in chapter (4) in the context of glass nanocapillaries and in chapter (8) for silicon nitride pores. The width of the EDL depends on the salt concentration c_0 and is represented by the Debye length[51]:

$$\lambda_D = \sqrt{\frac{\epsilon k_B T}{2(Ze)^2 c_0}}, \quad (1.2)$$

where ϵ is the dielectric constant of the liquid, $k_B T$ the thermal energy, Z the valency of the ions, and e the elementary charge. This length can vary between 0.3 nm at 1 M KCl solution, up to 30 nm for 100 μ M KCl solutions. If a nanopore becomes small enough that the Debye lengths between the two sides of the pore overlap then fluid transport properties can change drastically[52]. The Gouy-Chapman length is an associated scale that describes the distance from the charged wall where the interaction between an ion and the wall is on the order of the thermal energy. In contrast to the Debye length it depends explicitly on the surface charge σ and does not depend on the bulk electrolyte concentration:

$$\lambda_{GC} = \frac{2\epsilon k_B T}{\sigma(Ze)^2} \quad (1.3)$$

These length scales define the structure of the ionic species in the region of the surface. Descreening effects may also take place under high electric fields inducing longer range interactions. These have been quantified numerically in the nanopore geometry with the presence of a gate electrode and induce field effects despite the lack of Debye layer overlap[53]. The Dukhin length quantifies the importance of these surface effects to the conductance of the pore. The Dukhin length describes the scale at which surface conduction through the EDL will dominate over bulk conduction. This implies modifications to equations (1.1) above[54]. The Dukhin length is defined as the ratio of surface conductance to bulk conductance and can be given as[55]:

$$\lambda_{Du} = \frac{|\sigma|}{c_0} \quad (1.4)$$

The Dukhin length for a surface charge of $\sigma = -50 \text{ mC/m}^2$ typical for silicon nitride, would vary from 0.5 nm at 1 M KCl, to 5 μ m at 100 μ M KCl. This drastic scaling with salt concentration shows the importance of the Dukhin length and surface conduction in nanopore systems, especially as pore sizes decrease, as relatively high salt concentrations may already incur significant deviations from equation

(1.1).

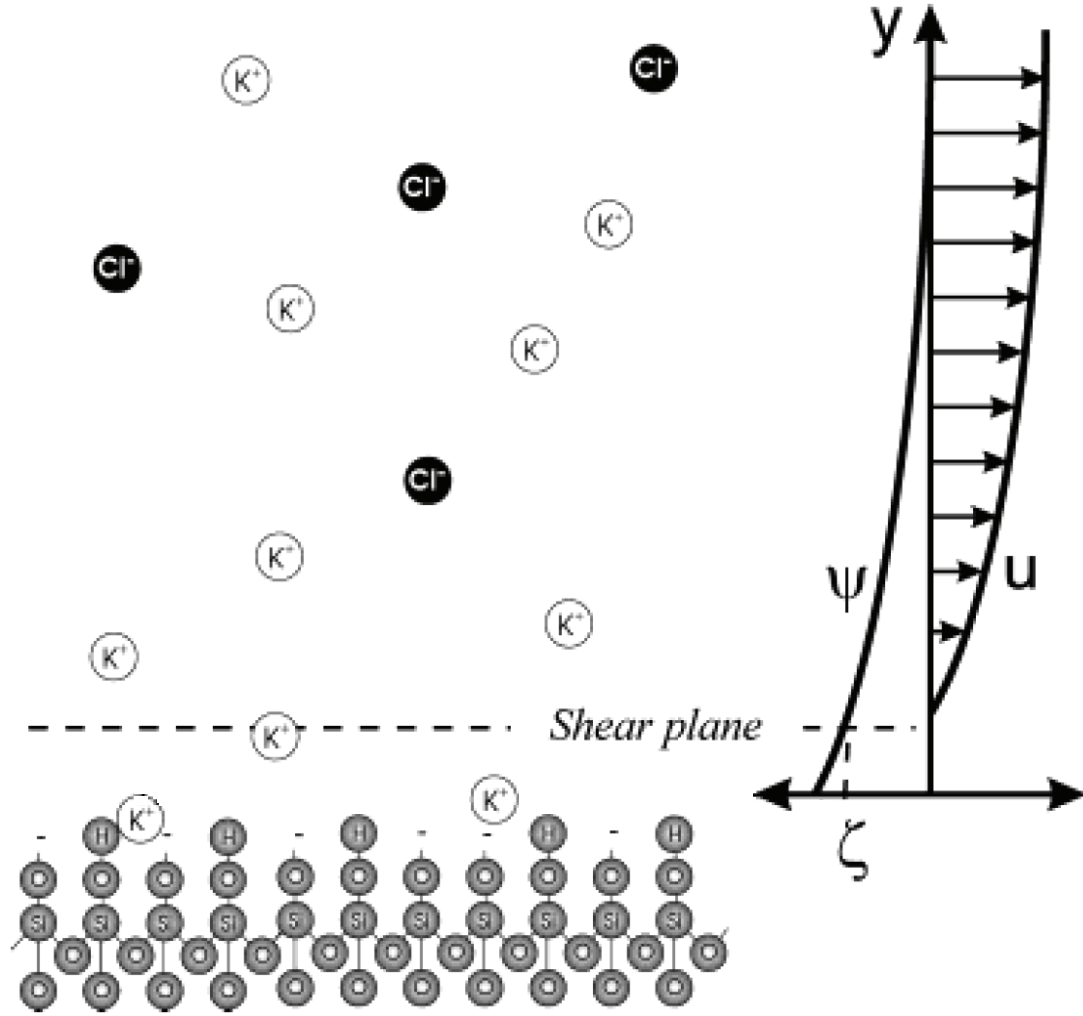


Figure 1.2 – **Zeta potential definition.** Schematic representation of a charged silica surface in a low concentration KCl solution, and the associated surface potential Ψ as a function of the distance to the surface y . The shear plane is the plane at which hydrodynamic velocity u goes to zero and defines the slip length b . This shows the case for $b > 0$. For $b < 0$ the velocity at the wall is non-zero and the slip length defines the imaginary distance at which this velocity would die off. The surface potential at the slip length defines the zeta potential: $\Psi(y = b) = \zeta$. Figure is adapted from ref. [56].

A final length scale that depends on the surface properties is the slip length b . This slip length defines the distance from the surface at which hydrodynamic motion becomes impossible. It is the transition length between the immobile and diffuse regions of the EDL. The surface potential at the slip length is defined as the zeta potential ζ . Figure (1.2) shows a schematic of a charged surface in liquid with associated variables. The zeta potential is a proxy for the measurement of surface charge as it describes the surface potential due to EDL formation. The zeta potential varies with both pH, and ion concentration, due to its dependence on the surface chemistry induced surface charge, and the electrical screening in solution respectively[56]. Models of zeta potential behaviour are possible although solutions are usually restricted to the Debye-Hückel limit which assumes a small potential as compared to thermal energy (i.e. $\Psi < 25$ mV)[56]. Measurements of zeta potential are possible by applying a fluid flow to the system.

Due to the broken electro-neutrality of the double layer such a flow will pull a net surplus of one ion type thus leading to a current or a potential build up between the two reservoirs. These are called streaming current/potential (I_{str} and V_{str} respectively) and are given as a function of the zeta potential for the approximated case of a tube as[56]:

$$I_{\text{str}} = - \frac{\epsilon(2d)^2\pi}{\eta L} \Delta P \xi, \quad (1.5a)$$

$$V_{\text{str}} = \frac{\epsilon}{\eta \sigma_B} \Delta P \xi, \quad (1.5b)$$

where η is the viscosity of the fluid, and ΔP is the pressure gradient applied to generate fluid flow. These equations allow to estimate the zeta potential for a nanopore via streaming measurements. All these effects are due to ions and their interaction with the pore surface. However most nanopore experiments are carried out for the resistive pulse sensing of analytes such as DNA.

1.2 Motivation

DNA translocations in nanopores are widely used and studied. However, much of this research is based on the free translocation of analytes which occur at speeds on the order of $8 \mu\text{m/ms}$ [57]. This high speed means that most studies restrict themselves to conclusions based on population statistics of thousands of translocations. Perhaps the least understood part of the translocation process is the DNA capture by the electric field and threading through the pore. Indeed, the exact path and physical conformation of DNA as it translocates is not an easy characteristic to measure within $100 \mu\text{s}$ time traces while only having the current to base conclusions on. This motivates the two parts of this thesis. Firstly, to focus on the mechanical control of translocations and the added precision allowed by that control. Secondly, the addition of an extra measurable, in addition to conductance measurements, to better characterise and probe the nanopore system.

In order to shed light on the DNA threading piece of the translocation event puzzle, enabling mechanical control over DNA passage is a first and useful step. Control, such as offered via optical or magnetic tweezers, allows to better isolate the exact moment of capture and quantify it with available variables. The combination of optical tweezers with nanocapillaries has been achieved by a handful of groups[58; 59]. The versatility of this tool is not limited to nanocapillaries and may be used with other types of nanopores in order to probe previously unquantifiable aspects of their function[60; 61]. However, the extension of this tool into more dynamic studies of DNA translocation behaviour are rare[62] and have as yet not been applied to unravelling the DNA threading behaviour.

While the field of nanopores is widespread there are still many unknowns. Indeed, while the principles behind nanopore sensing are easy to explain, the exact microscopic physics at the nanoscale are often varied and complex. This complexity has been eluded to in the previous section where a rich environment of physical effects have been shown to be present at length scales between $1 - 100 \text{ nm}$. Most studies of this nanoscale physics is reduced by the fact that the probe is restricted to electrical characterisation. While this sort of characterisation can be powerful, as is shown also in this thesis, adding more strings to the bow of nanopore sensing would multiply the available data. Considering that flows and liquid transport across nanopores is of crucial importance to understand many of the most

promising applications (desalination[34], osmotic power generation[36], or mechanosensing[63; 64] for example) the addition of hydrostatic pressure sensing is a vital addition to the standard nanopore setup. In addition room-temperature ionic liquids (RTIL) are a promising new electrolyte for DNA translocations due to their high viscosity that slow down the passage of DNA through the nanopore, while remaining conductive enough to measure current drops[65]. However, much of RTIL behaviour, especially on the nanoscale, is still unknown. Considering this more fundamental investigations of RTIL and their properties on the nanoscale are of interest.

1.3 Thesis Layout

This thesis is split into two distinct parts. The first focuses on the wide topic of controlling translocations with optical tweezers. An in-depth introduction to glass nanocapillaries as well as the optical tweezers tool is given. The first main result discussed is the localisation and discrimination of DNA-protein complexes via controlled translocations[66]. The second result is that of measuring the fast relaxation of tensed DNA. Here, an overview of DNA polymer physics is given before moving on to DNA relaxation results. Related to both previous topics is the presence of electroosmotic flow. Considering and removing its effect on the dynamic measurements of DNA is vital and so discussions of EOF reduction are also deliberated. Finally, the combination of optical tweezers and MspA biological nanopores is discussed in the framework of force calibration for the single picometer resolution nanopore tweezers (SPRNT) technique. Biological pores in general and the SPRNT technique will be introduced before preliminary data on the combination of optical tweezers with free-standing lipid bilayers is presented.

The second part of the thesis focuses on confinement and nanofluidics. This broad topic is split into three distinct sections, the first of which links the thesis by using glass nanocapillaries to study the effect of nanoconfinement on room-temperature ionic liquids[67]. Introductions to the field of RTIL and their behaviour in confinement is given before main results are discussed. Secondly, the notion of applying additional hydrostatic pressure to silicon nitride nanopores is introduced with an emphasis on wetting behaviour and issues of contaminants or nanobubbles[48]. An overview of silicon nitride nanopores and the field of nanobubbles is given prior to the main result. A separate chapter discusses the main characteristics of correctly wetted silicon nitride nanopores under pressure with special attention paid to ionic current rectification and elastic deformation of membranes[68]. Finally, these topics are linked in the final chapter where the hydrostatic pressure system is used to probe RTIL in silicon nitride nanopores. Preliminary data is discussed and analysed within the nanofluidics framework detailed in the prior chapters.

Ultimately a global conclusion is given along with outlooks both for the controlled translocations and nanofluidics aspects of the thesis which place this thesis in the broader context of nanopore research and point towards exciting new opportunities in the field.

Controlled Translocations

Part I

2 Nanocapillaries combined with optical tweezers

This chapter will serve as a global introduction to the first part of this thesis focused on optical tweezers enabled control of DNA translocations. First an introduction to glass nanocapillaries and their usage as a high throughput, cheap, nanopore is presented. Next a brief discussion of the optical tweezers tool is made before discussing the combination of these two techniques.

2.1 Glass nanocapillaries as nanopores

Glass capillaries were first used in biological applications in the field of electrophoresis and patch clamping. In these early techniques, pipettes with opening diameters in the micrometer sized range were used. In the patch clamp technique a cell is trapped via suction onto the pipette tip that then allows the local application of potential to excite the cell membrane and read the response. This allowed pioneering research, for example into action potentials of neurons, or the behaviour of voltage gated trans-membrane channels[69]. In capillary electrophoresis, tubular capillaries are used for the separation of small analytes due to their different migration in electric field[70]. More recently however, pulled nanocapillaries have also been used in combination with fluorescence microscopy to detect analytes in the femtomolar concentration range[71].

During the development of solid state nanopores, glass capillaries became a fast and easy way to produce alternative pores to standard silicon nitride membranes[72]. This is due to their ease of fabrication which requires only a pipette puller, and a scanning electron microscope to verify the opening diameter. In this way, no complex and expensive clean-room procedures are needed, and batches of several dozen capillaries can be made with relative ease. Capillaries have been used for similar experiments as other solid state nanopores. Namely the translocation of DNA[41; 73], and the translocation of both free[33], and DNA bound proteins[74]. They can also be applied to other nanoparticle detection and characterisation including viruses[75], vesicles[76], or even to quantify the occurrence of immunoreactions[77].

Much research has also gone into the description of the shapes of such pulled glass nanocapillaries. A comprehensive study of the different pulled shapes was made using helium ion microscopy imaging, and categorised three main shapes: bullet, blunt, and hourglass[78]. These shapes were also studied in their effect on the electrical characteristics of capillaries such as linear and non-linear conductance, as well as the bearing on the translocation of charged analytes.

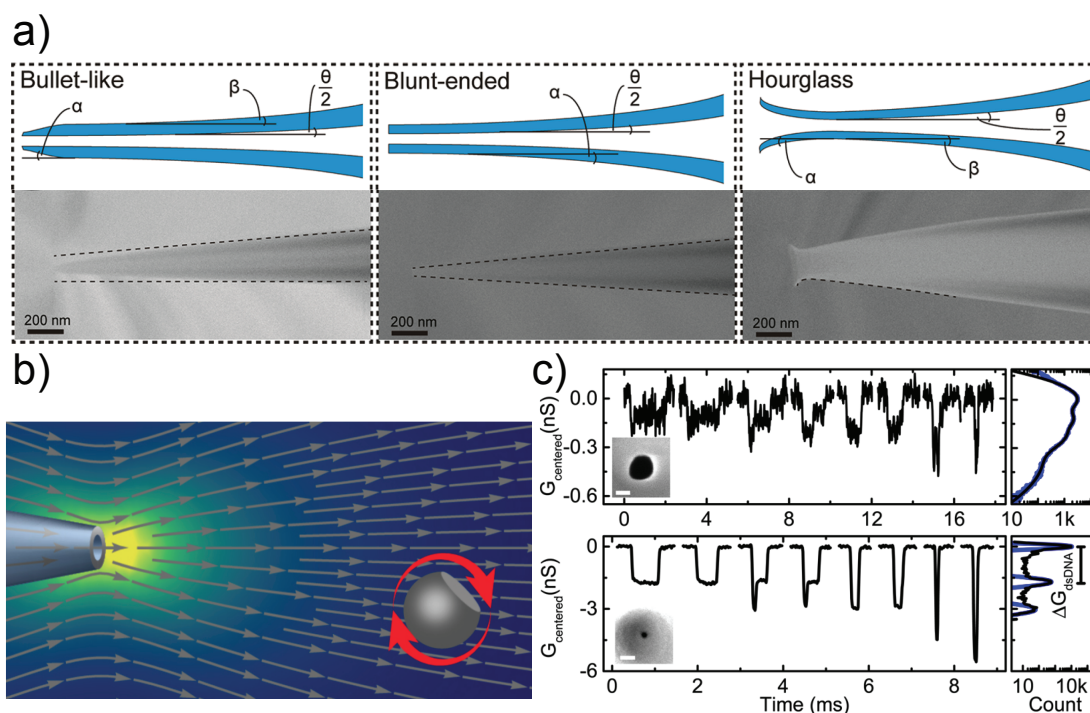


Figure 2.1 – Glass nanocapillaries as nanopores. **a)** Types of glass nanocapillary endings based on pulling parameters. Three different shapes can be discerned. Top row shows the models for each while the bottom row is a helium ion microscopy image of a representative capillary of that type. Image is adapted from ref. [78]. **b)** Visualisation of the electroosmotic flow outside a nanocapillary along with the truncated bead used to quantify it. Image is adapted from ref. [79]. **c)** Measurements of DNA translocations through large (top row) and small (bottom row) glass nanocapillaries. The graphs show how the signal to noise for translocations increases as the size of the pore is reduced. This is due to the fraction of the blocked pore growing larger. The large capillary is 75 nm in diameter while the small one is 14 nm in diameter as can be seen on the insetted SEM micrographs. Image is adapted from ref. [41].

Glass nanocapillaries can attain pores as small as 5 nm and as large as 100s nm allowing them a wide range of applicability. However, while glass nanopores cannot attain the ultimate size ranges of their silicon nitride or 2D material counterparts (sub-nm 1 nm pores), their size can be modified with relative ease. This modification can be made with the scanning electron microscope itself that shrinks the pore size due to electron irradiation[80]. Alternate options include the use of atomic layer deposition to controllably close the pore mouth[81], chemical reaction based modifications of size[82], or the coating with lipid bilayers[83]. In addition to modifying the opening size of glass nanocapillaries, multiple methods to modify the surface properties have been engineered. These surface modifications allows the tuning of properties that affect translocation behaviour, or to introduce controlled interaction between the analyte and the surface. Modifications range from the lipid bilayers mentioned previously that reduce surface charge, to hydrogel filled nanopores that modulate translocation properties[84]. Coating with single stranded DNA brushes in order to modulate target DNA interaction with the surface have also been engineered[85]. This allows the detection of ssDNA target binding in the nanocapillary. Other types of chemical modifications are also possible including fluorescent gold nano-cluster attachment[86].

This part will focus on the combination of glass nanocapillaries with optical tweezers. While a union of

2.2. Fabrication and characterisation of nanocapillary devices

optical tweezers with standard silicon nitride nanopores is possible[59; 60] it has one large disadvantage. Indeed the localisation of the pore in the membrane is more complex than with nanocapillaries due to a homogeneous and flat membrane. In nanocapillaries this issue is easily resolved due to the asymmetric shape immediately showing the tip in optical microscopy images. In glass nanocapillaries the combination with optical tweezers has allowed the direct characterisation of electroosmotic flow[79]. This is done by measuring the rotation of a truncated bead in an optical trap. The technique has allowed to map the flow outside a glass nanocapillary for different parameters such as salt concentration, thus observing different regimes where surface charges plays more or less of a role[87]. In addition to this, controlled translocations of DNA, and DNA constructs are possible. The added control over the translocation speed allows a higher accuracy when measuring translocation characteristics such as dwell time or current drop.[49; 58; 88].

2.2 Fabrication and characterisation of nanocapillary devices

The following sections will describe in detail the fabrication process of glass nanocapillaries along with their size characterisation. Nanocapillary-based devices used in the following chapters in combination with optical tweezers are fabricated first through laser assisted pipette pulling. Fabrication is followed by scanning electron microscope imaging with the possibility of shrinking, and finally, integrating into an optical tweezers compatible flow cell. The following sections describe these steps in detail.

2.2.1 Laser assisted pulling

In order to fabricate nanocapillaries a P-2000 laser pipette puller (Sutter) is used. The principle of action of this puller is the following: two mechanical arms are screwed to hold the ends of a glass pipette tube, a laser then illuminates the center of the pipette which heats the glass until melting point, once this point is reached the two ends of the glass tube start to move which triggers the mechanical arms to pull both halves apart thus creating two nanocapillaries. This device offers a large range of parameters that are user defined: the spot size of the laser, the laser power, the velocity that triggers the mechanical pull, the force of the pull, and any delay between the triggering and the force application. This versatility allows the user to define protocols that will pull a variety of pipette tube types (outer diameter, inner diameter, glass type) into various types of glass pores. These may be from the micron sized pores used in patch clamping, down to $\approx 5\text{-}10\text{ nm}$ nanopores that are the ultimate limit of the puller.

Examples of pulling protocols are given in the tables below. These serve only as an examples as different machines have different calibrations. Within the same machine over time, even if maintained properly, some creep in resulting pore distribution is also present. It is therefore crucial to always verify the quality and characteristics of such obtained glass nanopores.

Heat	Filament	Velocity	Delay	Pull
600	4	10	145	-
600	4	10	145	140

Table 2.1 – **Example pipette puller parameters for quartz nanocapillaries.** Quartz capillaries with an inner diameter of $300\text{ }\mu\text{m}$ and an outer diameter of $500\text{ }\mu\text{m}$ are used. Protocol yields nanocapillaries with a size distribution around $100 \pm 25\text{ nm}$

Chapter 2. Nanocapillaries combined with optical tweezers

Heat	Filament	Velocity	Delay	Pull
540	4	10	145	-
540	4	10	145	160

Table 2.2 – **Example pipette puller parameters for small silica nanocapillaries.** Silica capillaries with an inner diameter of $200\ \mu\text{m}$ and an outer diameter of $360\ \mu\text{m}$ are used. Protocol yields nanocapillaries with a size distribution around $50 \pm 20\ \text{nm}$

Heat	Filament	Velocity	Delay	Pull
430	4	10	145	-
430	4	10	145	160

Table 2.3 – **Example pipette puller parameters for silica microcapillaries.** Silica capillaries with an inner diameter of $200\ \mu\text{m}$ and an outer diameter of $360\ \mu\text{m}$ are used. Protocol yields microcapillaries with a size distribution around $3 \pm 2\ \mu\text{m}$

In this thesis two distinct types of glass tubes were used for experiments: quartz, and silica. The quartz tubes were used when possible as quartz has the best noise characteristics for electrical measurements such as those done in nanopore studies. The silica tubes on the other hand had the advantage of being coated on the outer wall in a layer of polyimide thus rendering the bulk tubing flexible. This coating was of course removed at the tip of the capillaries for the purpose of pulling, but the remaining coating on the blunt end of the capillary tube allowed easy interfacing with a wide variety of setups such as microfluidics connectors which would have otherwise shattered the quartz capillaries.

2.2.2 Scanning electron microscopy characterisation and shrinking

Once pulled it is crucial to measure the physical diameter of the obtained nanopore, which also acts as a verification of the pulling protocol. Throughout this thesis scanning electron microscopy (SEM) is used to verify the size of pulled nanocapillaries as well as in some cases to shrink them to desired size[72; 80]. To do so a batch of capillaries is placed in a custom holder such that they are 45° off of horizontal. In this way, by tilting the SEM stage by exactly 45° the capillaries are vertical and thus their orifice can be observed with the SEM.

When imaging glass nanopores the beam current of the SEM must be kept relatively low (100-200 pA) to reduce any charging effects due to the imaging of a non conductive substrate. It is also possible to shrink the size of the nanocapillary opening in situ with the SEM[72]. To do so the focus is left on the tip of the capillary for several minutes with a higher beam current (400-600 pA). The electrons interacting with the glass tip heat up the capillary until the opening begins to constrict. The advantage of this method is that the opening is continuously imaged allowing the user to stop the shrinking at the desired size of pore. It also allows to move the focus of the beam to correct for small asymmetries during the shrinking procedure.

The dynamics of shrinking can be altered by both the beam current and the accelerating voltage of the SEM. Larger currents lead to increased shrinking rates due to higher electron bombardment, and heating. Conversely, a higher accelerating voltage implies a higher penetration depth of the electrons into the glass, this means the tip itself is no longer the main focus of the heating, and the shrinking effect is reduced. In this thesis the accelerating voltage was kept constant at 3 kV.

2.2. Fabrication and characterisation of nanocapillary devices

In reality the geometry of pulled capillaries is complex and contains many variations between each capillary, pulling protocol, etc. This leads to a large spread in electrical characteristics especially for small pores[89] due to small shifts in the geometry close to the mouth of the pore. Shrinking procedures alter this geometry even more by rearranging the tip conformation into a double cone geometry as seen in figure (2.1).

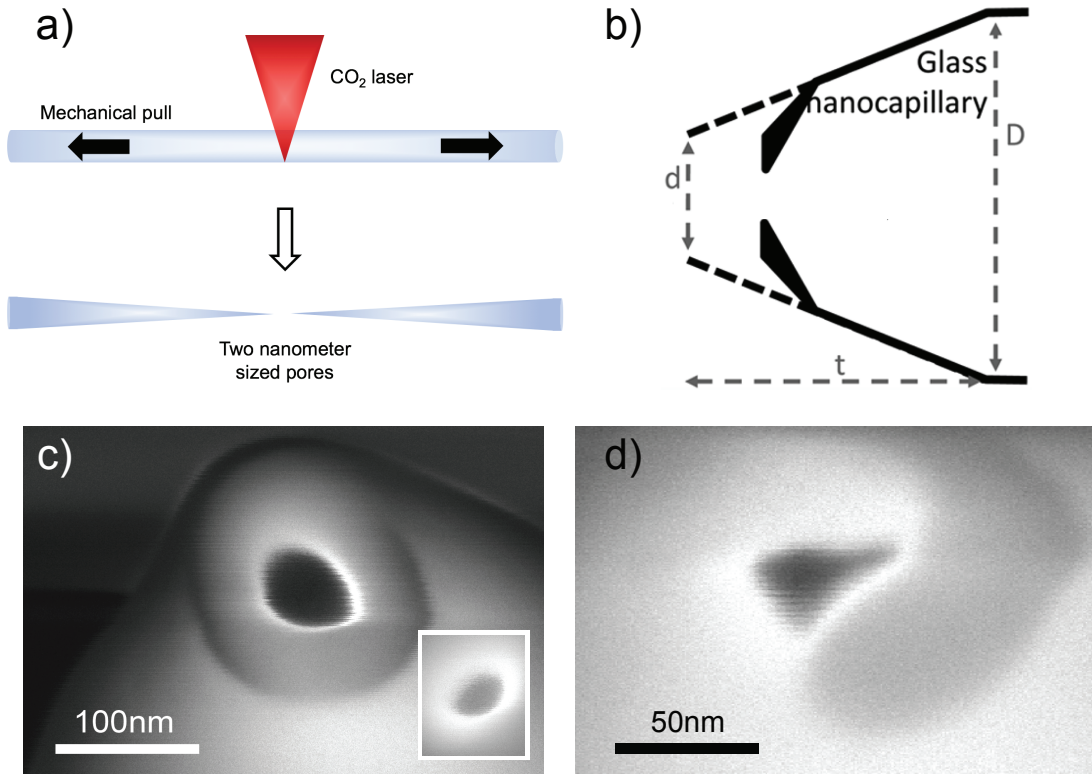


Figure 2.2 – Nanocapillary fabrication and SEM imaging. **a)** Schematic of operation of a laser pipette puller. CO_2 laser heats the center of the glass capillary before mechanical arms pull the tube apart. This creates two asymmetric glass nanopores whose size depends on the exact parameters of pulling. **b)** Geometry of a pulled and shrunk glass capillary. Normal capillary geometry is shown by the dashed lines where d is the pore size, D the large opening of the capillary tube, and t the taper length. These correspond exactly to the parameters of the conductance equation (1.1). Shrinking modifies the geometry into a double cone due to the local melting at the tip. Image is adapted from ref. [41]. **c)** Example SEM micrographs of capillary openings. Main image shows a ≈ 60 nm capillary whose geometry is circular and symmetric. The inset shows a 30 nm pore at the same scale. Main image is adapted from ref. [67] **d)** SEM micrograph showing a capillary with an asymmetric pore opening. Capillaries such as the one shown in panel d) should be rejected for experimental use due to the asymmetric geometry.

It was found that this double cone geometry lead to more characteristics that were hard for the user to control and therefore shrinking should be kept to a minimum to obtain the best results. Large pores (≈ 250 nm) are also inefficient to shrink with the SEM. Three major factors are responsible for this. The first is the time spent on a single pore to shrink it to a desired size as it takes a long time for the initial diameter to change. The second is that over such spans of size it is difficult to retain enough control on the shape of the pore opening and in most cases undesirable asymmetric pores are obtained (figure (2.1d)). Thirdly the shape of the taper will be greatly affected by such large shrinking, inducing more

irreproducibility in geometry.

The diameter of nanocapillaries is extracted by hand using the Fiji software from images such as that on figure (2.1c). The ultimate resolution of this technique is defined by the resolution of the SEM, taking into account the image quality due to charging, drift induced by a non conductive sample, and the angle of the capillary not being perfectly vertical. The smallest reliably obtainable pore size was found to be ≈ 10 nm. This image analysis also allows the user to discard nanopores that may have deformed due to shrinking and are no longer symmetric, or have some other impediment for use in experiments (figure (2.1d)).

2.2.3 Mounting into fluidic cells

Once diameters of nanocapillaries have been obtained, they must be mounted into experimental cells. The type of cell can be modulated depending on the final use of the nanopore: free translocations, optical tweezer experiments, interfacing with microfluidic adapters, etc. The most common experimental cell referenced throughout this thesis consists of two reservoirs, connected only by the nanocapillary. This cell is made by casting PDMS into a metal mould and heat curing. A nanocapillary is then manually positioned within the cell, and bonded to a glass microscopy slide with PDMS glue. These mounted nanopores may be kept in a dust free environment for months.

In order to fill nanocapillaries the following protocol is used. First, in order to render both the PDMS chamber, and the capillary hydrophilic, the whole cell is placed in an O_2 plasma cleaner for 2-5 minutes. The chambers are then filled via pipettes with the experimental buffer of choice, paying close attention to the fact that it be filtered through 20 nm filters, before being placed in a desiccator. The nanopores are then left in a reduced pressure environment for numerous cycles of ≈ 5 minutes with regular checks using an optical microscope to determine if the tip is filled. As one would naïvely expect the smaller the opening size the harder to fill a nanocapillary is. Heating or cooling the capillary was also found to aid in the removal of bubbles, and in many cases the nanocapillaries were prepared a day in advance and left at $4^\circ C$ overnight to absorb bubbles in order to obtain the best filling statistic.

Recently, a tremendously effective high throughput method of filling nanocapillaries has been described [89] that relies on thermal filling through microwave irradiation. This is similar to previous attempts at high success rate filling based off heating with filaments[90; 91], but has the advantage of being simple and possible for batch processes. Unfortunately, this came too late to be used in the experiments described in this thesis, but is highly recommended for any future work involving nanocapillaries, especially if opening sizes of < 50 nm are required where the classical method is less effective.

If stored in buffer and in humid conditions clean samples were found to be stable over several days, up to weeks. This time was drastically diminished once biological or other materials were inserted such as: DNA, polystyrene beads for optical tweezers, polymer coatings, lipid bilayers and their solvents, or other possible contaminants. These foreign materials tend to clog or affect the opening of the pore and render future experiments either impossible, or doubtful as to the reliability of their results. This is especially true if the only way to unclog a pore is via the application of voltage. If additional pressure is available then this is hypothesised to be less of an issue as discussed in great detail for the case of silicon nitride nanopores in chapter (7). These nanocapillaries mounted in PDMS flow cells are then ready to be interfaced with the optical tweezers tool.

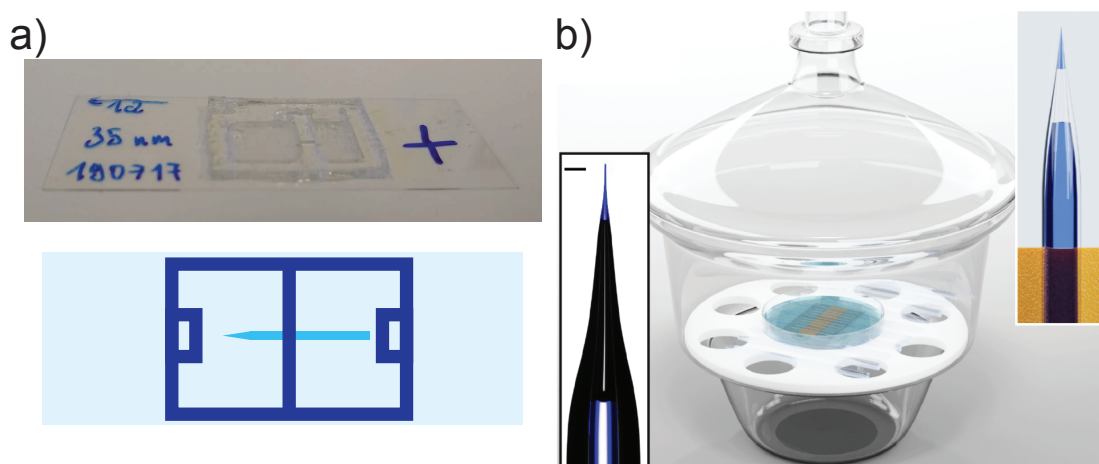


Figure 2.3 – **Mounting and filling glass nanocapillaries.** **a)** Top, photograph of a nanocapillary mounted into a microfluidic chamber and bonded to a glass microscopy slide. Dry samples may be stored in a dust free environment for months therefore labelling allows the cataloguing of mounted capillary sizes. Number references the SEM batch so as to link each capillary with an SEM micrograph of the tip. Bottom shows a schematic of the upper photograph with microscopy slide, and nanocapillary embedded in a PDMS chamber allowing pipetting of solutions through an inlet on each side of the chamber. **b)** Capillary filling procedure by placing the filled microfluidic chamber into a dessicator and performing cycles of degassing to remove bubbles from the tip of the nanocapillary. Upper right inset shows a schematic of the capillary tip and lower left inset an optical image of a capillary in the same state. Solution is coloured blue for better contrast and the scale bar is 50 μm . Image is adapted from ref. [89].

2.3 Optical tweezers

Optical tweezers (OT) are a useful tool for biophysics since they allow the precise manipulation of micron sized objects as well as allow the possibility of measuring forces down to piconewton resolution. Optical traps were first demonstrated by Arthur Ashkin who, in 2018, won the Nobel Prize in Physics for his development of this technique and its application to biophysics[18]. Since 1986 they have been used for a wide variety of studies including the manipulation of biologically interesting samples such as bacteria[92], or single cells[93]. Optical tweezers can also be applied to smaller scale objects such as organelles within cells[94], even down to applications in single atom trapping for supercooling experiments[95].

In biophysics though their real power lies in their coupled ability to be a force transducer able to measure the most fundamental forces acting on or within biological systems. To achieve this a micrometer sized bead is used as a force transducer. By measuring the displacement ΔX of the bead in the trap, the force being applied to it can be computed as $F_{\text{OT}} = \kappa \Delta X$. The stiffness of the optical trap is κ and must be calibrated as discussed below. Thanks to OT, researchers have been able to gain insights into the workings of a myriad of different fundamental biological principles. Examples of such studies are proteins' interaction with DNA[96]. Specific examples of such interactions are RNA polymerase (RNAP)[97; 98], helicases[99], or dynamics of nucleosome disassembly[100]. Secondary structure and unfolding of RNA[101], or even proteins[102] can also be studied with such a tool leading to descriptions of unfolding transition states as well as the stability of such states. This is possible due to the fundamental single molecule nature of optical tweezers experiments allowing to extract

Chapter 2. Nanocapillaries combined with optical tweezers

information from non-equilibrium experiments. Force is not the only measurable in OT as rotation may also be probed as is exemplified in the previous discussion of EOF outside nanocapillaries[79]. It was also put to use to describe the mechanisms of viral packing[103].

Optical tweezers also played a crucial role in the minute understanding of DNA and its elastic properties which will be introduced in detail in chapter (4) since it deals with elasticity of DNA retraction from a tensed state. This non-exhaustive list of the applications of optical tweezers convinces that it is a tool of many varied uses. Its exact functioning and calibration is detailed below before the combination with nanocapillaries is briefly explained.

2.3.1 Principle and calibration

Optical tweezers work on the fundamental principle of photon momentum, and the fact that, at small enough scales, this momentum can affect particles interacting with a light beam. The interaction of laser light with an object can be divided into two contributions called the scattering force and the gradient force[104; 105]. These two forces arise from the fact that when a light beam interacts with, for example, a polystyrene bead, part of the beam will be reflected and part of it will be refracted. This refraction and reflection will lead to a change in the photons' momentum which in turn through conservation of momentum will lead to a change in momentum of the bead. The momentum change due to reflection will always be in the propagation direction of the light beam thus pulling the bead along with the beam, this is the scattering force. The gradient force comes from the fact that laser beams have a Gaussian profile and thus more momentum change will happen at the point of highest intensity, i.e. the center of the beam. In this way the forces due to refraction of the beam will pull the bead to the center of the laser.

This of course does not create an optical trap as the scattering force pushes the object along the laser trajectory. In order to create a trap two basic procedures are possible[106]. One of the simplest is to use two counter propagating lasers perfectly aligned. In this way the gradient forces that are perpendicular to the direction of propagation remain while the two lasers compensate for each other's scattering force. The second possibility to create a trap, and the one used in this thesis, is to use a high numerical aperture lens to focus a single laser beam creating a trapping point just above the focus of the laser. The explanation of why this trap is created depends on the length scale of the particle in comparison to the wavelength of trapping light. In the case where the object is larger than the wavelength, the Mie regime, ray optics can be used to explain the phenomena as on figure (2.4b). In the case where the particle is smaller than the wavelength of the trapping light, the Rayleigh regime, quantum optics must be used. A detailed physical explanation of the Rayleigh regime can be found elsewhere[107] since this thesis will only deal with microscopic beads large enough to be considered within the Mie regime.

The reason this discovery allowed so many new breakthroughs in biophysics is that both the size of particle able to be trapped (25 nm - 10s μ m) and the force it is able to measure (1-100 pN) are exactly in the range of interest for biological samples. As an example both kinesin and myosin motors apply forces in the single digit pN range[108; 109; 110]. RNA transcription has been shown to exert higher forces with measured values being ≈ 14 pN[111].

There are different ways of calibrating an optical tweezer setup in order to obtain the stiffness κ of the trap and relate the displacement of a particle to the force it sustains. The most common, and the one used throughout this thesis, will be presented here as it only requires a measurement of the Brownian motion of a trapped particle. Other methods utilise a bead stuck to a surface along with a

measurement of the Stokes drag on a moving bead. Another possibility that allows for calibration to be performed once per instrument as opposed to once per measurement is to directly measure the change in momentum of the light beam by collecting the scattered light[112].

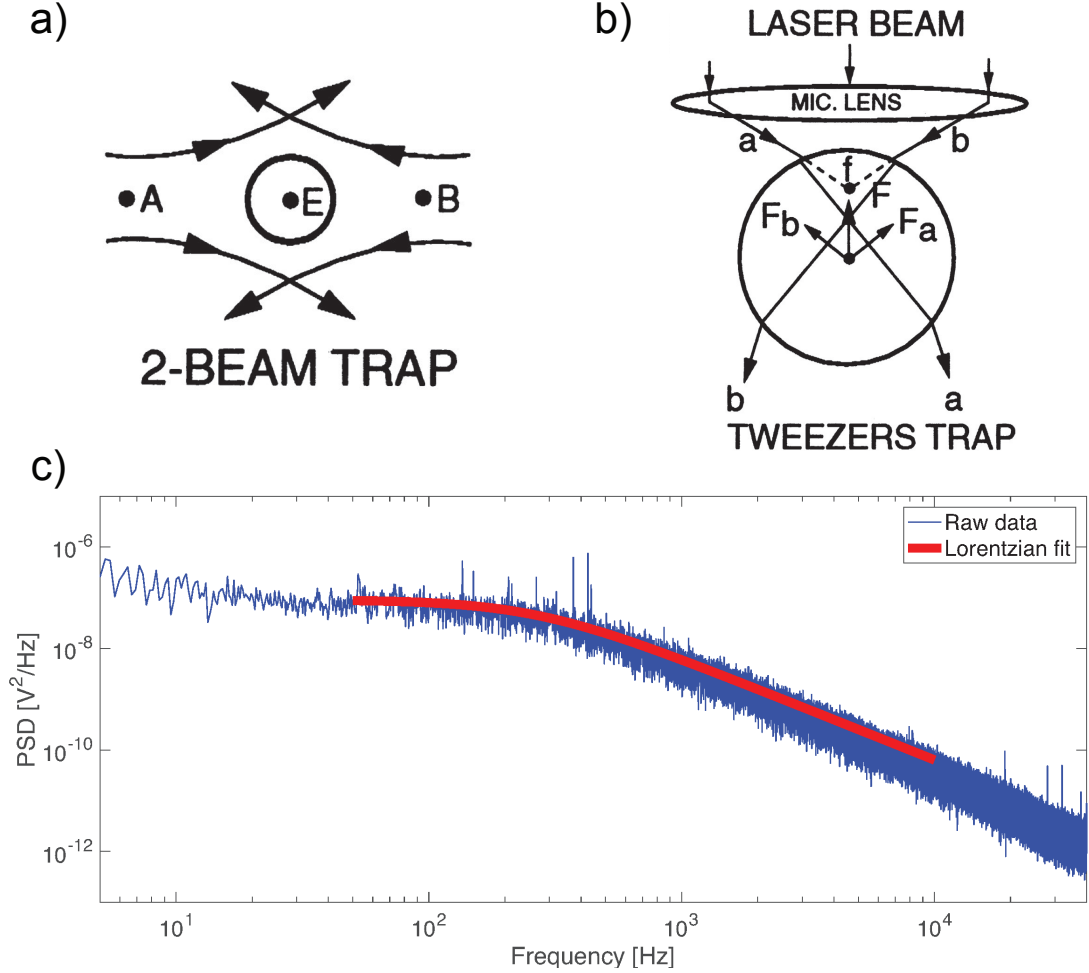


Figure 2.4 – Principle and calibration of an optical trap. **a)** Schematic of a dual beam optical trap. The counter propagating beams automatically negate the scattering force yielding an optical trap. **b)** Ray optics for a single beam optical trap. The focusing of the lens induces the trapping of objects close to the focus of the beam. Rays *a* and *b* and the optical forces induced by them are shown as well as the resultant trapping force. Panel a) and b) are adapted from ref. [106]. **c)** Example of the calibration of an optical tweezer setup via the power spectrum method. Both the raw PSD and the Lorentzian fit are shown. Stiffness as extracted from the fit parameters is $\kappa = 35 \text{ pN}/\mu\text{m}$.

While measuring the brownian motion of a trapped bead a quadrant photo diode (QPD) detects the laser beam after the trapped object and gives a signal proportional to the laser beam displacement, and thus to the trapped bead displacement. The power spectral density (PSD) of the voltage readout of the quadrant photo diode can then be extracted. The PSD of an optically trapped bead follows a Lorentzian profile[105]:

$$S(f) = \frac{s^2 k_B T}{\pi^2 \beta (f_0^2 + f^2)}, \quad (2.1)$$

Chapter 2. Nanocapillaries combined with optical tweezers

where s is the sensitivity of the detector, k_B is the Boltzmann constant, T the temperature, f_0 the cut-off frequency, and $\beta = 3\pi\eta d$ the drag with η the viscosity of the solution and d the diameter of the particle. By fitting a Lorentzian profile to the power spectral density of the restricted Brownian fluctuations of a trapped particle, the sensitivity and the cut-off frequency can be extracted. These two quantities allow to compute the stiffness of the trap through:

$$\kappa = 2\pi\beta f_0. \quad (2.2)$$

This shows the power of the PSD method where both the sensitivity of the detector and the trap stiffness are obtained from one fit (figure (2.4c)). From a practical perspective, at the end of each experimental day, beads with no analytes attached are flowed into the microfluidic chamber and high acquisition rate (500 kHz) traces of their restricted Brownian motion are recorded (≈ 10 different beads). These are then analysed with a home-made Matlab program and the average stiffness and sensitivity are recorded for use with the experimentally obtained data.

2.3.2 Optical tweezer setup

Figure (2.5) shows the experimental layout of the optical tweezers setup. Shortly, the laser beam is expanded by a telescope to overfill the back aperture of a high numerical aperture objective. After having travelled through the sample plane the light is then gathered by a condenser before being deflected to a quadrant photo diode for detection. This quadrant photo diode measures the deflection in both the X and Y axis to determine the deflection of the trapped object, and through calibration the force acting on it. The white light path is inverse to the laser beam and two dichroic mirrors are used to separate these paths and ultimately direct the white light to a CCD camera.

Two such optical tweezers setups exist in the laboratory each with slightly different characteristics. One has at its core a $Nd : YVO_4$ solid state laser with a wavelength of 1064 nm (chapter (4) onwards) while the other has a fibre coupled $Nd : YAG$ laser with a wavelength of 839 nm (only used for chapter (3)). In both cases to avoid fluctuations in intensity the lasers are run at maximal power (2 and 1 W respectively). A power control system using a polariser is put in place in order to control the power at the objective which is in the range of 30-150 mW and is directly related to the obtained trap stiffness.

2.4 Combination of nanocapillaries with optical tweezers

To perform experiments combining nanopores with optical tweezers the sample cell (section 2.2.3) is mounted on to a nanopositioning stage (three axes with $\pm 50 \mu\text{m}$ range) on the optical tweezers and additionally combined with a current amplifier (axopatch 200B unless otherwise specified) in order to read the ionic current through the nanopore. This requires the use of electrodes placed in either chamber of the microfluidic cell. Unless otherwise specified, throughout this thesis the choice of electrodes are AgCl electrodes. These are created by chlorination in a 3 M KCl solution by applying a ≈ 1.5 -2 V DC bias for ≈ 30 minutes with a sacrificial silver electrode. Chlorination is confirmed by the change in colour of the electrode. AgCl electrodes were always made fresh for each experiment to ensure best current characteristics.

Readings from the quadrant photo diode and the current amplifier are digitised and read into a custom LabVIEW software which allows real time tracking of the values and the application of bias

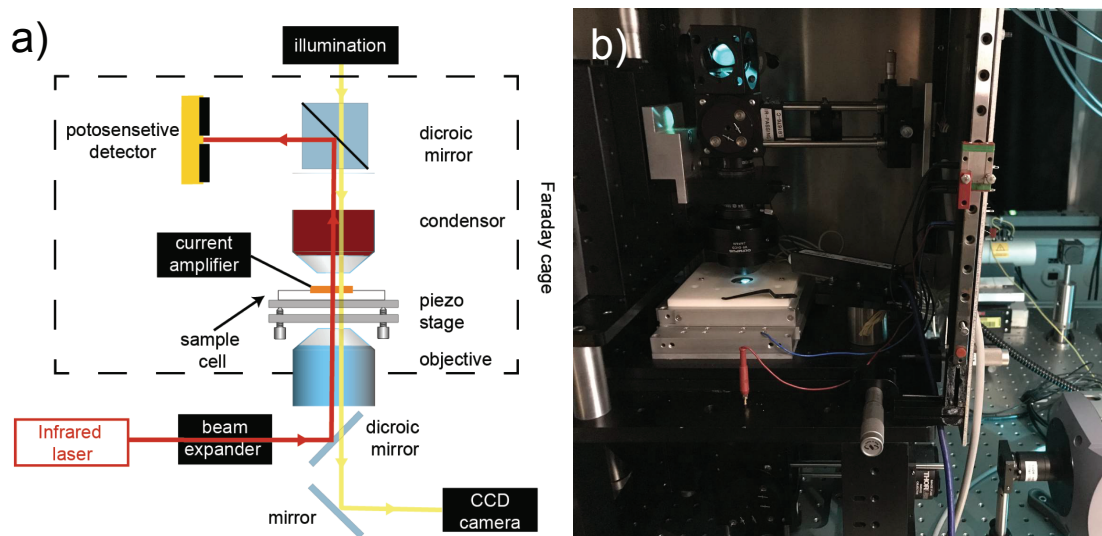


Figure 2.5 – Optical trap setup. a) Schematic of the optical tweezers setup with the laser beam path in red and the white light path in yellow. These two paths are separated by two dichroic mirrors allowing the laser beam to be directed to the quadrant photo diode while the white light is detected by a CCD camera. The high NA objective allows to create the steep light gradient necessary for the optical trap, and the amplifier allows simultaneous current measurements on the nanopore system. Image is adapted from ref. [113] b) Photograph of the augmented OT setup with addition of a metal Faraday cage and LED-filter combination for simple fluorescence imaging as used in chapter (5).

voltage as well as nanopositioning stage control with the help of a joystick. Data is acquired using a National Instruments FPGA which allows nine variables to be acquired at fast acquisition rates (from 10 kHz up to 500 kHz). This allows the four outputs of the QPD (dX , dY , S_x , and S_y), three axes of the nanopositioning stage (X , Y , and Z), the applied voltage V , and the measured current I to be simultaneously acquired. Later analysis is performed using a variety of home-made scripts in Matlab and Python.

Some additions were made to the optical tweezers setup for chapters (4) and (5). They will be shown in detail later but shortly the custom LabVIEW program was augmented with the possibility of automating cycles of data acquisition. This relied on the automatic detection of level changes in the force trace that allowed DNA entering events to be the trigger for stage movement and voltage application. Furthermore a metal plated Faraday cage was built out of aluminium in order to obtain a better signal to noise in the current measurement. Finally the white light illumination was modified such as it could be switched to a LED illumination which, in parallel with an appropriate filter in front of the camera, allowed for simple fluorescence imaging (figure (2.5b)).

3 Localisation and discrimination of DNA-protein complexes

Results contained in this chapter can be found in the following publication: R. D. Bulushev, S. Marion, E. Petrova, S. J. Davis, S. Maerkl, and A. Radenovic, "Single Molecule Localization and Discrimination of DNA-Protein Complexes by Controlled Translocation Through Nanocapillaries", *Nano Letters*, 2016, 16, 12, 7882-7890.

Author contributions: R.D.B., A.R., and S.J.M. designed the study. R.D.B. carried out experiments. S.J.D. wrote analysis scripts and performed data analysis. S.M. performed simulations and implemented analytical and numerical models that allowed data interpretation. E.P. synthesized dCas9 and guide RNAs. A.R. supervised the research. S.J.D. and S.M. wrote the manuscript. All authors provided important suggestions for the experiments, discussed the results, and contributed to the manuscript. R.D.B., S.M., E.P., and S.J.D. contributed equally to this manuscript.

Results are also contained in ref. [113].

3.1 Introduction to DNA-protein complex detection

Cellular functions from DNA replication, transcription regulation, repair, to chromosome maintenance are all regulated and maintained by DNA protein interactions[114]. This makes the thorough understanding of such interactions a key to better modelling and approaching cellular function. Indeed, studying these interactions allows not only a better fundamental understanding of cellular processes, but allows the design of better biotechnological applications[115]. DNA-protein interactions occur mainly through the protein binding to specific recognition targets on the DNA sequence[116]. Characteristics such as the binding mechanism, search mechanism, and strength of interaction are thus key factors in describing them[117]. Specificity and the occurrence and relative importance of non-specific binding is also a factor to study, especially since non-specific binding is postulated to be an important factor in the efficient search for specific binding targets[116]

Because of their ubiquity and importance many bulk and single molecule assays have been designed over the years to quantify DNA-protein interactions. A plethora of such methods exist such as the gel based electrophoretic mobility shift assay (EMSA)[118] and nuclease footprinting[119]. Other microfluidic based approaches such as protein binding microarrays and chromatin immuno-precipitation based microarrays[120; 121; 122], or mechanically induced trapping of molecular interactions (k-MITOMI)[123] have emerged more recently. The use of gel electrophoresis, in the example of EMSA

Chapter 3. Localisation and discrimination of DNA-protein complexes

is used to directly visualise a shift between the control DNA strand and DNA-protein complex due to its different migration under electric field. In nuclease footprinting DNA strands are protected from degradation via DNAase by the protein interaction and a gel assay verifies this fact. While gels can be powerful predictors of protein binding the more recent microfluidic based approaches allow for more quantitative outputs of protein binding affinity[121]. They also allow higher throughput than standard gel assays allowing, in some cases, the genome-wide mapping of protein-DNA interactions[122].

While these ensemble methods are successful in measuring average characteristics of DNA-protein interactions, they inherently possess drawbacks that may bias the measurements or miss certain fine details completely. Indeed, due to the ensemble nature of the techniques they are blind to fine molecular detail. Important characteristics such as transition states, multiple pathways of interaction, back-stepping, or any multimodal distributions are ironed out by the average over an ensemble of molecules. To fill this gap, single molecule techniques have been employed to measure the finer structure of DNA-protein interactions. Another possible effect is that these bulk assays often employ the use of labelling, chemical cross linking, or complex amplification protocols that may hinder the native molecular protein conformation. Since this structure is one of the key driving forces of protein activity, any modification, however small, may skew the DNA-protein binding and thus miss key elements of the interaction.

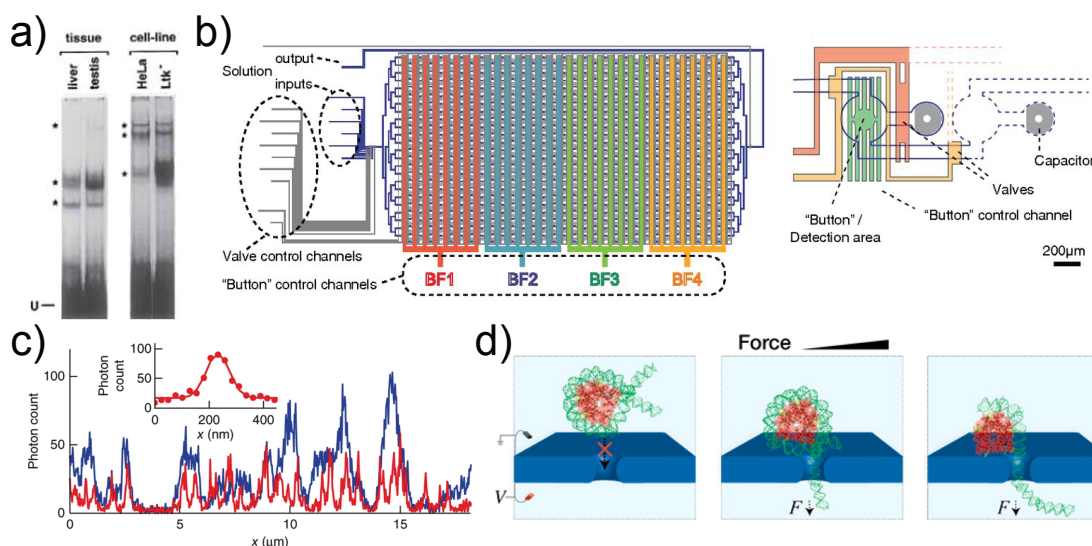


Figure 3.1 – Measuring DNA-protein interactions. **a)** Image of EMSA to distinguish protein binding. Image adapted from ref. [124]. **b)** Microfluidic setup for kinetic MITOMI experiment. Left panel shows the whole microfluidic blueprint used for a device capable of 768 different molecular interaction assays. Right hand side shows one of the unit cells which performs the assay. Image was adapted from ref. [123] **c)** Comparison of dye localisations between standard confocal microscopy (blue) and STED microscopy (red) on a stretched λ -DNA molecule. The molecule is stretched via optical tweezers. Image is adapted from ref. [125] **d)** Schematic of the unravelling of DNA nucleosome complexes within a nanopore. Unravelling of the nucleosome structure is mediated by the higher and higher application of voltage bias, and thus force on the DNA. Image was adapted from ref. [126]

The purpose of applying single molecule techniques to DNA-protein interactions is then to complement the knowledge obtained through bulk techniques but with higher sensitivity to molecular details. Different single molecule tools may be applied to such interactions, including AFM that can be used to measure, for example, the activity of RNA polymerase on DNA deposited on mica surfaces[127].

3.2. Using nanocapillaries combined with optical tweezers

Microscopy methods such as fluorescence resonance energy transfer (FRET) gives signals depending on distances in the range of 10-100 Å allowing great precision when it comes to structural components of DNA protein interaction[128]. Optical, and magnetic tweezers also take an important role in this study of DNA-protein interactions at the molecular level. Magnetic tweezers have been used to probe the translocation kinetics of helicases with varying temperature[129]. When combined with fluorescence detection optical tweezers have enabled tools such as stimulated emission depletion (STED) microscopy to probe DNA-protein interactions even on crowded DNA with much higher resolutions than possible with standard confocal microscopy[125].

Nanopores are also a single molecule tool and are routinely used to detect single DNA molecules passing through them. In this way they may also be applied to gain information on DNA-protein interactions[130; 131; 132; 133; 134]. Their fabrication allows an easy control over the exact opening size of the nanopore and they can thus be tailored to the protein of interest[74; 135]. Their surface may also be modified[136] in order to change the interaction between the pore and analyte thus offering a highly tunable tool for DNA-protein sensing. Surface modifications range from polymers[137; 138], to lipids [83; 139; 140; 141], gels[142], or other chemical modifications [143]. Nanopores may also be used for force spectroscopy by using a pore too small for the passing analyte thus trapping the biomolecule. By increasing voltage bias the force on the complex increases until bond rupture[126]. Alternatively bond lifetimes may be probed by monitoring the trapped state[144].

Deducing characteristics from the ionic conductance drop of a freely translocating DNA-protein complex is possible, and high throughput compared to other single molecule tools. However, due to the speed of translocation being relatively high and the spread of conductance drops being large it is not the ideal tool to localise and characterise such interactions[132; 145]. Most free translocation experiments are conducted at high salt concentration as compared to physiological conditions which allows only a fraction of relatively robust proteins to be studied as well as affecting the exact conformation, charge, and thus interaction characteristics which are no longer comparable to physiological states[146; 147].

To resolve the issues of fast translocation and non-physiological salt conditions, combinations of nanopore sensing with optical tweezers[49; 60; 61] are used. Combining OT with nanopores allows a high enough detection precision at physiological salt concentrations while simultaneously controlling the movement and removing the translocation speed from the equation. Two different proteins will be used in this chapter to show the localisation and discrimination power of the technique. The choice of studied proteins was RNAP and dCas9 due to their importance for transcription, and recent gene editing studies respectively[148; 149]. This choice was additionally motivated by the fact that creating multiple different binding sites at different locations along a DNA template is relatively simple. Indeed dCas9 with its RNA guide binding system allows to synthesise multiple guides for a single DNA strand. In the case of RNAP, different primers for a PCR reaction allow to modify the location of the binding site along a DNA template.

3.2 Using nanocapillaries combined with optical tweezers

The following sections will show the power of the combination of OT with nanopores by precisely localising two types of proteins on DNA and allowing two distinct methods of discrimination based on charge and size of the protein complex. This also serves as an example of the resolving power and versatility of controlled translocations before applying them to more complex experiments (chapter 4 probes dynamics of DNA retraction). Optical tweezer compatible microfluidic cells containing nanocapillaries with an opening size in the range 30-60 nm are prepared as described in chapter (2).

Chapter 3. Localisation and discrimination of DNA-protein complexes

These are then used for controlled translocations of DNA-protein complexes as described below. All experiments were conducted at physiological salt and pH conditions. The buffer was 100 mM KCl, 10 mM HEPES, 5% glycerol, pH 7.5 with the addition of 0.01% TWEEN for the RNAP experiments to reduce sticking of the complex to the glass nanocapillary.

A controlled translocation experiment is conducted as follows. First, a bead, previously incubated with DNA-protein complexes is trapped in the OT and is brought via a micro-manipulation stage to the tip of the nanocapillary. Bias voltage is then turned on and the bead approached to the tip of the nanocapillary until a DNA entrance event is seen as a discontinuous shift in the measured force and current level. Once this is detected the nano-positioning stage z is moved such that the capillary moves away from the bead at a constant speed $v = dz/dt = 500$ nm/s until the DNA exits at y_x and both the force and current retrieve their open pore values. During this controlled translocation the force and current profile are flat due to the constant size and charge of bare DNA. However, if a protein complex is present on the DNA a spike at y_p in both force and current is observed. An example trace in both current and force is seen on figure (3.2b). The stage position z and bead-nanocapillary distance y are used interchangeably, and distances labelled s are along the contour of DNA.

The shape of the force spike is dependent on the charge of the protein complex. For the considered case of an effectively positive complex the protein will jump out of the nanocapillary once it senses the electric field in the tip. An increased coiling of the DNA is caused by the jump of the protein outside the nanocapillary and as the stage is moved further the protein complex stays in the same position until the tension in the DNA is returned to the pre-jump level at which point the complex moves away from the nanocapillary with the DNA (upper inset of figure (3.2b) shows schematics of these different states). If the protein were oppositely charged this behaviour would be inverted with a symmetric shape of the jump[61]. Namely a tension applied to the protein until the force overcame the electric field by jumping out.

As described in chapter (1) the electric field in nanocapillaries is extended in space as compared to flat silicon nitride membrane pores or quasi-2D pores due to geometrical effects. This can be taken into account with a potential of the form $1/(1 + x/\xi)$ where x grows inside the capillary and ξ is the electrostatic decay length. ξ can be extracted by fitting the decay in force profiles of bare DNA events and in this case was approximately 75 nm[49; 58]. This extension will affect the localisation precision in capillaries with respect to nanopores as the sensing region is enlarged leading to more of the DNA and protein to contribute to the signal. This is also the reason why nanopores designed to sequence DNA are engineered to have ultimate thicknesses (biological pores or quasi-2D membranes) as the contribution from too many nucleotides at once reduces the resolving power.

3.2.1 Localisation of DNA-protein complexes

To show the localisation power of nanopores combined with OT, DNA-protein complex rulers are designed. Five different RNA guides are synthesised for dCas9 so as to have five distinct binding sites all along a 16.2 μm λ -DNA. For RNAP, a shorter DNA template is used which is 2.45 μm long with two distinct binding sites having been engineered. These two rulers allow to probe the difference in behaviour between short and long DNA constructs. Data was acquired both with single binding sites active and with the possibility for multiple sites. This did not have an effect on the data and some events were recorded with multiple protein complexes bound. This shows that the technique may be optimised for multiplexed detection of proteins.

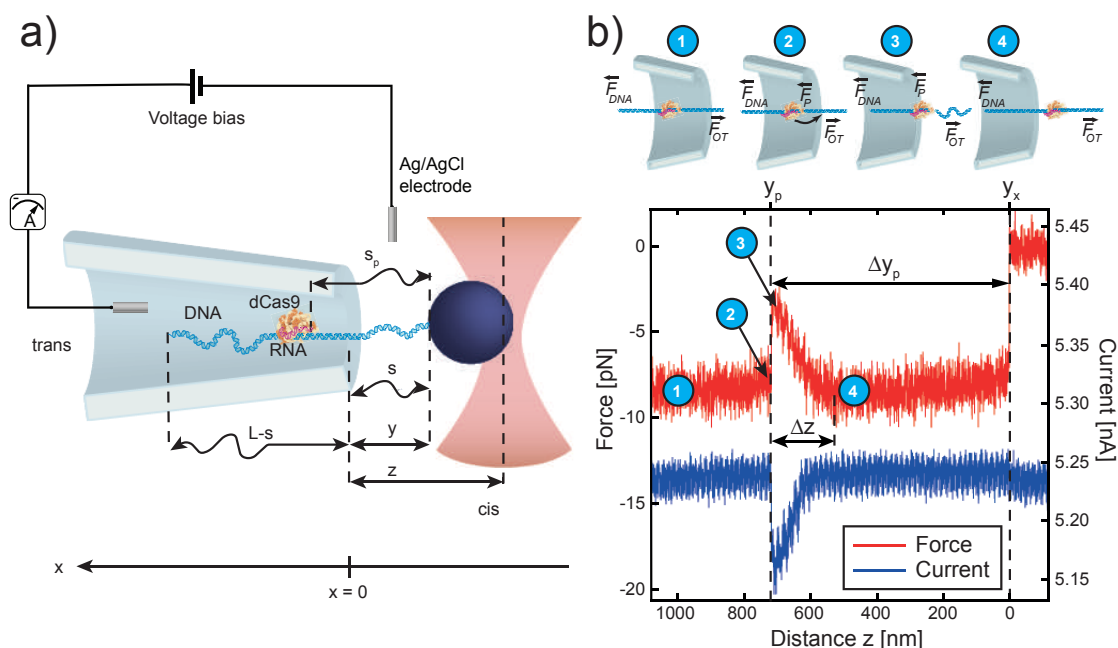


Figure 3.2 – Schematic of the OT-nanopore setup and example of raw data traces. **a)** Schematic of the experimental setup with a glass nanocapillary, electrodes with current detection, optically trapped bead, and extended DNA with protein complex present. Values along y and z axes are equivalent and values along the s axis represents distance along the DNA contour. **b)** Examples of raw data in both force and current showing the flat DNA trace with an additional jump in both force and current due to the protein complex. Trace ends with the exit of the DNA molecule returning the current to the open pore value and the force to 0. Schematic above the graph represent the different positions of the protein at key moments of the translocation and are signaled by the corresponding numbers on the raw traces. 1: Protein prior to the jump event. Force and current profiles are flat. 2: Protein just before the jump event when entering the electric field zone. 3: Protein just after the jump event when the tension is relaxed in the DNA due to the Δz jump. 4: Protein once the stage has moved sufficiently that the tension in the DNA is restored and the flat profile in both force and current is regained. Figure is adapted from ref. [66].

Localisation was also verified to be equal for both forwards (i.e. from in to out) and backwards (i.e. from out to in) controlled translocations of the DNA-protein complex. This was done by flossing a single DNA-protein complex back and forth multiple times without allowing the DNA to exit completely in order to build up enough statistics to estimate the distribution. Both for RNAP and for dCas9 the direction of travel made no difference to the extracted binding site position as is seen on Figure 3.3.

The binding site position Δy_p is determined thanks to the protein complex peak position y_p and the DNA exit position y_x : $\Delta y_p = y_x - y_p$. In this way histograms of locations are obtained for all binding sites and both proteins. Non-specific binding of these proteins is possible[150; 151; 152; 153] and so distinguishing a specifically bound protein from an unspecific event is important for the accuracy of the result. In order to avoid bias in the determination of the binding site locations they were not known a priori. First, data was acquired and was analysed to determine the measured length of the DNA. If the error in the DNA length was more than 10% the trace was discarded as being a sheared DNA molecule. This shearing is common with long molecules such as λ -DNA and is usually due to experimental manipulation (i.e. pipetting or centrifugation) or due to inadequate storage (freeze thaw

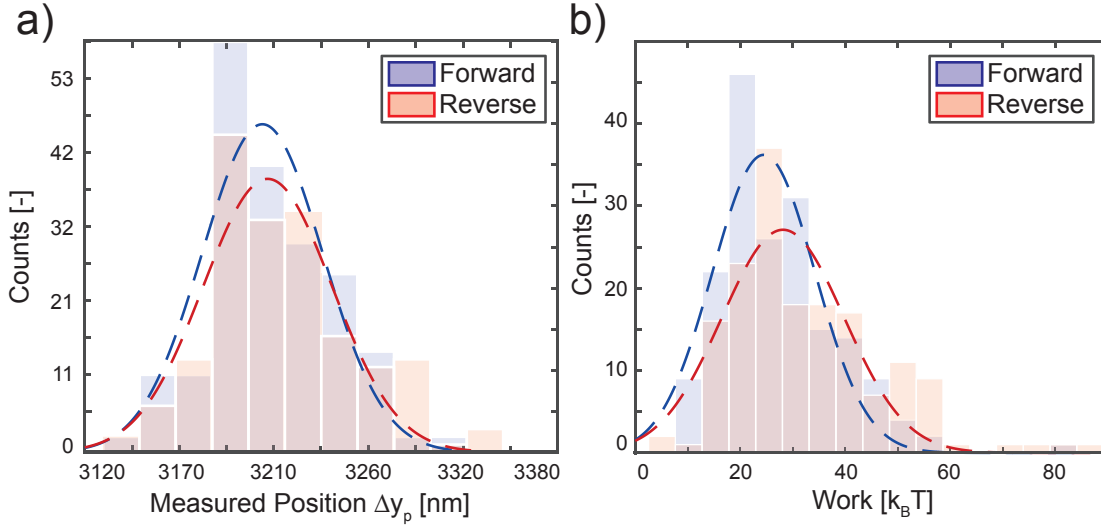


Figure 3.3 – **Forwards or backwards localisation and work.** **a)** Distribution of binding site localisations Δy_p for dCas9 protein binding site at 3567 nm. This data was obtained from ten different DNA-protein complexes with each complex being subjected to approximately 20-40 in-out cycles. No difference is observed in the distributions confirming the localisation does not depend on the direction of the protocol. **b)** Distribution of non-equilibrium work W_i obtained by integrating the force-distance curve from the events on panel a). A small difference is observed between forward and reverse works but not large enough to warrant a more thorough analysis. Work is introduced in the context of discrimination below. Figure is adapted from ref. [66].

cycles)[154]. After this first filtering of traces a statistical analysis of the population using a modified Z score is used to distinguish what is a specifically bound protein[155]. This Z score allows to distinguish events from the distribution and is defined as:

$$Z_{\text{score}} = \left| \frac{0.6745(y_i - |y|)}{\text{MAD}} \right|, \quad (3.1)$$

where $|\cdot|$ represents the median value of \cdot , y_i is the location of the protein to classify, and MAD is the median absolute deviation $|y_i - |y||$. If the Z_{score} is above 3.5 for a given trace this is considered as not part of the distribution of proteins and as an unspecific site. This analysis for each binding site can be seen in Figure 3.4. On this figure the non-specific data does not show any clustering. However, a relatively small amount of non-specific binding is present. An interesting extension to the study would be to extract many more non-specific events to determine if they cluster around specific regions of the DNA. For example for dCas9 it may be that non specific events are due to one base-pair mismatches between the RNA guide and the template DNA which would affect the distribution of non-specific events.

Once protein events are classified as being specific they can be plotted on the whole length of the DNA and compared to the theoretical position of the protein s_p . Relatively good agreement is found between the experimentally measured locations and the theoretical ones, especially for binding sites close to the free end of DNA, as seen on figure (3.5). The standard deviation of the localisation is 97 nm and 49 nm for dCas9 and RNAP respectively (over all binding sites). This error is attributed to the large variation in electroosmotic drag (figure (3.6d)) induced by subtle variations in the nanocapillaries used,

3.2. Using nanocapillaries combined with optical tweezers

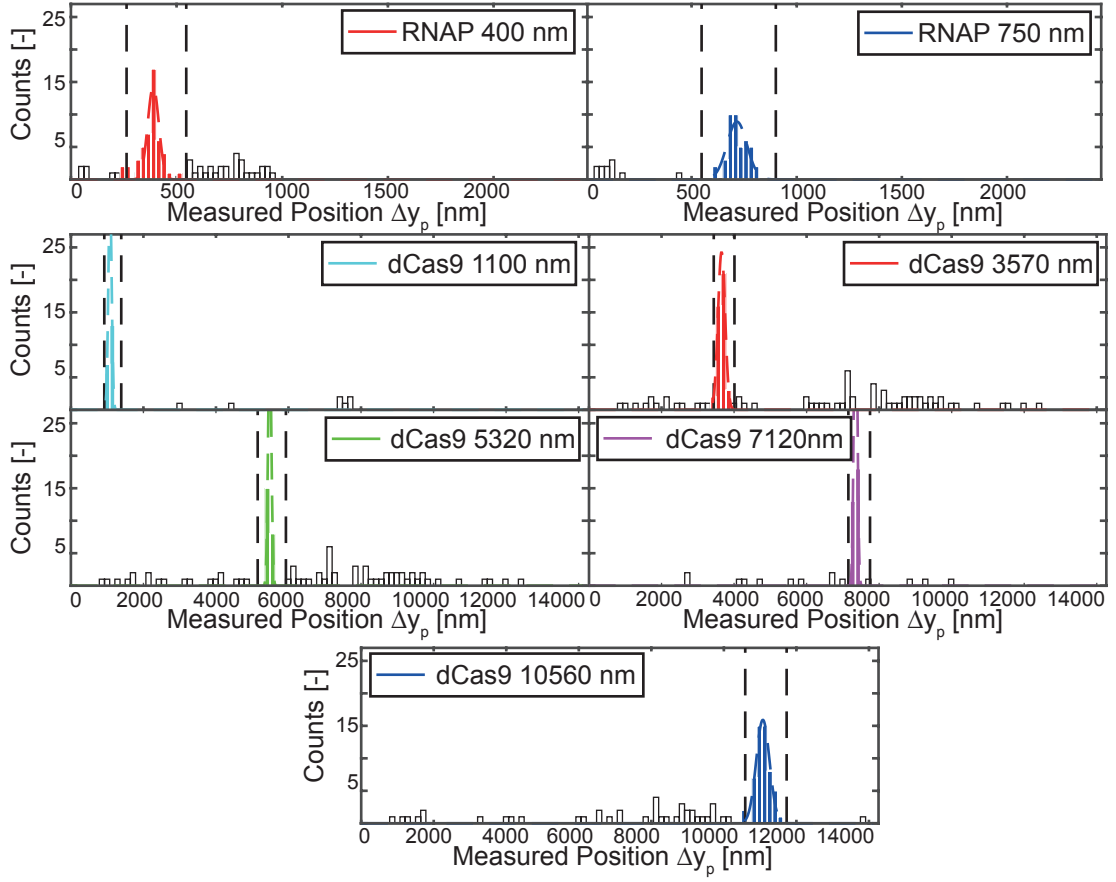


Figure 3.4 – **Distinguishing non-specific binding via statistical analysis.** Each figure represents a histogram of every protein jump event measured. The coloured events represent the data distinguished as specific by the Z score test and the white bins are the rejected data based on the same test. Black dashed vertical lines show the limit between specific and non-specific binding. No clear distribution of non-specific events is found, mostly due to the lack of statistical relevance of the number of non-specific data. Figure is adapted from ref. [66].

as well as other effects such as the stochastic nature of the process, and non-specific interactions such as sticking. The error reduces with the distance of the free end of DNA and thus is more precise for shorter DNA scaffolds as used with RNAP.

While the raw localisation Δy_p can be close to theoretical values for some binding sites, for examples those close to the free end of DNA, the error in localisation can become large close to the tethered end (up to $1 \mu\text{m}$ in the extreme case). This issue is due to the fundamental difference between distances as measured with the stage position z (equivalently the bead-nanocapillary distance y) and the position of the protein along the contour of DNA s . The true position s_p of the protein takes into account the coiling or stretching of DNA, and these effects must therefore be taken into account to obtain the true localisation.

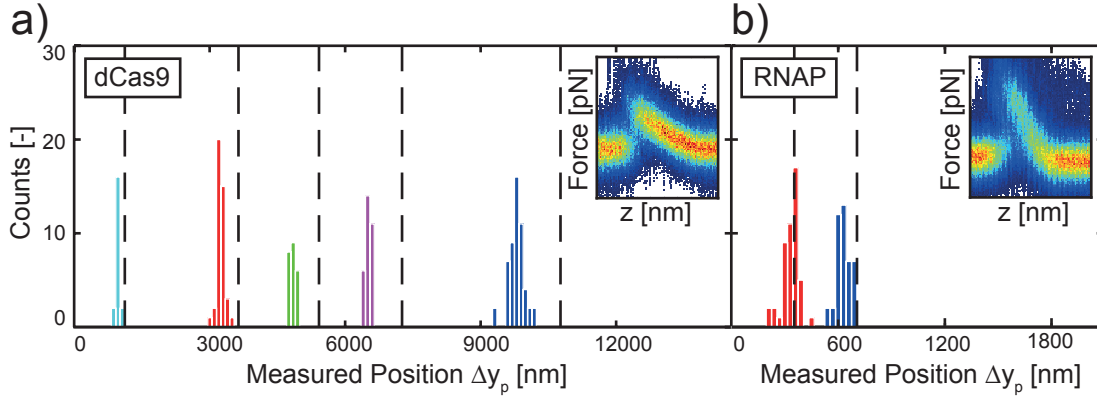


Figure 3.5 – **Localisation of DNA-protein complexes.** a) and b) Measured localisation of DNA protein complexes shown along the DNA length for dCas9 and RNAP binding sites respectively. Each binding site is shown in a different colour with dashed black lines corresponding to theoretical binding site locations. Insets show a density plot of all the protein jump event force-distance curves showing the reproducibility in jump shape (binding site at 1100 nm and 750 nm for dCas9 and RNAP respectively). Figure is adapted from ref. [66].

Shift in protein detection

In the previous section, localisation of DNA-protein complexes thanks to optical tweezers was demonstrated. However, despite being able to distinguish specific and non-specific binding through statistical analysis, the differences between theoretical binding site and observed position can have large shifts. As the distance of the binding site to the free end grows, so does the shift. This trend is shown on figure (3.6) as the shift $\Delta_{\text{shift}} = (L - s_p) - \Delta y_p$ as a function of the theoretical binding site s_p . As stated previously this shift occurs because the measurement of the position via the stage is not equal to the location along the DNA contour. To measure the true binding site, tension in the DNA must be taken into account, as well as the stochastic exit of the DNA. Meaning that $s_x < L$ where s_x is the contour length at the exit corresponding to position y_x , and L is the theoretical length of the whole DNA scaffold. The extension of the DNA can be defined as: $\mu(s) = y/s < 1$, and takes into account the coiling or tension. The location of the protein complex can therefore be rewritten as a function of s :

$$\Delta y_p = s_x \mu(s_x) - s_p \mu(s_p) \quad (3.2)$$

The extension of the DNA $\mu(s)$ can be computed analytically if the assumption of strong stretching is made[156]. This assumption is correct in the range of forces undergone by the DNA in these experiments[58; 98]. First the force on DNA is computed to be $F_{\text{DNA}} = \lambda_{\text{DNA}} V f(s)$, where λ_{DNA} is the effective linear charge density of DNA, V the voltage bias, and $f(s)$ is a geometrical factor. The computed linear charge density of DNA is not equivalent to the literature values (figure (3.6d)) due to the fact that the force measured by the optical tweezers is a balance of the electrophoretic force and the electroosmotic flow-induced drag force $F_{\text{DNA}} = F_{\text{EP}} - F_{\text{EOF}}$. The geometrical factor $f(s)$ is due to the extension of the electric field in nanocapillaries discussed previously. It takes the form:

$$f(s) = 1 - \frac{1}{1 + \frac{L-s}{\xi}} \quad (3.3)$$

3.2. Using nanocapillaries combined with optical tweezers

In silicon nitride or quasi-2D nanopores this geometrical factor would simplify to 1. Next the extension force on the DNA can be given as $F_{\text{ext}}(s) = F_{\text{DNA}}(s) - F_p(s = s_p)$, where the force on the protein is given as a function of its effective charge q^* as $F_p(s = s_p) = q^* V / \xi$. With all these considerations the extension can then be written as:

$$\mu(s) = 1 - \sqrt{\frac{k_B T}{4L_p F_{\text{ext}}}}. \quad (3.4)$$

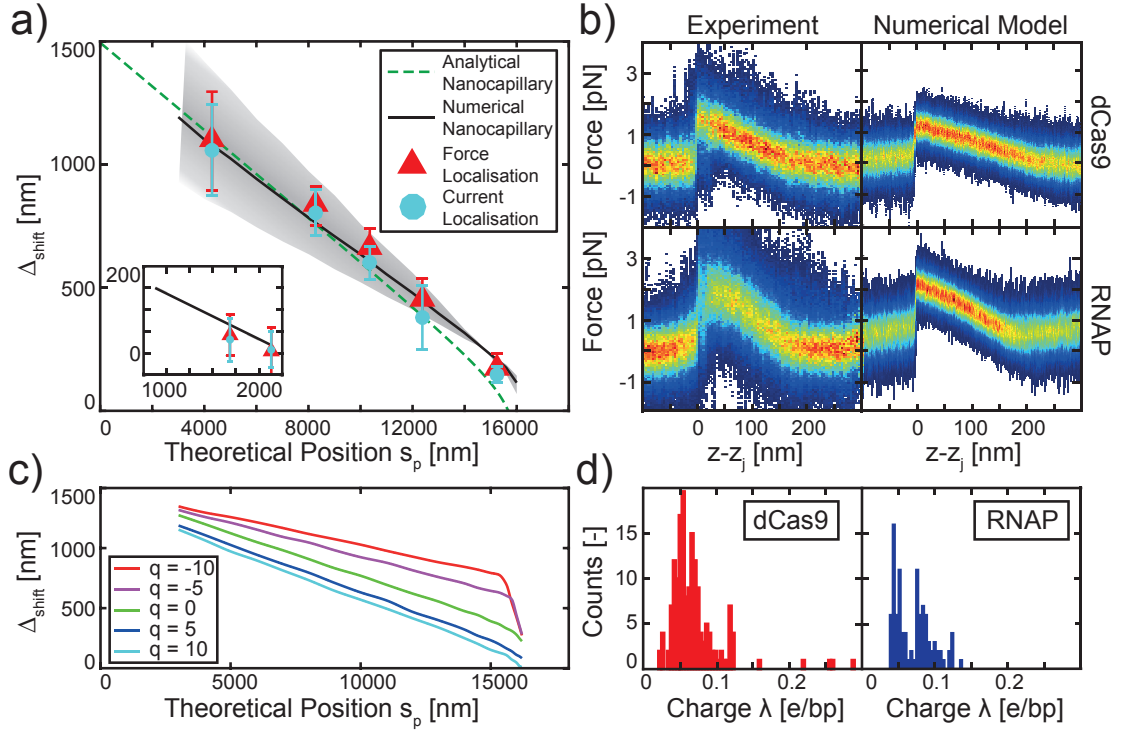


Figure 3.6 – Localisation shift and correction. **a)** Shift in localisation of the protein complexes $\Delta_{\text{shift}} = (L - s_p) - \Delta y_p$ as a function of theoretical position along the contour s_p . Symbols show the experimental values extracted both from force data and current data. Green dashed line shows the analytical fit to the behaviour, and solid black line shows the numerical values as obtained from a FEM model. Gray area shows the numerical predictions while taking into account the variability in drag force as measured by the apparent linear charge density on DNA shown in panel d). Inset shows the same graph for the RNAP binding sites. **b)** Comparison of force-distance curve density plots as obtained from experiment (left column) and FEM model (right column). This figure shows that the FEM model is in good agreement with experimentally measured curves. **c)** Dependence of protein localisation shift on theoretical binding position as extracted from a FEM model described in detail in ref. [66]. Multiple curves for different effective protein charges q^* are shown. **d)** Histograms of apparent linear charge density of DNA, $\lambda_{\text{DNA}} = F_{\text{DNA}} / V$, in dCas9 and RNAP experiments respectively. A large distribution of values is obtained due to the number of different capillaries used and their distribution in electroosmotic induced drag force. Figure is adapted from ref. [66].

The persistence length of double stranded DNA is $L_p = 50$ nm. This analytical model then allows a fit to the shift in binding position for the dCas9 protein from which the following are extracted: $\lambda_{\text{DNA}} = -0.06$ e/bp which corresponds to the mean of the experimentally extracted values (figure (3.6d)), $L - s_x \approx 200$

nm the average length of the early exit of DNA due to stochastic processes, and $q^* \approx 5$ e the effective charge of the protein complex. The details of the numerical solutions as derived from a FEM model are described in detail in ref. [66].

3.2.2 Discrimination of DNA-protein complexes

The previous sections explained how to precisely localise DNA-protein complexes thanks to controlled translocations through nanocapillaries. This though is not the only information that can be obtained from the data extracted during controlled translocation curves. Indeed both the force and current are measured and these offer two distinct ways to discriminate different proteins based on effective charge or size. The following sections shall go into the details of such extraction for both cases.

Discrimination based on charge: Non-equilibrium work

Measuring the force on the optical tweezers during a controlled translocation event is equivalent to force spectroscopy such as can be performed in other setups to extract quantities such as free energy of folding for proteins, or DNA hairpins[107; 157]. Indeed, the same sort of analysis may be performed here. By measuring the force-distance curve and the area beneath the protein peak gives the non-equilibrium work performed during such a translocation due to the stochastic nature of each protein translocation event.

The protein bound to DNA begins in an equilibrium state (z_A, t_A) where the protein is completely inside the nanocapillary, and ends in an equilibrium state (z_B, t_B) where the protein has completely exited the nanocapillary. To move between these states the control parameter z is changed at a speed $v = dz/dt$ thus doing work. By integrating the force distance curve between (z_A, t_A) and (z_B, t_B) yields the work \tilde{W}_i :

$$\tilde{W}_i = \int_{t_A}^{t_B} v \frac{\partial H}{\partial z} dt = \int_{z_A}^{z_B} F_{OT}(z) dz, \quad (3.5)$$

where H is the Hamiltonian of the system. The only requirement is that the whole protein jump event is contained between the start and end state. This work is then corrected by the work performed on the bare DNA to obtain the work for a single protein translocation event $W_i = \tilde{W}_i - F_{DNA}\Delta z$, where $\Delta z = z_B - z_A$. This correction should be the same before or after the protein translocation event as the force profile due to bare DNA is flat (figure (3.2b)).

The so called Jarzynski equality[158] can then be used to relate the non-equilibrium work to the free energy difference between state A and B : ΔG_{AB} . The Jarzynski equality is a special case of the Crooks fluctuation theorem[159], the latter takes into account both forward and reverse pathways between the two states whose probability distributions cross at the value of the free energy. Therefore, the Jarzynski equality does not contain the full information of trajectories and as such is more biased than the Crooks fluctuation theorem[160]. Nevertheless, the Jarzynski equality is powerful in that it relates non-equilibrium measurements such as the work performed in a controlled translocation event to an equilibrium quantity. In this case, the forward and reverse work distributions as seen on figure (3.3b) do not show a clear enough separation that the Crooks fluctuation relation could be used. However,

3.2. Using nanocapillaries combined with optical tweezers

the Jarzynski estimator given below is used:

$$\left\langle \exp\left(-\frac{W_i}{k_B T}\right) \right\rangle = \exp\left(-\frac{\Delta G_{AB}}{k_B T}\right). \quad (3.6)$$

The change in free energy can be used to infer properties of the DNA-protein complex system by making the following assumptions. First, the free energy change in the worm-like chain is assumed to be negligible. This is true as long as the force level on the bare DNA is the same before and after the translocation event. The second assumption is that the change in contour length of the DNA is approximately equal to the change in stage position $z_A - z_B \approx s_A - s_B$. Taking these two conditions as being true the free energy difference can be expressed solely as a function of the bias potential V , the width in displacement of the jump event Δz , the electrostatic decay length of the capillary ξ , and the effective charge of the protein complex q^* :

$$\Delta G_{AB} = q^* V \frac{\Delta z}{\xi + \Delta z}. \quad (3.7)$$

Here, the geometrical factor ξ would vanish in membrane nanopores and the free energy would solely be a function of the effective charge and bias. Using this framework, effective charge values for the two studied proteins: RNAP, and dCas9, can be computed. All events over multiple binding sites and multiple nanocapillaries are grouped together to allow for enough statistical power of the Jarzynski free energy estimator. The only requirement being that the bias voltage be the same for all experiments. An average protein complex translocation event width is determined to be $\Delta z = 220$ nm and 170 nm for dCas9 and RNAP respectively, and the electrostatic decay length of $\xi = 75$ nm is used. Using these values the effective charge is computed to be $q^* = 3.1$ e and 3.4 e for dCas9 and RNAP respectively.

One of the issues with using the Jarzynski equality in this instance is the lack of statistical power without combining all binding sites. Ideally, separate estimations would be made for different binding sites as this may yield extra information as to possible subtle differences between them. The more problematic issue with this is combining different nanocapillaries. Indeed, as seen in the previous section concerned with localisation, differences in capillary geometry lead to large variations in drag force and/or decay length ξ which will in turn affect the effective charge q^* and induce errors. These variations are postulated to be the largest effect on the error in the free energy estimation. If a similar study were to be repeated, acquiring all data in the same capillary should reduce this variability and yield more satisfactory discrimination results. As previously mentioned, the Jarzynski equality only uses one direction of trajectory (in our case $A \rightarrow B$) and so induces an additional bias, in our case in underestimating the effective charge of the protein complex.

This underestimation is confirmed when comparing q^* obtained from the Jarzynski estimator and from the analytical fit of the localisation shift Δy_p . Both proteins used in this work have similar hydrodynamic radii [134; 161] which, in this configuration due to high electroosmotic drag, is the main contributor to the computed effective charge. Some effect of electrostatic charge may remain but, despite this, the work distributions obtained, as well as the effective charges, still support discrimination based on non-equilibrium work analysis.

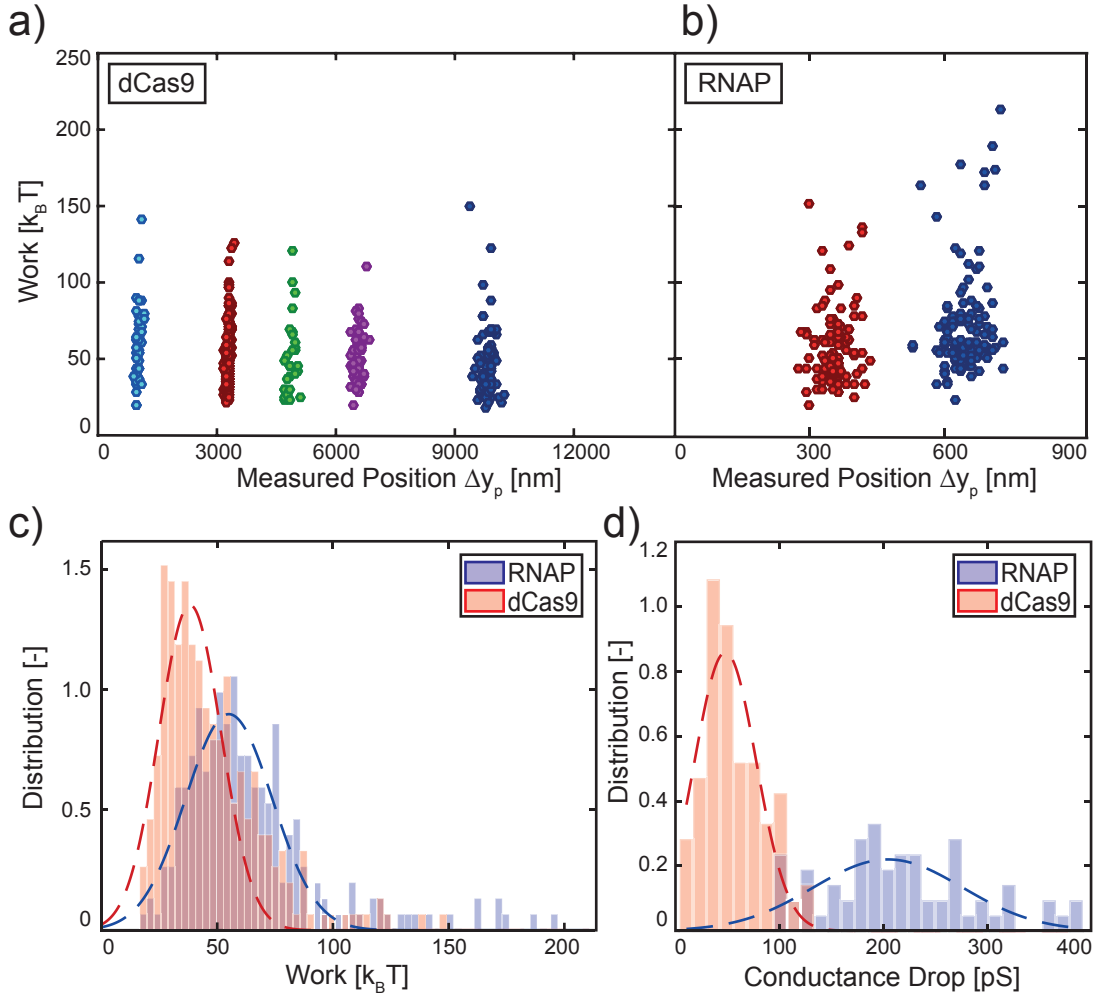


Figure 3.7 – **Discrimination of DNA-protein complexes.** **a)** and **b)** show the distributions of non-equilibrium work extracted from protein jump event force-distance curves for dCas9 and RNAP respectively. Each binding site is shown at its position along the DNA strand with colours corresponding the figure (3.5). **c)** Distribution of non-equilibrium work for dCas9 and RNAP as obtained from adding the contributions from each individual binding site. The distributions show a small difference that is then represented in the different effective charge, as calculated by the Jarzynski free energy estimator. **d)** Distribution of conductance drops for dCas9 and RNAP. As on panel c) all the binding sites have been assumed to be the same and are pooled for this distribution. This shows clear discrimination between RNAP and dCas9 conductance drops, with higher values for RNAP protein-complexes. Figure is adapted from ref. [66].

Discrimination based on size: Conductance drop

The second method of discrimination which is obtained directly while performing controlled translocation experiments is customary with nanopore studies (chapter 1). Namely, to use the current drop associated with the protein translocation event to discriminate between different protein complexes[33].

Conductance drops which are confirmed to be simultaneous to the detected force peaks are extracted. Since the buffers used both for RNAP and dCas9 are of same ionic strength these values are directly

comparable and show better discrimination capabilities than the non-equilibrium work analysis. The conductance drop itself is attributed to different possible causes ranging from geometrical current blockage due to size[162], to molecular friction[163]. Whatever the exact mechanism, the discrimination power may be higher in this case due to the fact that the large electroosmotic force in nanocapillaries has less of an effect on the conductance mechanism than on the force mechanism, thus affecting the spread of the conductance drops less. This is despite the fact that the conductance drop depends strongly on the salt concentration[164], reason why free translocations are carried out at high salt which only allows certain restricted studies to be performed with proteins.

In practice, having the possibility to discriminate thanks to both conductance drop and non-equilibrium work analysis will provide better sensitivity in the case where proteins are similar in either charge or size. Optimisations of the experimental buffer, voltage bias for translocation, speed of controlled translocation, or size of nanocapillary opening can easily be made to tailor the experiment to have the best sensitivity for given proteins in order to detect and discriminate.

3.3 Conclusion

Despite combining data from multiple nanocapillaries and, via their different EOF drag forces reducing the precision of the measurement, both localisation and discrimination of proteins is shown to be possible. This technique could be extended to interesting studies such as more quantitative measures of non-specific binding of proteins such as dCas9 that were not possible here due to statistical relevance of the non-specific events. It could also be used in situations where standard techniques fail such as the presence of large repeats in nucleotide order. This is characteristic of fragile X syndrome[165] and could be a powerful technique to detect and characterise such repeats.

Due to the single molecule nature of the optical tweezers experiment, the throughput is relatively low. This is estimated to be ≈ 10 beads/h with an average occupancy of proteins in this study of $\approx 20\%$. This is one of the key factors limiting the amount of statistics for single nanocapillaries, and inducing errors by using multiple samples. One method that could obtain a much higher throughput is scanning ionic conductance microscopy (SICM)[166]. While sacrificing the force feedback of the optical tweezers is a major drawback, experiments could be optimised in the optical tweezers in order to obtain a high resolution in current before transferring to a SICM setup. In SICM, the DNA is bound to a planar surface and the nanocapillary tip is approached until capture occurs. Similar current traces as obtained in this study can then be obtained, and the process can be automated to measure tens of curves a minute at low salt concentrations. Such an extension to SICM is under way by collaborators (Leitao, Navikas et al. in preparation) with the addition of fluorescence microscopy. Detection of DNA origami molecules with DNA dumbbell barcodes was successfully carried out similarly to previous free translocations in glass nanocapillaries[167]. The use of surface attached DNA in the SICM method also easily lends itself to multiplexed sensing where regions of the surface could be patterned to allow the measurement of many different assays in one experiment. For example, different binding proteins, or different binding sites, all measured on the same device.

4 DNA retraction measured with optical tweezers

Contributions: S.J.D. performed experiments and data analysis, S.M. performed FEM modelling, S.M. and A.R. supervised the research.

The previous chapter showed how optical tweezers combined with nanocapillaries can be a powerful single molecule tool to probe nanopore translocations. This chapter will extend the use of this technique to the high precision dynamic measurements of taut DNA relaxation. Dynamic measurements are used as a benchmark to show that such experiments could yield interesting data on the capture event in free DNA translocations thus elucidating what is perhaps the least understood part of DNA translocations.

4.1 Introduction to DNA elasticity for taut relaxation

While the previous chapter delved into the intricate interactions of DNA-protein complexes, DNA itself exhibits a wealth of interesting phenomena. Understanding the translocation dynamics of DNA can lead to a better fundamental understanding of nanopore measurements. Indeed, while nanopore measurements seem simple enough to describe, the exact physical process of DNA capture, and translocation contains a multitude of physical effects, not all of which are well understood. The first concepts of polymer physics and the elasticity of polymer chains were developed by Flory[168] and expanded greatly in the 80's and 90's by De Gennes and others[169; 170; 171; 172].

The first theoretical developments that pertain to DNA extension are the descriptions of polymer chains and their extension in strong flows[173; 174]. Subsequent studies were then broadened to the extension or unwinding process both by external force and uniform flows[175]. Following the same formalisms it is then possible to describe the transient dynamics of polymer relaxation from a taut state[176; 177; 178; 179]. These are the dynamics that are of interest when measuring relaxation of taut DNA.

Assuming a completely tensed length of polymer it is expected to go through transitions in its relaxation depending on the residual tension along the chain. Initially the chain being taut is in the strong stretching regime (SS), after some time the tension will have relaxed sufficiently that the free end of the polymer will start to take on a more globular shape while the remaining chain is still rod-like. This is the regime of the stem-flower (SF). By the continued relaxation of the taut stem part the globular flower portion will grow until finally the remaining tension is so low that the polymer transitions again into a brief trumpet regime (TP). This trumpet regime is very short lived as it exists only in a

small range of tensions and soon thermal motion overcomes the relaxation process entirely. These different relaxation regimes are shown on figure (4.1) in the case of nanopore translocation. From these theoretical descriptions it is possible to extract behaviours of the DNA length over time and quantify it via its power law dependence on time. The stem-flower regime is theoretically predicted to behave in a $L_t \propto t^{-1/2}$, where L_t is the length of the taut stem part of the stem-flower. However, depending on the exact boundary conditions and magnitude of the force, many different scaling behaviours are possible[180; 181].

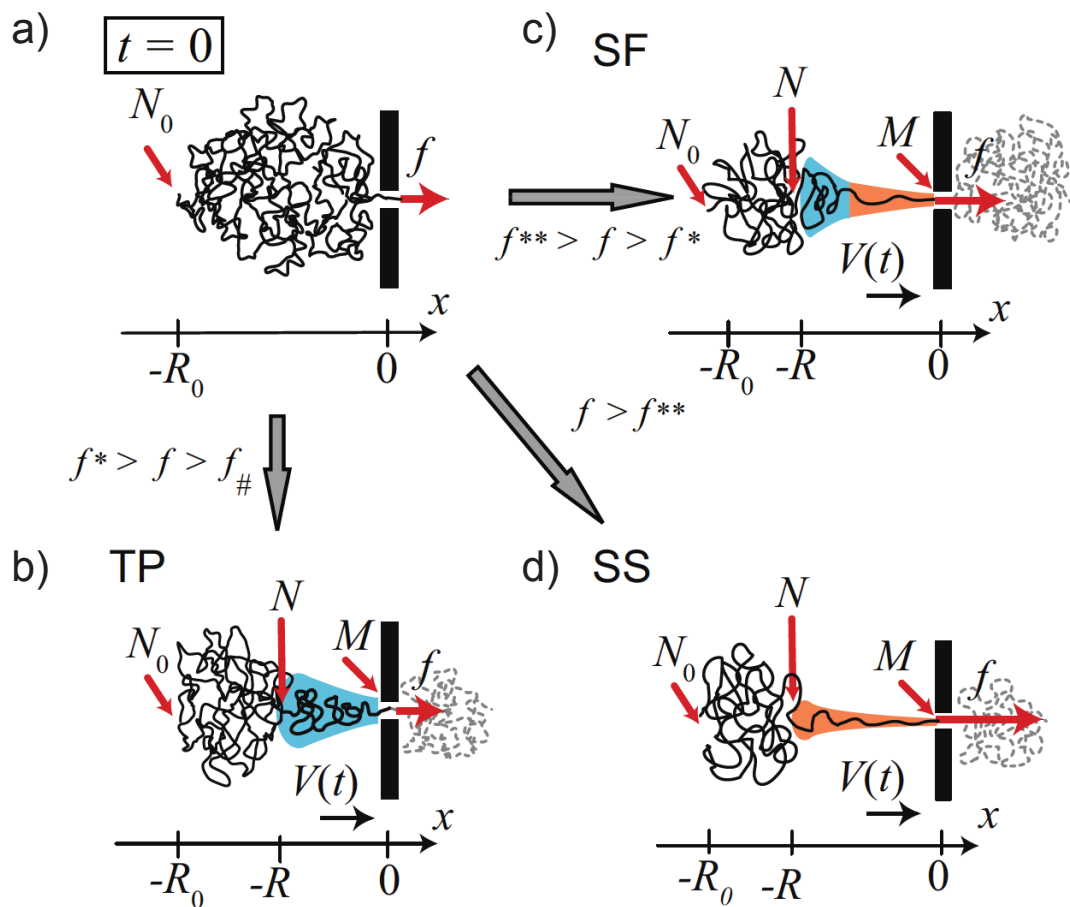


Figure 4.1 – DNA tension propagation models and their relevance during a translocation event. a) Initial conformation of DNA molecule at the instant of capture into a nanopore $t = 0$. The first chain link will then be subjected to the force f which will start to propagate along the chain. R_0 represents the gyration radius of the molecule. **b)** Shows the conformation in the case where the threading force is low $f < f^*$ while remaining larger than the thermal forces $f > f_{\#}$ and the trumpet regime is the dominant form of tension propagation. In this case no significant extension of the molecule is present, only a local deformation of the globular structure. **c)** The stem flower regime of tension propagation for a threading force f higher than in panel b) but lower than the critical force for the strong stretching regime f^{**} . The stem flower is characterised by one part of the chain being in an extended rod-like conformation while the rest is a deformed globule (flower). **d)** Tension propagation in the strong stretching regime when the threading force is larger than the critical force $f > f^{**}$. In this case strong stretching implies an almost completely rod-like shape of the tensed DNA. Figure is adapted from ref. [182].

4.1. Introduction to DNA elasticity for taut relaxation

The advent of single molecule experiments allowed the verification of these elastic models. First, static pictures of stretched and looped DNA were obtained via DNA extension and grafting at a receding water meniscus[183]. Soon dynamical studies such as freely relaxing DNA was observed by fluorescence microscopy and was well described by the stem-flower regime discussed above[184]. Perhaps the most important single molecule tool was optical tweezers that revolutionised the field of biophysics as it allowed for the attachment of DNA to microscopic beads that could be manipulated[185]. Figure (4.2) shows some early results of DNA behaviour obtained with optical tweezers measurements.

First experiments used the optical tweezers as tethers and used liquid flow in combination with fluorescence to measure the relaxation of long DNA[186]. These early experiments were already interested in the elastic properties of DNA[187; 188; 189] as well as its interaction characteristics. For example the dynamic behaviour of DNA in crowded media[190]. These first experiments confirmed the theoretical predictions discussed above[191] although conditions where the relaxation was coupled with hydrodynamic flow necessitated corrections[192]. Other tools such as magnetic tweezers and AFM were also used to measure similar properties. The probing of taut DNA[193] and DNA melts[194] with magnetic tweezers resembles similar contemporary studies done with optical tweezers. AFM was also a tool instrumental in first studies of DNA conformations. Indeed modifications in DNA conformation due to ligand binding were observed[195]. Liquid AFM was also able to resolve movements and changes in shape of single DNA molecules and plasmids[196]. More recent AFM studies were also applied to the unfolding of proteins[197] similarly to what can be carried out with optical tweezers[157] extending these elasticity models to amino acid polymer chains.

The early studies of DNA discussed above made use of microscopy and optical tweezers to measure the decaying length of taut DNA. However, they did not measure the DNA tension on the optical bead directly. Later, optical tweezers were used with the measurement of force to expand studies and were able to yield more knowledge on the exact behaviour of DNA as a polymer[198; 199]. The overstretching transition of DNA was for example measured with optical tweezers, whose force transduction is key to these measurements[200]. The overstretching transition is a conformational change of DNA at high force ($F > 65$ pN) where the DNA melts into its single stranded form and was also measured in small silicon nitride nanopores[201]. In addition to linear force related elastic behaviours rotational and torque characteristics of DNA were also studied. Perhaps the most surprising result from these studies is the fact that DNA overwinds when stretched[202] showing that DNA exhibits a richness of different effects under tension. Finally the study of DNA structures such as hairpins allowed to better understand secondary structure of DNA, its stability, and elastic properties[203; 204].

Applying these results to DNA behaviour during nanopore translocation is not trivial. Some theoretical advances have been made extending previously described works to the confinement and translocation of polymer chains. Polymer chain confinement in both slits and pores was described and depends highly on the elastic properties of the chain along with the size of the confinement[205; 206]. The exact nature of the dynamic process DNA undergoes during translocation can then be broached. Indeed, DNA translocations are not an equilibrium process and the DNA shape, and tension, will change throughout the process due to tension propagation and deformation dynamics[207; 208]. Considering this fact, it is clear that the polymer chain could undergo all the regimes of trumpet, stem-flower, and strong stretching depending on the magnitude of the driving force[182; 209]. The regimes theoretically described above are represented during nanopore translocation on figure (4.1). Additional details of translocation dynamics may be extracted from the extension of polymer theory to the nanopore translocation case. Indeed it is expected that the dynamics of translocation be asymmetric and that the compressed coiling and blob-like nature of the DNA on the trans side of the pore is not equivalent to

the process of constant electrophoretic threading of the DNA from the cis side of the pore[210].

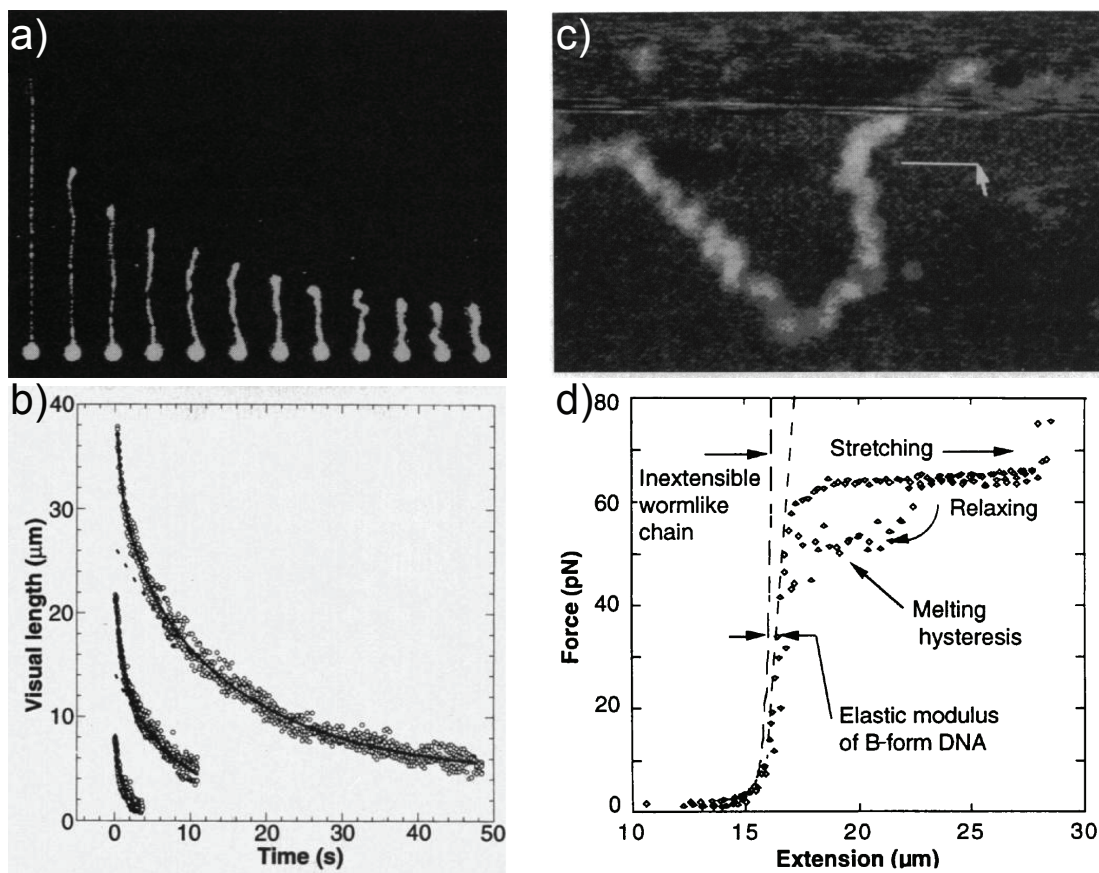


Figure 4.2 – First measurements of DNA elasticity. **a)** Optical images of a long DNA molecule attached at one end to a bead held static in an optical trap. The DNA is tensed by a strong liquid flow before the flow is abruptly halted. The relaxation from a tensed state is then observed optically. **b)** Optically measured length of DNA as a function of time for molecules such as shown in panel a). Different total lengths of molecule are shown. Panel a) and b) are adapted from ref. [190]. **c)** AFM image of a single DNA molecule and its conformation. Images such as these were able to elucidate DNA bending and movement in different conditions. Image is adapted from ref. [196]. **d)** Force extension curve of DNA obtained with optical tweezer experiments. The overstretching transition is observed to take place at ≈ 60 pN where the curve diverges strongly from the inextensible worm-like chain (WLC) model (dashed lines). Fits to such models allow the extraction of the elastic parameters of DNA in various forms. Image is adapted from ref. [200].

While these studies are of great interest to more fully understand the details of DNA translocations in nanopores a lack of experimental verification exists. Studies of the effect of nanoscale pre-confinement of DNA before[211] or after[212] translocation have been shown to affect the translocation time distribution. However, correlating these free translocation experiments with exact DNA conformation is challenging and no tension information is available. One measurement of the relaxation of taut DNA in the nanopore geometry was made using a similar setup as used in this thesis of nanocapillaries and optical tweezers[62]. However, the time resolution of the study was ultimately too limited to extend to the measurement of decay exponents or to more complex situations more closely related to DNA translocation. The following chapter therefore attempts to measure the relaxation of taut DNA

with enough precision to be able to extract the exponent of the force relaxation and compare it to the theoretical predictions discussed above. This opens up the possibility to extend the technique to situations more closely resembling the dynamics occurring during a translocation event.

4.2 Experimental description

In this chapter, as in the previous one, a polystyrene bead, previously coated in λ -DNA, and trapped with optical tweezers, is brought close to the opening of a nanocapillary (size range 25-100 nm). By applying a voltage bias, the DNA is driven inside the nanocapillary which is confirmed by a corresponding sharp increase in the force signal. Once the DNA is inside the capillary a nanopositioning stage moves the capillary in the opposite direction by 10 μm until the DNA is in a taut state. The size of λ -DNA being $\approx 16 \mu\text{m}$, and taking into account the distance between the bead and the opening of the nanocapillary at capture ($\approx 1\text{-}2 \mu\text{m}$), this distance leaves the DNA in an almost completely tensed state. Once this conformation is achieved the voltage bias is turned off and the DNA relaxes (schematic on figure (4.3a)). This relaxation in DNA tension is measured via the decay to zero of the force on the optical tweezers. This force decay is what will be probed and its time dependence quantified via a power law decay. A typical example of such data is shown on figure (4.3b) both on a linear axis and on a log-log axis which shows the expected power law shape of the curve. Experimental data shown in the following sections are averaged sets of, in most cases, $N > 20$ curves taken at the same parameters.

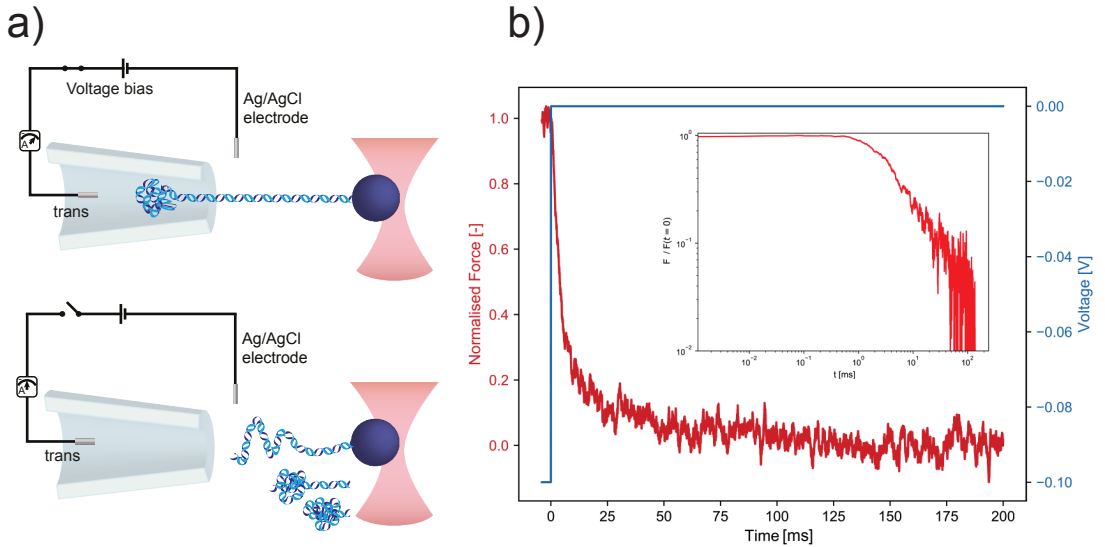


Figure 4.3 – Experimental setup and detected signals during taut relaxation of DNA. **a)** A nanocapillary separates two chambers filled with buffer. Ag/AgCl Electrodes allow to apply voltage bias. Once DNA has been detected in the force and current signal a nanopositioning stage moves the capillary away by a distance $d = 10 \mu\text{m}$ such that the DNA is close to fully tensed (upper sketch). Once this position is achieved the voltage bias is shut off in order to let the taut DNA relax back to its equilibrium state (lower sketch). Three schematic representations of the relaxation of DNA are shown going from most extended to fully coiled with time. **b)** Typical normalised force-time curve ($F_{OT}(t)/F_{OT}(0)$) of the decay along with voltage-time curve that shows the simultaneity of the decay with voltage drop. Inset is a log-log plot of the main figure showing the power law shape of the curve. Note importantly that no smoothing is applied to the data, the low noise is due to the fact that the curve shown is an average of $N = 47$ individual curves taken at the same stiffness $\kappa = 32 \text{ pN}/\mu\text{m}$ and in the same nanocapillary.

Such data sets are obtained thanks to a custom LabVIEW program that allowed the automation of this measurement protocol in order to extract many curves from each bead in a much shorter time than is possible manually. The LabVIEW program is modified to detect sharp transitions in the force curve and thus uses this as a trigger for the scripted movement of the stage, shutting off of the bias voltage, and return to the zero stage position before again applying the bias and waiting for a trigger event. This allows automated acquisition of tens of curves per bead. Such an increase in statistics along with a high acquisition frequency allows to measure scaling exponents more precisely without overt usage of filters. This is compared to previous studies where the data was less reproducible only allowing few data sets to be obtained[62].

Considering the wide variety of theoretically possible scaling exponents, that are mostly extracted for the length decay and not the tension behaviour[180; 181], no a priori value of the exponent is assumed. Finite element model (FEM) simulations of the process are carried out which allow qualitative comparison to the experiments and their dependencies. Simulations of relaxation dynamics give a qualitative control of experimental measurements. The exact retraction process is simulated using FEM by assuming that, at the initial condition ($t = 0$), a length L_t of chain is under uniform tension of magnitude f_0 , while the remaining length inside the capillary $L - L_t$ remains un-tensed. The following evolution equation is then solved for non-linear worm-like chain (WLC) backbone tension:

$$\frac{\partial f(s, t)}{\partial t} = D_0 f^{3/2} \frac{\partial^2 f(s, t)}{\partial s^2}, \quad (4.1)$$

where $D_0 = \frac{4}{\zeta} \sqrt{\frac{L_p}{k_B T}}$ is the diffusion constant of tension along the backbone. In this case ζ is the DNA friction, and L_p the persistence length of DNA. This equation is then solved on the domain $[0; L]$ with the following boundary conditions: the tension at the free end $f(s = L, t) = 0$ for all times $t > 0$, and the bead follows a Langevin equation as described below (equation (4.2)) which fixes the evolution for the bead end of the DNA $f(s = 0, t)$. The bead contribution will be discussed later when deconvoluting the bead effect from the DNA relaxation. When plotting single curves as are seen on figure (4.4e and f) noise is added to the simulated curves to more clearly represent experiments.

4.3 Measuring DNA retraction with nanocapillaries combined with optical tweezers

On figure (4.4) experimental decay curves as well as simulated curves are shown. Different optical trap stiffnesses are compared on the same graph to show the dependence of the decay on this key parameter. The curve shape as well as the dependence on stiffness is comparable between the simulated and experimental curves showing that the FEM model is in good agreement.

The key to the experimental measurements allowing the extraction of force relaxation exponent is the time resolution of the position detection. Indeed in previous studies the bead dynamics, and through it the tension on the DNA, is captured via particle tracking on the image from the CCD camera. This is limited to 10^4 Hz due to the frame rate of the camera[62]. In contrast the electrical signal from the quadrant photo diode that directly tracks the motion of the bead through the laser displacement can be acquired at $5 \cdot 10^5$ Hz. This 50 times increase in time resolution, along with the capability of obtaining many more curves via the automated LabVIEW are what separates this study from previous attempts at measuring taut DNA relaxation. Curves on figure (4.3) are raw data and the high signal to noise ratio is

4.3. Measuring DNA retraction with nanocapillaries combined with optical tweezers

due to an averaging of $N > 20$ curves that enables filtering to only be used sparingly when studying the exponent of the decay itself.

When measuring the force relaxation of the bead in the optical trap $F_{OT}(t)$, it could be naïvely postulated that it is directly proportional to the tension of the DNA at the bead end. In fact this is not the case due to the bead being displaced in the optical trap by $\Delta x = f_0/\kappa$, where κ is the stiffness of the optical trap. The bead displacement is in the range of 50-1000 nm in typical experiments. Since the bead detection $r(t)$ is used to measure the tension on the DNA, the measured signal $F_{OT}(t) = \kappa r(t)$ is a convolution of the true DNA tension $f(s=0, t)$ with the bead's intrinsic response.

4.3.1 Deconvolution from the effects of the colloidal bead

As stated previously, the measured quantity, the force on the optical bead, is a convolution of the DNA behaviour with the bead dynamics within the optical trap. In order to take this into account the exact dynamics of the bead must be known. The bead follows the Langevin equation given below, where the inertial terms can be readily ignored since friction dominates:

$$\gamma \dot{r} + \kappa r = \eta(t) + f(s=0, t). \quad (4.2)$$

By partial integration the measured response is obtained as:

$$F_{OT}(t) = f_0 e^{(-t/\tau_b)} + \frac{1}{\tau_b} \int_0^t f(s=0, t') e^{-(t-t')/\tau_b} dt', \quad (4.3)$$

where $\tau_b = \gamma/\kappa$ is the characteristic time-scale of the bead defined by the ratio of friction γ to stiffness κ . This implies that, at very high stiffnesses where τ_b is small, the effect of the bead on the measured response will be negligible and thus the measurement will approach the true value of DNA relaxation. In contrast, if τ_b is non-negligible compared to the time-scale of the DNA relaxation, then the bead contribution must be taken into account.

Subtracting the contribution of the bead is done, both on experimental data and in FEM simulations, by deconvoluting in Fourier space $\tilde{F}_{OT}(\omega)$ before returning the signal to real space. Experimentally, before deconvolution, all curves are first normalised by the zero time value of the force $F_{OT}(t)/F_{OT}(0)$ before being filtered using a Savitzky-Golay filter. Filtering was found to improve noise in the deconvoluted curves and allowed further processing to extract a relatively clean value of the exponent. The correct tension along the DNA, without the contribution from the bead, is thus obtained as:

$$\tilde{f}_t(\omega) = \tau_b \left(\frac{\tilde{F}_{OT}(\omega)}{g(\omega)} - 1 \right), \quad (4.4)$$

Where $g(\omega)$ is the Fourier transform of the response function $g(t) = e^{-t/\tau_b}$. Examples of such deconvolution applied to both experimental and simulated curves are shown on figure (4.4c) through f)). As expected in the low stiffness case the deconvolution has a more pronounced effect since the bead contribution is larger. For stiffnesses $\kappa > 30$ pN/ μ m the bead influence becomes small and the deconvolution step can be omitted without much loss of information. Figure (4.4) shows how, despite the experimental noise and the convolution effects with the bead, the higher experimental acquisition

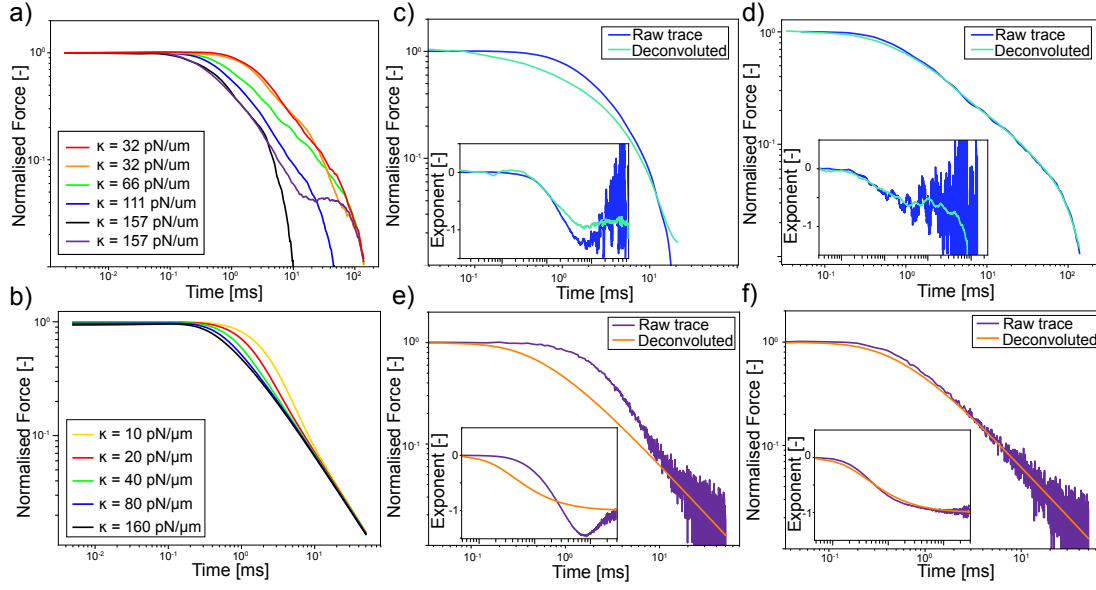


Figure 4.4 – Dependence of DNA relaxation on optical trap stiffness and contribution due to con- volution with bead dynamics. **a)** Log-log plot of experimental force versus time curves for different stiffnesses of the optical trap. All experiments were done in 100 mM KCl buffered with 10 mM Tris, pH 7.5. The number of individual experiments averaged is as follows: $N = 23, 35, 25, 50, 47, 26$, and 23 (in the order given by the figure legend). **b)** Simulation of force relaxation for different trap stiffnesses as a comparison to panel a). Panels **c)** and **d)** show experimental force decays versus time as well as insets of the exponent versus time (on the same time axis) for low ($\kappa = 32 \text{ pN}/\mu\text{m}$) and high ($\kappa = 111 \text{ pN}/\mu\text{m}$) stiffness respectively. For each graph both the raw experimental data and the deconvoluted data is shown. Panels **e)** and **f)** show the same deconvolution behaviour for simulated curves. The low stiffness is $\kappa = 8 \text{ pN}/\mu\text{m}$ and the high stiffness is $\kappa = 111 \text{ pN}/\mu\text{m}$. Similar to the experimental panels both the raw data and deconvoluted data is shown as well as the inset of the exponent behaviour with time on the same axis as the main panel. Noise is artificially added to the single simulated curves on panels **e)** and **f)** to more clearly represent the experimental case.

rate allows to extract the exponent for the force decay as a function of time $f(t) \propto t^\alpha$.

4.3.2 Force decay exponent analysis

Having correctly extracted the DNA contribution to the force decay, this can now be analysed further in order to observe the scaling relationship and how this varies with important physical variables in the system (f.ex trap stiffness, DNA tensed length). To extract the exponent the local slope along the smoothed, deconvoluted force curve is extracted. This allow to observe the exponent changes as a function of time (as seen in the insets of figure (4.4) or figure (4.5)). The exact scaling relationship for long time-scales is based on entropic driving forces of DNA extension, as described by Marko and Siggia:

$$f(z) = \frac{k_B T L^2}{4L_p(L-z)^2} \quad (4.5)$$

When balanced with an effective friction force $\zeta L \dot{z}$ one obtains a scaling of the form $f(t) \propto t^{-2/3}$. This

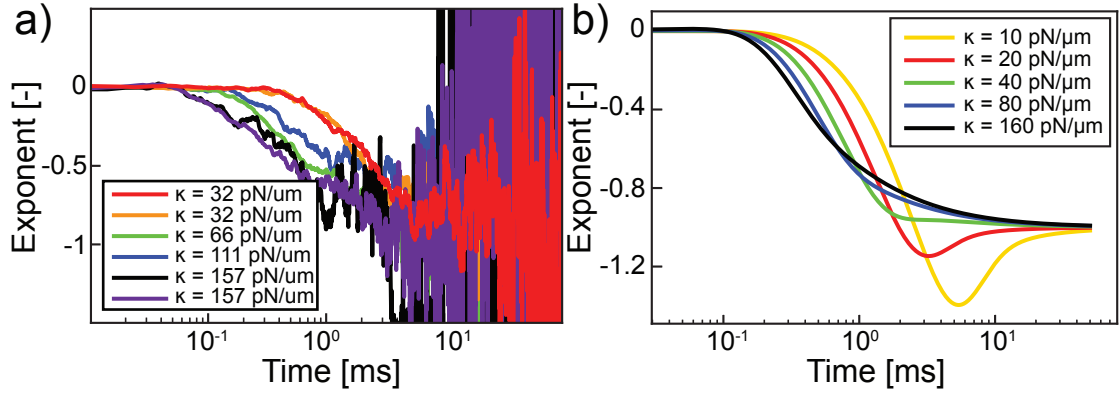


Figure 4.5 – Extraction of exponent for long time-scales and comparison to simulation. **a)** Experimental measurement of the exponent by taking the local slope of the curves on figure (4.4a)). Data shows similar convergence to -1 . Due to noise in the experimental data, especially when the curve approaches $F_{OT} = 0$ the exponent is only plotted until the curve reaches the level of thermal forces ($F_{OT} = k_B T / L_p$). This is also the level where the regime of tension relaxation is expected to change from taut dynamics to a stem-flower or trumpet regime. Unfortunately, experimental noise is too large to speculate on any change of exponent. **b)** Simulation of exponent for different stiffnesses of the optical trap. All of the simulated exponents converge to -1 for long time-scales which supports the experimental measurement.

is the same exponent as calculated by Otto et al[62]. One problem with this view arises at the end of the decay where, once the tension on the DNA is comparable to the level of thermal energy, the picture as given by taut dynamics is no longer valid and the regime of stem-flowers as described by Brochard-Wyart is more relevant[176]. It is not trivial to compute this exponent exactly and many regimes with different exponents exist in the literature[180; 181]. In order to avoid any a priori assumption of exponent, comparison between experiments and simulations are used to qualitatively verify the behaviour of decaying DNA. Figure (4.5) shows both experimental and simulated exponents. In both cases for all stiffnesses the exponent converges, for long time-scales, to a value of -1 .

4.3.3 Length dependence

Due to the expected dependence of the DNA on the decay regime: taut, stem-flower, and trumpet, the most interesting physical quantity to vary is the length of tensed DNA. Indeed if the DNA starts in a conformation more similar to the stem-flower it will contain a large globule of DNA which will affect the decay via drag force.

The exponent of the decay should then change in these cases. Experimentally for the case of shorter tensed length, instead of moving the stage by a distance of $d = 10 \mu\text{m}$, the stage was moved by smaller values of $d = 6$, and $3 \mu\text{m}$. The DNA conformation at time $t = 0$ is therefore no longer a quasi fully tensed rod but resembles more the stem flower as seen on the inset of figure (4.6b).

From a simulation point of view, in order to properly approximate the system, a tensed length of DNA $L_t < 10 \mu\text{m}$ is used. An un-tensed part of DNA is then added onto the end of this rod. Both experimental, and simulated results are shown on figure (4.6) where the force-time plots as well as the different exponents are shown. Some small changes of time to convergence or irregularities in the dynamical behaviour are present, some of which are seen in the experimental data. However, the long

time-scale behaviour of the exponent stays the same as in the fully tensed case. It is postulated that the effect of stem-flowers, in this case, due to relatively large forces (as compared to thermal force) and relatively short length of DNA (small drag from the un-tensed region) lead to no large modification to the scaling regime.

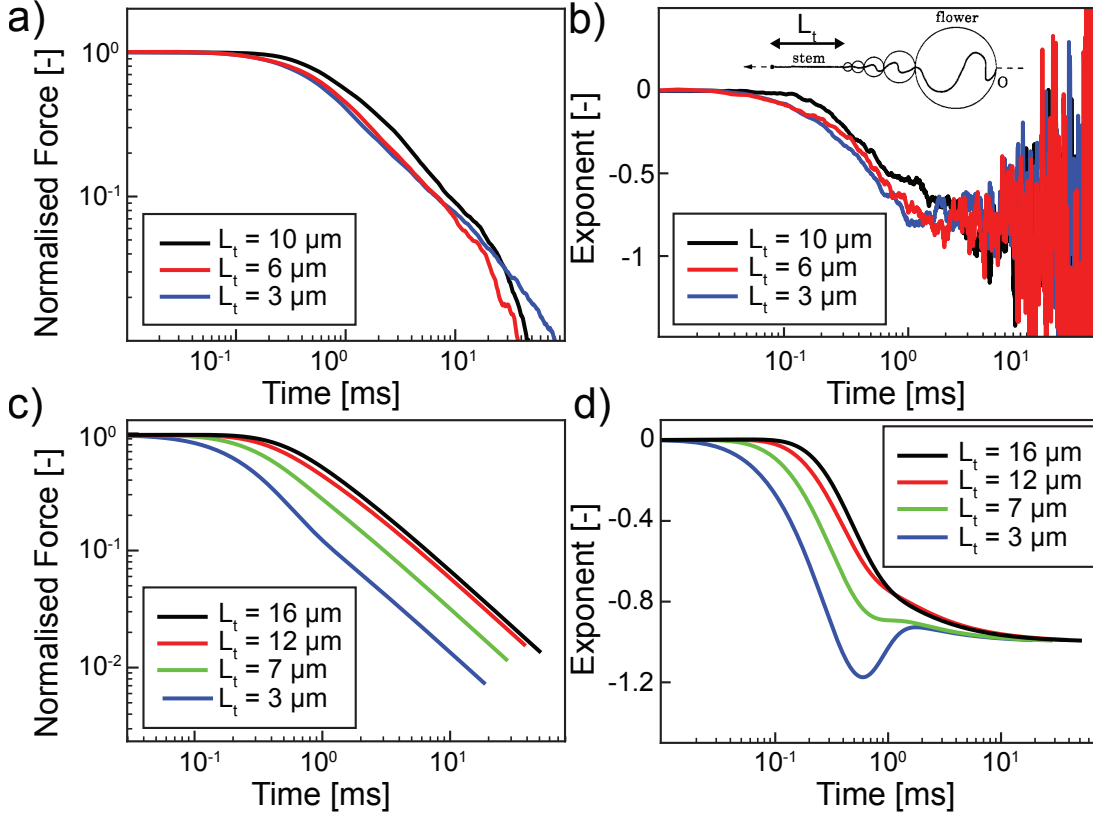


Figure 4.6 – Length dependence of taut DNA dynamics. **a)** Experimental log-log curves for different lengths of tensed DNA. These were all carried out in the same capillary, and with the same stiffness of $30 \text{ pN}/\mu\text{m}$. The number of averaged curves is $N = 25, 106$, and 31 in the order given by the figure legend. **b)** Exponents corresponding to the curves on panel a). Inset shows the starting position of the DNA with a length of tensed rod L_t and an untensed flower region. Inset is adapted from ref. [176]. **c)** Simulations of DNA relaxation for different lengths of tensed DNA. Similar to panel a) force decay in time is shown. **d)** Exponents corresponding to the simulations in panel c). The exponent does not change from its long time-scale convergence of -1 , as confirmed by both experiments and simulations.

In order to tell conclusively if any large variation in scaling exponent is induced by a change from the taut dynamics regime to the stem-flower regime less noise in the force trace would be needed. This would allow to adequately resolve the behaviour of the exponent once it reaches the thermal force limit ($< 1 \text{ pN}$). In addition to this a much longer length of DNA could be used in order to have the drag of the 'flower' dominate the dynamics. Nevertheless, the experiments conducted in this chapter show that the high temporal resolution, granted by the use of a quadrant photo diode for bead deflection measurement, adequately resolve the taut dynamics even for very short lengths of taut DNA.

4.4 Controlled translocations and the role of electroosmotic flow: Conclusions

A combination of nanocapillaries with optical tweezers has now been shown to accurately measure, not only biologically relevant quantities such as precise protein localisation, or discrimination of DNA bound proteins, but also that they can contribute to a more fundamental understanding of the physics of DNA by measuring with high temporal precision the relaxation of taut DNA in several configurations. This precision, along with the ability to obtain large statistics and thus avoid over-filtering by simply averaging curves together allows to experimentally measure the scaling exponent of the dynamic relaxation of DNA. The importance of simulations is also brought to the fore as a tool to support the validity of such measurements and to bridge the gap between experiments and existing physical models.

If the problems of large noise at the thermal force limit can be resolved then it would be of great interest to use the technique of optical tweezers combined with nanocapillaries to investigate the physics of DNA translocation. Indeed, little is known about the exact dynamics of capture and translocation of DNA through nanopores. Studies could be conducted using the same technique as described in this chapter but studying the inward trajectory of the DNA. This trajectory would not be driven by the entropic collapse of a tensed rod but by the electrophoretic force dragging the DNA through the pore. Similar knowledge may be gleaned by using other protocols such as the decay in a $L_t = 0$ case (equivalent to not moving the stage in the discussions above). A third way may be to study the relaxation of DNA but, instead of dropping the voltage to $V = 0$, switching the polarity of the voltage from $+V$ to $-V$. In this way the free end of DNA would be driven towards the bead in relatively the same way that a translocation takes place. All of these techniques have been fleetingly attempted with the current state of the experimental setup along with modifications of the solution viscosity to slow dynamics[213] or the use of ssDNA. Unfortunately no clear patterns were readily observed.

The difference between theory and the measured force decay exponent as well as the difficulty in extracting dynamics more closely related to translocations is postulated to be due to electroosmotic flow in capillaries. In glass nanocapillaries, electroosmotic flow is known to be large[79] and unrepeatable due to slight variations of surface charge, and geometrical factors. This is a large hindrance to studies such as the ones discussed in these preceding sections. A solution to the variation in EOF would lead to many interesting avenues of research, such as studies into DNA translocation dynamics, being made more consistent.

4.5 Polymer coating of nanocapillaries

This section was performed in collaboration with: S. Marion, Z-Q. Wu, L. Sola, M. Chiari, and A. Radenovic.

Contributions: S.J.D. performed experiments and data analysis, Z-Q.W. performed experiments, L.S. and M.C. designed and synthesised polymers, S.M. and A.R. supervised the research.

4.5.1 Electroosmotic flow and ionic current rectification in nanopores

Electroosmotic flow was introduced in chapter (1) as being due to the coupling of surface charge induced electrical double layers with external electric field. Indeed, when electrical double layers build up in the fluid close to charged surfaces electro-neutrality is broken[24]. This lack of electro-neutrality coupled with local electric field will exert a net body force on ions of the double layer inducing a liquid flow via viscous drag coupling[214]. Electroosmotic flow is highly dependent on the electric field as well as the surface charge[215]. Surface roughness has also been shown to play a role in EOF with increased local surface curvature due to roughness leading to flow suppression[216]. Flow in glass nanocapillaries has been directly experimentally measured with a system very similar to that used in chapter (3) and (4) where a truncated bead's rotation can be measured[79]. From the rotational frequency of the bead the velocity of the flow as well as its spatial distribution is mapped. Velocities can be extremely large, on the order of $u_{\text{EOF}} \approx 0.5$ m/s for pore opening sizes $d \approx 20$ nm[87; 217], which shows how important EOF is to take into account in these systems. Such flow velocities can lead to forces on the order of several pN on proteins[49]. This large flow effect can, not only adversely affect dynamics of translocations in nanocapillaries as seen in the previous section, but can contribute to the conductance of charged nanopores. This contribution is quantified through ionic current rectification (ICR).

Ionic current rectification is defined as being $r = |I(+V)/I(-V)|$, with $r = 1$ for completely symmetric pores that follow ideal ohmic behaviour. However, in pores where the IV characteristic is non linear, where current grows super-linearly for one voltage polarity and sub-linearly in the opposite polarity, $r > 1$ will quantify the ionic current rectification. Electroosmotic flow alone is not enough to induce ICR as it is symmetric in electric field. However whenever an asymmetry in the system is present EOF will enhance ICR[218; 219]. Asymmetry may be present in many forms and its effect on flow and ICR has been studied. Asymmetry in the underlying surface charge, for example with half treated pores (see figure (4.7b) for an example of such a pore), can lead to extremely large rectification $r \approx 100$: these are usually termed nanofluidic diodes[220; 221]. This terminology is accurate considering solid state based diode equations such as the Shockley equation (derived for PN junction current behaviour[222]) can qualitatively describe the IV characteristic of such pores[24]. Asymmetry in the buffer solutions on the *cis* and *trans* side of the pore also leads to ICR whether it be viscosity differences[223], pH differences[224], or salt concentration differences[225]. Geometrical asymmetry is one of the simplest ways of inducing ICR, as many etching techniques will yield cone shaped pores. This is also the symmetry break that induces ICR in pulled glass nanocapillaries[226].

Ionic current rectification in conical pores will depend on electric field strength through its enhancement due to electroosmotic flow[227]. Due to its origin being intimately coupled to surface charge properties it also depends on pH[214; 228] as well as ionic strength[215]. Indeed, lower salt concentrations lead to larger electrical double layers (see introduction chapter (1) on Debye and Gouy-Chapman lengths) which increase the flow. In geometrically asymmetric nanopores, the amplitude of ionic

current rectification depends on pore size with smaller pores showing larger rectification effects[229]. This is due to surface conduction playing a larger role as pore size is reduced (see Dukhin length in chapter (1)).

Recently, ionic current rectification of conical pores has been shown to depend on hydrostatic pressure[230; 231; 232]. Applying a pressure difference between the *cis* and *trans* side of the pore was shown to reduce the ICR effect and linearise IV characteristics. This is shown to be due to the fluid flow disturbing ion concentrations inside the pore[232]. The lack of such a pressure induced reduction in small pores confirms the flow importance and is due to drastically smaller flow rates at smaller pore sizes ($Q \propto R^4$ if Poiseuille flow is assumed, $Q \propto R^3$ when access regions dominate). This pressure dependence of ICR will be discussed in detail in chapter (8) for the case of symmetric pores.

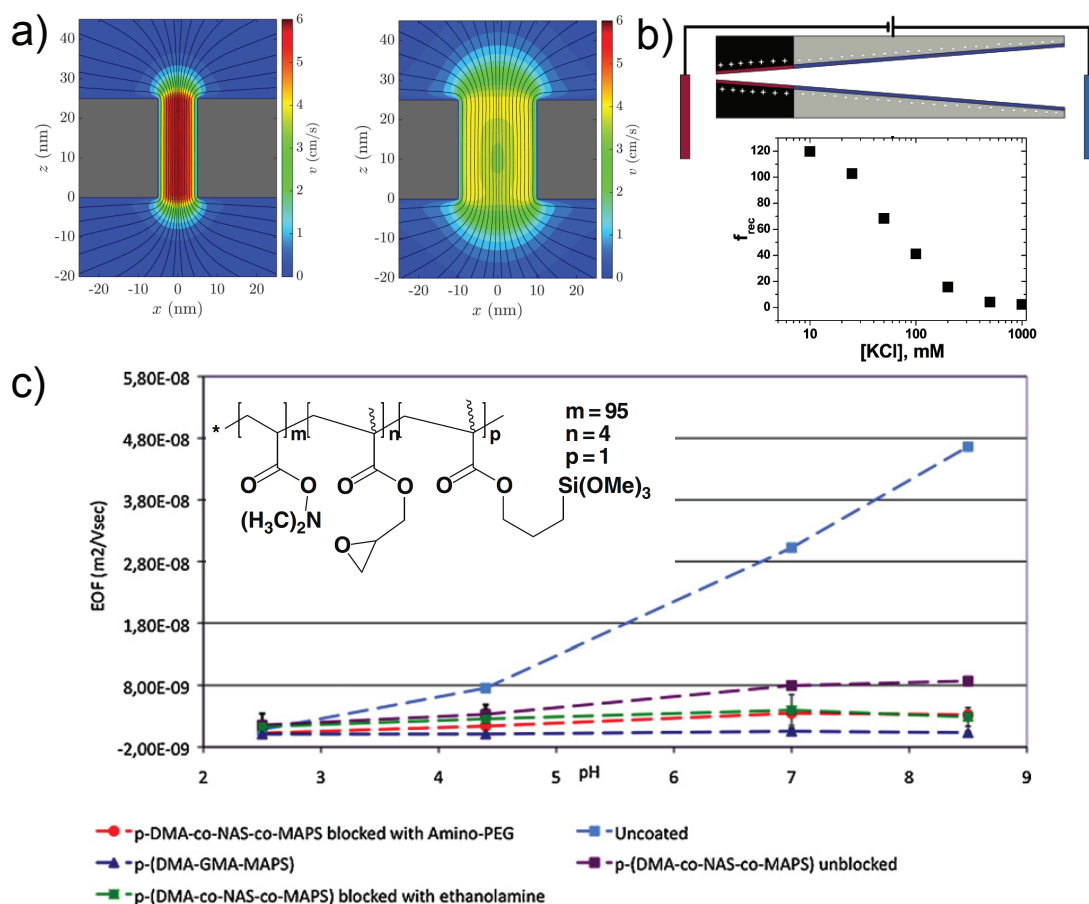


Figure 4.7 – Electroosmotic flow and ionic current rectification in nanopores. **a)** Electroosmotic flow velocity in a 5 nm (left) and 10 nm (right) silicon nitride nanopore. Image is adapted from ref. [227]. **b)** Schematic of a conical nanopore made out of PET foil with asymmetric surface charge along the pore length. This leads to very high rectification $r \approx 100$ for low salt concentrations exemplifying a nanofluidic diode. Image is adapted from ref. [220]. **c)** Examples of electroosmotic flow velocity as a function of pH for bare and polymer coated capillaries used for capillary electrophoresis. Inset shows the chemical structure of the polymer PDMA-GMA-MAPS. Main image is adapted from ref. [137] while inset is adapted from ref. [233].

Techniques for reducing EOF have been studied in different systems. The simplest way of reducing

the flow is to reduce the surface charge, for example by changing the pH of the solution to find the iso-electric point of the surface and thus having little to no charged double layer to couple with the field. While this is a simple method it can easily lead to issues since the iso-electric point for glass and silicon nitride is $pH_{\sigma=0} \approx 1.5$ and $pH_{\sigma=0} \approx 3$ (depending on growth parameters) respectively[234; 235] meaning that DNA in such solutions would be unstable and damaged[236]. Use of different salts has also been shown to modulate EOF[237] due to a modification of the zeta potential with different cationic species[238]. Another technique lies in modifying the surface with a coating that reduces flow[136; 239]. Biological coatings such as lipid bilayers have been used to reduce flow in pores[83; 140]. In solid state pores this was confirmed by an increase in the measured threading force in optical tweezers experiments[83; 140] as well as having the added benefit of reduced sticking of analytes to the pore walls[141]. This reduction of wall-analyte interaction during free translocations enables the extraction of shape, volume, charge, rotational diffusion coefficient, and dipole moment of individual proteins[139; 240]. However, lipid bilayers induce an increase in $1/f$ noise in coated pores postulated to be due to the fluidity of the lipid bilayer[83].

Charged polymer coatings can also be used to diminish ICR or, by using oppositely charged polymers to the surface, invert the ICR behaviour as compared to bare pores[241]. Neutral polymers are perhaps most common to reduce EOF since their lack of charge does not bring its own flow generation[242]. Many such neutral polymers are available: from poly vinyl alcohol (PVA), polysaccharide coatings, or the acrylamide based polymers that will be discussed below[239]. These types of coatings have the benefit of being bound or adsorbed to the pore wall and thus should not increase the $1/f$ noise as lipid bilayers do. Acrylamide based polymers have been widely used in the field of capillary electrophoresis where EOF affects the separation speed, resolution, and reproducibility of experiments[137; 243]. Surface coating of such capillaries leads to reduced flow due to two effects. The first is surface charge screening where the polymer acts as an additional screen for the surface charge or saturates binding sites through covalent bonding and thus reduces the flow[241]. The second effect is that viscous fluid drag between the liquid and the polymer film reduces the build up of the flow[242]. Such polymer coatings have thus shown to be effective in EOF reduction if the coating thickness extends past the Debye length of the system[244].

4.5.2 Measuring and reducing effects of electroosmotic flow

Results from the previous chapters such as the spread of measured effective linear charge density of DNA (chapter (3)), and the difficulty in obtaining exponents of tensed DNA force-time relaxation, point to electroosmotic flow being an uncontrollable factor that may adversely affect results. This is especially true when comparing data between different nanocapillaries. While single capillaries can be used for experiments such as free translocations, often for lower yield experiments such as optical tweezers, it is necessary to use several samples. This is a larger factor when pore size dependent phenomena are studied. Taking this into account, an approach to reducing electroosmotic flow in glass nanocapillaries was undertaken.

The chosen strategy to reduce electroosmotic flow in glass nanocapillaries is to coat the surface with a neutral polymer. As described above the effect is expected to be two fold. A small amount of charge screening will reduce the flow. Secondly, the viscous drag entailed by the multitude of polymer strands at the surface reduce the build up of liquid flow in the capillary. The polymers are specially designed to reduce flow in classical capillary electrophoresis and have been used extensively in that field[137; 242; 243; 244] where they can also serve to render microfluidic pathways hydrophilic[233]. They have not yet been applied to small glass capillaries in the nanometer range of the type discussed

in this thesis.

A family of polymers was synthesised by collaborators for use in glass nanocapillaries. These polymers are all based on the same poly(dimethylacrylamide) (PDMA) base. One is plain PDMA, the next is modified with a silane moiety [3-(methacryloyl-oxy)-propyl]trimethoxysilane (MAPS), and the last contains the silane along with a functionalisation of glycidyl methacrylate (GMA). The chemical structure of PDMA-GMA-MAPS is shown on the inset of figure (4.7c). PDMA will coat the surface due to non-covalent interactions such as hydrogen bonding, Van der Waals, or hydrophobic forces. In contrast to this, the polymers containing a silane will covalently attach to the silanol surface group of the glass capillaries[233].

The two more complex polymers are of added interest due to the possibility of functionalising them with additional molecules in order to create brushes or cross-linked gels at the surface of the nanocapillary. In order to confirm the attachment of polymers, observe the coverage density, nanoscale organisation, and height of polymer layers, liquid AFM images were taken of coated silicon nitride chips. This is achieved with a simple plasma, dip, and rinse protocol (the full protocol for nanocapillary coating is described later). Density of polymer coating has been shown to be a factor in the reduction of EOF[245], however AFM studies confirm that the polymer coating is uniform and dense with height differences within the film on the order of 0.1 nm (figure (4.8)). This is comparable to bare silicon nitride implying no extra roughness due to the coating layer[246].

Further investigation of the mechanical properties of these polymer films was done by taking images in contact mode with the AFM tip. First, concentrically smaller images with higher and higher contact force are made. Subsequently, the whole area is imaged and the polymer coating's indentation is observed. Figure (4.8b and c) shows a concentric pattern of squares in the height and phase images. From the height image it is clear that indentation is maximum (≈ 1 nm) in the center most square in which ≈ 1000 nN of force was applied on the polymer. The phase image is proportional to the rigidity of the substrate and so the amount of indentation is seen to correlate with the rigidity of the polymer layer. The hypothesis is that the polymer layer is hydrated in solution and relatively loose at a thickness of approximately 5 nm[233]. When applying high forces such as with the AFM tip in contact mode the polymer layer is flattened against the underlying substrate thus increasing in rigidity.

The protocol for coating nanocapillaries with polymer contains the following steps. First, the nanocapillaries are subjected to oxygen plasma for 10 minutes so as to clean the surface from any contamination, along with activating the surface oxygen groups. Then, and without delay so as to keep the surface activation as fresh as possible, the capillaries are placed in a liquid droplet of 2% w/w of polymer, previously filtered through 20 nm filters. Next, the immersed capillary is placed in a dessicator so the lower pressure forces the liquid to enter the tip. The capillaries are left in low pressure conditions for 30 min so as to ensure proper coating of the tip region. Finally, capillaries were mounted in a PDMS flow cell and attached to a microscopy slide (as described in chapter (2)). Polymer coatings are stable for hundreds of hours regardless of pH, temperature or denaturant concentrations[247] so even long term storage should not affect the coating efficacy. Coated nanocapillaries are then probed in several different experiments to assess whether the polymer coating is present, robust under voltage application and with time, and whether coated nanocapillary electroosmotic flow characteristic are in fact reduced.

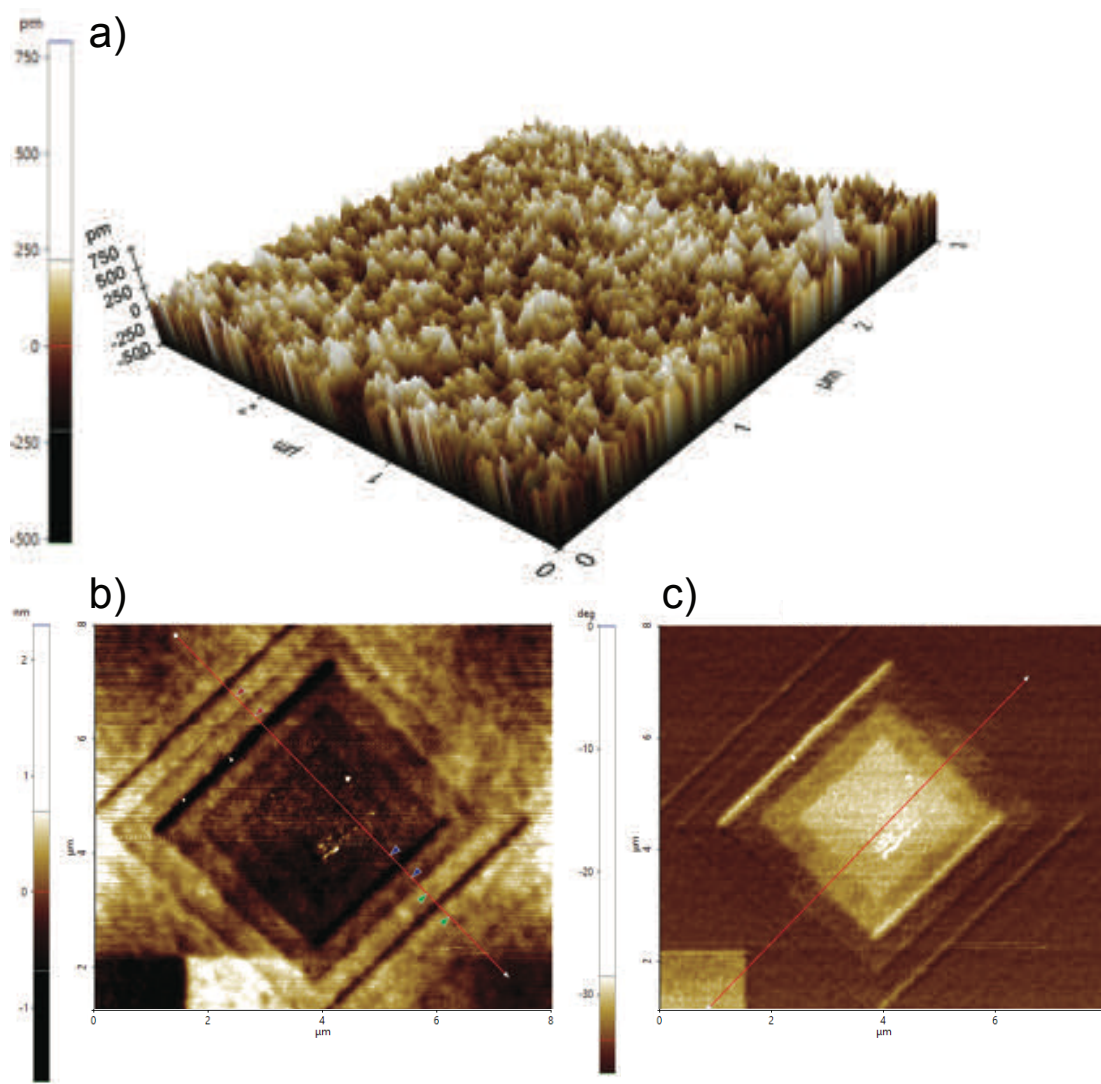


Figure 4.8 – **Liquid AFM measurements on PDMA-GMA-MAPS coated silicon nitride chips.** **a)** Height map of undisturbed polymer coating showing the uniform coverage over micron sized areas. **b)** Height map after contact mode indentations with different forces. Force is applied in higher and higher increments as the area of the contact image was reduced. Maximal indentation at ≈ 1000 nN of force is ≈ 1 nm. **c)** Phase image corresponding to panel b) showing the increased rigidity of indented polymer regions. AFM imaging courtesy of R. Foschia.

Precise measurements of ionic current rectification as a measure of EOF

Due to the correlation between ionic current rectification and electroosmotic flow in conical pores, the first quantification of EOF is attempted by measuring ICR in polymer coated capillaries. ICR can easily be measured by measuring a standard IV curve as defined previously $r = |I(+V)/I(-V)|$. There is however another method of measuring the rectification: via a lock-in amplifier. A sinusoidal bias voltage $V(t) = V_0 \sin(2\pi f t)$ at a frequency f is applied and the resulting current $I(t)$ is read. The measured current is characterised by the admittance of the system $Y(V)$ as: $I = Y(V)V$. Any non-linearities in the system are therefore contained within the admittance. By assuming that the system is made up

of a parallel conductance $G(V)$ and capacitance C the admittance is written $Y(V) = G(V) + j\omega C$. The Taylor expansion of $G(V)$ for small perturbation voltages would then be:

$$G(V) \approx G(V=0) + \frac{\partial G(V)}{\partial V} \Big|_{V=0} V + \frac{1}{2} \frac{\partial^2 G(V)}{\partial^2 V} \Big|_{V=0} V^2 + \dots = G_1 + G_2 V + G_3 V^2 + \dots \quad (4.6)$$

Where the G_1 term is the linear term of the conductance and corresponds to equation (1.1). By plugging the sinusoidal applied voltage into the system response the current is obtained as:

$$I = \frac{1}{2} V_0^2 + \left(G_1 V_0 + \frac{3}{4} G_3 V_0^3 \right) \sin(\omega t) + \omega C \cos(\omega t) + \frac{1}{2} G_2 V_0^2 \sin\left(2\omega t - \frac{\pi}{2}\right) + \frac{1}{4} G_3 V_0^3 \sin(3\omega t + \pi) + \dots \quad (4.7)$$

Considering that the lock-in amplifier can detect several different harmonics $I_n \propto \sin(n \cdot (2\pi f t))$ these can be connected to the conductance contributions in the above equation.

$$I_1 \approx G_1 V_0 \sqrt{1 + \frac{\omega^2 C^2}{G_1^2 V_0^2}} \quad (4.8a)$$

$$I_2 = \frac{1}{2} V_0^2 G_2 \quad (4.8b)$$

Harmonics higher than $n = 2$ are ignored since their contribution is assumed to be small, the ionic current rectification can then be given as a function of the ratio of second harmonic current I_2 (non-linear contribution) to first harmonic current I_1 (linear contribution) as:

$$r(V) \approx 1 + 4 \frac{I_1(V)}{I_2(V)} \quad (4.9)$$

This approximation is valid in the limit of dominant first harmonic current, $G_1 \gg G_2 V_0$, and in the limit of low frequencies $2\pi f \ll \frac{G_1 V_0}{C}$ (i.e. close to DC). This description also assumes that the second harmonic current is the dominant harmonic and that other additional harmonics (third, fourth, and so on) are negligible in comparison. This may not be true for highly rectifying samples, but for low voltages it was found to be in good agreement with values computed from DC IV curves for all the studied samples.

Bare and polymer coated capillaries are electrically characterised both with AC and DC measurements. Figure (4.9a) shows examples of DC IV characteristics of three capillaries: one control, one coated with PDMA, and one coated with PDMA-MAPS. This shows that for some capillaries the expected behaviour of ICR reduction is obtained via a linearisation of the curve and a slight increase in resistance. An increase in resistance is expected due to the thickness of the polymer layer (≈ 10 nm total). Panel b) of the same figure shows the noise PSD as extracted from the DC current traces for the bare and PDMA coated capillaries. The noise spectra show no clear increase in $1/f$ noise as was seen with lipid coating[83]. This is also consistent with the fact that the layer of polymer is adsorbed to the surface and so is not expected to have the same degree of freedom as a fluid lipid bilayer.

Aggregated data of AC extracted ICR versus resistance of nanocapillaries is presented on figure (4.9c),

where the coated capillaries are shown in red and bare control capillaries are shown in blue. All data is acquired at a bias amplitude of $V_0 = 100$ mV RMS and a frequency of 10 Hz. The acquisition frequency is chosen while taking into account the conductance response of the system in frequency.

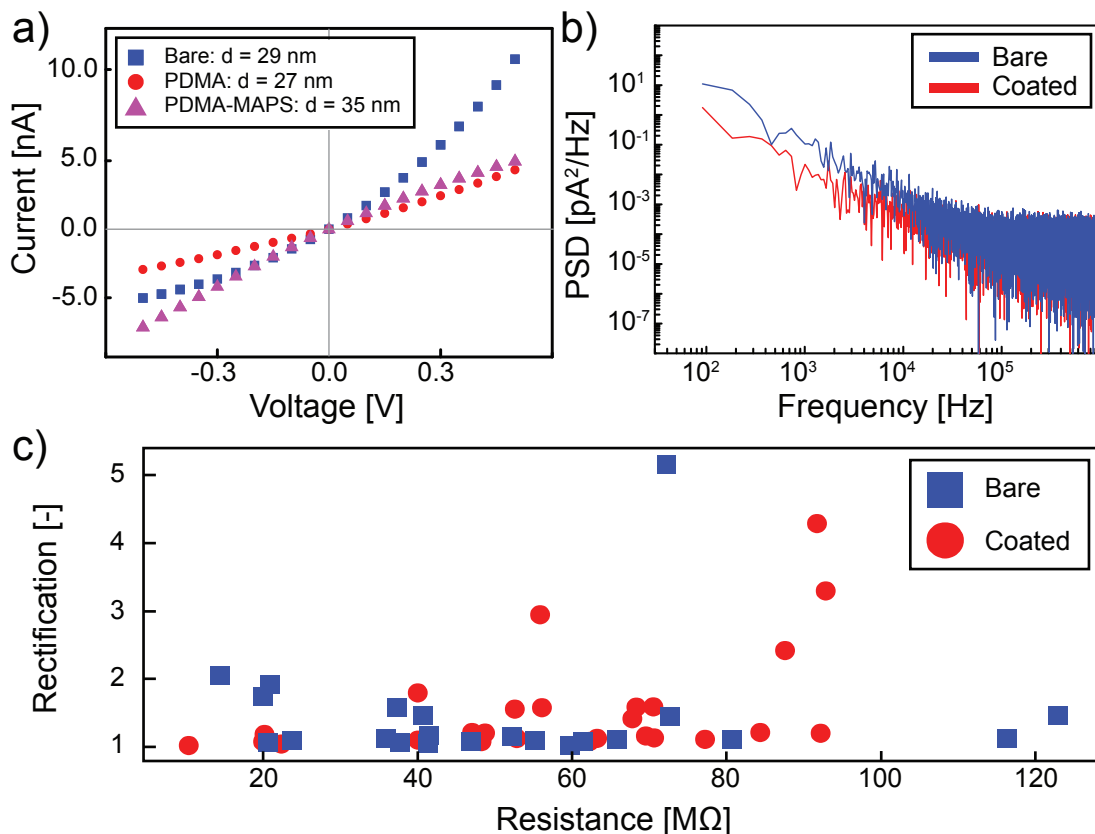


Figure 4.9 – Electrical characterisation of polymer coated nanocapillaries. **a)** Three typical DC IV curves showing bare nanocapillary's high rectification and coated nanocapillaries' reduction in rectification. It is also clear that due to the coating procedure the size of the capillary opening is diminished thus yielding a higher overall resistance. **b)** Noise analysis from panel a) where no significant noise increase is seen for the coated nanocapillary. The noise behaviour is postulated to be due to the fact that the polymer layer is adsorbed to the glass and thus is less prone to fluctuation. This is in contrast to other coating techniques, such as lipid bilayer coating, that increases the noise due to fluctuations of the lipid layer. **c)** Ionic current rectification as measured with the lock-in amplifier as a function of the resistance of the pore. The resistance is chosen as the comparative measure since for small capillaries the correlation between measured size of the opening via SEM and its resulting resistance is low. While some outliers both from the coated group and bare group have large rectification values it is not possible to deduce a lowering of rectification for the majority of the coated capillaries.

Nanocapillaries show a frequency response where at low frequencies $f < 1$ Hz electrode polarisation is non-negligible, this is followed by a plateau region $1 < f < 100$ Hz where the measured AC linear resistance (G_1) corresponds to the DC value, and finally for high frequencies leakage dominates $f > 100$ Hz. This is shown on figure (6.2) (in this case capillaries are not filled with aqueous solvent but the frequency dependence is not qualitatively different). A second factor in the choice of frequency is that ionic current rectification has been shown to be frequency dependent[241] with the effect being largest at low frequencies close to DC and dropping off sharply at frequencies $f > 30$ Hz. The rectification data

shows a large spread independently of the coating status of the capillary with some capillaries showing higher ICR with increased resistance as expected[229].

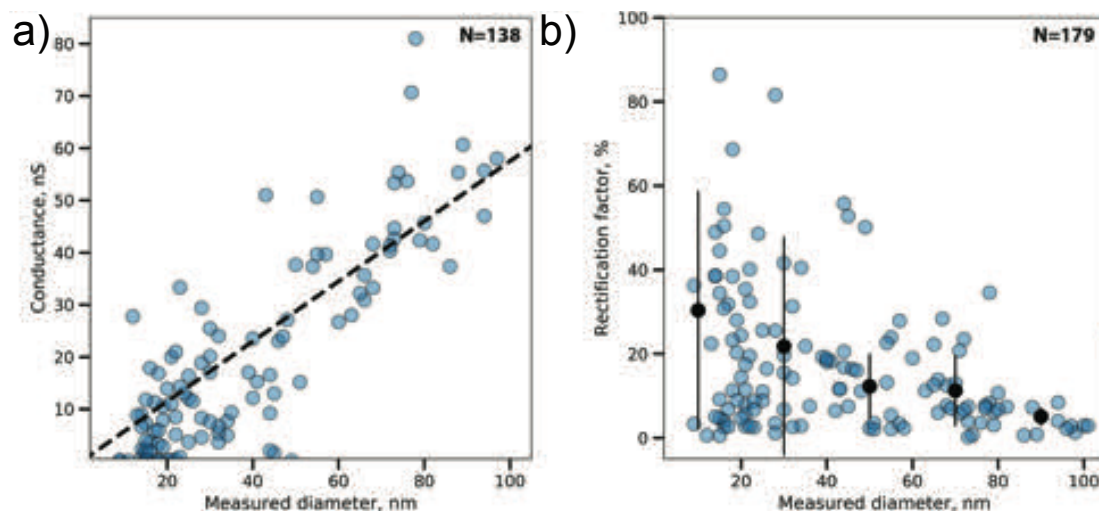


Figure 4.10 – Conductance and ionic current rectification spread in small glass nanocapillaries. **a)** Conductance as function of SEM measured nanocapillary opening diameter for 138 bare nanocapillaries. Dashed line is a fit to equation (1.1). **b)** Ionic current rectification as a function of SEM measured diameter for 178 bare nanocapillaries. Both panel a) and b) show how irreproducible nanocapillary electrical properties become below 100 nm. Figure is adapted from ref. [89].

The spread of nanocapillary rectification is attributed to the inherent spread of their electrical characteristics. Indeed the conductance of such pores shows a large variation, especially at low pore diameters. Figure (4.10) shows the conductance and rectification of $N > 130$ bare nanocapillaries as a function of the SEM measured diameter. It is clear that once a capillary's diameter is below approximately 100 nm the spread in conductance becomes large and the theoretical dependence on diameter[41] (equation (1.1)) is no longer precise. The observed conductance spread has contributions from small variations in geometry of the pulled tips that are not controllable with the pulling protocol. These pulling variations will also affect surface roughness of the capillaries that has been shown to have a large effect on ICR[216]. The rectification is also shown to have a large spread especially for small opening diameters. Another possibility is that ionic current rectification and electroosmotic flow are not well correlated in the nanocapillary system and that the asymmetric geometry is dominantly responsible for ICR with flow playing only a small additional role. While the measurements of the rectification via the lock-in amplifier are precise (see chapter (8) where variations $< 1\%$ are measured), it is impossible to conclude a reduction of flow due to coating solely using these measurements.

DNA translocations through polymer modified nanocapillaries

Free translocations of DNA molecules can be a marker for electroosmotic flow. It has been shown that the electroosmotic induced drag force on free translocating DNA molecules, in addition with the asymmetric confinement conditions, affects the translocation time distribution in nanocapillaries[248; 249]. Electroosmotic flow being asymmetric in voltage polarity for nanocapillaries the flow induced drag force will be larger for positive voltage biases and smaller for negative biases. A shift in forward (*cis* to *trans*) versus reverse (*trans* to *cis*) translocation time distributions thus marks a high electroosmotic

flow.

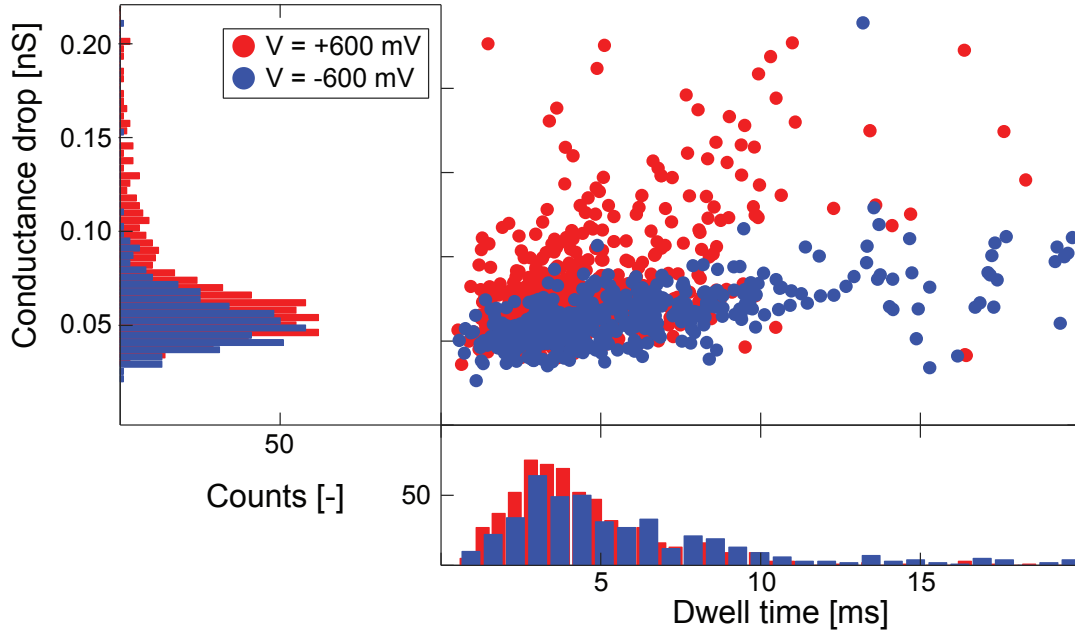


Figure 4.11 – **Free translocations of DNA as a marker for electroosmotic flow reduction.** a) Scatter plot of free λ -DNA translocations through a bare 20 nm nanocapillary at ± 600 mV in 1 M KCl buffered to pH 8. Histograms of dwell times and conductance drops are also included.

In order to probe this, a subset of the nanocapillaries presented above are used for the free translocation of λ -DNA. Long DNA molecules were chosen so as to have a long translocation dwell times. The use of λ -DNA has the added benefit that larger molecules will be more affected by electroosmotic drag force due to their larger gyration radius. Figure (4.11) shows a scatter plot of current drop magnitude versus translocation time in a 20 nm bare capillary. On the horizontal and vertical axis is also shown the global distributions of the conductance drops ΔG and dwell times Δt . No statistical difference in translocation time distributions was seen between $\Delta V = \pm 600$ mV. This is assumed to be due to a smaller electroosmotic drag force as compared to previous literature studies[248; 249] therefore not affecting the translocation times sufficiently to discriminate forward versus backward events. The lack of effect in bare capillaries also means that a reduction in flow would be difficult to see with such an experiment.

Measurement of threading force as a marker of electroosmotic flow

Considering the lack of evidence for electroosmotic flow reduction from both electrical characterisation and free translocations of DNA, a more direct approach was used. The optical tweezers setup is used to measure the threading force of DNA (f_0 value from the previous sections) in coated and uncoated nanocapillaries. The force measured by the optical tweezers setup is always the balance of the electrophoretic driving force reduced by the electroosmotic drag force. In this way the threading force value as measured in the optical tweezers is a more direct measurement of electroosmotic induced drag[83; 140].

Measurements of f_0 are made using at least 10 different DNA molecules whose force is recorded at

least 10 times each in order to build a sufficient statistic of threading forces per capillary. While using coated capillaries it was noted that threading events were harder to obtain than in bare capillaries. In bare capillaries the capture of DNA is relatively straightforward, and the centering of the bead with respect to the pore opening is easy to do by visually comparing the position of the trapped bead with the visible capillary on the live microscopy image. In coated nanocapillaries it was harder to find the exact location where DNA threading events occurred, and higher voltage was often used to induce more events. Considering this bare nanocapillary data was always conducted at the same voltage for correct comparisons to be made.

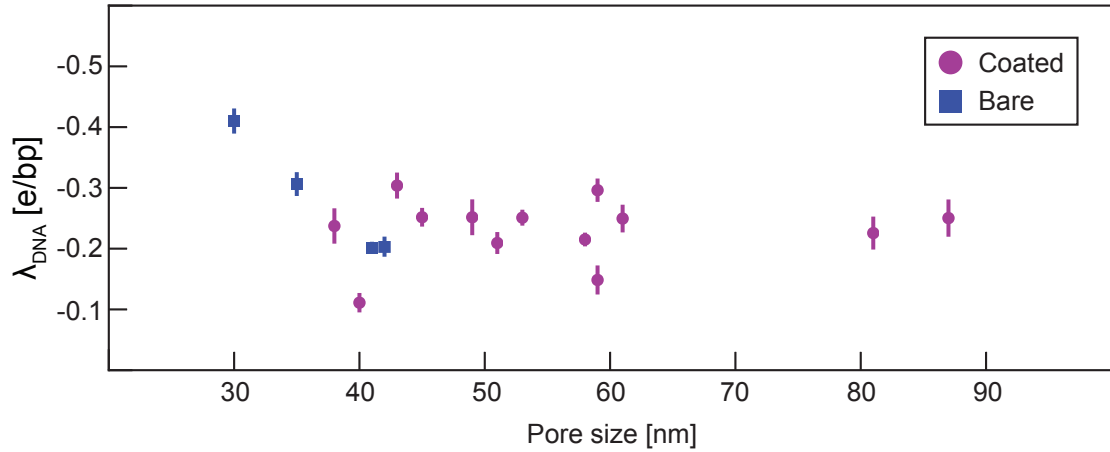


Figure 4.12 – **Comparison of force measured in the optical tweezers setup. a)** Effective linear charge density of DNA as extracted from the force of threading in the optical tweezers setup. Considering that the threading force in the optical tweezers is the balance of the electrophoretic driving force and the electroosmotic drag force $F_{OT} = F_{EP} - F_{EO}$ a higher threading force should be observed if electroosmotic flow is reduced by polymer coating. This is clearly not the case as the spreads overlap considerably.

Figure (4.12) shows the effective linear charge density of DNA as computed from the threading force $\lambda_{eff} = f_0 / V$ in both coated and bare capillaries. The spread of this value is quite large and again attributed to geometrical and surface property differences between capillaries within the same group. There is no clear trend of higher force for the polymer coated nanocapillaries which would indicate a reduced flow due to coating. The fact that translocation events were harder to obtain in coated pores does point to some effect of the polymer coating. However, this may be due to external coating only that causes interactions between DNA molecules and polymer hindering DNA capture by the pore. It is possible that the coating does not penetrate inside the capillary in order to coat the inner walls that are responsible for flow generation.

4.5.3 Conclusion

While the results of this study were inconclusive with respect to reducing the electroosmotic flow of nanocapillaries it did however bring experience with the use of PDMA based polymer coatings that allowed a similar study to be performed in collaboration with Awasthi et al.[250]. This study shows that polymer coatings are comparable to lipid bilayer coatings on silicon nitride nanopores when it comes to decreasing the clogging of pores and decreasing non-specific protein-pore interactions. Polymer coatings allowed the correct determination of protein characteristics such as volume, and shape similarly to other investigated coatings. However, in the case of silicon nitride pores the polymer

coating did slightly increase the $1/f$ noise. This again points to the fact that in the nanocapillary case no internal wall coating took place. The thickness of the silicon nitride nanopores used by Awasthi et al. was $L = 30$ nm showing that the polymer must penetrate at least 15 nm into nanometer sized pores. However, as previously discussed in chapter (3), the extent of the electric field in nanocapillaries can be significantly larger, up to 150 nm in some cases. This tenfold increase in distance could explain the lack of effect seen here if the penetration depth of the coating solution is small. Despite the lack of EOF reduction the liquid AFM results conducted here point to some interesting properties of polymer films such as their indentation and rigidity and could be expanded.

The use of glass nanocapillaries can be extremely practical as a low cost, easy, and fast fabrication nanopore. Indeed they can easily be used for free translocation and controlled translocation experiments to detect various analytes such as proteins, DNA, or DNA-protein complexes. However, when a statistical comparison between a population of pores is necessary, for example when studying more fundamental phenomena such as flow in pores, or dynamical properties of DNA translocations, their irreproducible geometry, surface, and flow effects hamper the precise detection and study of such characteristics.

5 Combining protein pores with optical tweezers: SPRNT calibration

This was a work performed in collaboration with: D. Jankunaite, A. Laszlo, S. Marion, J. Gundlach, and A. Radenovic.

Contributions: S.J.D. modified OT setup, performed experiments and data analysis, D.J. performed preliminary experiments, A.L. and J.G. provided MspA along with lipid bilayer knowledge and assistance, S.M., J.G., and A.R. supervised the research.

5.1 Introduction to protein nanopores

So far in this thesis, discussion of nanopores has been limited to one type: pulled glass nanocapillaries. However these are not the only type of nanopores to be used, as introduced briefly in chapter (1). Biological nanopores are another category of nanometer sized pores that are often used in biophysical studies, most notably in DNA sequencing applications[251]. Such pores are transmembrane protein channels that have openings of the size of single stranded DNA thus making them ideally suited to such applications[252]. The fact that they are self-assembled biological proteins means that each unit is identical enhancing the reproducibility in such experiments from the purely geometrical standpoint. Protein pores are, due to their nature as transmembrane pores, inserted into free-standing membranes. While membranes may be formed of block copolymers the most common membrane of choice is lipid bilayers[253].

While the geometrical characteristics of biological pores are perfectly tailored to bio-sensing applications some of their inner amino acid structure may render the charge of the pore unhelpful to ssDNA applications. This is why most of the pores used today for bio-sensing have undergone extensive genetic engineering to modify the apparent charge of the pores and thus facilitate DNA translocations. The most common pores used in the field are bacteriophage phi29 packing motor[254], staphylococcus aureus alpha-Hemolysin[255], and Mycobacterium smegmatis porin A (MspA)[39].

This study will focus on MspA which is an octameric protein. In the case of MspA, the first mutant (M1MspA) used for DNA translocations, designed by Butler et al.[39] contains three major mutations of interior aspartate residues to neutral asparagines (24 mutations in total due to the octameric nature of the pore). Another mutant (M2MspA) replaces these neutral charges with positive charges allowing for better capture of negatively charged DNA. The capture rate is reported to be five fold higher than in M1MspA, and it was also reported to have less clogging of the pore at higher currents[256].

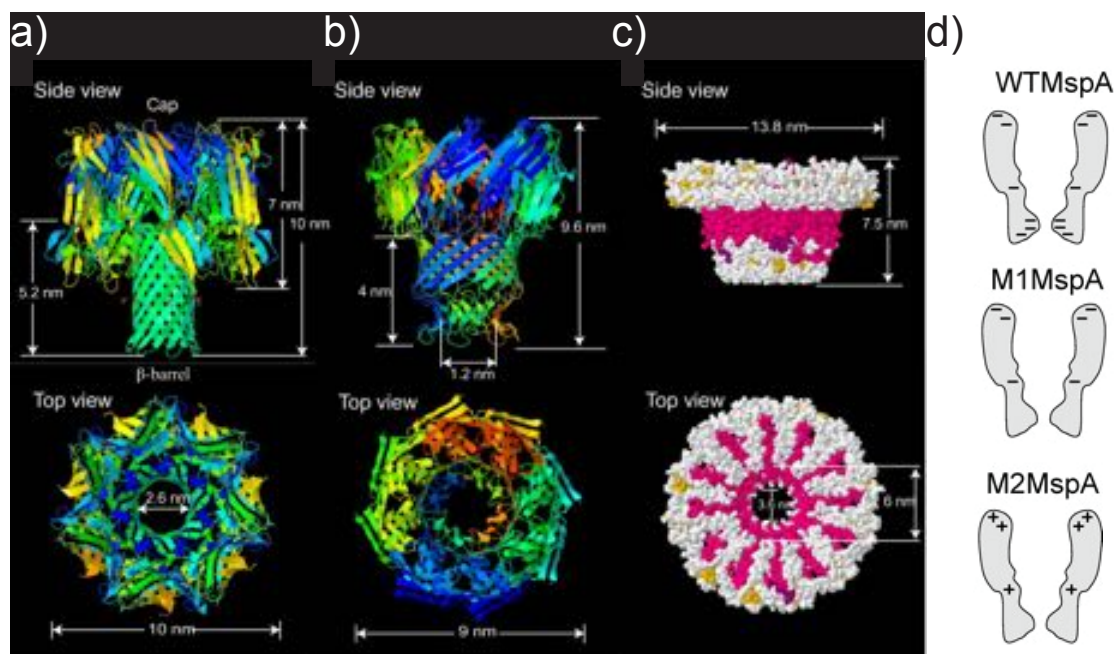


Figure 5.1 – **Most common biological nanopore structures.** a) α -Hemolysin pore with associated dimensions b) Octameric MspA pore with associated dimensions. Panels a), b), and c) are adapted from ref. [252]. d) Schematic showing the amino acid charge mutations between wild type MspA (WTMspA) and the two mutations used in nanopore experiments: M1MspA and M2MspA (used in this study). Image is adapted from ref. [39].

M2MspA's constriction is approximately 1.2 nm wide and 0.6 nm deep meaning that nucleotides of ssDNA (0.9 nm wide) fit snugly within it[39]. The equivalence in analyte and constriction size means that, when translocations occur, the current drop due to nucleotide passage is a significant fraction of the open pore current. In MspA this is as much as 83%[257]. DNA threading events are thus easy to distinguish, and the small current differences due to nucleotide variability in size or charge are also resolvable. It also means that ssDNA must pass through the pore in single file and no issue of double or folded events is present. The depth of the confinement is also important as it defines how many nucleotides are being sensed at any given time due to the extension of the electric field (in comparison to the extended field in glass nanocapillaries). In MspA, the constriction is shallow enough that the given current during a translocation event is only due one nucleotide in the narrowest constriction of the pore. However, Brownian motion of the DNA strand extends this region to approximately four nucleotides. In addition to these structural considerations, MspA pores have shown remarkable stability, able to withstand temperatures up to 100°C and pH values from 2 to 14[258].

While free translocations of ssDNA through protein pores such as MspA was ground-breaking[39], the translocation times were too short to be able to accurately sequence the passing strand. The first practical demonstration of DNA sequencing by MspA was done by Manrao et al. in 2012[32]. Single nucleotide resolution was obtained by using a molecular motor to process the DNA through the pore at much lower speeds. This control offered over the translocation (similarly to what is engineered in chapter (3) with optical tweezers) allowed the discrimination of nucleotide steps and proved the possibility of nanopore sequencing. The motor used by Manrao et al. was phi29 DNA polymerase which locates itself above the MspA pore and is responsible for pulling the DNA strand through the pore.

Other motors such as the polymerases of *E. coli*, bacteriophage T7 and phi29 helicases have also been used as a check on the fast free translocations of DNA through biological nanopores. Such proteins move along DNA in a controlled stepwise manner thus reducing the translocation speed significantly, in addition to translocating the DNA strand in well known incremental steps. This motor restricted movement allows for unprecedented accuracy and precision in the reading of ssDNA strand sequences.

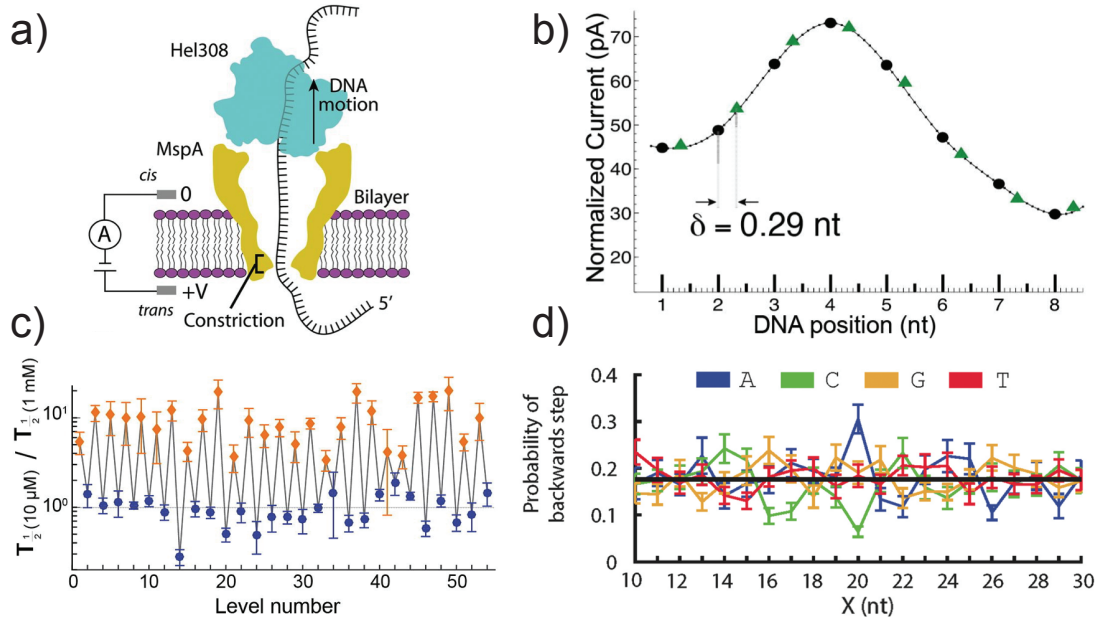


Figure 5.2 – SPRNT technique and its application. **a)** Schematic of the SPRNT technique here probing the Hel308 motor. Image is adapted from ref. [259]. **b)** Normalised current levels as obtained through the MspA nanopore at two different voltages. Figure shows that both profiles can be described by the same universal spline with the larger voltage being shifted by a value δ due to DNA stretching under bias. **c)** Extraction of two sub nucleotide steps in the Hel308 motor. Data taken at different ATP concentrations shows that only one of the levels depends on ATP. Panel b) and c) are adapted from ref. [256]. **d)** Probability of back-stepping of the Hel308 molecular motor as a function of the nucleotide X nucleotides away from the MspA constriction (i.e. within the motor). Each colour represents a different nucleotide showing the probability of back-stepping is position and nucleotide dependent. Image is adapted from ref. [260].

This resolution can also be turned on its head to characterise the motor proteins themselves. Indeed, in sequencing, the motor is assumed to be understood and the DNA strand is the unknown. By using a known DNA strand the measurement becomes a measurement of the kinetics of the motor. This method is what is known as single-molecule picometer resolution nanopore tweezers (SPRNT)[257]. In SPRNT the current trace corresponding to the known DNA strand is interpolated by a spline. This underlying smooth curve then relates the ionic current within the pore to the position of the motor protein along the DNA strand. With measurements of the current levels and the underlying smooth spline, other motor proteins can be compared and the translocation kinetics of these motors can be extracted for a given DNA strand. The fitting of a spline means that even sub-nucleotide steps can be resolved and analysed. In this way effects of pausing or back-stepping, that are known to be DNA sequence specific[261], can be analysed as a function of the exact base distribution[260].

The SPRNT technique offers unprecedented resolution with position changes as small as 40 pm being

resolved at the millisecond time-scale[256]. This, at first, seems counter-intuitive since Brownian motion of the DNA and motor would smear out any resolution of the device. However, the obtained resolution shows that these Brownian fluctuations take place on a fast time scale meaning that the time averaged position permits the high precision of the measurement. Despite this unprecedented spatial and time resolution, a large unknown remains in this technique. Indeed, the exact electrophoretic force that the DNA is undergoing during translocation is not well quantified. While it can be approximated by various different methods this is a key parameter to measure with high precision since it defines the load under which the molecular motor is functioning. While there are many ways of estimating the electrophoretic force caused by the MspA pore there are, as of yet, no direct measurements of it.

This chapter discusses the details of an attempt at such a measurement by combining the nanocapillary and optical tweezers setup discussed previously with the protein pore MspA and its lipid bilayer system. The ultimate goal of this study would be to calibrate the force on DNA in the MspA pore for many different salt concentrations, temperatures, pHs, etc. This would allow to completely describe the SPRNT technique allowing its incomparable resolution to be applied to many different biological motors of interest.

5.2 Combination of protein pores with nanocapillaries

In order to combine the MspA system with the glass pores discussed previously, insight into lipid bilayer forming techniques is necessary. Several methods are available to create lipid bilayers for use with biological pores. A few of the most common will be described here. The first method is to use lipid vesicles. In this case, similar to cellular patch clamp studies, a vesicle is usually trapped onto a microscopic pipette tip by suction force[262]. The first layer of the lipid membrane is then broken either by suction or bias voltage such that only one layer of lipids separate the inside, and outside of the pipette.

The second method is the so called Mueller-Rudin method[263], or painting method, where a solution of lipids is painted over the aperture on which the bilayer is to be suspended. The solvent used can be adjusted to change the ease of bilayer formation, and the thickness of the bilayer. The third method, or Montal-Mueller method[264], is a solvent free method where a monolayer of lipid is deposited on the surface of a buffer solution. This lipid layer will stay at the water-air interface. The scaffold over which the bilayer is to be formed, for example a capillary, or a teflon film, is then dipped through the interface into the liquid. Equivalently the liquid level can be raised so as to move the aperture through the lipid film. The exact process of formation of the layer over the aperture is a zipping of the film where the lipids from either side of the aperture join their hydrocarbon chains (figure (5.3b)). Variants of this method can be performed by letting lipid solution drip along the tip of a submerged capillary and applying slight suction[265].

More recently a novel method of forming an optically available lipid seal was designed in a microfluidic device[266]. The microfluidic channels are made out of NOA81 which is a chemically resistant, and optically transparent polymer. This study showed the formation of lipid bilayers by exchanging solutions between an organic solvent and an aqueous lipid solution. In this way the lipids dissolve into the organic solvent forming a bilayer at the aperture. Such bilayers were then shown to be able to insert α -hemolysin.

In all cases the formation of a bilayer is verified by a resulting jump in resistance between the two chambers. Fully formed and stable lipid bilayers have been shown to have resistances on the order

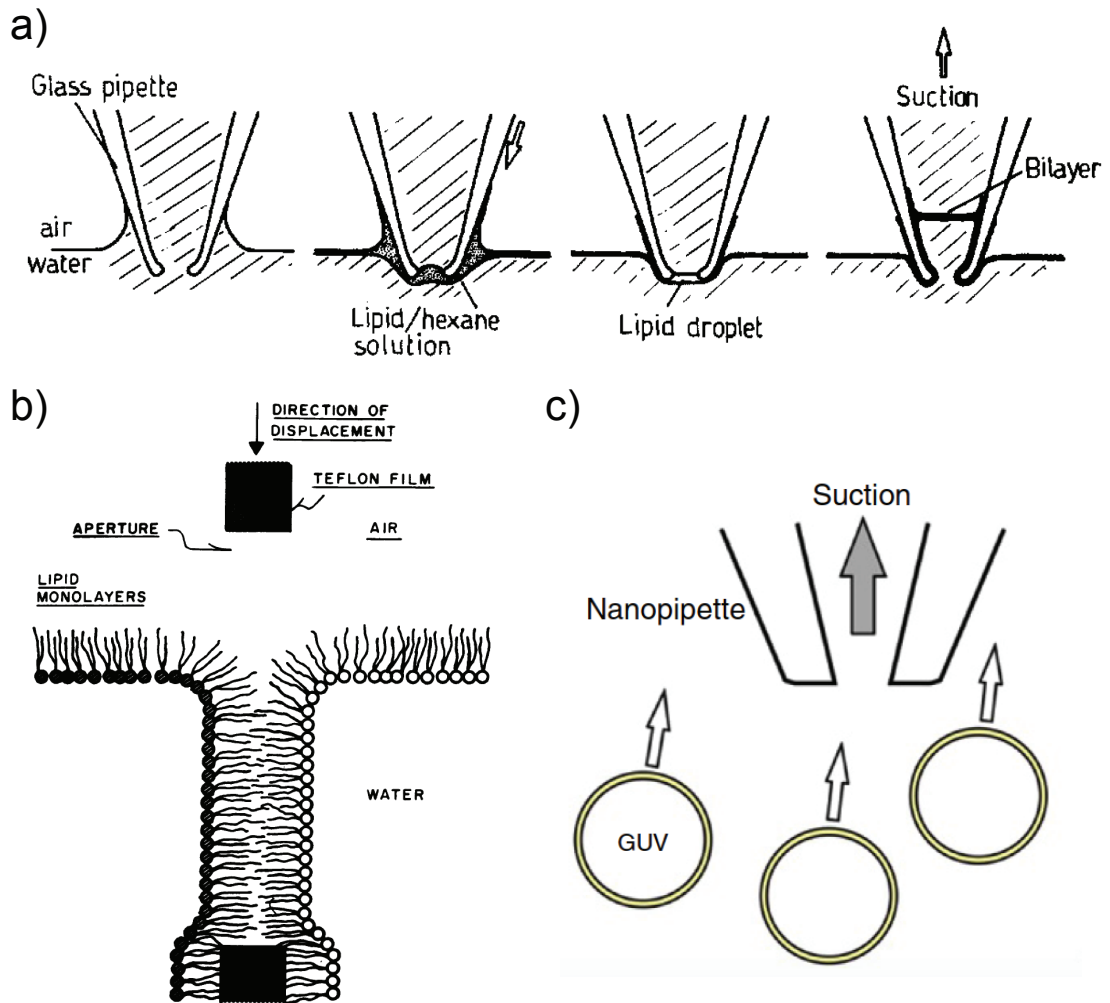


Figure 5.3 – Methods for forming lipid bilayers and combining with glass capillaries. **a)** Modified Montal-Mueller method of solvent-free lipid bilayer formation. A glass pipette immersed into liquid is then coated with a small amount of lipid in hexane solution by applying it to the tip region. As the hexane evaporates a lipid droplet is formed at the tip that can be formed into a bilayer via suction from the back of the capillary. Image is adapted from ref. [265] **b)** Schematic of the zipping of the lipid leaflets via hydrocarbon chain bonding in the Montal-Mueller approach to lipid bilayer formation. Image is adapted from ref. [264] **c)** Method for forming lipid bilayers with free-floating giant unilamellar vesicles (GUV). Image is adapted from ref. [262]

of $10^{10}\Omega$ and are stable under voltages up to 300-500 mV[264; 267]. The following section describes in detail the protocol used to form stable lipid bilayers at the tip of microcapillaries that are easily interfaced with optical tweezers experiments. Figure (5.4) shows a schematic of the experiment with an MspA pore inserted in a lipid bilayer spanning a glass microcapillary. This figure also shows expected current and force traces caused by the threading of DNA through the MspA nanopore similar to what has been seen in previous chapters.

5.3 Combination of glass capillaries, optical tweezers, and the MspA system

5.3.1 Lipid bilayer formation on glass microcapillaries

The method chosen to integrate lipid bilayers in the optical tweezers setup is the Mueller-Rudin or painting method. It is briefly described here. First 1,2-diphytanoyl-sn-glycero-3-phosphocholine lipid (DPhPC) previously dissolved in hexane is dried onto clean glass slides. This dry lipid is then rehydrated into "paint" with the addition of hexadecane. The ratio of hexadecane to lipid is the most crucial aspect of this process. Too little hexadecane and the bilayers will be difficult to form and easily broken. Too much hexadecane and the lipid flows too easily and clogs the aperture.

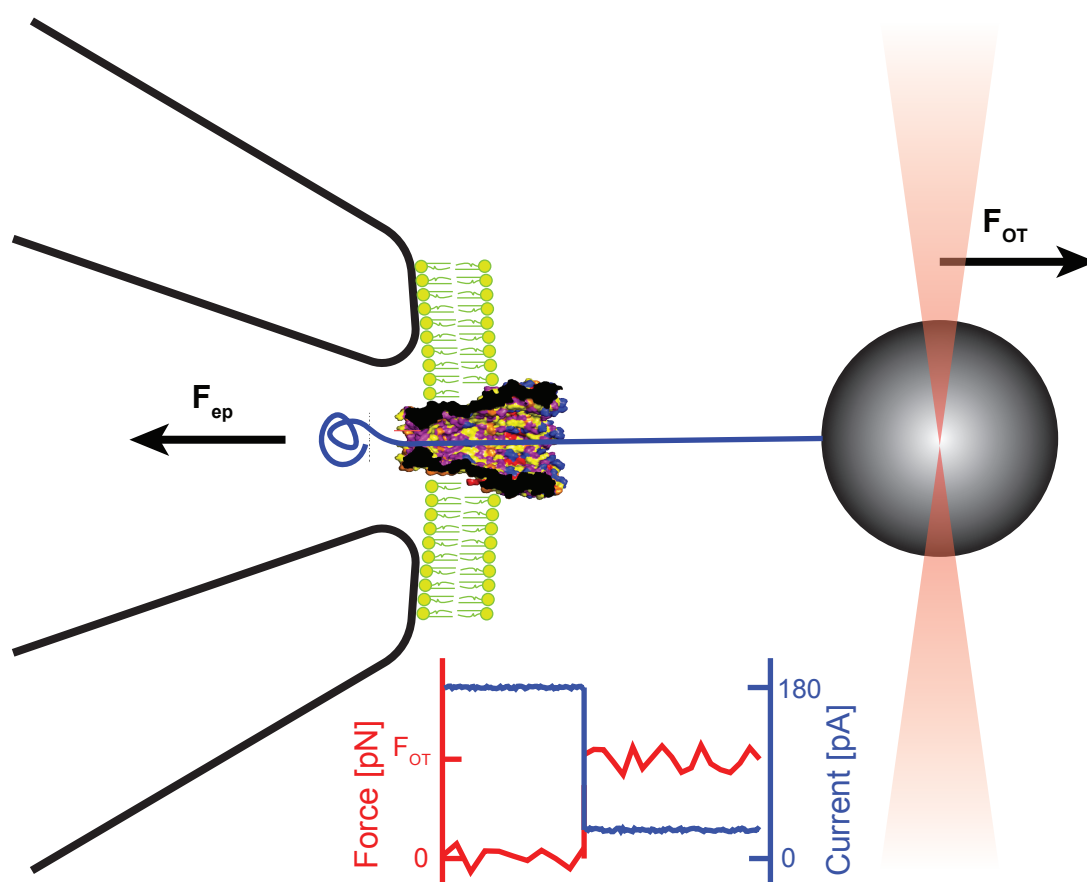


Figure 5.4 – **Schematic of electrophoretic force measurements in MspA nanopore system with optical tweezers.** Schematic of the MspA optical tweezer experiment with an MspA biological pore inserted into a lipid bilayer spanning a glass microcapillary. A polystyrene bead coated in λ -DNA is brought close to the pore to initiate a threading event. The force measured by the optical tweezers F_{OT} is equivalent to the electrophoretic threading force of MspA, F_{ep} . Inset shows a schematic of expected current and force traces where the measured force increases from zero to the threading force simultaneously to the current drop due to translocation.

This paint is then spread over the tip of a microcapillary with a thin, flexible paintbrush. Microcapillaries

5.3. Combination of glass capillaries, optical tweezers, and the MspA system

have been created with the same procedure as detailed in chapter (2) with the parameters found in table (2.3), yielding microcapillaries with opening sizes of 2-10 μm . The surface of the capillaries should ideally be hydrophobic in order to have good adherence between the lipid-hexadecane mixture and the glass surface ensuring bilayer stability. To achieve this the microcapillaries are briefly plasma cleaned to ensure cleanliness of the surface before being silanised in gas phase with a hydrophobic silane (3-cyanopropyltrimethylchlorosilane).

Such capillaries are then mounted into modified PDMS microfluidic cells. The microfluidic cells normally used for nanocapillary experiments (figure (2.3)) are closed on both sides and do not allow any application of pressure to the back-side of the capillary. Since such back-pressure is necessary to clear lipid clogs during bilayer experiments a modified cell and back electrode setup was designed. The PDMS cell is halved allowing the back-end of the capillary to be connected to a back electrode construction made of plastic pipette tips which can be connected via a teflon tube to a syringe.

Brushing the tip of the microcapillary with hexadecane-lipid "paint", with care so as not to break the tip, clogs the capillary with lipid solution. This is observed by an increase in resistance of the sample that cannot be cleared by the application of voltage bias (1 V zap of 50 μs). This clog is then cleared by applying pressure through the back-electrode syringe. It is important to remove the syringe after this operation as the residual pressure is enough to burst bilayers. This yields a cleared capillary that has a residue of lipids over the tip. In order to finally form a bilayer an air bubble is dragged across the aperture of the capillary with a pipette. The air-water interface interacts with the lipid solution still present at the tip and forms a bilayer across the capillary. This is again confirmed by an increase in resistance, and the fact that this is due to a bilayer and not a clog is verified by voltage application. An example of the current trace at bilayer formation is seen in figure (5.5) along with the optical image of the simultaneous bubbling.

Following the successful formation of a lipid membrane longevity tests are carried out in order to optimise the ratio of hexadecane in the lipid paint. Indeed if this ratio is not optimal bilayers will be stable for 1-5 min which is not enough to carry out optical tweezers measurements. If the ratio is optimal lipid bilayers were observed to be stable for 20-30 min.

5.3.2 MspA insertion and free translocation confirmation

Once stable bilayers over microcapillaries are obtained, the MspA nanopore can be inserted. The MspA pore is stored in 0.1% OPOE detergent to help the octameric protein to not form aggregates in the stock solution. Additions of MspA are made close to the capillary tip and the current trace observed until insertion events occur (figure (5.6a)). Once an insertion event is observed the whole front-well of the microfluidic chamber is perfused using syringes to remove the non-inserted MspA protein. This has a two fold effect. First it removes MspA from the solution thus stopping any additional insertions of pores. Multiple pores make the current trace harder to interpret as blockages may come from any number of pores. Secondly it also removes the detergent from solution. Indeed detergent, while favourable for the correct formation of MspA pores from monomers, has a destabilising effect on lipid bilayers.

Once a pore insertion event is seen an IV curve may be measured in order to confirm the fact that it is an MspA pore thanks to the measured conductance value. The conductance of a single pore should be ≈ 1 nS. The IV curve also allows the verification that the pore direction is correct. Indeed MspA may insert in one of two directions, only one of which is correct for DNA translocations from the cis side. It is however relatively easy to tell from the current trace which direction the pore has inserted due to

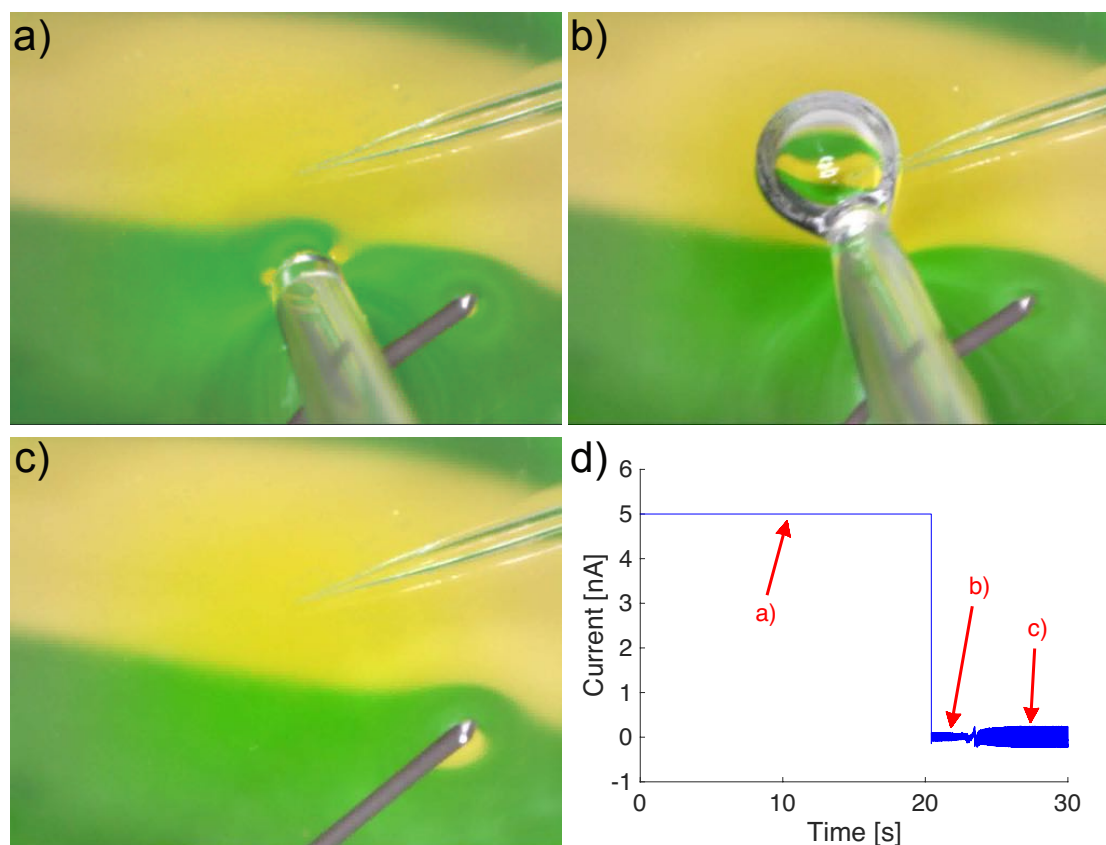


Figure 5.5 – Lipid bilayer formation over glass nanocapillaries. **a)** Optical image taken with a USB microscope of the capillary inside the flow cell prior to lipid bilayer formation. Silver chloride electrode as well as the pipette tip used to create the air bubble are also seen in the image. Prior to this step the capillary has been painted with a lipid hexadecane mixture. The same microscopy images are used as a guide to the user as the tip of the capillary is extremely prone to mechanical breakage. The green and yellow colours are tape placed beneath the microscope slide and allow better contrast of the capillary tip region for this painting step. **b)** An air bubble is formed with the pipette and brought into contact with the capillary tip. This is confirmed by a drop to zero current as seen on panel d). **c)** The air bubble and pipette are then removed as a check of bilayer formation. If the current remains at zero without the obstructing air bubble then a lipid bilayer is formed. This is additionally verified by probing the voltage characteristics of the bilayer as it should not survive a 1 V, 50 μ s zap. **d)** Current trace recorded simultaneously to the figures shown in panels a) through c). Red arrows show the state of the current in the different panels. When no lipid bilayer is present the current is only due to the microcapillary opening and is of the order of μ A, considering the range of the amplifier it is saturated at 5 nA in this case. Once the air bubble obstructs the pore on panel b) the current drops to zero. The bubble is then released and can be seen in the current trace by a fluctuation at $t \approx 23$ s. Once the air bubble is released however the current stays at zero thus proving bilayer formation. The noise in this trace is large due to the fact that the Faraday cage must be open to perform these formation steps.

MspA's gating behaviour at negative voltages ($-V$ larger than ≈ -100 mV). An IV curve is shown on figure (5.6b) along with the current trace in time, and an inset showing the gating behaviour. Little about the origin of the gating behaviour of the pore is known. It is responsible for the drop in current when high negative voltages are applied and can be rectified by switching the polarity of the voltage. Gating also occurs at positive voltages but with far less abundance than at negative ones. It has not

5.3. Combination of glass capillaries, optical tweezers, and the MspA system

been shown to be due to contaminants in solution and the exact cause is postulated to be protein conformational changes under bias.

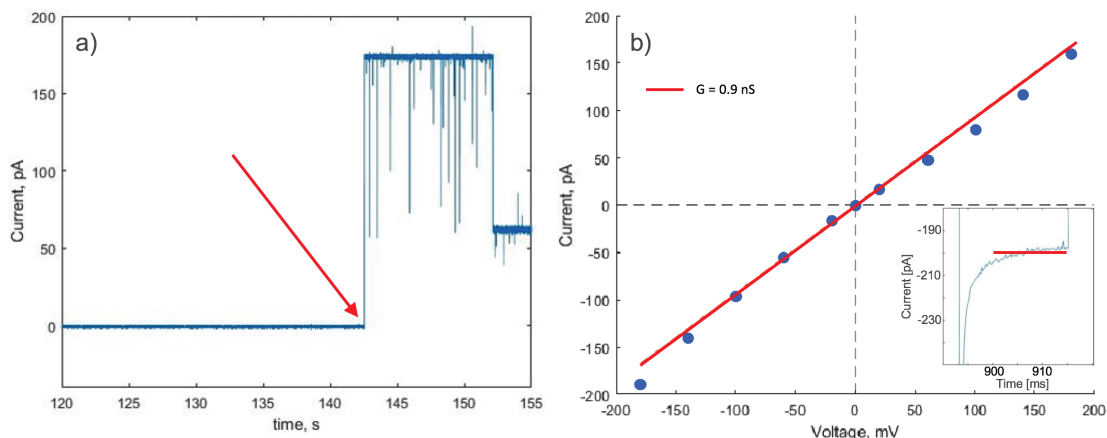


Figure 5.6 – Current voltage curve characterising MspA biological pores. **a)** Current trace showing an insertion event of a single MspA pore. Red arrow shows the insertion event at ≈ 142 ms with a bias of 180 mV. Reduction in current at ≈ 152 ms is due to a reduction in bias voltage. **b)** IV characteristic of the MspA pore shown in panel a). The extracted conductance of 0.9 nS is in good agreement with literature values for the 400 mM KCl salt solution used here[268]. Inset shows the gating behaviour at low voltages. The trace at -180 mV is stable for approximately 10 ms before gating occurs. The red line shows the current level represented in the full IV curve.

While for an optimal experiment a single pore is mandatory to correctly interpret the current trace, considering the small capture radius of MspA pores, multiple pore insertions (up to five) were used in order to increase the probability of DNA capture with optical tweezers experiments. In order to conduct such experiments, once pores in a suspended membrane are achieved, polystyrene beads with attached λ -DNA are inserted into the front-well of the microfluidic chamber. However prior to such optical tweezer experiments it was verified that double stranded λ -DNA was able to freely translocate in MspA pores.

Indeed the pore size of MspA protein pores is 1.2 nm as stated in the introduction of this chapter. Double stranded DNA being 2.4 nm in size would therefore not be able to translocate through the nanopore. λ -DNA however contains a 12 base pair single stranded overhang at each end. The assumption is that this overhang is long enough to interact with the MspA pore to initiate threading, and that subsequently the threading force would then be enough to unzip the remaining double stranded DNA. Free translocation experiments were performed and a time trace containing events is shown on figure (5.7). Current drops with correct current blockages of $\approx 80\%$ appear when λ -DNA is perfused into the front well. The time-scale of such translocations are of several ms. While this is a first test that lends credence to the fact that the force due to the MspA pore is enough to unzip the double stranded DNA by first capturing the 12 base pair overhang it is not sufficient to claim with authority that the whole length of DNA is passing through the pore. Indeed unzipping under constant force may be a very long process with plateaus or metastable states able to withstand for the force for seconds at a time[269; 270]. However in this context interaction of the DNA with the pore may in itself be enough to measure on the optical tweezers system and no in depth analysis of this translocation behaviour was made. In the future it would be important to quantify the voltage dependence of the time-scale of such events as they should vary greatly with diminished force.

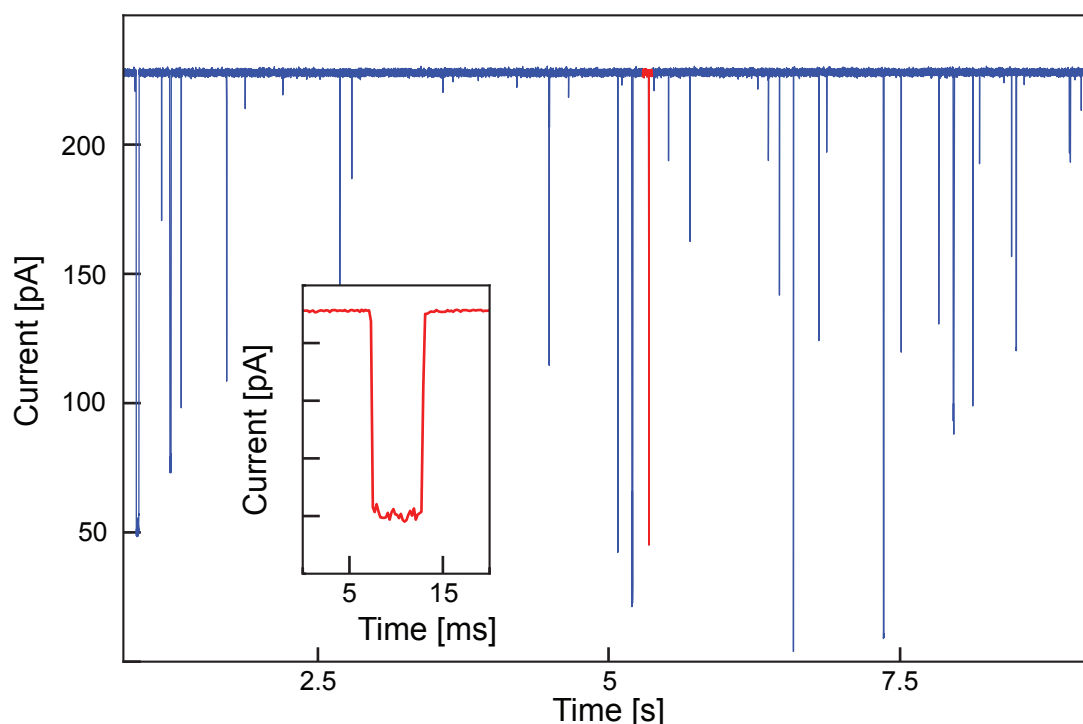


Figure 5.7 – **Free translocations of λ -DNA through MspA biological pores.** Current trace of free translocations of λ -DNA through an MspA pore. Driving voltage was 180 mV. Inset shows a zoom of one translocation event that is shown on the full graph in red. Free translocations show that the 12 base pair overhang on λ -DNA is enough to initiate translocations whereby the MspA pore unzips the rest of the double strand.

Following the proof of principle with free translocations, optical tweezers experiments were carried out with λ -DNA coated beads (figure (5.4)). These beads were brought up to the tip of a microcapillary with a suspended lipid membrane and at least one MspA pore. None of these experiments showed any force signal that would be the signature of a capture event. The lack of effect is assumed to be due to the DNA/bead being too far away from the pore/bilayer for interaction to occur.

5.3.3 Locating and optimisation of lipid bilayer position

The distance between the optically trapped bead and the bilayer has a vital role in attracting the DNA into the pore. Indeed the capture radius of MspA pores is small due to their small constriction and so the DNA coated bead should be brought close in order to initiate interactions. While the bead may be brought into close proximity to the microcapillary tip via the nanopositioning stage, it cannot be brought into contact due to the residue of lipid that irreversibly sticks the bead to the tip. However this assumes that the bilayer is formed at the very tip of the capillary, something that is not a given. To verify this, the optical tweezers setup was modified in order to allow for basic fluorescence visualisation (figure (2.5)).

This was achieved by the implementation of a LED light source that can be switched with the white light source usually used for imaging the sample. In addition a filter can be positioned in front of the camera in order to separate only the fluorescent emission. Fluorescein dye can be added to the experimental

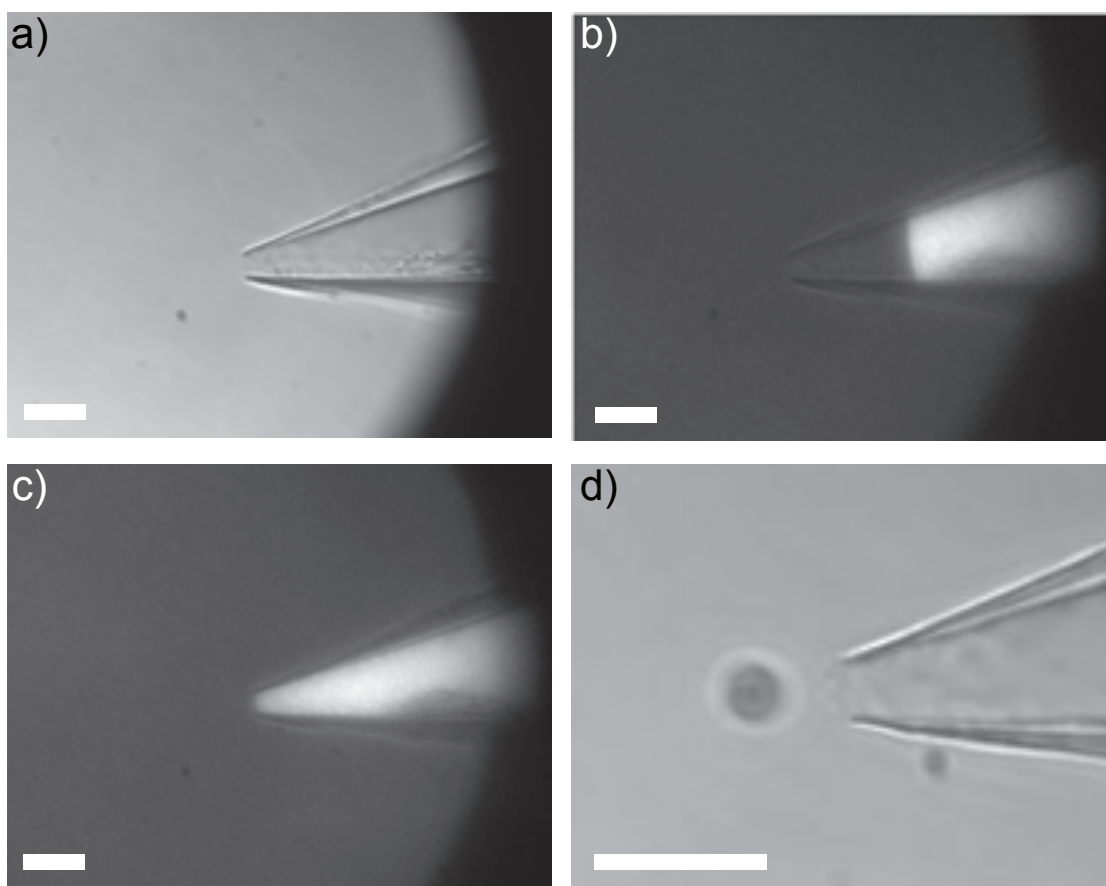


Figure 5.8 – Conformation of lipid bilayer position on glass nanocapillaries. **a)** optical image of a representative capillary in white light illumination. Scale bar represents $10\mu\text{m}$ on each panel. **b)** Fluorescence image using 490 nm LED illumination and a filter. The interface between fluorescence and background is due to the presence of the lipid bilayer spanning the capillary. It is clear from this image that the lipid bilayer is too far into the capillary to be accessible by DNA attached to a bead. **c)** Same image as in panel b) but with a larger back pressure due to raising the back-electrode tubing by ≈ 10 cm. In this image it is clear that the interface between fluorescence is at the tip of the capillary therefore allowing access with a DNA coated bead. **d)** Zoom of a white light image with the bilayer in the correct, accessible position and an optically trapped bead coated in DNA. This shows the experimental setup allowing to test DNA translocation through MspA biological pores.

buffer within the capillary to allow fluorescent images to be acquired. The absorption and emission peaks of fluorescein being 495 nm and 512 nm respectively, a green LED at a wavelength of 490 nm, and a high pass filter at 500 nm are used. In this way, once a lipid bilayer is obtained, the buffer in the front-well may be exchanged for buffer not containing fluorescein. The perfusion allows the interface between the back-well (with fluorescence) and the front-well (without fluorescence) to be clearly seen on the microscope image thus giving information about the bilayer location.

Thanks to the added fluorescence detection it was found that the bilayer in fact forms some distance inside the capillary tip (from 10-50 μm), as seen on figure (5.8b). This distance being comparable or larger than even the fully extended length of λ -DNA (16 μm), no insertion events could ever be seen in such a conformation. Moving the bilayer position would require the application of small pressures

Chapter 5. Combining protein pores with optical tweezers: SPRNT calibration

from the capillary back-side. Applying such pressures is rendered relatively easy due to the design of the back-electrode. Indeed, since the back-electrode already contains a length of teflon tubing filled with fluorescent buffer it is as easy as raising the level of this tubing a given height above the level of the microcapillary tip. The additional hydrostatic pressure ΔP will be applied to the bilayer depending on the elevation of the tube ΔH : $\Delta P = \rho g \Delta H$, where ρ is the density of water, and g the acceleration of gravity.

The additional pressure this creates is relatively small. For example at an elevation of $\Delta H = 10$ cm the additional pressure is only $\Delta P = 10$ mbar (as compared for example to the up to 7 bar that are applied to silicon nitride membranes in chapters (7) and (8)). However, these small pressures are more than sufficient to displace the lipid membrane within the capillary. This can clearly be seen on figure (5.8) where the same capillary is imaged in fluorescence with zero additional pressure and with the tubing being raised by ≈ 10 cm. The optimal position of the tubing in order to obtain a lipid bilayer exactly at the capillary tip will depend on the force applied to the membrane. The added hydrostatic force F_h will vary for each capillary depending on the opening size as: $F_h = 4\Delta P/\pi d^2$. In this way larger openings will require less elevation to move the lipid bilayer to the tip. It is also verified that the elevation of the tubing does not hinder bilayer formation/reformation allowing the tubing to be left in place once the optimal height for a given capillary is determined.

Another avenue to increase the likelihood of capture is to modify the salt concentrations. It is known from free translocation nanopore literature (both biological and solid state) that salt gradients allow improved translocation frequency i.e. a higher capture probability[46; 271]. This trick was also applied in this study by raising the buffer in the back-well from 400 mM KCl to 1 M KCl while simultaneously reducing the front well buffer from 400 mM KCl to 40 mM KCl. This also gives an added benefit to capture as by lowering the front-well solution concentration the DNA extension is slightly larger due to a small persistence length increase[272].

However, none of these optimisations led to observing capture events in the optical tweezers, even at high bias voltages of 200-300 mV (close to the rupture limit for the considered bilayers). This was, however, only based off of a low statistic of tests $N \approx 15$ due to the large number of steps from bilayer formation to a bead being brought in front of the capillary tip. These steps are: bilayer formation, insertion of MspA, front-well buffer perfusion, checking of MspA current characteristics, switching to fluorescence and optimisation of bilayer location, addition and mixing of DNA coated beads, bead capture and transfer to capillary tip. All of these manoeuvres involve some probability of breaking the bilayer. This is especially true of any task that may mechanically move the setup or where electrostatic discharge may occur between the experimenter and sample. More importantly each task takes some time. Considering the maximal lifetime of a bilayer was 40 min this leaves little time for testing DNA insertions.

5.3.4 Optimising stability of lipid bilayers on capillaries

Considering the bottleneck in optical tweezers experiments is the lifetime of lipid bilayers, a method to increase the lifetime of suspended bilayers was undertaken. A recent study of lipid bilayers on SU8 polymer membranes[273] gave an insight into solving the stability issue for optical tweezers experiments. Indeed in this study, stability up to 8h is reported as well as increased voltage stability.

Increased stability is attributed to the addition of two characteristics. Firstly the SU8 membrane is formed into a wedge cross section (figure (5.9b)) at the aperture which allows a small merging angle of

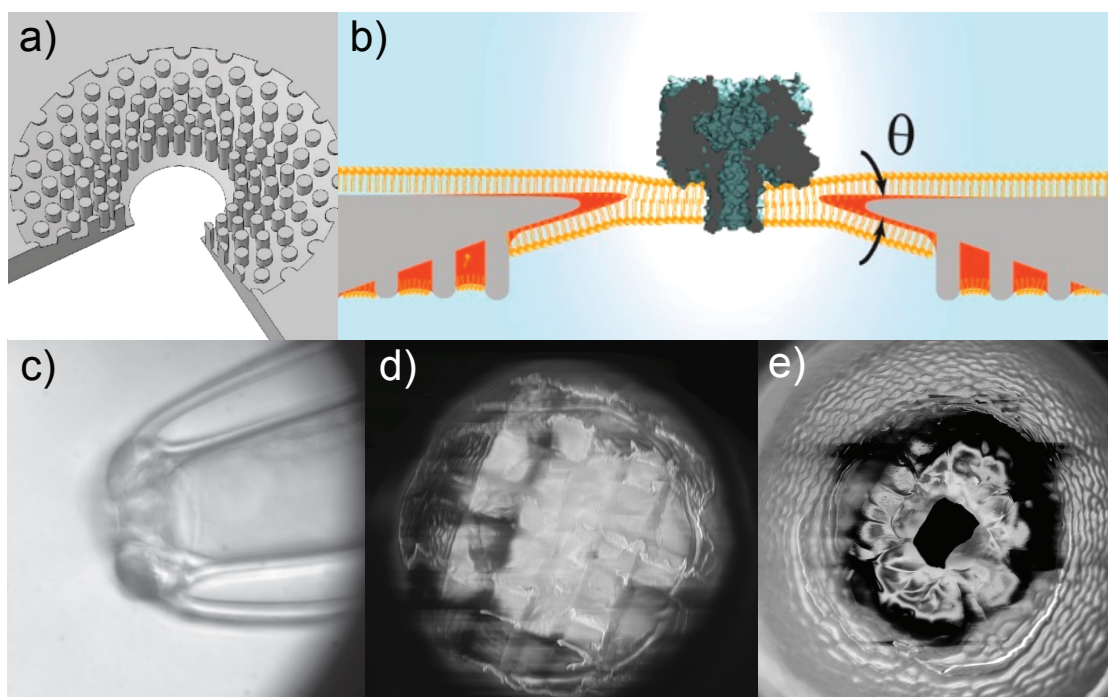


Figure 5.9 – Parylene C coating and micro-structuring on glass capillaries. a) and b) are adapted from ref. [273]. These two figures show how Kang et al. designed a photolithography micro-structured SU8 aperture. This aperture was reported to support lipid bilayers for durations up to 8h. c) Optical image of a parylene C coated, and micro-structured glass capillary in the optical tweezers setup. As compared to normal glass capillaries (f.ex on figure 5.8) the 5 μm parylene coating is shown as an extra layer on each surface. d) SEM micrograph of a micro-structured capillary. Square pillars are created in this type of design being made more evident by the clogging of this capillary. e) SEM micrograph of the second type of micro-structuring attempted with parylene C. In this case concentric circles are created to simulate the profiles seen on panels a) and b). Parylene C laser ablation courtesy of J. Pernollet.

the two lipid leaflets shown to increase stability. Secondly a concentric pillar system (figure (5.9a)) is also added which allows lipid/solvent reservoirs to form thus allowing for less solvent drainage that normally destabilises membranes over time.

While the angle of merging is difficult to control with microcapillaries used in this study, the solvent reservoirs could be beneficial to the long-term stability of membranes. A protocol to add micro-structure to the tips of capillaries is therefore developed. To do this the capillaries are first coated with 5 μm of parylene C, a polymer that is deposited in gas phase and whose most attractive property is its large scale conformal adherence to structures. Parylene has been shown to be useful in the conformal coating of objects up to macroscopic scales[274] and is easily structured through various techniques such as laser ablation[275]. To aid in the stability of coating, the microcapillaries are first coated in a silane routinely used for parylene applications: 3-(trimethoxysilyl)propyl methacrylate. The coating procedure is done in liquid phase in a 150:10:1 mixture of propan-2-ol, water, and silane.

Once a layer of parylene C is deposited it is then sculpted using UV laser ablation. Several patterns of the laser may be used creating different structures on the tip of the capillary. Figure (5.9) shows two such patterns measured with SEM after the laser ablation step. While less reproducible than the photo-lithography approach of SU8 structures that this technique is inspired by, the micro-structures

created are similar in dimension and are argued to serve the same purpose as solvent wells.

Lipid bilayer experiments were attempted with parylene C micro-structured capillaries both with and without post processing with the hydrophobic silane used in the previous section. In both cases lipid bilayers did not show increased long term stability with optimal lipid paint conditions. The maximum lifespan of a lipid bilayer measured with such capillaries was ≈ 20 min. Taking this into account it would seem that the biggest contributor to lipid bilayer lifetime is the low merging angle of lipid leaflets that is hard to reproduce with sharp capillary tips.

5.4 Conclusion

Continuing these experiments would necessitate more stable lipid bilayers in order to increase the number of DNA, MspA, OT experiments. In order to do this, preliminary experiments using giant unilamellar vesicles (GUV) have been conducted. The principle behind this is that GUV could be incubated with MspA pores in order to combine the bilayer formation step with the MspA insertion step thus reducing the time between the start of the experiment and having a DNA-coated bead in position for testing. Due to time restrictions only preliminary steps such as observing GUV in the optical tweezers setup and manipulating GUV with the OT were performed. Next steps include the insertion of MspA and the creating of a stable bilayer over the tip of the microcapillary via optical tweezer transport followed by application of suction.

Another method for stabilising bilayers over longer time-scales may be to add cross-linking agents or other additives to the lipid solution. For example the addition of cholesterol, oleanolic acid, or ursolic acid have been shown to increase the stability of lipid membranes[276; 277]. Cross linking the two lipid leaflets is also possible by modifying the lipid molecules themselves such that the hydrophobic tails of lipids form bonds that stabilise the bilayer[278]. Whatever avenue is chosen it is imperative to increase the lifetime of lipid bilayers if calibration of the electrophoretic force in MspA pores is desired.

Confinement and Nanofluidics **Part II**

6 Confinement of room-temperature ionic liquids

Results contained in this chapter can be found in the following publication: S. Marion, S. J. Davis, Z.-Q. Wu, and A. Radenovic, "Nanocapillary confinement of imidazolium based ionic liquids ", *Nanoscale*, 2020,12, 8867-8874

Author contributions: S.M. and A.R. designed the study. S.M. performed the experiments. S.J.D and Z.-Q. W. prepared the samples. S.M. and S.J.D. wrote the paper. All authors provided important suggestions for the experiments, discussed the results, and contributed to the manuscript.

A review of ionic liquid properties with a focus on the nanoscale confinement of room-temperature ionic liquids is also in preparation.

The previous chapters of the thesis focused on mechanical control of the translocation of biological molecules through nanopores in order to extract more information than available through free translocations. Pressure, temperature and viscosity are also variables that can change the dynamics of analyte translocations in nanopores[213; 279]. The following chapters will concern these methods and their effects on the nanopore system. Room-temperature ionic liquids (RTIL) have been used as a novel solvent for DNA translocations and have shown how their high viscosity can slow down translocations[65]. Due to the complexity of the nanopore system, most studies have restricted themselves to aqueous electrolyte such as solutions of KCl, NaCl, LiCl, etc. Even in this more simple context, nanopores contain a richness of available properties depending on the molarity, pH, valency of the electrolyte, geometrical or other asymmetries, pore size in comparison to physical length scales, etc. Few studies have therefore been performed with electrolytes such as room-temperature ionic liquids or other exotic liquids[280]. Although showing promise, the physical behaviour of RTIL in nanoconfinement is not well understood and requires detailed analysis before more advanced experiments can be performed. This first chapter will consider room-temperature ionic liquid behaviour in glass capillary confinement before following chapters tackle the addition of hydrostatic pressure added to nanopore experiments.

6.1 Introduction to room-temperature ionic liquids

Room-temperature ionic liquids (RTIL) are salts that, due to poorly coordinated ions, are liquid at or near room temperature. They exhibit interesting characteristics such as a large electrochemical window. Due to their sheer number, 10^{18} different types have been theoretically predicted to exist[281] and over 10'000 have been synthesised[282], it is possible to tailor the exact properties to whatever

Chapter 6. Confinement of room-temperature ionic liquids

application is necessary. This versatility explains why they have been used in such varied applications as supercapacitors[283; 284], next generation lubricants[285], solvents for chemical reactions[286], and even applications in nanopore experiments[65].

Partially due to the sheer number of possible compounds, and partially due to the complexity of their behaviour that shows a wealth of chemical and physical effects, detailed understanding of ionic liquids is still at its onset. Basic properties such as phase behaviour and density can be described by including long range Coulomb and dipole interactions[287]. However, these non-local contributions are not trivial to include in the modelling of ionic liquid behaviour[288; 289]. In bulk RTIL exhibit large changes of conductance with temperature similar to glasses[286]. This similarity is extended to effects such as long range crystalline ordering[290]. Interfaces and confinement of ionic liquids have been shown to produce additional effects. The size and shape of ions has been shown to play a role in the local structure of ionic liquids at interfaces where a competition between crowding and over-screening takes place[291].

This surface structure is also dependent on the ionic liquid concentration as mixtures in propylene carbonate show drastically different ionic organisation[292]. In addition to theoretical models, recent experimental studies were able to show, thanks to surface force apparatus (SFA) experiments, that the standard Debye-Hückel model usually applied to dilute aqueous electrolytes does not predict RTIL or concentrated electrolyte behaviour[293]. The exact nature of charge carriers in ionic liquid systems is also under debate. It is possible that in certain configurations the charge carriers are neutral solvent molecules or impurities similarly to conduction of "holes" in semiconductors[294]. This effect could also be at play in the atypical increase in diffusion coefficient for small neutral molecules[295]. All of these effects point to an intimate link in these liquids between structural process' and dynamical properties.

This link between structure and properties is of heightened interest when dealing with confinement and ionic liquids on the nanoscale. Porous media have been widely used to study such effects. Confinement has been shown to affect local density[298; 299], has shown evidence of a superionic state[300], and even changes in measured glass temperature[296]. All these effects are postulated to be due to an interaction between steric limitations, configurational constraints, and the long-range dipole effects discussed previously. Confinement or surface mediated long-range structural ordering has also been reported in many experimental configurations. Some of these include optical measurements on surfaces[301; 302; 303] and small angle x-ray scattering on colloidal suspensions[304]. Experiments using tuning forks to probe ordering at surfaces, similarly to what AFM measurements are capable of, have shown structural ordering on very large length scales from 10-150 nm[297]. The size of the effect is seen to depend highly on the surface material properties with metallic surfaces inducing the most long range interaction.

This stabilisation is due to the build up of image charges in the perfectly metallic surface which reduces the electrostatic contribution to the free energy by acting as a single bulk lattice thus favoring a crystal phase at metallic interfaces as compared to insulating ones. This is compared to a freezing transition in confinement. However, surface force apparatus experiments have only detected structure on the scale of several molecular layers and argue that pre-wetting surface layers are responsible[305]. Nevertheless, these SFA studies also see a larger effect in metallic surfaces[306].

Clearly the rich array of interesting phenomena along with the abundance of different families of ionic liquids means that the detailed picture of underlying physical phenomena is still unclear. While previously mentioned studies dealt with interfaces, surfaces, or porous media, few studies have been

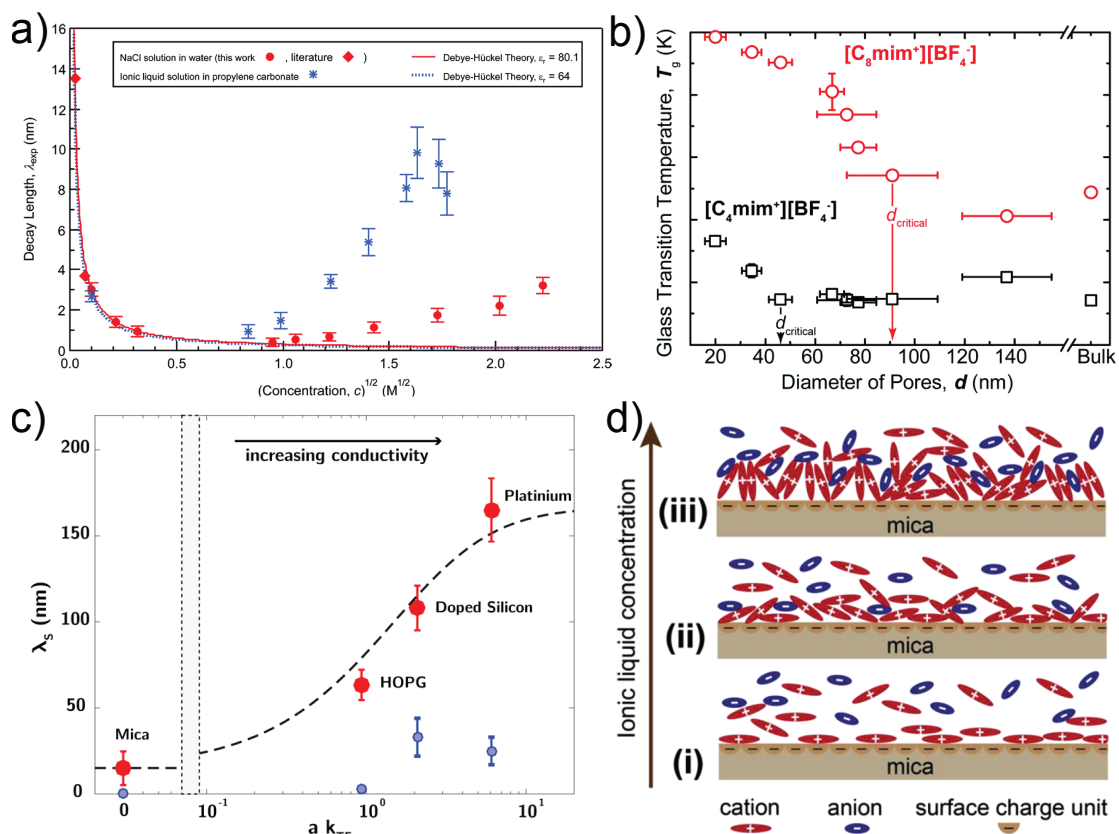


Figure 6.1 – Ionic liquid structural properties at surfaces and in confinement. **a)** Data from literature on the screening length as a function of concentration for aqueous solutions (red) and ionic liquids (blue). Both types of liquids show an anomalous increase in screening length at high concentrations. This is seen as a divergence from the standard Debye-Hückel behaviour (lines). Image is adapted from ref. [293]. **b)** Change in glass temperature of ionic liquids in confinement. Measurements are done in alumina porous membranes with modulated differential scanning calorimetry. The confinement induced increase of glass temperature is seen to depend on the cation size with longer cation chains inducing a transition at larger pore sizes as compared to small chain length cations. Image is adapted from ref. [296]. **c)** Tuning fork AFM-like experiments in pure RTIL. Figure shows the measured solidification length λ_s as a function of the normalised Thomas-Fermi wavevector. This shows that with increased metallicity (i.e. growing $a k_{TF}$) the solidification length increases. Image is adapted from ref. [297]. **d)** SFA measurements of ionic liquid structure at surfaces show different ordering depending on concentration of RTIL. Here propylene carbonate mixtures with ionic liquids are probed in a wide concentration range showing drastically different ordering at the surface depending on the concentration of ionic liquid. Schematics representing the different organisation of ions at the surface. Image is adapted from ref. [292].

able to probe single pore confinement effects on RTIL behaviour. This is an important step as while porous membranes such as alumina can now be made with relatively low dispersion of pore sizes, the effects measured will always be averaged over the population of pores. This leads to a lack of precision on phenomena that have been shown to depend highly on exact physical size. One study has probed confinement of ionic liquids in single pores and found a large increase in pore resistance below a threshold pore size of ≈ 50 nm [307]. However, no further interpretation or explanation of the nature of the drop in conductance was given in this case.

The following sections therefore attempt to allay the lack of single pore confinement of RTIL by measuring the conductance behaviour of RTIL in single glass nanocapillaries. The size range of the opening is varied in the large range of 20-800 nm, and temperature dependent measurements are made. This allows a thorough study of the parameter space in order to present any structural changes of RTIL in confinement.

6.2 Measuring room-temperature ionic liquids in confinement

In this section the experimental setup is explained and the choices of electrodes, pore material, and RTIL for best measurements of high resistance samples are motivated. Precise measurements of RTIL conductance without contaminating the sample motivated the choice of platinum electrodes (90% Pt, 10% Ir) as opposed to the standard AgCl electrodes used throughout this thesis. Platinum is chosen so as to have no chemical reactions between electrodes and electrolyte thus limiting any possible contamination due to electrochemical reactions at the electrodes (non-faradaic processes only). However, the fact that no faradaic processes are present prevent the use of DC measurements due to the low currents being able to be driven through the electrodes. An AC measurement method is therefore chosen, as in chapter (4), where the platinum electrodes drive a sinusoidal bias voltage and the resulting current is measured by a lock-in amplifier.

The choice of glass nanocapillaries is motivated by the fact that their capacitance is extremely low ≈ 1 pF which allows the precise measurement of even highly resistive samples such as ionic liquids. This is important because due to the high viscosity of ionic liquids (≈ 30 -100 times more than water), their resistance especially at low temperatures can be as high as several tens of G Ω . In comparison standard silicon nitride membrane pores have a capacitance on the order of ≈ 1 nF which highly restricts the working frequency of the AC conductivity measurements. The choice of ionic liquid is motivated by previous studies discussed above, especially the seminal work by Comtet et al.[297]. Therefore a trio of imidazolium based RTIL are chosen: emim BF₄, bmim BF₄, and bmim PF₆. This choice also changes the cation and anion once which allows comparisons between effects of the ion type to be observed. These ionic liquids also present high enough conductivity to be measurable even at low temperatures of -20°C and their viscosity, while high, does not impede the filling of small nanopores.

Nanocapillaries between 20-800 nm are pulled using the same technique as described in chapter (2). They are then imaged in a scanning electron microscope to ensure a symmetric opening and to measure their exact dimensions (figure (6.2b)). Oxygen plasma for ≈ 5 minutes is then used to render filling easier and remove contaminants from the surface. Immediately after plasma cleaning nanocapillaries are inserted into a drop of ionic liquid and placed in a dessicator to pre-fill the capillary. After half an hour most of the capillary is filled with ionic liquid and an air bubble only remains in the tip (similar to figure (2.3)). The back-end of the capillary is then fixed, via microfluidic connectors, to a syringe filled with ionic liquid that can be placed in a syringe pump. The tip of the capillary is submerged in ionic liquid heated to 80°C while pressure is applied to the back of the capillary via the syringe pump. Heating is an important step since the assumption is made that if an ionic liquid will freeze at room temperature in a given size of capillary, then it will also not fill it correctly. The nanocapillary is then left overnight in this configuration in order to remove the air from the tip of the capillary.

After this filling procedure the tip is imaged with a standard white light microscope in order to verify that no visible bubble, or other contaminant, is present. It is then mounted in a PDMS fluidic cell and bonded to a glass microscope slide as in chapter (2). The glass slide is then mounted on a Peltier element to allow for temperature control of the sample. A platinum resistor is also glued to the top of

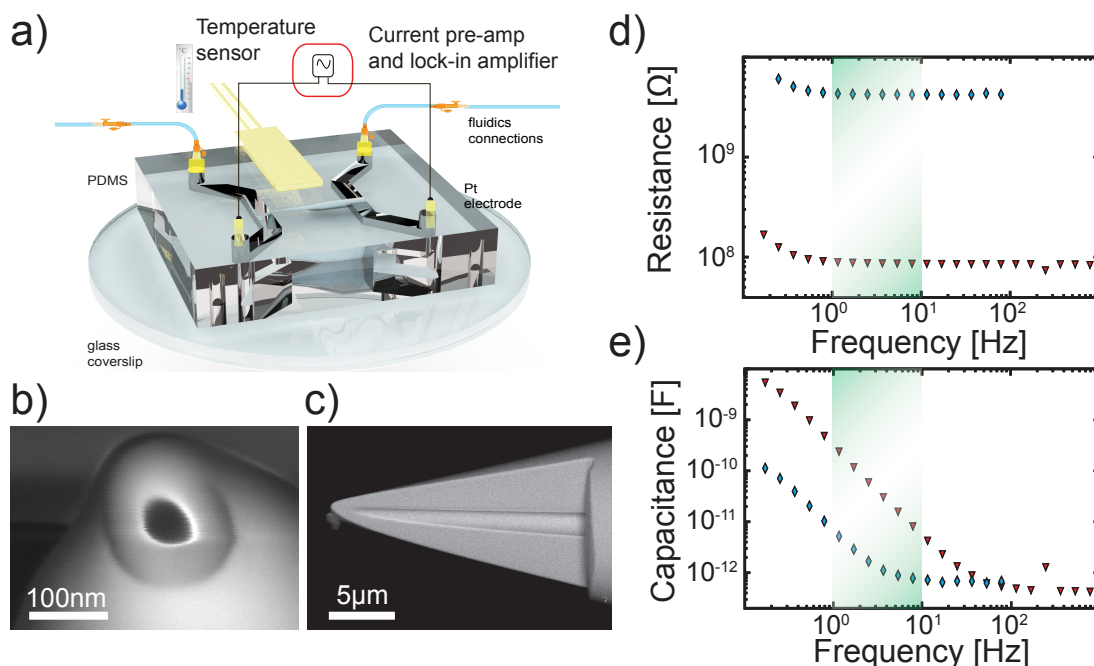


Figure 6.2 – Probing nanoconfinement of room-temperature ionic liquids. **a)** Schematic of the experimental setup with a nanocapillary in a PDMS microfluidic chamber. Platinum electrodes and AC measurement via lock-in amplifier are shown. A Peltier element is placed beneath the glass slide to regulate the temperature which is measured by the temperature probe. **b)** and **c)** SEM micrographs of typical capillaries. Panel **b)** shows the top view that allows the measurement of the pore size (50 nm in this case). Panel **c)** shows a cross section obtained via focused ion beam (FIB) milling of the capillary prior to SEM imaging. This confirms the inner tapering of the capillaries. **d)** Measured AC resistance as a function of frequency for the same RTIL filled capillary at two different temperatures (70°C in red and -20°C in blue). This capillary is a 50 nm pore filled with emim BF₄. The shaded area shows the plateau region that is used for the extraction of the resistance as a function of temperature. **e)** Capacitance measured simultaneously to the resistance in panel **d)**. Blue and red curves correspond to the same temperatures as on panel **d)**. Here capacitance is seen to converge to the known value of capillary capacitance ≈ 1 pF for intermediate frequency values regardless of temperature. Shaded region is the same as on panel **d)**. Figure is adapted from ref. [67]

the chamber above the capillary tip. By monitoring the resistance changes of the platinum resistor, accurate measurements of the temperature are possible (schematic on figure (6.2a)). This whole temperature control system was enclosed in a box in which a small overpressure of pure nitrogen gas is continuously maintained so as to avoid any additional contamination of the sample.

The resistance and capacitance of the capillary are simultaneously measured as described in chapter (4) and frequency sweeps of a typical nanocapillary behaviour is shown on figure (6.2d and e) for two different temperatures. The frequency response of RTIL filled capillaries is similar to what can be measured in aqueous solvent. Namely at high frequencies $f > 100$ -1000 Hz capacitive leakage occurs, in intermediate frequency range where $1 \text{ Hz} < f < 100 \text{ Hz}$ a plateau region is observed where the measured AC resistance is equivalent to the DC resistance of the sample, at lower frequencies $f < 1 \text{ Hz}$ electrode polarisation effects are present. Electrode polarisation occurs when the exciting frequency is too low and polarisation of the electrolyte on the electrode happens quicker than the switch in polarity of the AC bias voltage. Considering the lack of faradaic current this polarisation effect lowers the total

measured current inducing a higher measured resistance. Figure (6.2d) shows how increasing the resistance of the sample (for example at low temperatures) decreases the contribution of the electrode polarisation. A temperature sweep of the sample in 2°C increments is then performed while recording the resistance and capacitance at a chosen frequency in the plateau region.

6.3 Temperature dependent measurements of room-temperature ionic liquids

Temperature sweeps of the samples are carried out as described by the arrows on figure (6.3). Namely the temperature is first increased to 70°C before being brought down to the minimum attainable stable temperature, between –10 and –20°C. Following this the temperature is again raised to room temperature. This allows a measurement of hysteresis in the sample that could point to ageing, contamination with time, or more importantly be a signature of a freezing and thawing transition at low temperatures. No such hysteresis is found in samples, even when experiments are conducted over the timespan of several days.

Assuming a freezing transition takes place, it is hypothesised to result in a dramatic change in the conductivity of the sample. This is due to the structural change in the frozen layers of RTIL affecting their transport properties[308]. Another possibility is that the nanocapillary would behave as if the diameter of the pore was reduced by the size of the frozen layer of RTIL. The transition temperature of these effects is expected to follow a Gibbs-Thompson relation[297; 309] as shown below:

$$\Delta T \propto T_B \frac{\Delta\gamma}{\rho L_h D}, \quad (6.1)$$

where ΔT is the change in transition temperature from the bulk value T_B , $\Delta\gamma$ is the difference in surface energies between a liquid and solid phase in respect to the surface-ionic liquid interface, ρ is the density of ionic liquid in liquid phase, L_h the latent heat of melting, and D the size of confinement. This change can be estimated by using literature values for the given parameters. For bmim BF4 this yields a detectable change within the temperature range studied for confinement values of ≈ 25 nm[297]. This varies within the chosen ionic liquids but should be a larger effect in emim BF4 due to its larger native glass temperature (see figure (6.4a) for details).

Figure (6.3) shows the large dependence of sample resistance on temperature. This is due to a slowing of the charge carrier dynamics in ionic liquids and can be approximated by a Walden rule relating conductance to viscosity as $\sigma \propto \eta^\alpha$. In this case for the studied ionic liquids $\alpha \approx 0.9$ [312]. In this way the large increase in resistance seen in the temperature sweeps is directly related to an increase in viscosity at the tip of the nanocapillary.

The capacitance behaviour with temperature is also shown on figure (6.3). In this case despite the high resistance of the sample electrode polarisation effects do have some bearing on the measured capacitance at high temperature at the chosen frequency. However, at low temperature the capacitance stabilises due to the resistance increase and the expected value for glass nanocapillaries (< 1 pF) is retrieved. These values correlate well with the values measured in aqueous salt solutions.

Considering the RTIL as a glass-like system their temperature behaviour may be fitted to the Vogel-

6.3. Temperature dependent measurements of room-temperature ionic liquids

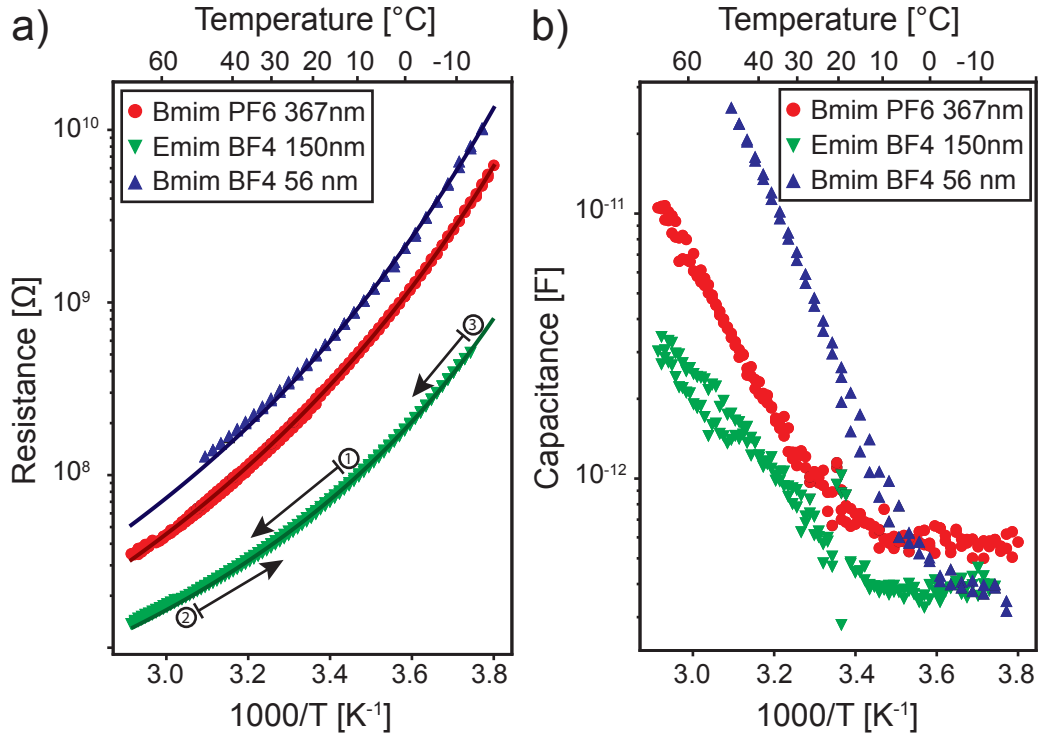


Figure 6.3 – **Room-temperature ionic liquids behave as glassy liquids with temperature.** Temperature dependence of the resistance **a)** and capacitance **b)** for all three types of ionic liquids. The resistance behaviour is fitted to the VFT formula (equation (6.2)) and shown as solid lines. The pore size corresponding to each ionic liquid type is 50 nm, 150 nm, and 367 nm for bmim BF4, emim BF4, and bmim PF6 respectively. Fits are made with a fixed $B = -800$ ($B = -600$) for bmim BF4/PF6 (emim BF4) taken from literature[310; 311] and show that regardless of pore size or ionic liquid type the curves follow the expected behaviour over the whole temperature range. Arrows on panel a) show the direction of the temperature sweep that allows the measurement of any hysteresis present. The capacitance is again shown to converge to the expected values of ≈ 1 pF. Figure is adapted from ref. [67]

Fulcher-Tammann (VFT) model[313] that was developed for these situations.

$$R(T) = R_0 e^{-B/(T-T_0)}, \quad (6.2)$$

Where R_0 is an effective resistance, B a parameter related to energy barriers in charge transport, and T_0 the effective glass transition temperature. Fits to this equation for large opening sizes yields values for B and T_0 that are consistent with literature indicating that the ionic liquids behave as expected in such pores[310; 311]. Values for the effective resistance and glass transition temperature can then be extracted (in this case B was kept fixed at literature values of -800 and -600 for bmim BF4/PF6 and emim BF4 respectively[310; 311]) as a function of the diameter of the nanocapillary. This probes for any freezing effects caused by confinement induced structural arrangement. Figure (6.4b and c) show the data for the effective resistance and the effective glass temperature as a function of the confining diameter.

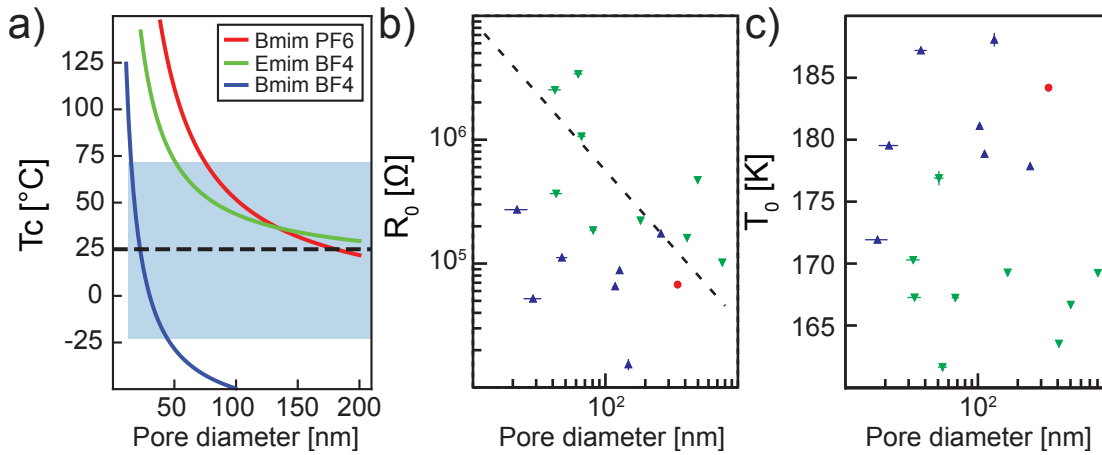


Figure 6.4 – **Size dependence of room-temperature ionic liquid glass temperature.** **a)** Predicted change in confinement induced freezing temperature for ionic liquids. Computed from equation (6.1) with literature values for T_B , $\Delta\gamma$, ρ , and L_h . This predicts that a freezing transition should be observable for all three investigated ionic liquids within the measured size and temperature range. Shaded area shows the available experimental temperature and confinement range. **b)** Effective resistance R_0 extracted from VFT fits as a function of the nanocapillary diameter. Dashed line shows the expected behaviour for nanocapillaries following equation (1.1). While a trend of increasing effective resistance with smaller diameters is present the spread is large. **c)** Glass transition temperature extracted from VFT fits of ionic liquid temperature sweeps. The behaviour with pore diameter shows no clear trend or discontinuities that would be expected if freezing was occurring. Image a) and b) are adapted from ref. [67]

Results for the effective resistance R_0 show no behaviour expected from effects of freezing. A trend is seen for increasing R_0 as diameter drops that should match the expected resistance behaviour for capillaries as described in equation (1.1). While this trend is observed in the data the spread of values is large and no detailed analysis of the behaviour may be performed. Similarly the effective transition temperature T_0 shows no changes in behaviour for small values of the pore diameter within experimental error. These facts along with the lack of large variations of resistance with temperature for small pores can be interpreted as a lack of freezing transition. Larger statistics in order to extract a dependence were also hard to achieve due to the relatively low filling percentage for capillaries. This percentage was estimated to be $\approx 30\%$ and was mostly due to the high viscosity of ionic liquids rendering the filling process for small pores challenging.

However, many factors may be at play to hinder the measurement of such an effect even if present. One of these factors is surface material. Indeed, previous studies have shown structural effects on surfaces to depend highly on the surface type with metal surfaces providing the highest effect[297]. In order to recreate this surface mediated enhancement in the nanocapillary system platinum was deposited via atomic layer deposition (ALD) on the capillary surfaces. It was verified that the platinum layers had coated the inside walls of the nanocapillaries by focused ion beam slicing followed by energy-dispersive X-ray spectroscopy (EDX). Unfortunately when resistances through the ionic liquid become too high the conductive layer of platinum acts as a short circuit and such characterisations as made above are impossible. The following section therefore summarises the issues with the present results and how to correct them in future studies, leading in to the following chapters focussed on pressure applied to solid-state nanopores.

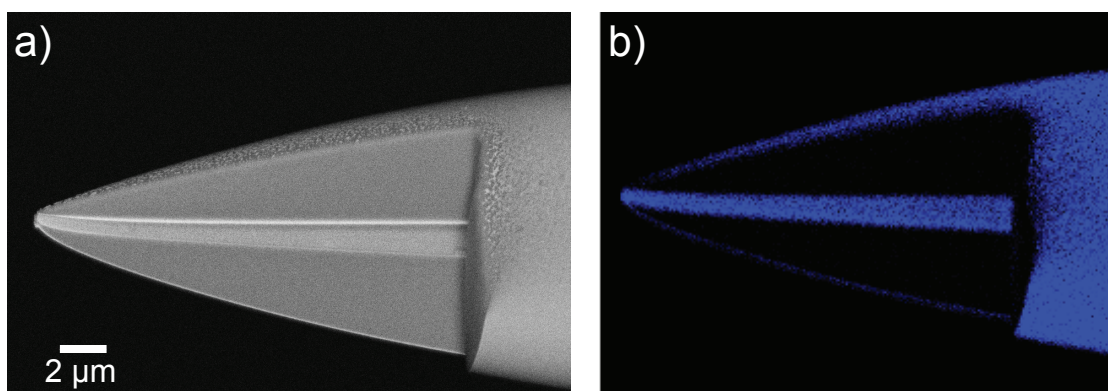


Figure 6.5 – **Platinum coated nanocapillaries.** **a)** SEM micrograph of a FIB milled capillary previously coated with platinum through ALD. Exterior surface shows some grain boundaries from the platinum growth. **b)** EDX analysis of panel a) showing the platinum spectra confirming that the ALD coating penetrated inside the pore. Scale is the same as in panel a). FIB milling courtesy of L. Navratilova.

6.4 Conclusion

While the results in this chapter do not conclusively show any effect of spatial confinement on the glassy behaviour of ionic liquids this is attributed to three main factors that affect the measurements. Firstly the inherent spread of nanocapillary resistance as a function of diameter is shown to be large, especially for small nanocapillaries ($d < 100$ nm as shown on figure (4.10)). This spread would mask finer effects due to structural changes in ionic liquids. This is the same sort of geometrical irreproducibility that hampered previous chapters and motivates the use of a more reproducible geometry in the following sections.

Secondly the resistance of nanopores is shown to vary largely if contamination such as gas bubbles are present in the pore vicinity. This is discussed extensively in the following chapter pertaining to silicon nitride membrane pores but is likely to be just as important for the glass capillaries used here. These wetting effects could be partly responsible for the large spread of resistance in small nanocapillaries, or could be a compounding factor. Bubbles could affect the conductance of nanocapillaries either through their direct effect on the resistance or by locally modifying surface charge. Taking into account the high viscosity of the RTIL used it is however very probable that filling and wetting issues are present for certain samples. Without the capacity to discern such issues the effect cannot be taken into account or remedied. The addition of control parameters such as the application of hydrostatic pressure are therefore useful tools for these situations.

Finally the question of the sample purity can also be a factor. Indeed, all of the RTIL used are hygroscopic and as such will absorb water from the surrounding air. This was reduced as much as possible by performing steps, especially long term storage of RTIL, in a nitrogen glove-box. However, due to the nature of capillary filling and mounting that requires many delicate hands on actions it was not possible to perform the whole experiment in such a dry environment. While no hysteresis is shown to be present during the temperature sweeps of the ionic liquids this does not necessarily mean that no contamination is present. Indeed, the RTIL could already be saturated with water at the point of starting the measurement. Any trace amount of water can change the conductivity significantly[314; 315] and is likely to change the ordering effects on the surface by disrupting the pure ionic liquid crystal-like structure[316; 317; 318] and is therefore to be avoided.

Chapter 6. Confinement of room-temperature ionic liquids

These results therefore while not giving rise to the desired result pave the way for future experiments with RTIL under more controlled conditions. The crucial additions being a more reproducible geometry giving rise to more controlled resistance values especially for small pores, a means of testing and modifying the wetting state of the pore, and an experimental setup allowing no ambient air to interact with the sample from mounting, filling, to ultimate measurement. The next chapters will elaborate on these solutions.

7 Pressure effects on wetting of nanopores

Results contained in this chapter can be found in the following publication S. Marion, M. Macha, S. J. Davis, A. Chernev, and A. Radenovic, "Wetting of nanopores probed with pressure", arXiv:1911.05229v2, 2019

Author contributions: S.M. designed and built the experimental set-up and designed the study. M.M. designed the microfluidic chamber. S.M. and M.M. performed the experiments. A.C. fabricated the devices, transferred and prepared MoS₂ devices. M.M. grew the MoS₂. A.R. initiated and supervised the research. S.M. analysed the data, made the FEM model and wrote the manuscript. All authors provided important suggestions for the experiments, discussed the results, and contributed to the manuscript.

Issues from the previous chapter (6) point to enhancements needed in order to more precisely probe RTIL filled pores. These additions are studied here. First an air tight sample chamber and pressure application system is shown to discern and solve wetting issues with aqueous solvent. Following this the setup is used to extract previously unknown information about pressure induced elasticity and rectification in silicon nitride pores. And finally the setup is used with ionic liquids in order to solve the previously encountered issues and show measurements of streaming currents with such exotic liquids.

7.1 Introduction to wetting of nanopores

Nanopores have been used extensively to study nanofluidic phenomena. Indeed, as presented in the introduction and throughout this thesis nanopores are shown to exhibit behaviour where many fine size effects may be of importance[24; 40; 319]. Sub nanometer channels, especially in quasi 2D membrane pores such as MoS₂, h-BN, and graphene have also been used to probe non-linear ionic transport phenomena[320; 321; 322]. All these applications using small pores, especially those dealing with non-linear effects, require a good assurance of pore filling. Indeed, as the radius of pores decreases they become more and more prone to wetting or filling artifacts that may masquerade as physical effects. This is not a new phenomena and has been reported in nanopore research from its inception[323]. Many studies have claimed that wetting artifacts and in particular bubbles in the micron or nanometer range plague nanopores. Most of these studies center around ionic current noise level as an indicator of the pore wetting state. The increase in noise is attributed to an improperly wet state[324; 325; 326].

This has been supplemented by studies that use in situ heating to nucleate gas bubbles at the pore

Chapter 7. Pressure effects on wetting of nanopores

directly, thus confirming the noise effects. This heating can come in the form of a laser[323], by large electric fields and joule heating at the pore[327; 328], or plasmonic pores[329].

Most of these studies revolve around small gas bubbles. Research into the existence, nucleation, and stability of such nanobubbles has been a much explored and debated topic for nearly 20 years[330; 331]. Indeed, the physical explanation for the stability of such small bubbles despite naïve explanations ruling out their possibility raised great controversy until recently[332]. Their characteristics, of which their lifetime is a key one, have been shown to depend highly on their substrate. However, they have been shown to be exceedingly stable on even mildly hydrophobic surfaces such as Mica, highly oriented pyrolytic graphite (HOPG), or hydrophobically coated silicon, with proof of lifetimes up to months[333; 334]. A naïve definition of hydrophobic is that the static contact angle of a solvent with a surface be above 90 degrees[335]. However, nanobubbles have demonstrated stability on surfaces with contact angles as little as 70 degrees. While defining hydrophobicity on the basis of receding contact angle may clarify this grey zone the key issue is their ubiquitous presence in micro- and nanofluidics.

The method of formation of such bubbles requires two ingredients, a nucleation site or catalyst, and a source of gas. The source of gas can come from the ambient atmosphere, mixing, trapped air due to geometrical effects, and oversaturated or not adequately degassed solutions while the catalyst may be heating as previously described, changes in pressure, or solvent exchange[330]. It is good to dwell on the method of solvent exchange for nanobubble formation to understand how this may be problematic for nanopore experiments. In the course of a solvent exchange protocol a liquid with a higher gas capacity, such as alcohol, is exchanged for one with a low gas capacity, such as water. During this process gas molecules directed by diffusion due to a gradient of gas solubilities create local gas saturations near the substrate which enables the formation of pinned nanobubbles upon exchange[338].

Detection of nanobubbles has been achieved using transmission electron microscopy on graphene surfaces[339]. Importantly for the results presented hereafter atomic force microscopy studies (figure (7.1c)) have been possible in combination with a graphene nanopore thus being able to confirm in situ that nanobubbles obstructing pores is a phenomena that can affect ionic conductance[337]. Indeed, this study showed current voltage characteristics that were interpreted to be due to hydration layer shredding of ions having to pass the gas bubble boundary that was obscuring the pore. Quasi-2D materials such as graphene[340; 341], MoS₂[342; 343], and h-BN[344] will be more susceptible to nanobubble formation due to their inherent hydrophobic nature, and the impossibility of using standard techniques such as oxygen plasma to render the surface hydrophilic for fear of damaging the material. However, this does not preclude wetting artifacts being present in the standard silicon nitride nanopore as will be shown extensively in the next sections.

As described above distinguishing between wetting artifacts and filled pores based solely on the ionic transport characteristics of the pore is a risky business. It is possible but should be coupled with robust modelling as well as imaging of the pore before and, if possible, after use to take into account any size variation (this is especially true of quasi 2D pores that can be unstable under relatively low applied voltages ≈ 400 mV). Claims of non-linear transport require the highest level of proof to rule out wetting artifacts as these have been shown to be present in cases of bubbles[337]. In order to obtain more control over the pore and any contaminant or bubble present in its vicinity, as well as many more measurements and features (chapter (8)), hydrostatic pressure application is added to the standard nanopore setup.

This is not a novel approach in the nanopore field, but the addition of hydrostatic pressure application has mostly been reserved to characterizing surface charge[345; 346] or influencing protein, DNA, or

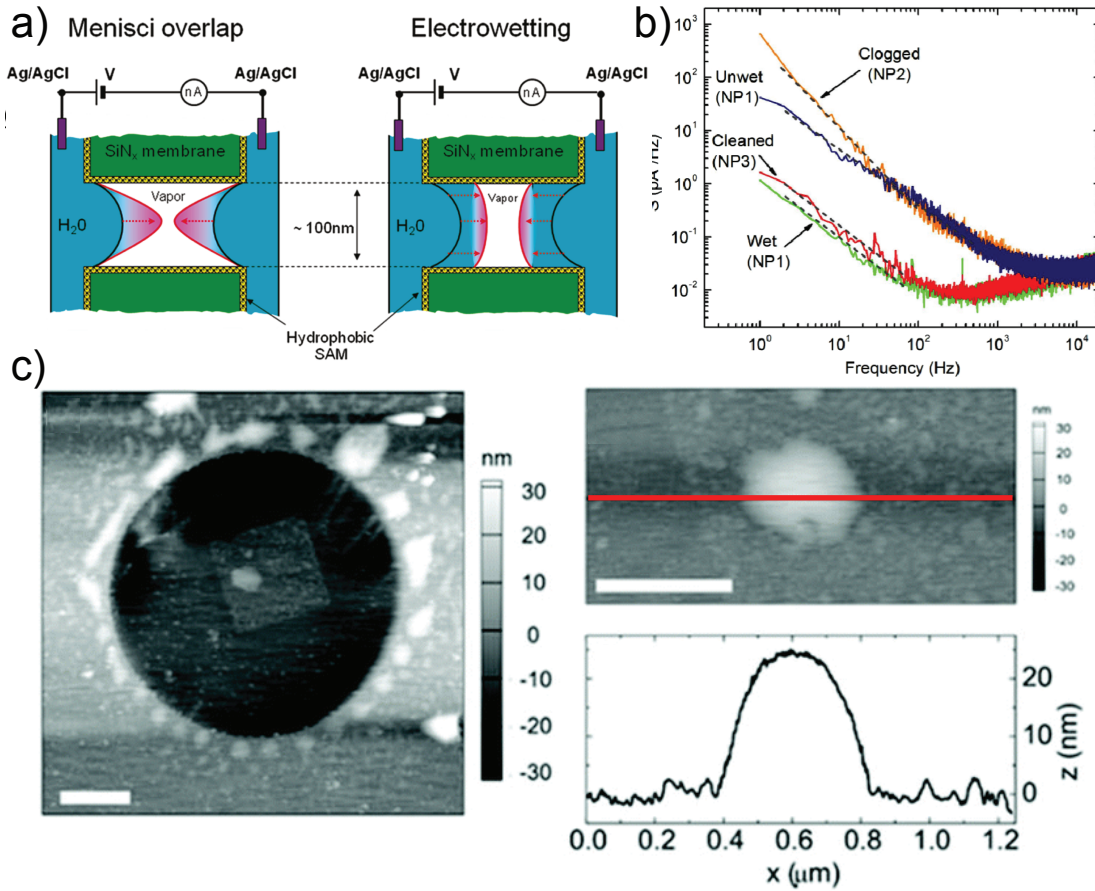


Figure 7.1 – Wetting of nanopores. **a)** Schematic of the two hypothesised mechanisms of electro-wetting hydrophobic pores. The first being the menisci of the air-water interface being driven towards each other by the electric field. The second being the creep of the pinning site up the hydrophobic wall. In reality a coupled effect could be taking place and similar mechanisms are postulated for pressure wetting. Image is adapted from ref. [336]. **b)** Power spectrum densities of pores in different wetting states. This image shows that clogged, dirty, or unwet pores show a higher noise level, especially in the $1/f$ part of the spectrum. The fully wet pore always shows the minimum in noise level. Image is adapted from ref. [326]. **c)** Experimental demonstration of nanobubbles pinned in the pore region with liquid AFM. Left shows a large area AFM image showing bubbles pinned at the contour of the graphene and in the pore region. This could be due to modification of the surface due to the drilling technique. Right shows a zoom and line profile (corresponding to the red line) of the bubble over the pore. The scale bar is $1\mu\text{m}$ in the large view and 500nm in the zoomed view. Image is adapted from ref. [337].

polymer translocations[347; 348; 349]. One group has studied the combined effect of pressure and voltage gated wetting in hydrophobic porous materials but it has not yet been demonstrated in single pores[350]. In contrast voltage gating is known to control the wetting state of single hydrophobic pores[336; 351].

The importance of pressure and flow as a control parameter is clear. Indeed, just like with the conductance measurement, the hydrostatic access resistance is the dominant effect in small pores[215; 352] and thus the convergence of flow lines around the lip of the pore is able to drag, push, or modify any

contaminant that may rest there[353; 354]. This is also true for the electrophoretic driving of particles to and through the pore although the force in this case will depend highly on the charge of the particle whereas in the pressure driven state Stokes drag is the main driver. This yields a pressure driven force mainly dependent on size of the particle. The addition of pressure therefore permits the user to claim with much more authority the exact wetted state of the pore. The following sections will describe in detail the additions made to allow these measurements as well as a review of certain wetting artifacts on silicon nitride nanopores.

7.2 Hydrostatic pressure system

In order to apply hydrostatic pressure to the nanopore system a sealed chamber is required. A water tight seal along with drastically reduced gas permeation so as to avoid regassing the pre-degassed solutions are the most important characteristics of the chamber. These characteristics offer the added benefit of avoiding evaporation which allows experiments to take place over the time-scale of days without any change in salt concentration. In order to achieve the required water tightness up to 10 bar, as well as chemical resistance allowing use with more reactive solvents, a chip holder compatible with standard microfluidics connections is machined out of PEEK (figure (7.2a)). Special attention was paid during the design of the chamber so as to avoid, as much as possible, any geometry that would be conducive to bubble nucleation or pinning (i.e. corners, crevices, dimples, roughness, etc)[355].

The mechanism of clamping the silicon chip is by two nitrile o-rings while the two halves of the chamber are tightened by screws. Each side of the chamber contains one inlet channel, and one outlet channel which bifurcates into two separate exits. One of these is the normal outlet channel while the other is a dead channel for the electrode. Inlet and outlet PTFE tubes are attached to the chamber by using standard microfluidic fittings consisting of a screw and a ferrule that secures the tube to the threaded adapter in the chamber. The outlet tube is then attached to a shut-off valve allowing the complete sealing of the chamber (figure (7.2b) shows the channel geometry). Filling and exchanging of solutions is made easy through this shut-off valve as it can easily be interfaced to a degassing hose or a luer lock syringe. The degassing hose allows to flow freshly degassed liquid straight into the chamber without any contact with ambient air, or mixing due to transfer to a syringe/pipette. When first filling or exchanging the solution in the chamber a minimum of 5 mL is used (internal volume of the chamber $\approx 500 \mu\text{L}$) to ensure that sufficient freshly degassed liquid has been passed through. This method ensures the easiest filling of the nanopore with the least wetting artifacts.

The inlet on each side of the chamber is connected to a fluid reservoir which is linked to the microfluidics pressure controller. This microfluidics pressure controller is then used to apply pressure to the reservoir and through the tubing to the chip. The range of pressure that can be applied is $P = 0\text{--}7$ bar with the resolution being 2-4 mbar. A simple hand valve up stream from the fluid reservoirs allows the application of pressure to one, the other, or both reservoirs. In all the following chapters a positive value of pressure is defined as a pressure being applied from the front side of the chip, a negative pressure from the back side of the chip (both these situations are referred to as a gradient pressure condition), and a compression P_c is defined as a given value of pressure being applied from both sides simultaneously. In order to attach AgCl electrodes without inducing leakages, 250 μm thick silver wire is used to prepare the electrodes, these are then inserted into PTFE adapter sleeves allowing the diameter of the electrode to be equal to standard tubing and thus sealed in the same way.

Once the chamber is mounted, it is placed inside a Faraday cage in order to reduce electrical noise pickup. It is important to note here that the fluid reservoirs are also placed inside the Faraday cage

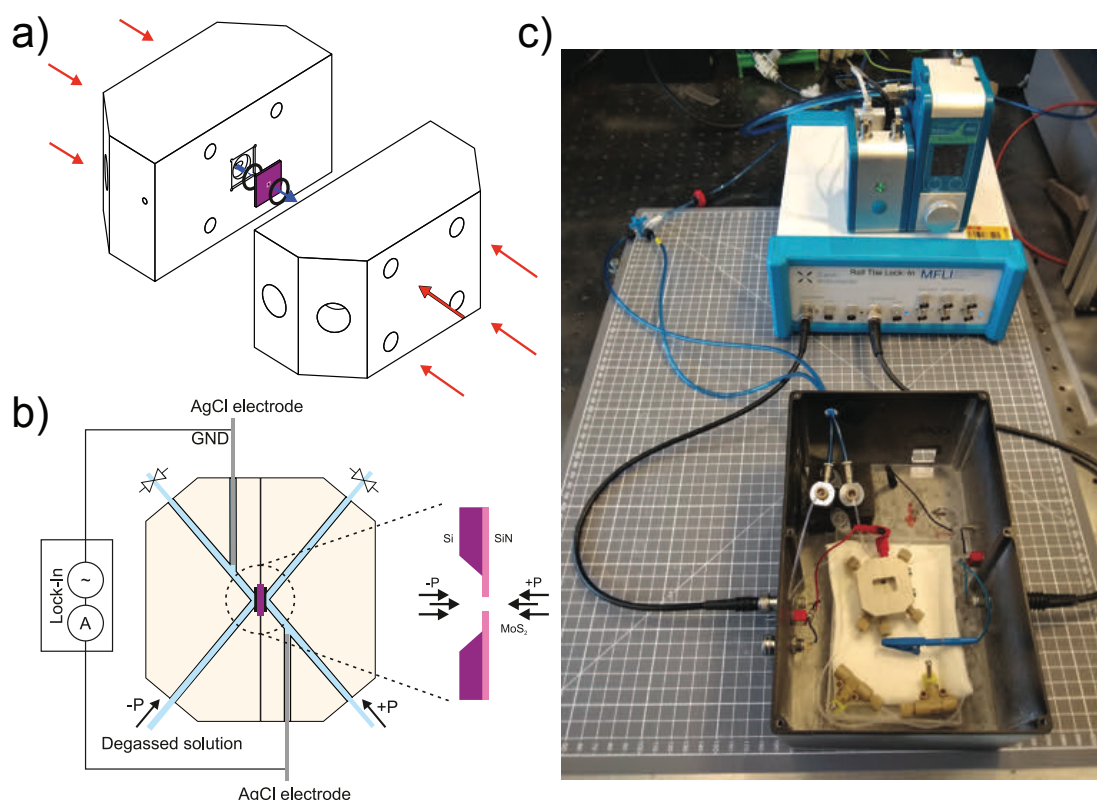


Figure 7.2 – Nanofluidics chamber and pressure system. **a)** Solid view of the two halves of the pressure tight sample chamber. A chip and the two nitrile o-rings are shown with the blue arrow showing fluid flow through the chip. Red arrows show the screw holes that allow the clamping of the chip. **b)** Shows a schematic cross section of the closed pressure chamber with channel geometry and electrical measurements. Shut off valves and pressure direction is shown. The inset shows a zoom of the chip area with the definition of the pressure direction that is chosen throughout this thesis. Panels a) and b) are adapted from ref. [48]. **c)** Photograph of the pressure setup. Nanofluidic pressure chamber and fluid reservoirs are shown within a Faraday cage and connected to a microfluidic pump. Mechanical hand valve selecting for positive, negative, or compression pressure is also seen. Electrical connections within the Faraday cage (crocodile clips) and external connections (via BNC cables) to a lock-in amplifier are also shown.

so as to avoid liquid pathways from out to inside the cage as this will produce noise pickup (figure (7.2c)). Once in the cage both pressure and electronic characteristics of the nanopore may be probed. Many combinations of DC voltage, AC voltage, and pressure may be used and are explained hereafter. Standard IV curves may be performed by sweeping the DC voltage bias and measuring the current through the pore. It is also possible to fix a given value of DC voltage and probe the behaviour in pressure (both gradient and compression). From these measurements noise analysis may also be performed as well as computing the DC ionic current rectification as $r = |I(+V)/I(-V)|$.

Secondly sinusoidal AC voltage may be used to probe the system and the corresponding current measured by a lock in amplifier. As in chapters (4) and (6) this allows the extraction of resistance, capacitance, and rectification factor simultaneously at high precision and with electrical drift averaged out. This may be measured by sweeping the excitation frequency as discussed in chapter (6) to observe

the frequency dependence of the nanopore. The same model as discussed in chapter (4) of a parallel resistor R_{AC} and capacitor C is used. The frequency response of silicon nitride nanopores varies slightly from that of glass nanocapillaries due to their higher capacitance values (≈ 1 -5 nF as compared to ≈ 1 pF for capillaries). However, the main plateau that corresponds to the DC value of resistance is still present and the only large variations are at higher frequencies (see figure (6.2)).

Measurements at a fixed AC voltage and frequency ($f = 1$ Hz is chosen from frequency sweep data for all samples) and probed in gradient and compression pressure conditions are also possible. The protocol for such experiments is as follows: a pressure sweep starting at $P = 0$ is performed, but, between each non-zero pressure value a point at $P = 0$ is measured in order to observe the pressure application effects on the baseline values of the resistance/capacitance/rectification. This sweep continues up to the maximum pressure P_{max} before returning to the lowest value ($P = 0$ if compression $P = -P_{max}$ if gradient) which allows the detection of hysteresis if present. The time spent at each pressure point is defined by the excitation frequency of 1 Hz and the associated time constant of the lock-in amplifier and allows enough settling of the response to be precise (minimum 10 s measurement time). These are powerful measurements, especially when it comes to probing the filling of the pores under pressure. Noise analysis may also be performed on AC data but is not discussed here.

Finally, by grounding one of the electrodes, streaming measurements may be performed. This chapter will deal only with wetting artifacts in nanopores and will not contain streaming data since for now the signal cannot be deconvoluted from the wetting artifact. The mechanism of streaming current and its measurement will be discussed in detail in the chapter (8).

7.3 Wetting of nanopores

The following results sections will explain in detail the sorts of wetting artifacts that are possible with both hydrophilic and hydrophobic pores in silicon nitride. Note that the size of the pores in all these measurements is on the order of $d = 80$ nm, i.e. a large pore. Wetting being in general more complicated for smaller pores these artifacts will most likely be even more prominent in those size ranges. Reference [48] discusses in detail artifacts for small pores in MoS₂ and how they may affect conductance measurements.

7.3.1 Wetting of hydrophilic pores

This section will discuss effects of wetting in silicon nitride nanopores where the chip has been exposed to oxygen plasma for ≈ 2 minutes. This is a standard procedure in the field for such silicon nitride chips and renders the surface hydrophilic. Despite this plasma pre-treatment and the hydrophilic nature of the surface wetting artifacts can still be observed and are rendered visible thanks to the application of pressure.

Once a chamber and chip are mounted as discussed in the previous section all the fluidic channels are filled with freshly degassed liquid from a degassing hose. The chamber is then sealed and placed in a Faraday cage for measurements. In most cases the nanopore is not perfectly filled in this state. The first measurement to be performed on a sample is an AC measurement with compression pressure. Indeed, compression of degassed solution has been shown to be very effective at wetting pores, comparable in effectiveness to alcohol wetting[355]. The logic behind compression wetting is that under compression any gas remaining as bubbles on the membrane or in the pore will be absorbed into the liquid due to

its low gas content. It is important to note that this is only the case for degassed liquids that have a low amount of gas to start with. If the same is performed with non-degassed solutions after releasing the compression the liquid is over-saturated in gas and so bubbles will nucleate on the membrane or in the pore.

Figure (7.4a) shows the measured capacitance of a hydrophilic membrane undergoing a compression sweep protocol just after being filled with degassed solution. It is clear from the step-wise increase in capacitance at compressive pressure points, that the compression of the liquid is absorbing gas bubbles on the membrane and thus increasing the total capacitance of the sample. Indeed, it is well known that the highest contributor to the low frequency (1-10 Hz) capacitance of silicon nitride pores is the suspended membrane[356]. A simple argument shows that the capacitance of the membrane reduces if covered with gas bubbles. If a membrane with a gas patch covering a surface A is considered it is clear that the total capacitance will be reduced by a value $\Delta C \propto A$. This is due to the increased thickness and changes in dielectric constant of the un-wetted part. The gas patch can be anywhere on the chip surface including pinned between the o-rings and the surface or in the etched back-side crevice. Henry's law[357] then states that under high pressure, as is present during the compression protocol, the solubility of gas will increase thus allowing more bubbles to be absorbed into the liquid. Once the gas patch reduces due to absorption of gas into the liquid the capacitance of the membrane grows as more and more surface is exposed to liquid. Repeating successive compression sweeps, or leaving the compression pressure at its maximum value of 7 bar for ≈ 5 minutes until the capacitance value stabilises is a way to enhance the probability of proper wetting of the pore.

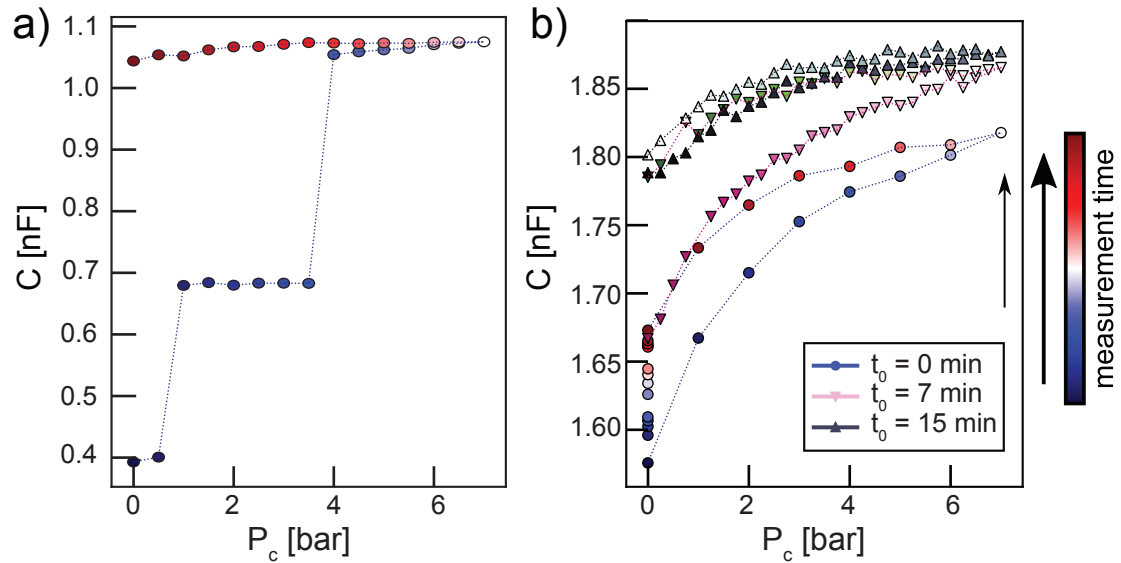


Figure 7.3 – Capacitance under pressure: a measure of membrane wetting. **a)** Capacitance of a hydrophilic silicon nitride chip measured with AC stimulus under compression pressure. Pressure is increased in steps from $P = 0$ to $P = 7$ bar, returning to $P = 0$ at each successive step. Colour of the data points (blue to red) shows that along the compression pressure sweep the capacitance increases in steps. This is consistent with compression pressure absorbing membrane pinned gas bubbles and achieving full wetting. **b)** Similar to panel a) but for a hydrophobically coated silicon nitride chip. In this case a single compression sweep is not enough to remove all the bubbles from the surface. Three successive compression sweeps (1: blue to red, 2: red to black, 3: black to white) are shown after which the capacitance behaviour is stabilised. Image is adapted from ref. [48]

This wetting capacitance behaviour is normal as despite all measures being taken to eliminate nucleation sites and bubble forming geometries it is very unlikely for no gas to be present on the membrane while going from a dry to a wet state. In contrast to the normal wetting behaviours hydrophilic silicon nitride membranes also show wetting artifacts under pressure or electric field. These artifacts come in the shape of temporary obstructions, rises in noise, or other unpredicted phenomena. An example of this is given on figure (7.4a) where three IV curves on the same sample are shown. The first is a non-linear and highly resistive state, 15 M Ω (blue curve), that is termed the obstructed state. This non-linear activation barrier-like IV curve is similar to measurements performed on small pores in quasi-2D materials where the origin of such a curve is postulated to be an additional physical effect[320; 321]. However, as seen here it is possible to obtain such activation curves purely from silicon nitride pores with obstructions (examples with 2D pores are also shown in [48]). By applying some negative pressure up to $P_{\max} = -3$ bar, the resistance value is seen to drop to a more expected value for this sized pore of 1.6 M Ω . In this unobstructed state the IV curve is linearised (orange curve). The fact that an IV curve is able to be measured and is stable is proof that both these states are stable on the order of minutes with no applied pressure. On the other hand by applying a positive pressure $P_{\max} = 3$ bar for several seconds the pore is returned to another obstructed state as seen by the final IV curve (green curve). This is not claimed to be the exact obstructed state previously seen but this does confirm that at least two states one filled and one obstructed exist and can be switched between via the application of pressure.

In depth discussion of the noise as extracted from the current traces is important as previous studies on noise in un-wet nanopores have correlated increases in noise with the presence of bubbles, further solidifying the interpretation[323]. The most important feature of the noise spectrum described in those studies as well as the focus of this analysis is the flicker noise, commonly known as $1/f$ noise due to its dependence at low frequencies (below 1 kHz). Flicker noise in all samples is larger if the pore is in an obstructed or un-wet state and lower in a filled state[358]. This behaviour is shown on figure (7.4b) showing the PSD at 200 mV from the previously discussed IV curves and is consistent with the theory that bubbles are obstructing the pore. The exact nature of the noise behaviour during these transitions will likely depend on the position of the bubble and whether it is obstructing the pore mainly in the access region or the pore interior as well as the characteristics of the bubble itself such as size, shape, and surface charge[359].

The interpretation of such behaviour is the following. Pressure will induce flow, with flow lines converging on the pore. The behaviour is then argued to be an obstructing object (whether this is a contaminant or a gas bubble cannot be resolved by this measurement) being pushed and pulled by the pressure induced flow and partially obstructing it. Due to the convergence of the flow lines it is possible to drag both objects freely floating in solution and those pinned to the membrane in the vicinity of the pore. If the object were small enough flow could induce a pressure driven translocation but no such signature is observed in the DC measurement data under pressure. As discussed previously both the electrophoretic and pressure driven flow may affect particles. The difference in mechanism between the two being that the pressure driven flow will depend on the size of the object via Stokes drag whereas for the electrophoretic driving force it will depend on the charge of the object.

Having seen this obstruction behaviour and how it modifies the IV characteristic and noise it can also be seen via the AC characteristics. This will give more detailed information about the transition from obstructed to unobstructed state. Figure (7.4c) shows how the resistance starts in the obstructed state, as the positive pressure is applied the resistance lowers but never reaches the value for an open pore. Once the pressure switches to a negative value and reaches a value of $P = -2$ bar a sharp transition in resistance is seen to the open pore value. It then remains in this state for the remainder of the

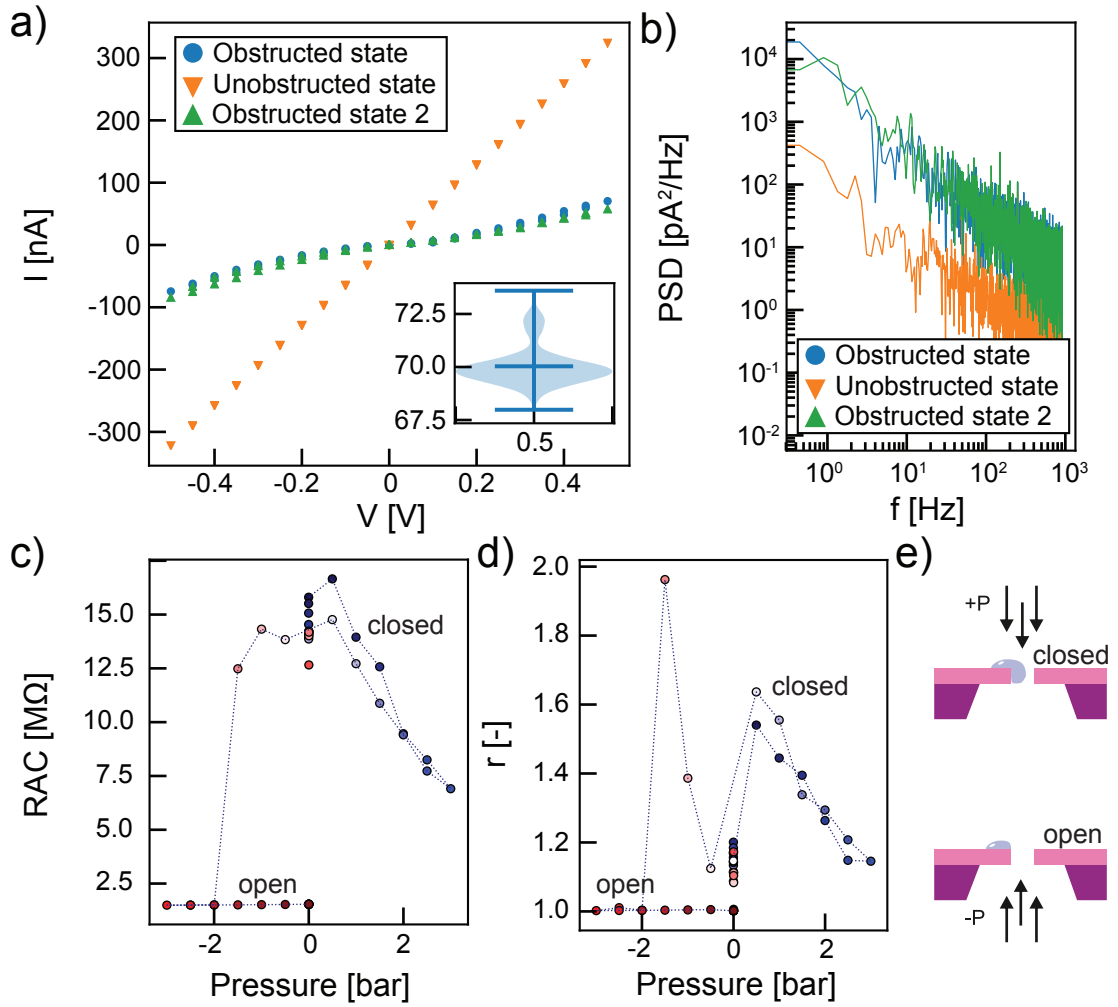


Figure 7.4 – **Wetting artifacts in hydrophilic pores.** **a)** DC IV curves of the same pore in three different states switched by pressure. First the obstructed state is shown to be non-linear. After application of negative pressure ($P = -3$ bar) the pore conductance increases to expected values. Finally by applying positive pressure the pore switches back to an obstructed state. Inset shows the extrema and probability density for the obstructed state at $V = 500$ mV. The probability density shows the fact that two distinct states are present with fluctuations between them. **b)** Noise power spectral densities obtained from panel a) at $V = 200$ mV. The unobstructed pore shows the lowest noise as expected. **c)** AC resistance value during a pressure sweep for the pore shown in panels a) and b). A discontinuous shift at $P \approx -2$ bar shows the clearing of the obstruction. **d)** Ionic current rectification measured simultaneously to panel c). The rectification shows the same qualitative behaviour as the resistance of the pore with higher ionic current rectification in the obstructed state. In the unobstructed state a value of $r \approx 1$ consistent with symmetric pores is retrieved. **e)** Schematic of the proposed toy model to explain the behaviours on panels a) through d). An air bubble is shown pinned on the positive pressure side. Pressure applications change the shape of the bubble to cause observed conductance behaviour. Figure is adapted from ref. [48].

sweep. The AC measurement allows the simultaneous observation of resistance, capacitance and ionic current rectification. The rectification is especially interesting for these wetting artifacts. Indeed, on panel d) of the same figure a matching behaviour can be seen in the ionic current rectification. In

the obstructed state the rectification is $r > 1$ whereas in the open state is $r \approx 1$ as it should be for a non-rectifying symmetric nanopore (i.e. $|I(+V)| = |I(-V)|$). Ionic current rectification is known to increase for asymmetrical pores whether in geometry or surface charge, and to be modulated by pressure[230; 232] (chapter (4) discusses ionic current rectification in detail),. Silicon nitride pores being symmetrical no rectification is expected in the filled state. Due to the high precision of working with an AC bias and a lock-in amplifier small differences of rectification are measurable despite the amplitude of the bias being only 100 mV. Indeed, it is hard within a voltage range of 100 mV to detect rectification differences below 10% on a DC IV curve. In fact the precision of this measurement is even higher as will be discussed in the following chapters focusing on the pressure dependence of fully filled nanopores (chapter 8).

Time resolution between the AC and DC approach varies. Indeed, for the AC based approach the time resolution is on the order of several seconds considering the integration time of the lock-in amplifier at the excitation frequency of 1 Hz. However, DC measurements are much faster with an acquisition frequency of 1.8 kHz allowing a time resolution in the millisecond range. Transitions between obstructed and unobstructed states are seen as instantaneous even in the DC measurements pointing to an un-clogging process faster than milliseconds. This timescale for unclogging is backed by dwell time measurements of pressure driven translocations of objects being in the hundreds of micro-seconds range[353; 354].

Here a toy model is discussed in which an obstruction partly obstructing the pore may qualitatively explain the resistance and rectification measurements (schematic on figure (7.4e)). Indeed, a bubble partially obstructing the pore on the front side of the membrane thus changing the resistance of the pore is discussed. When positive pressure is applied the shape of the bubble may be modified in a way that liberates more of the pore for ionic conduction thus leading to a lower resistance. On the other hand applying negative pressure would induce drag away from the pore and could dislodge the bubble from its obstructing position thus restoring the open pore resistance. This change in shape is something not expected from a solid object and points more to the bubble hypothesis than the contamination one.

Finite element modelling was also performed to explain this behaviour. Four separate conditions were simulated: first an open pore, second a pore with an obstructing object on the membrane next to the pore entrance, third with the obstructing object on top of the pore clogging it, and lastly an obstructing object inside the mouth of the pore (see figure (7.5a to d for schematics)). Coupled Poisson-Nernst-Planck-Stokes equations are then solved in each case for different cross pore voltages and pressures. In all the studied cases the pressure dependent resistance is negligible.

The model does give changes in rectification due to flow in large pores as expected from studies on the rectification of glass nanocapillaries[230; 232]. This comes in the form of a reduction in rectification for applied pressure due to the liquid flow perturbing the local charge distribution responsible for rectifying behaviour (FEM model and simulated rectification is discussed in detail in the next chapter for filled pores). For small pores this effect is drastically reduced due to the smaller total flow rate. None of the simulated static conditions were able to explain the large variation of resistance and rectification observed in experiment thus lending more weight to the interpretation that a dynamical change of shape of the obstructing object is the cause. In addition no non-linear conductance effects were observed in the simulations. These sorts of activation barrier IV curves have previously been described as being due either to hydration layer shredding or to electro-wetting[320; 336; 337]. In this context hydration layer shredding is considered improbable due to the fact this requires the narrowest part of the conductive pathway to be on the order of the ion sizes which seems unlikely with such large

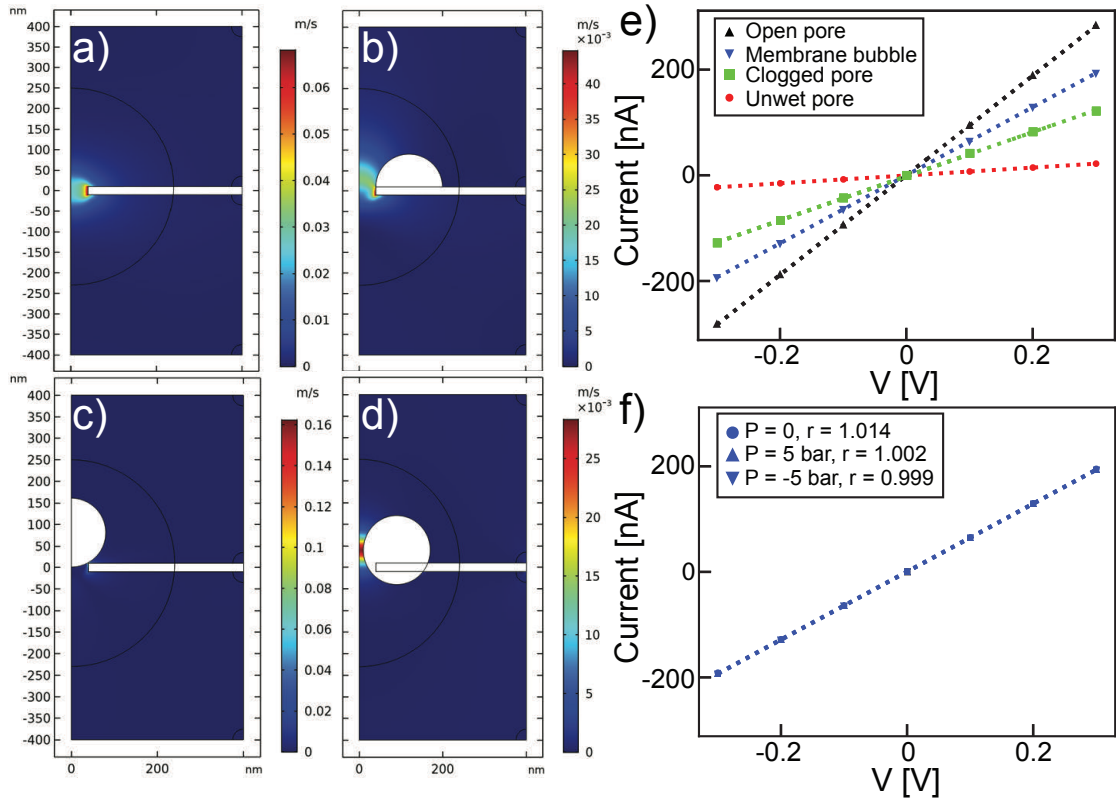


Figure 7.5 – **Finite element modelling of obstructed pores.** a) through d) Fluid velocity profiles at 300 mV of applied potential and $P = 0$ bar in the case of the open pore, membrane bubble, clogged pore, and unwet pore respectively. The system is axially symmetric around zero and black circles denote areas where the mesh is additionally refined. e) IV curves as extracted from the models presented on panels a) to d). The open pore shows the highest current with decreasing current for each subsequent condition. No non-linearity of IV characteristic is seen however obstructions do change the resistance and ionic current rectification (although smaller than in the experimental case for r). f) IV curves for the bubble on the membrane case for three different applied pressures: $P = 0, 5$, and -5 bar. Although no large changes in resistance are seen rectification is seen to decrease in the case of static bubbles. These results point to a dynamic case explaining the observed experimental behaviour. Figure is adapted from ref. [48].

variations in resistance and a large underlying pore.

7.3.2 Wetting of hydrophobic pores

Having investigated the different behaviour that hydrophilic silicon nitride nanopores can provide when wetting issues are present this section will describe briefly the behaviour of hydrophobic pores (details are found in [48]). In order to render silicon nitride membranes hydrophobic they are coated with hydrophobic hexamethyldisilane (HMDS). This coating is verified to be of good quality by measuring the contact angle of a water droplet on the surface, which yields an angle of $\approx 84^\circ$. The assumption is made that the coating also covers the interior of the pore.

Following the protocols set out above it is possible to measure the state of the pore using IV characteris-

tics and pressure sweeps. Most samples show obstructed states either over the whole pressure range or part of the pressure range similarly to hydrophilic nanopores. Differences arise in the stability of the filled states that only last for a matter of minutes before reverting to a high resistance and non-linear IV curve. In addition these partially wet states do not correspond in resistance to the open pore state, and the flicker noise in these pores is still higher than the open pore state.

Electro-wetting phenomena, which have been described in detail for porous membranes are present in the hydrophobic pore case[336; 350; 351]. In order to completely wet the pore large voltage biases are applied across it which bring the menisci of the trapped air bubble closer together until they touch. This sort of high voltage wetting in combination with applied pressure is able to irreversibly wet such hydrophobic nanopores restoring a correct value of the resistance and of the $1/f$ noise level. However, the critical voltage and pressure at which this complete wetting arises is dependent on the diameter of the pore and for smaller hydrophobic pores it was impossible to attain complete wetting. This underlines the importance, not only of chip-pre treatment in order to help the wetting procedures, but also the cleanliness of the substrate and liquids used, and the correct degassing of experimental buffers.

7.4 Conclusion

This section has served both as an introduction to the nanopore system with added pressure control capabilities as well as an overview of the measurable quantities, their precision, and importance. It is clear that the addition of another control variable in pressure is an important factor in being able to ascertain the filling state of a pore as well as controlling it. It also brings home the importance of degassing solutions and pre-treating chips in order to fill nanopores reliably without wetting artifacts. All these factors become of heightened importance when using smaller nanopores for example for translocations of DNA molecules. Using such pores without proper checks of the wetting state could lead to different translocation behaviours that may then mislead the conclusions of the study. Indeed, the conductance of such clogged pores mimic the behaviour of smaller pores. Any phenomena produced during DNA translocation could be interpreted as coming from a size effect when it would be due to a clogged pore. Other analyses based solely on the conductance of the pore, such as non-linear IV curves, are equally biased in the case of clogged or unwet pores and should be supplemented by additional measurements.

8 Nanofluidics

Results contained in this chapter can be found in the following publication S. J. Davis, M. Macha, A. Chernev, D. M. Huang, A. Radenovic, and S. Marion, "Pressure Induced Enlargement and Ionic Current Rectification in Symmetric Nanopores", Nano Letters, 2020

Author contributions: S.J.D. performed the experiments, analysed the data and performed FEM simulations. S.M. designed and built the experimental set-up and built the FEM model. M.M. designed the microfluidic chamber and performed AFM imaging. A.C. fabricated devices. A.R. and S.M. supervised the research. D.M.H. provided an explanation for the ionic current rectification. S.J.D. and S.M. wrote the manuscript with all authors providing important suggestions for the experiments, discussing the results, and contributing to the manuscript.

8.1 Introduction to nanofluidics

By using the knowledge gained in the previous chapter on how to correctly fill nanopores, and discriminate between wet and non-wet states, it is possible to push the analysis of nanopores under pressure further. Indeed, nanopores are a single molecule tool which, apart from their bio-sensing capabilities discussed in the first part of this thesis, can be applied to many nanofluidic applications from osmotic power generation[36] to water desalination[360]. Measuring the conductance of the pore allows the measurement of non-linear phenomena such as previously presented ionic current rectification[218; 361] (chapter (4)) and other nanofluidic effects concerning mass transport[362], and overlap of length scales[24]. Solid state nanopores are typically fabricated in silicon nitride suspended membranes due to well-established protocols that are compatible with standard lithography techniques. Pores in these suspended membranes can be used as such, as in this thesis, or with the addition of quasi 2D materials such as MoS₂, hexagonal boron nitride, or graphene in which a small pore is drilled[38; 363].

While nanopores have previously been combined with pressure, this was motivated by the need to add an additional control on analyte translocation. Indeed, pressure has been used as an opposing force to the electrophoretic force responsible for driving translocations. This has the effect of slowing down translocations[279], allowing even very small proteins $< 6.5\text{ kDa}$ [347] that would normally translocate too fast, or near neutral molecules[364] that induce very little conductance drop to be detected. By effectively tuning the flow such that the total force on the molecule is negligible a trapped state near the pore was also reported[365]. Other uses have been to extract in-situ zeta potential measurements

of the pore as this is known to affect the translocation speed of analytes[346].

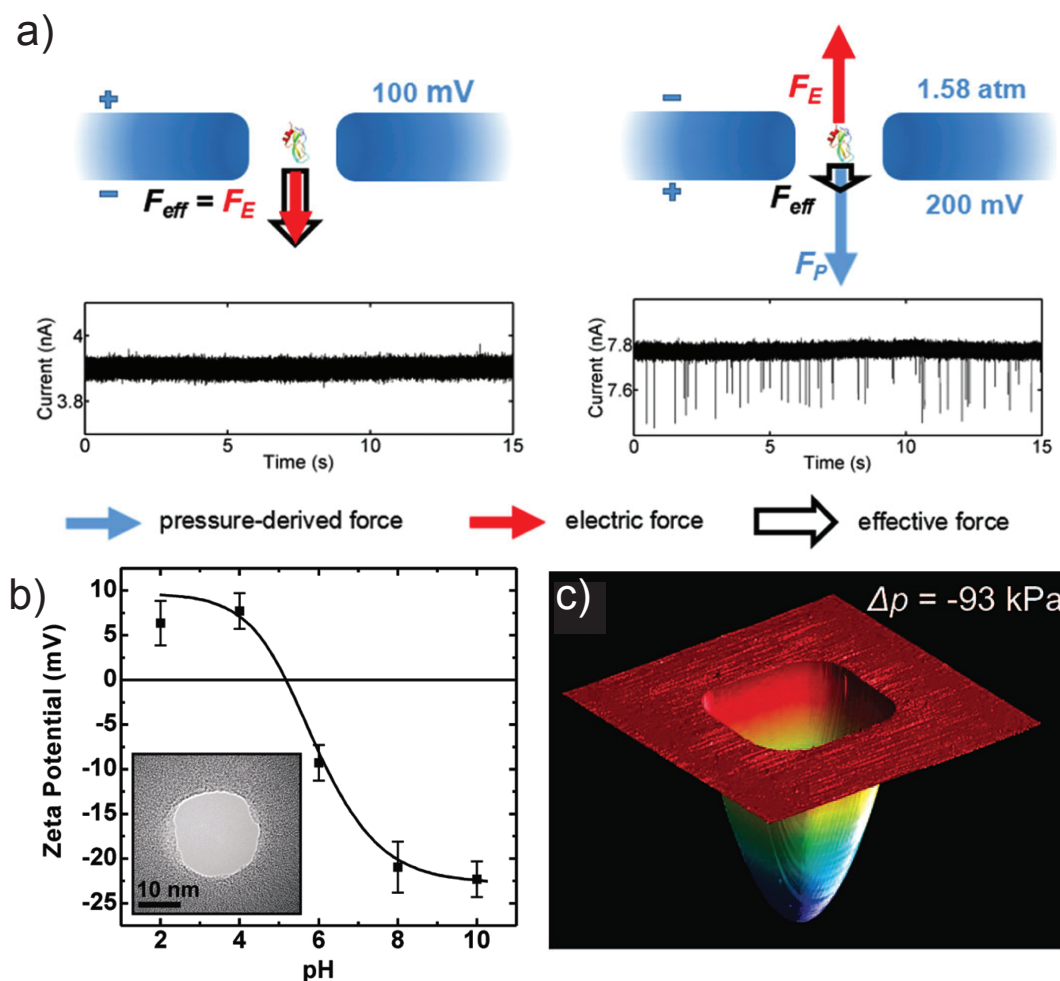


Figure 8.1 – Combinations of nanopores and nanoscale materials with pressure. **a)** Translocations of small proteins with added pressure control. Left hand side shows translocation schematic along with current trace in applied electric field only. No translocations are observed due to the speed of the protein translocation. Right hand side shows translocation schematic with added pressure. In this case the force exerted during translocation is the resultant of the electrophoretic force and the pressure flow force. The application of pressure reduces the total force enough that translocations are measurable. This is confirmed by the current trace showing translocations. Image is adapted from ref. [347]. **b)** Pressure enabling the measurement of the zeta potential. Silicon nitride pores are interfaced with a pressure system allowing the measurement of the streaming current at different buffer pHs. The transition from negative surface charge at high pH to positive surface charge at low pH is seen. In this case the point of zero charge is $\approx \text{pH } 4$. Image is adapted from ref. [346]. **c)** Measured deflection of multilayer suspended graphene under pressure application. AFM measurements allow to map the exact deflection of multilayered graphene. The maximal deflection at the center point is in this case $\approx 140 \text{ nm}$ for a 9 nm thick multi-layered graphene flake over a $4.75 \times 4.75 \mu\text{m}$ aperture. Image is adapted from ref. [366].

Pressure driven particle translocation has also been shown to precisely quantify hydrodynamic permeability with high precision[354]. Recently fluid flow tangential to the nanopore membrane was shown

to modulate capture rate and DNA translocation dynamics due to viscous drag[367].

Whereas the bulk of nanopore studies use pressure to modify or quantify translocations it has also been used as a more fundamental probe of nanopore behaviour under pressure. By using a combination of flow and fluorescence spectroscopy it is possible to measure the depletion of ionic concentration within a single nanochannel due to the application of pressure and so quantify the mass transport due to flow[362]. Ionic current rectification is a fundamental quantification of the asymmetry and role of surface charge present in the nanopore system. This has been shown to be influenced by pressure[230]. It is hypothesised to be due primarily to the fluid flow generated by pressure affecting concentration distributions within the nanopore itself. Reductions in ICR are seen for asymmetric conical pores with the hypothesis that pressure induced liquid flow disturbs the ionic cloud polarisation present due to the geometric asymmetry[232]. For a small pore radius ($R \approx 15$ nm) the pressure no longer affects ICR due to the much lower flow rates[230; 231]. This shows how pressure can affect the non-linear conduction of nanopores.

Considering that the use of nanopores or nanochannels with the addition of a pressure control system is not yet explored sufficiently, the basic understanding of such systems' responses to pressure gradients is needed. The blistering and delamination of thin membranes such as silicon nitride[368] or 2D materials[366; 369; 370] has been extensively studied. These rely on previous analytical work into the deformation of plates or shells under mechanical stress[371; 372]. While these studies are invaluable to understand the material properties of plates they are usually restricted to suspended membranes and do not characterise any effects that would happen at a pore. Some research has been done on elastic polymer nanopores[373; 374] but the ranges of strain in such systems is ten times larger than seen here with less ductile ceramic silicon nitride membranes and are thus difficult to compare. Pore effects are key to understanding the nanopore system under pressure as the electric field and fluid flow are confined to the close proximity of the pore and define the resulting measurements in nanopore systems.

This chapter aims to quantify the role that hydraulic pressure has in modulating ion transport in thin symmetrical silicon nitride nanopores. Deformations of the nanopore supporting membrane are found to produce an enlargement of the nanopore diameter. This change in diameter is a measure of the local induced strain in the silicon nitride substrate. Considering silicon nitride is routinely used as a support for quasi 2D pores this motivates the establishing of a robust calibration of such systems. Quasi 2D systems will be intimately linked to their support and have been predicted to show high mechano-sensitivity in strained conditions[64; 375; 376; 377; 378]. This has been predicted to be as an over 20 fold increase in conductance at 0-4% strain in MoS₂[376]. Mechano-sensitivity is of great interest for osmotic power generation or water desalination applications as it could influence the membrane ion selectivity key to these effects[360; 379]. Pressure induced asymmetry in the ion transport is also discussed, in particular as an increase in ICR is shown in contrast to previous measurements which demonstrated that pressure only reduced ICR. This is explained via pressure induced changes in ionic concentration polarisation within the pore. The key to this technique is the AC approach coupled with hydrostatic pressure introduced in chapter (7). This method is not only able to measure differences in conduction below 1% but has the added benefit of separately extracting the linear and non linear contributions to conduction thus justifying its use in compliment to standard DC measurements.

8.2 Pressure induced strain enlargement measured via pore resistance

Following the same protocol as described in the chapter (7) silicon nitride nanopores are first oxygen plasma cleaned in order to render them hydrophilic before mounting them in the custom designed chamber. Following this the chamber is filled using a degassing hose with freshly degassed buffer. The chamber is then put in a Faraday cage and connected to the microfluidic pump upon which filling protocols consisting of compression pressure sweeps up to 7 bar are performed (see figure (7.2) for details of the experimental setup). Once the capacitance is stable as a function of compression, which should guarantee that no gas bubbles are left on the membrane measurements begin.

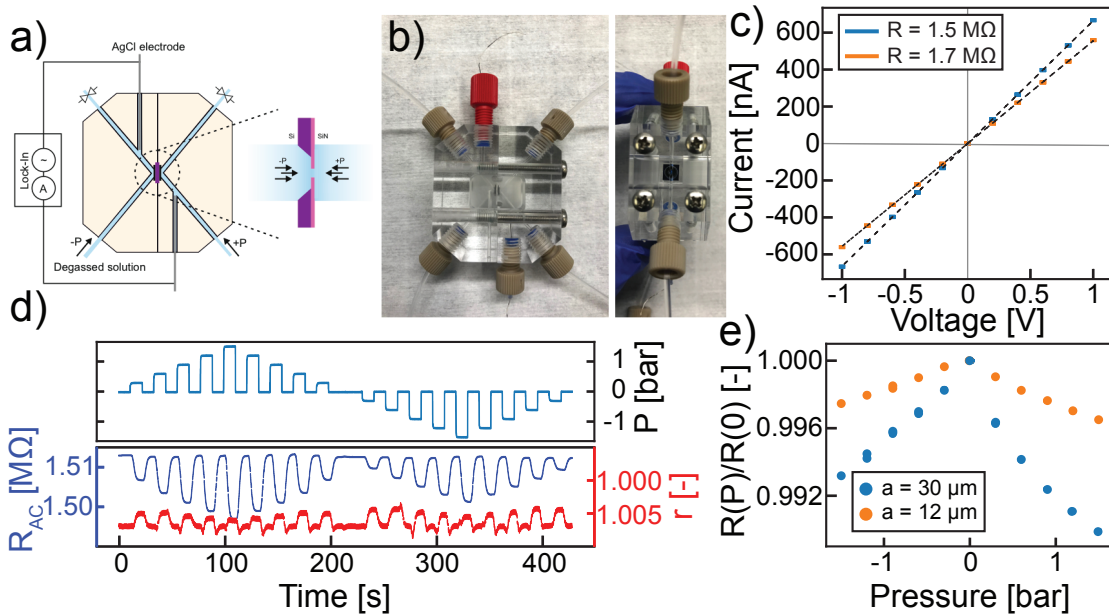


Figure 8.2 – Application of pressure to perfectly filled solid state nanopores. **a)** Schematic in side view of the sealed pressure chamber channels and electrical measurement. Zoom on the right shows the chip area and the convention of pressure sign chosen for this study. **b)** Photographs of the sealed pressure chamber in a side view (left) and top view (right). These photos are taken of an identical poly(methyl methacrylate) (PMMA) chamber since PEEK is not transparent. **c)** DC IV curves for two representative samples having two different membrane sizes but similar pore sizes of $d_0 \approx 80 \text{ nm}$. **d)** Time trace of the lock-in AC detection. Top is the pressure as a function of time (the resolution is 2-4 mbar). Bottom shows on a split scale the resistance and rectification simultaneously obtained to the pressure above. **e)** Mean values of resistance as a function of pressure as extracted from the raw time trace on panel d). The curves represent the same samples as on panel c) with two distinct membrane sizes of $12 \times 12 \text{ }\mu\text{m}$ and $30 \times 30 \text{ }\mu\text{m}$. Figure is adapted from ref. [68].

In a pressure gradient condition the membrane will undergo a certain stress. This is in comparison to the compression case where no net stress is assumed and which shows flat responses in conduction (figure (8.4a)). The resistance R depends on the size of the pore through the fundamental equations of nanopore conductance (equation (1.1)). The change in resistance is therefore attributed to a change in pore size brought on by the strained membrane. This is seen to be the case on figure (8.2e)) where any non-zero pressure gradient reduces the resistance. Considering the measured resistance is restricted to the linear voltage term due to the lock-in measurement technique this effect is ensured to not come

8.2. Pressure induced strain enlargement measured via pore resistance

from some complex coupling of voltage and pressure. A linear relationship between the strain and the pore enlargement is derived in the case of a circular pore in a thin square membrane[380]. Given the radius at zero pressure d_0 the enlargement takes the form $d(P) = d_0 (1 + (1 - \nu^2)\sigma_r/E)$ where σ_r is the radial stress in the membrane, ν the Poisson ratio of silicon nitride, and E the Young's modulus of silicon nitride. This allows the direct connection between a drop in resistance and an increase in strain via the pore enlargement.

To explain the strain induced enlargement of the pore the elastic properties of the supported silicon nitride membrane must be taken into account. It is known that materials such as silicon nitride will stretch or blister[368; 366]. The exact response will depend on the strain value as well as the geometric and elastic parameters of the membrane: a the size of the square membrane, L the thickness of the membrane, E the Young's modulus, and ν the Poisson ration. The stress in the membrane can then be expressed as the following cubic equation as shown by Vlassak[368]:

$$\sigma_r^3 - \sigma_0 \sigma_r^2 - \frac{EP^2 a^2}{6L^2(1 - \nu)^2} = 0, \quad (8.1)$$

where σ_0 is the residual membrane stress. By inserting the pressure dependent radius $d(P)$ into the conductivity of the nanopore (equation (1.1)) the observed behaviour is retrieved.

First, to confirm the validity of the model and justify the elastic behaviour is responsible for the effect, the dependence on the membrane size is investigated (as presented on figure (8.2e)). The positive pressure behaviour is fitted at a driving potential of 100 mV RMS to a simplified $\sigma_0 = 0$ case. The elastic parameters are assumed to be: $E = 200$ GPa, $\nu = 0.23$, and $L = 20$ nm. The membrane size can then be estimated. Results for the small and large membrane are $a = 12.8 \pm 1.0 \mu\text{m}$ and $a = 30.6 \pm 6.2 \mu\text{m}$ respectively. This is in good agreement with the optically measured membrane sizes of $12 \mu\text{m}$ and $30 \mu\text{m}$. Total deflections at the center of the membrane w_0 can also be computed and yield displacements on the order of $w_0 = 2.7 \pm 0.6 \mu\text{m}$ at $P = 1500$ mbar. One factor that can affect the error of these predictions are the differences in the Young's modulus or Poisson ratio depending on the manufactured silicon nitride. Indeed, tabulated values of Young's modulus vary from ≈ 100 -300 GPa depending on the fabrication type, parameters of growth, or composition[381].

While the prediction of the membrane size shows that the simplified $\sigma_0 = 0$ case is in good agreement with the behaviour it is not sufficient to completely explain the measurements. Indeed, the negative pressure shows a marked asymmetry at low voltage (as seen in figure (8.3a)). This is assumed to depend on the residual stress factor σ_0 . However, while silicon nitride membranes do show residual stress in the plane of the membrane, which is dependent on their growth conditions, this is usually compressive and restricted to below 500 MPa[384; 385]. In addition residual stress of the membrane would affect both the positive and negative pressures and as such does not explain the observed asymmetry. Tapping mode AFM images of the silicon nitride membranes are taken after experiments and no correlation between the $P = 0$ topology of the membrane and pressure behaviour is observed confirming intrinsic residual stress to be negligible in this effect (figure (8.4b)).

The only asymmetry present is on a chip scale and is due to the back side etched pit. The application of pressure to the back-side of the chip induces forces on the etched silicon walls thus (additional arrows on figure (8.3b)) imparting a stress parallel to the membrane plane that will act in addition to intrinsic membrane residual stress. A pressure dependent residual stress for the negative side of the form $\sigma_0 = \alpha P$ with α a fit parameter is therefore assumed. The value of α can be guessed at by taking into account the ratio of thickness's of the etched silicon walls and the membrane thickness. Indeed,

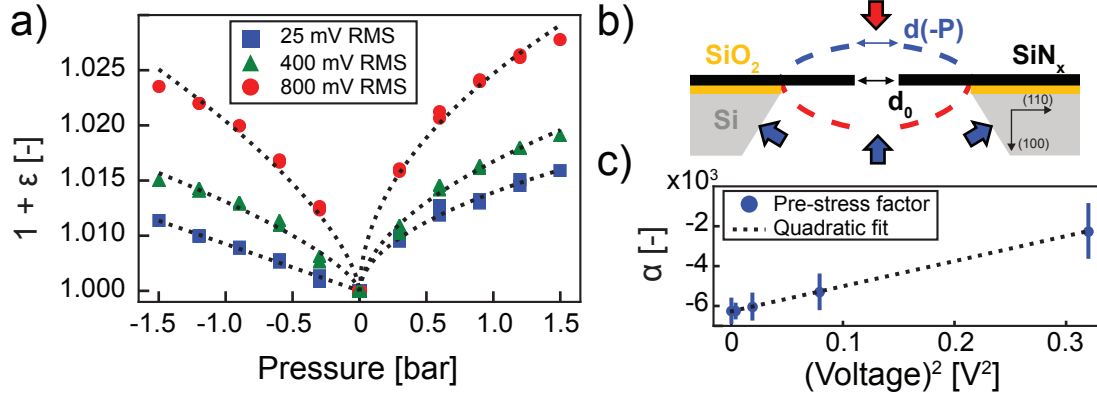


Figure 8.3 – Elastic response of membranes under pressure: strain induced enlargement. **a)** Normalised strain value as a function of pressure for the same membrane at a low bias voltage of 25 mV RMS (blue squares), and two larger bias voltages of 400 mV RMS (green triangles), and 800 mV RMS (red circles). Dashed black lines correspond to the fit of pressure behaviour, for the positive side in the $\sigma_0 = 0$ case, and for the negative side with the full stress equation (equation (8.1)). The positive pressure does not deviate from the simplified behaviour whereas the negative behaviour shows dominant residual stress at low voltages which disappears at higher voltages. **b)** Schematic of the chip and membrane with nanopore. The initial diameter d_0 is shown as well as dashed lines showing a schematic of the deformation of the membrane under pressure. This deformation due to strain enlarges the pore, $d(-P)$ is labelled. The negative pressure is also shown to act on the etched walls of the back-side of the chip explaining the asymmetry seen for low voltage on panel a). **c)** Voltage dependence of the residual stress factor α . The residual stress factor is shown to diminish quadratically with applied voltage. This is hypothesised to be due to electrostriction effects within the chip that modulate the stress response of the membrane. Electrostriction is known to vary quadratically with voltage[382; 383] lending support to this postulation. Figure is adapted from ref. [68].

the applied pressure will induce a force $F_{\text{in}} \propto L_{\text{Si}} P \sin(54)$, where $L_{\text{Si}} = 380 \mu\text{m}$ is the thickness of the silicon substrate, and the \sin is due to the etch angle defined by crystallographic planes. This force will then be transferred to the membrane where the stress is obtained by dividing by the thickness. The residual stress factor can thus be estimated as $\alpha \approx L_{\text{Si}} \sin(54) / L \approx -10'000$. Fits of the full cubic equation (8.1) are then performed for several different voltages and are shown on figure (8.3a). The value of the residual stress factor for low voltages is $\alpha \approx -6'000$ confirming the pressure induced residual stress hypothesis.

Although including a pressure dependent residual stress on the negative pressure side explains most of the measured behaviour, figure (8.3c) shows that the residual stress factor is voltage dependent. This is hypothesised to be due to electrostriction of the underlying chip materials. Electrostriction is a similar effect to the piezoelectric effect only it can occur for all dielectrics at high electric field regardless of crystal symmetry[382; 383]. Considering the thickness of the materials in question, the electric field at 800 mV RMS is on the order of 2 kV/m over the silicon substrate and on the order of 40 MV/m over the 20 nm thick silicon nitride membrane. These high electric fields are enough to impart significant stress on the membrane due to electrostriction. This stress is assumed to counterbalances the pressure induced residual stress discussed above returning a symmetric pressure profile at high voltage. The quadratic dependence of α on voltage lends weight to this assumption as electrostriction is known to be quadratic in voltage[382; 383]. At large voltages the measured data deviates from the model and the stresses in these cases are assumed to no longer be within the range of validity of equation (8.1). However, the low voltage behaviour as well as a simplified electrostriction does account for the

8.3. Pressure induced ionic current rectification in symmetric nanopores

measured data.

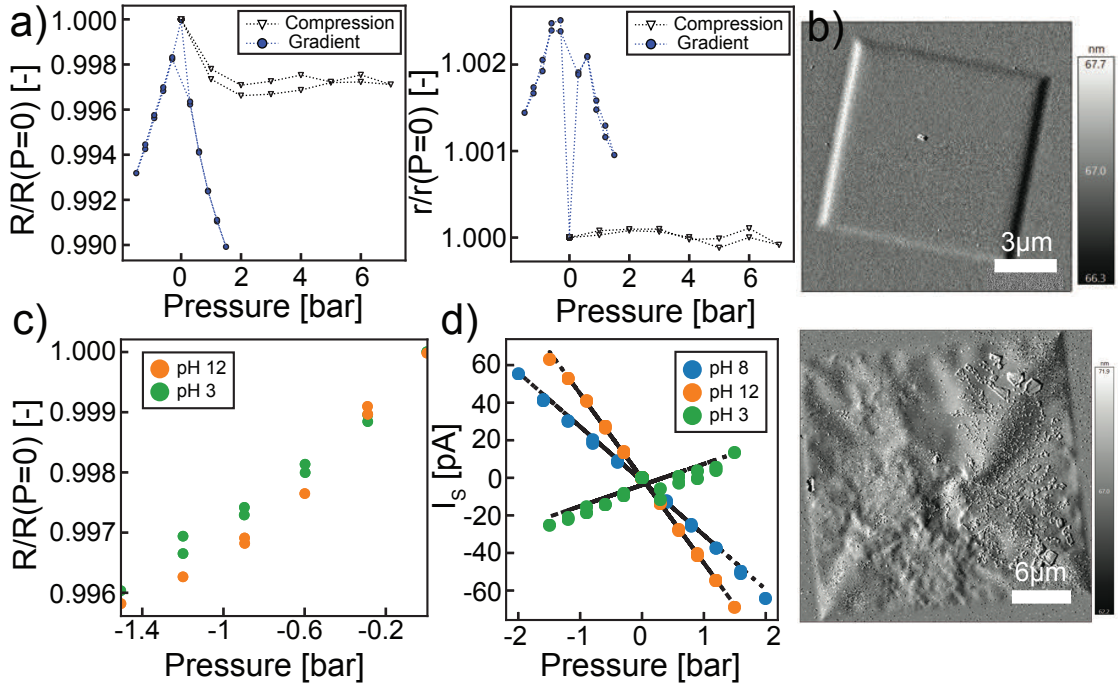


Figure 8.4 – **Compression pressure behaviour and elastic membrane phenomena.** **a)** Resistance and ionic current rectification behaviour with compression pressure. Compression pressures up to the maximal 7 bar available with the microfluidics pump show no significant effect in either resistance or ICR as compared to gradient pressure response. A small offset is present that could be due to non-perfect seal on one side of the chamber. **b)** Examples of two AFM height images taken of the silicon nitride suspended membranes after use. Different $P = 0$ conformations are seen, either flat and raised (top) or wrinkled (bottom). However, no correlation between zero pressure membrane shape as measured via AFM and gradient pressure conductance response is seen confirming that intrinsic membrane residual stress does not play a role in the pressure response of pores. **c)** Resistance as a function of pressure for the same pore at pH 3 and pH 12 showing the same magnitude of response. This confirms that the AC methodology can completely distinguish effects due to linear contributions to the conduction and non-linear contributions. Images are adapted from ref. [68].

8.3 Pressure induced ionic current rectification in symmetric nanopores

In addition to the large accuracy of the measured strain induced enlargement of the pore, the lock-in amplifier allows the measurement of higher harmonics to the same degree of accuracy. By measuring such harmonics (as is explained in detail in chapter (4)) it is therefore possible to measure the non-linear contributions to conductance much more accurately than is possible in DC measurements. Figure (8.2d) shows the raw time trace of the rectification during a pressure sweep.

By extracting the mean of each pressure level, as is done for the resistance, plots such as those on figure (8.5) are obtained. Panel a) shows the dependence on voltage of the phenomena for the same sample. Interestingly the rectification increases from the base value $r(P = 0) \approx 1$ with any gradient of applied pressure. While pressure reduction of rectification has been reported in the literature for asymmetric pores[230; 231; 232] an increase has, to the author's knowledge, never been measured. Indeed, it is

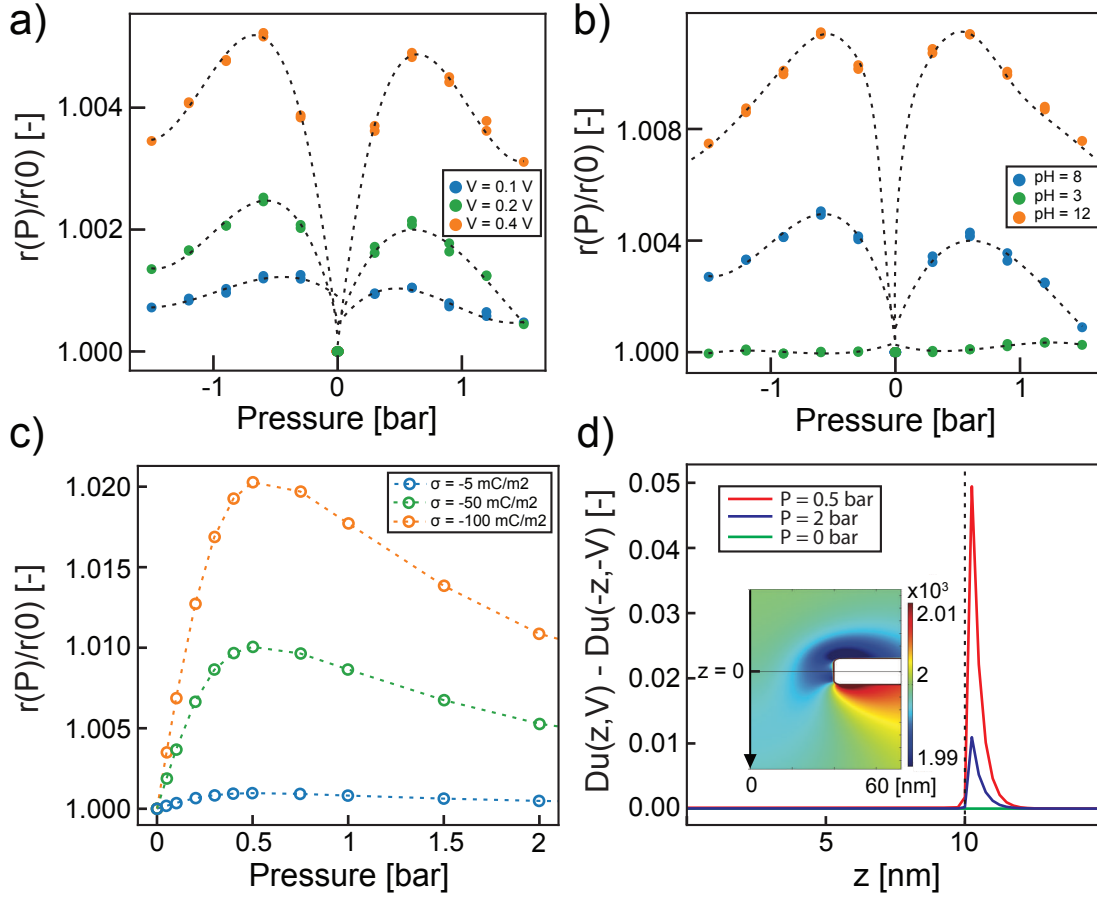


Figure 8.5 – **Pressure induced ionic current rectification in symmetric solid state nanopores.** **a)** Rectification as a function of gradient pressure for different driving voltages. The effect is seen to be approximately linear in voltage while the pressure dependence is not trivial. A growth of ICR with low pressure values is seen before a turnover at $P \approx 1$ bar leading to a decrease for high pressures as is known from literature[230; 232]. **b)** Measured rectification in three different pH values. Pressure dependent rectification grows with a high surface charge and is almost completely reduced for the pH 3 case. This is also in agreement with streaming current measurements shown in figure (8.4d). **c)** Rectification extracted from a COMSOL model of a solid state nanopore under pressure. The model shows only positive pressure as it is symmetric by design. Surface charges of -5 mC/m^2 , -50 mC/m^2 , and -100 mC/m^2 are chosen to simulate the pH 3, 8, and 12 case respectively. Model shows good agreement with the experimental behaviour of ICR with pressure. **d)** Spatial asymmetry in the Dukhin number for positive and negative bias $Du(z, V, P) - Du(-z, -V, P)$ along the pore axis. Three representative pressures are shown. For $P = 0$ no asymmetry is present confirming a $r = 1$ value in this case. For non-zero pressure it is clear that the intermediate value induces higher asymmetry thus leading to higher ICR. Inset shows the surface plot of $c_+ + c_-$ along with the geometry of the FEM pore and definitions of the z axis. Figure is adapted from ref. [68]

claimed that with large pressures the induced liquid flow disturbs the build up of charge responsible for the rectification. While this effect also seems to be present in the current data for pressures above $P \approx 800 \text{ mbar}$, the effect at low pressures is to increase the rectification. The effect is also symmetric in pressure and depends approximately linearly on voltage.

8.3. Pressure induced ionic current rectification in symmetric nanopores

Considering rectification is intimately tied to surface charge it is expected to be highly dependent on it. In order to confirm this, experiments were carried out with three different pH values: 8, 12, and 3. These pH values were chosen to probe most of the charge space of silicon nitride (figure (8.1b)). Indeed, silicon nitride's point of zero charge is \approx pH 4, above this value the surface charge grows until reaching a plateau around pH 12[346]. As expected the measured effect is seen to increase with increased pH and dies out almost completely at pH 3. The measured resistance dependence on pH is negligible, as is shown in figure (8.4c), which confirms that the lock-in amplifier can completely deconvolute the strain induced linear response previously discussed and this non-linear effect.

The same figure also shows the streaming current measured at these different pHs confirming the change of surface charge via the change of zeta potential. These measurements of ionic current rectification are made despite the high salt concentration (1 M KCl) being used. Considering ionic current rectification effects are enhanced in low salt concentrations[54] this effect is also expected to grow in those conditions (see chapter (4) for details and FEM simulations below).

In order to confirm the validity of the measurement finite element method simulations are carried out. Shortly an axially symmetric nanopore geometry with a surface charge σ is implemented in COMSOL multiphysics. Coupled Poisson-Nernst-Planck-Stokes equations are then solved with different static pressures between the two electrolyte reservoirs (similarly to what is performed in chapter (7), without any air bubbles present). Assuming the complete decoupling of the strain effect no change in shape of the pore is taken into account in these simulations. A change of the pore size on the order of 1% as is measured in the previous section is not expected to change the rectification of the pore. Considering that the model completely explains the experimental behaviour this confirms that no bending of the membrane is necessary for pressure induced ionic current rectification to be present.

Total current flowing through the pore is extracted and the rectification factor can be computed as $r = |I(+V, P) - I(0, P)| / |I(-V, P) - I(0, P)|$ where the streaming current contribution $I(0, P)$ has been subtracted to better represent the experimental data. Figure (8.5c) shows the FEM values of rectification as a function of pressure for three surface charge values chosen to simulate the effect of experimental pH changes. Only positive pressure gradients are shown since the model is by definition symmetric in pressure.

The FEM model captures well the behaviour of the rectification with an increase in r for low pressures before a turnover and decrease at higher pressures. The model also captures the surface charge dependence where the magnitude of the effect is proportional to surface charge. To explain the microscopic reasons behind this behaviour perturbations of ion clouds around the pore due to the advective pressure flow must be taken into account. It has been shown previously that spatial variations of the local Dukhin number along the pore axis $Du(z)$ are a measure of the magnitude of ICR[361].

The Dukhin number is the ratio of bulk to surface conductance and thus depends on the total concentration proportional to bulk conduction, $c_+ + c_-$, and on the difference in concentration proportional to surface conduction, $c_+ - c_-$. In the current case of no Debye layer overlap the Dukhin number can be given as a function of the positive and negative ion concentrations c_{\pm} simply as[361]

$$Du(z) = \frac{\langle c_+(z) - c_-(z) \rangle}{c_+(r=0, z) + c_-(r=0, z)}, \quad (8.2)$$

where the $\langle \cdot \rangle$ is the average over the radial coordinate r , and $c_{\pm}(r=0, z)$ is the concentration of ions through the center of the pore. Flow induced by pressure will change the ion concentrations across the

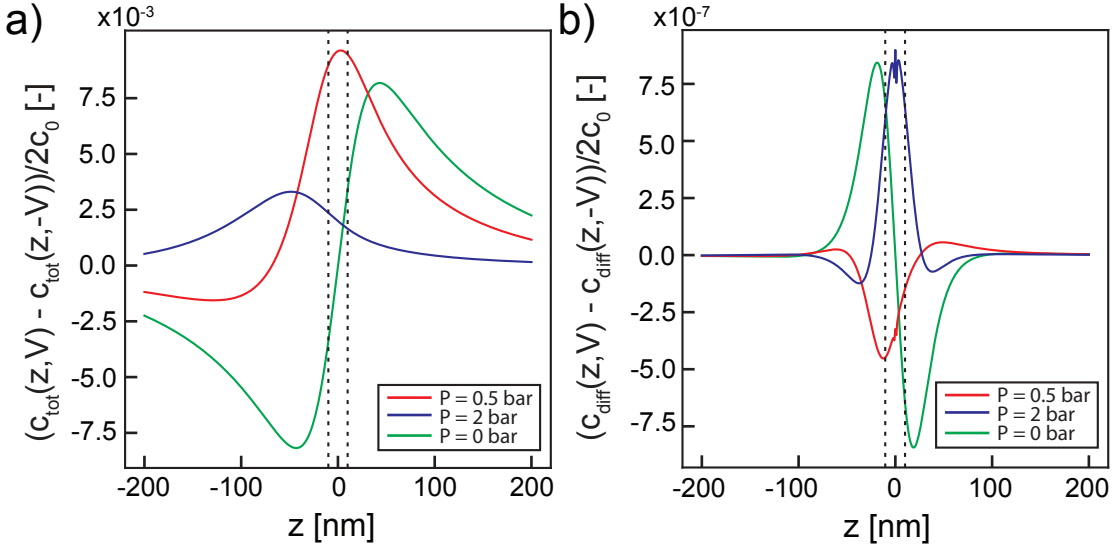


Figure 8.6 – **Spatial asymmetry in ion concentrations for positive and negative bias.** **a)** Spatial asymmetry of the total concentration normed by the reservoir concentration $2c_0$. Asymmetry is shown to be large at $P = 0.5$ bar and reduced for the large pressure of $P = 2$ bar. **b)** Similar to panel a) but for the difference in ion concentrations thus showing that both contributions to the Dukhin number are responsible for its asymmetry and through it to ionic current rectification. Figure is adapted from ref. [68]

pore, with low pressures inducing local asymmetry for both the charge density $e(c_+ - c_-)$ and the total concentration $c_+ + c_-$ which are both taken into account by the Dukhin number. For sufficiently high flow asymmetry is reduced due to complete replacement of the fluid inside the pore by bulk solution. This in turn reduces ICR for large flow values. Figure (8.5d) shows the spatial asymmetry of Dukhin number for positive and negative bias voltages $Du(z, V, P) - Du(-z, -V, P)$ at the three representative pressures $P = 0, 0.5$, and 2 bar. It is clear from this that the variation of Dukhin number comes at the pore entrance in these thin nanopores and that the asymmetry for the intermediate pressure value is the largest leading to the largest ICR.

Calculating that the effect is restricted to the pore mouth a Péclet number, which relates the importance of advection as compared to diffusion, can be used to describe the turnover of increasing to decreasing ICR. The Péclet number is defined as: $Pe = du/D$, with d the diameter of the pore, u the average fluid velocity within the pore, and D the ionic diffusion coefficient. The ionic current rectification is therefore expected to increase for $Pe > 1$ and return to $r = 1$ for $Pe \rightarrow \infty$. By approximating the fluid velocity through a nanopore under pressure as $u \approx \frac{d^2 P}{2\eta(16L + 2\pi d)}$ [386] with η the viscosity of the liquid yields $Pe \approx 7$ at $P = 0.5$ bar using experimental or FEM values for the fluid velocity.

Figure (8.6) shows the the two components contributing the the Dukhin number separately. First the asymmetry in total concentration $c_{tot} = c_+ + c_-$ due to pressure induced flow. This shows how pressure flushes bulk concentration through the pore. For intermediate pressure this skews the initially symmetric profile at $P = 0$ and induces a large asymmetry responsible in part for the ionic current rectification. However, at high pressures the bulk concentration almost completely replaces the fluid inside the pore reducing the asymmetry. The second contribution shown is that of the difference in concentration $c_{diff} = \langle c_+ - c_- \rangle$. In this case the same asymmetry is seen with a larger effect at intermediate pressure values.

8.4 DC pressure dependent measurements and FEM extensions

The power of the AC method shown in the sections above lies in the possibility to completely decouple the linear and non-linear contributions to conductance. By using DC methods standard to the field this deconvolution is not possible as all contributions are present at once. To illustrate this the following section shows DC pressure dependent measurements on the perfectly filled symmetric nanopores discussed above. These are acquired by applying a constant DC bias voltage and performing a pressure sweep.

In this case all contributions discussed previously will be present: the elastic contribution of the strained pore, the rectification behaviour with pressure, and finally the streaming current (figure (8.4d)). Figure (8.7) a) and b) shows the measured DC pressure sweep for one pore at pH 8 and at pH 3 respectively. In this case the pH 8 curve is highly non trivial seeing as it is asymmetric in voltage and non linear with pressure due to both the elastic and rectification behaviour. However, at pH 3 all surface charge effects such as streaming and rectification die out and the only remaining contribution is the strain induced enlargement of the pore. This is confirmed by the measurement that matches the strain induced behaviour previously presented.

The FEM model discussed with respect to the behaviour of rectification with pressure also allows to reproduce the DC pressure sweep data. Indeed, the model contains all the necessary physical phenomena apart from the pore enlargement. This can easily be added in post processing by adding a factor $I_e = aP^{2/3}$ to the current (in this case any residual stress effects are neglected and the constant used is $a = 10^{-3}$). By doing this curves on figure (8.7c) can be obtained that show the same qualitative behaviour as the full curves of panel a). Thus the FEM model obtains good qualitative agreement with measured DC curves when strain induced enlargement is taken into account.

The total conductance being measured at DC voltages is given by: $G_{\text{tot}} = G_1(P) + G_2(P)V + H_S(P)$. It is possible to measure each of these separately with the lock-in amplifier, $G_1(P)$ and $G_2(P)$ and streaming current measurements $H_S(P)$. In this way the whole DC curve can be reconstructed by the single contributions. A reconstructed curve as well as the corresponding DC data is shown on figure (8.7d). This acts as a final proof that the AC approach discussed above is equivalent to standard DC measurements with the added benefit of being able to separate and quantify each individual contribution to the nanopore conductance with high precision. This allows an unprecedented level of detail to be obtained on the behaviour of symmetric silicon nitride pores under pressure.

While the experiments discussed in this chapter are precise the throughput of obtaining perfectly filled pores that allow the all the quantities discussed above to be quantified is relatively low. Five such pores were obtained and their data is shown above. However, a total sample number nearing forty pores was used in order to obtain this data. While all pores do show glimpses of the discussed behaviour, wetting and contamination effects limit the ability to obtain precise data sets over the whole pressure, voltage, and pH range. Indeed, it is not necessary to have contamination effects of the magnitude discussed in the previous chapter ($\approx 10\%$ changes in rectification or resistance) but even small changes on the order of 1% can mask the observed behaviour. Considering this the FEM model was used as a quick verification of some of the expected behaviours when changing salt concentration or pore size.

As broached above, diminishing salt concentration enhances effects due to surface charge (see introduction for relevant length scale scaling) leading to much higher effects of ionic current rectification with pressure. Figure (8.8a) shows how reducing the salt concentration to 10 mM KCl increases the magnitude of the induced ICR by ten times. This can be qualitatively explained by the fact that the

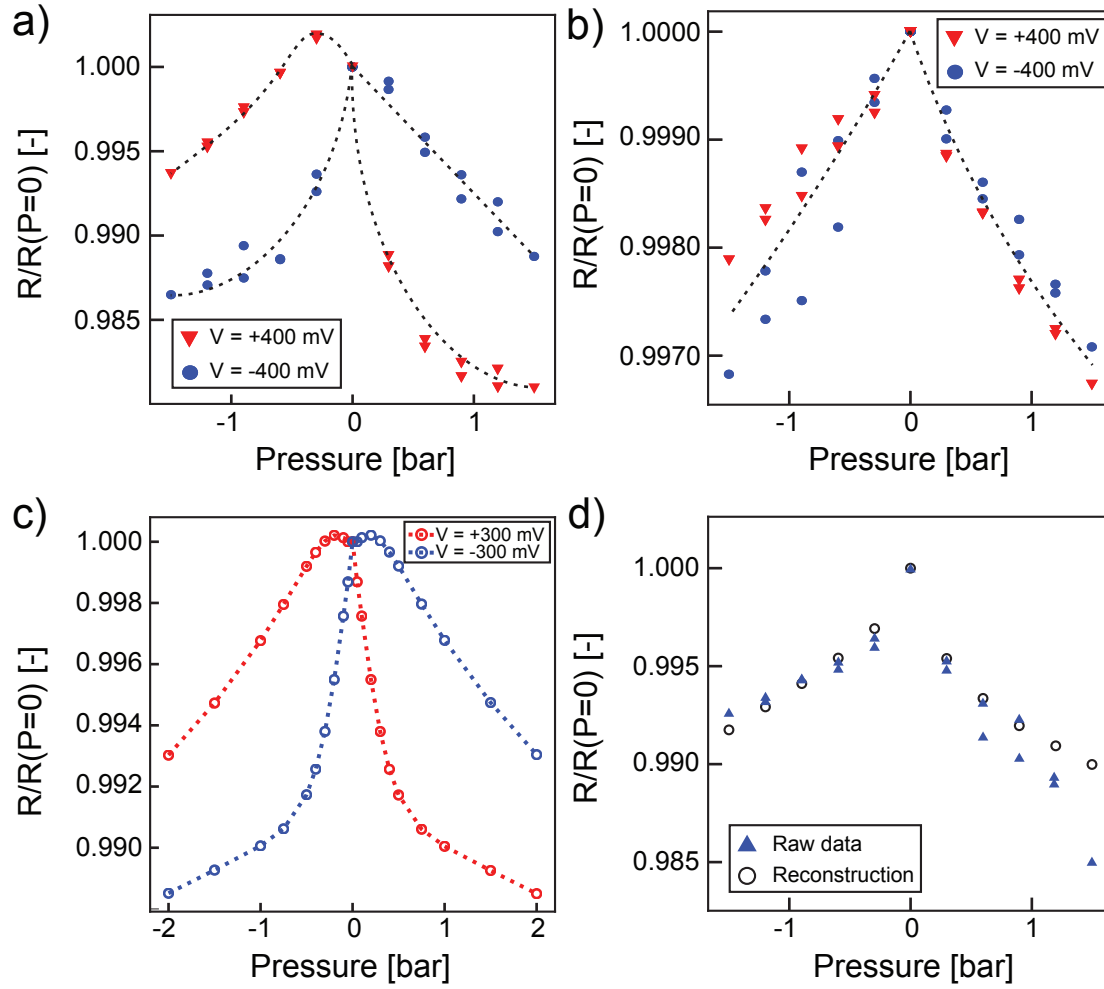


Figure 8.7 – DC pressure curves: merging phenomena. **a)** DC pressure sweep for the same pore under $V_{DC} = +400$ mV (red triangles) and $V_{DC} = -400$ mV (blue circles) at pH 8. Here a superposition of the elastic effect, rectification effect, and streaming is present leading to asymmetric and non-linear curves. Dashed black lines are a guide to the eye. **b)** DC pressure sweep for the same pore under $V_{DC} = +400$ mV (red triangles) and $V_{DC} = -400$ mV (blue circles) at pH 3. In this case due to pH reducing all surface charge effects no rectification or streaming behaviour is present. This shows that the behaviour collapses to the pure elastic behaviour described previously. Dashed black lines are a guide to the eye. **c)** DC pressure behaviour extracted from the COMSOL model. In this case since no elastic enlargement of the pore is present a current is added in post processing that is proportional to $\propto P^{2/3}$. However, despite this the qualitative behaviour is similar to the case in panel a). **d)** DC pressure sweep in blue and reconstructed pressure sweep taking information from streaming current measurements, as well as both first and second harmonic AC current. This allows to combine the elastic behaviour, rectification behaviour, and streaming behaviour showing how the AC method is equivalent to the DC method when the separate contributions are summed.

Debye length of the system scales as the root of concentration (equation (1.2)). Therefore a 100 fold decrease in concentration yields a 10 fold increase in Debye length. Regarding pore size variations, results from literature predict that diminishing the pore size will reduce the decrease in ICR observed in large pores due to decreasing fluid flow through the pore[231]. Panel b) of the same figure shows

8.5. Pressure phenomena in aqueous solutions: Conclusions

simulations for a larger 160 nm pore and a smaller 30 nm pore. In this case the ionic current rectification is plotted versus the dimensionless Péclet number introduced above. The Péclet number takes into account the average fluid velocity induced by the pressure and therefore accounts for the changes in pore size. While the magnitude of the induced ICR changes with pore size all the turnover points are in the same range of $Pe \approx 10$ confirming that fluid flow through the pore is the major driver of ICR modulation. This also explains why no reduction in ICR was previously seen in small pores. Indeed the maximal pressure used by Lan et. al.[231] is ≈ 0.2 bar. At this pressure the Péclet number achieved is far smaller than what is necessary to observe the reduction in ICR shown here (the transition point for the 30 nm pore corresponds to $P = 10$ bar).

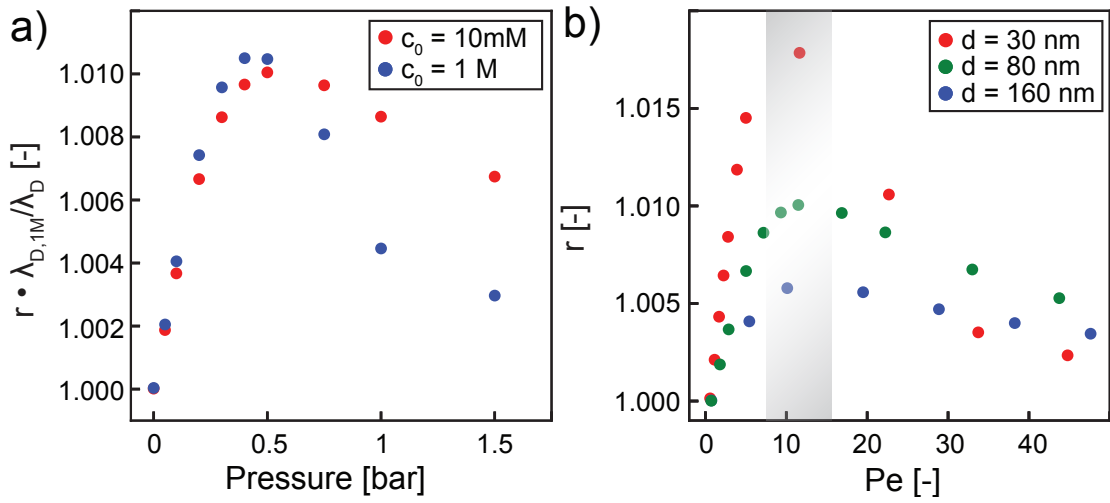


Figure 8.8 – Effects of varying salt concentration and pore size for ICR pressure behaviour. **a)** FEM simulations showing ionic current rectification as a function of pressure for 1 M KCl as compared to 10 mM KCl. The rectification value is normed by the Debye length showing that the enhanced effect for low concentration scales as λ_D . **b)** FEM simulations with three different pore sizes showing the rectification as a function of the Péclet number. The velocity for the Péclet number is extracted as the velocity at the center of the pore for each pressure value. This shows that the Péclet number controls the turnover point between the increasing rectification and decreasing rectification regime. The turnover happens at $Pe \approx 10$ for all pore sizes, illustrated by the shaded area.

8.5 Pressure phenomena in aqueous solutions: Conclusions

The nanopore system coupled to hydrostatic pressure shows the possibility of measuring strain induced pore enlargement thanks to AC conductance measurements. This is the first time such mechano-sensitivity has been measured in the conductance of silicon nitride based nanopores. These nanopores are the standard in the field and the calibration of their response to pressure is a crucial first step in experimentally measuring the high mechano sensitivity of quasi-2D pores that has, up till now, only been theoretically predicted[64; 375; 376; 377; 378]. This mechano-sensitivity could be put to use for osmotic power generation or desalination applications as it will have an influence on the ion selectivity of such small pores. The measurement of strain induced enlargement of shown here is a stepping stone towards successfully achieving these measurements by first understanding in great detail the response of the silicon nitride substrate to pressure.

In addition to strain induced enlargement, pressure induced flow in symmetric nanopores has been shown to not only reduce rectification, but in the low pressure regime, is responsible for an increase in rectification. This behaviour seems to be in contrast to what has been shown previously in conical pores[230; 231; 232]. Applying the precision given by this method to such pores would be of interest to elucidate the small pressure regime there. Such an effect of pressure controlled rectification could be utilised to tune the response of nanofluidic diodes and create new nanofluidic devices.

8.6 Applying hydrostatic pressure to room-temperature ionic liquid filled pores

Having shown in the previous chapters that the nanopore setup combined with a hydrostatic pressure is robust in discriminating between filled and unfilled pores as well as being able to measure with unprecedented accuracy effects due to gradients of pressure this setup can now be used to probe room-temperature ionic liquids. This will allow a level of control that was absent in previous chapters (chap (6)) as both the issues of irreproducible geometry and lack of control variables are remedied.

8.6.1 First measurements of pressure dependent phenomena in non-aqueous electrolyte

In order to measure RTIL in similar circumstances to what was previously achieved temperature control of the pressure coupled chamber was implemented. Two additional copper pieces can be inserted into the pressure chamber so as to deliver heat as close as possible to the chip and pore area. This is seen in figure (8.9) on which is also pointed out a small channel whose end is separated from the chip by only a 2 mm thick PEEK wall. This allows a thermocouple coated in thermal paste and inserted inside the channel to read the temperature of the sample accurately.

The chamber with both copper plates is then assembled sandwiched by two Peltier elements that are used for heating/cooling the sample in a range of -10°C to 70°C , the same range as previously used. This will allow new measurements with RTIL to be compared to the results from chapter (6) as a control for their temperature behaviour. This sandwich is then additionally placed between two liquid cooling blocks as seen in figure (8.9b). The whole temperature control system is placed inside a Faraday cage comparable to the one used for previous measurements in this chapter. The difference being the inputs of a thermocouple, the driving current wires of the Peltier elements, and the water cooling tubes. An example of the temperature control capabilities are shown on panel c) of the same figure. The temperature control system is controlled by a custom LabView program and allows settling to within 0.1% of the target temperature within ≈ 5 min.

The second difference is that due to chemical compatibility the use of a degassing hose is impossible with RTIL. RTIL are properly degassed as well as dried to ensure any water contamination present in the sample is removed. To do so RTIL are stored overnight in a heated Schlenk flask (90°C) while stirring under vacuum. Schlenk flasks are used to store, handle, and dry ionic liquids prior to experiments. To ensure proper wetting of the membrane the chip is then placed in a droplet of previously degassed RTIL under vacuum for 30 min before assembling and filling the chamber. The chamber is filled by connecting the shut-off valves to a luer-lock syringe filled with degassed RTIL. Controlled filling is ensured with little to no contact between the RTIL sample and ambient conditions.

8.6. Applying hydrostatic pressure to room-temperature ionic liquid filled pores

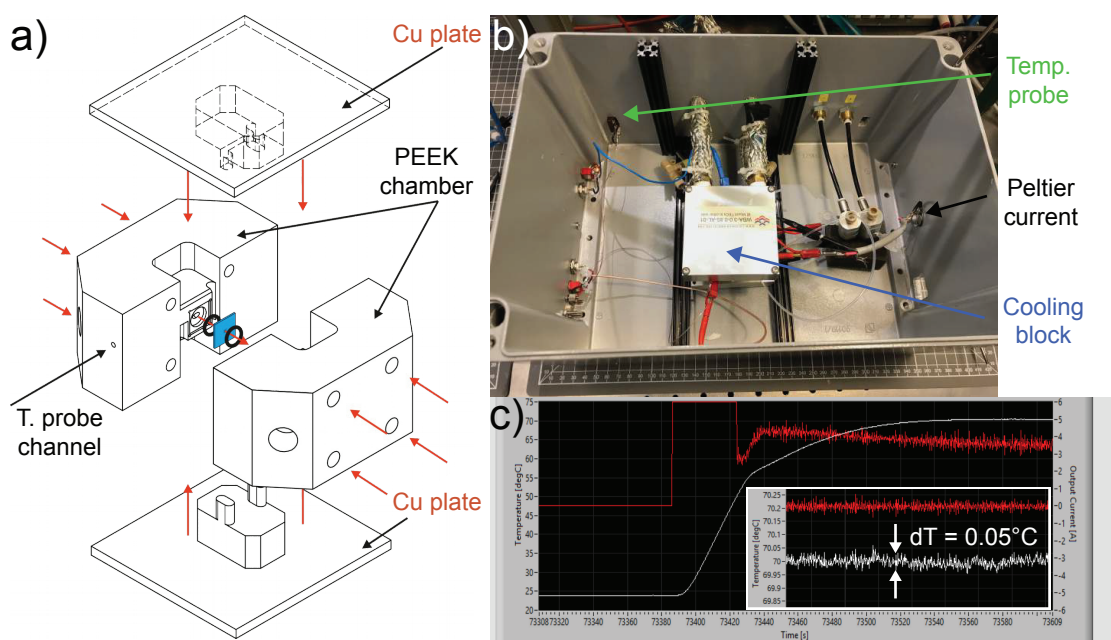


Figure 8.9 – **Pressure application setup for use with RTIL.** **a)** Liquid tight sample chamber with focus on temperature control aspects. Two copper pieces are added for good thermal contact. Arrow shows the temperature probe channel that allows the temperature measurement to take place as close as possible to the chip. **b)** Photograph of the temperature control sample chamber mounted inside the Faraday cage. Peltier elements are powered by the cables (black arrow). Liquid cooling blocks (blue arrow) allow correct cooling of the peltier elements. Green arrow shows the temperature probe input into the Faraday cage. **c)** Example of temperature settling using the experimental setup shown on panel b). The temperature is stable within 0.05°C. Settling time is approximately 4 minutes.

Once mounted, filled, and installed within the temperature control sandwich, the sample is left under compression for 5 min to remove any possible gas bubbles still present on the membrane. After this measurements can take place. First a set of measurements: IV curve, AC pressure sweeps both in compression and gradient, and streaming are performed at room temperature. Depending on the bulk resistivity of the ionic liquid, which can be as much as 100 times that of 1 M KCl solution at RT, it can be challenging to discern if the sample is correctly filled. Considering this the sample is then raised to the maximum temperature of 70°C at which the RTIL is much less resistive, for example for bmim PF6 this increase in conductance is ≈ 100 times. This allows the best measurements of the sample properties, especially when considering flow dependent variables such as streaming current. Once the highest temperature measurements are performed a sweep of temperature by steps is made until reaching the lowest achievable temperature of the system (between -10°C and -20°C). At this low temperature the glassy behaviour of the RTIL conspires against precise measurements as the conductivity is so low as to sometimes be unmeasurable within the error. Despite these limitations the following sections describe initial pressure dependent measurements of ionic liquids in confinement.

8.6.2 Resistance of room-temperature ionic liquids in silicon nitride nanopore confinement

First ionic liquids temperature dependent resistance is measured similarly as to what is done in chapter (6). In this case the resistance can be measured both with the AC signal and DC IV curves. Figure (8.10a) shows DC IV curves taken throughout the temperature range. This is equivalent to the behaviour shown on panel b) where frequency sweeps at a given AC voltage bias are shown. Both these measures show the expected trend of higher resistance with lower temperature. From the frequency sweeps it is clear that also that the working range of frequency becomes smaller the higher the resistance due to capacitive and resistive leakage[356]. This shows one of the largest setbacks of using silicon nitride based nanopores as opposed to the glass nanocapillaries previously presented for these studies. Indeed, for smaller pores than the chosen 80 nm silicon nitride pore the resistance will become so large that chip leakage will start to dominate the signal thus reducing the measuring range even at high temperature. Despite this the temperature behaviour can be extracted from these measurements and is equivalent to the glassy dynamics obtained previously thus confirming the equivalence of the measurements (8.10).

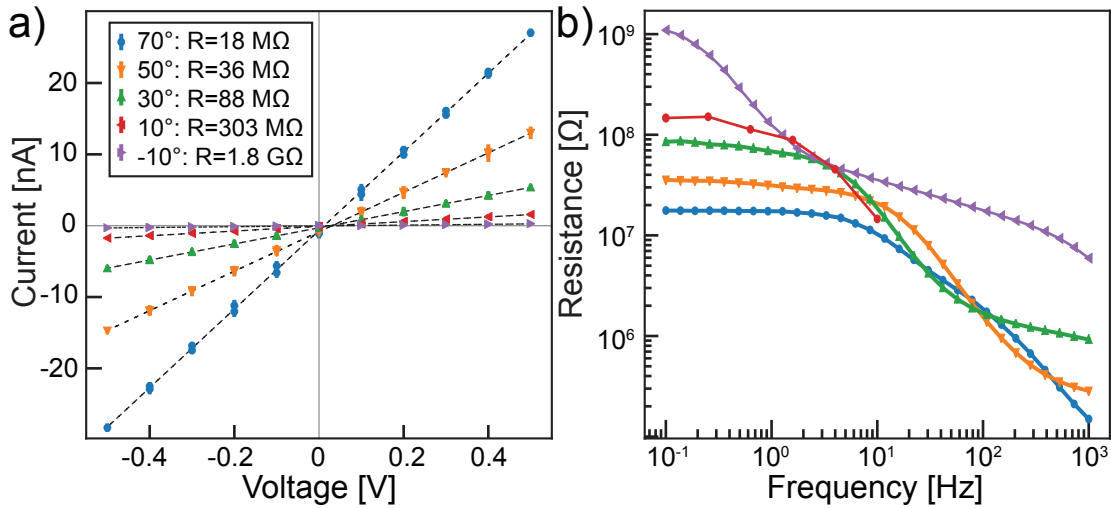


Figure 8.10 – **Temperature dependent resistance of RTIL in silicon nitride pores.** **a)** DC IV curves obtained for a bmim PF6 filled 80 nm pore at different temperatures. The glassy dynamics previously presented yield drastic changes in resistance as the temperature decreases. **b)** AC frequency sweep of the same pore on panel a) at different temperatures (legend is the same as panel a)). It is clear that at the lowest temperature of -10°C the chip leakage starts to dominate the signal even at the relatively low frequency of 1 Hz used for AC measurements. This shows how silicon nitride nanopore higher capacitance and resistive leakages[356] as compared to glass nanocapillaries induces measurement difficulties.

Considering the previous section on elastic contributions of membranes it is also of interest to measure the AC pressure sweep as described previously. In the case of RTIL it was even harder to obtain the perfectly filled pores needed to see such small effects. However, this was achieved in a handful of pores and no dependence of the resistance or the rectification is shown. Figure (8.11) shows a flat response within the error of the measurement in all three measured variables: resistance R , capacitance C , and ionic current rectification r . The flat trace in capacitance is not unexpected as capacitance is shown to fluctuate only when air bubbles on the membrane are present (chapter (7)). Concerning the resistance it is not clear as to why the strain induced enlargement is not present in this curve. However, few

8.6. Applying hydrostatic pressure to room-temperature ionic liquid filled pores

samples filled with RTIL showed perfect traces such as the ones previously presented for aqueous solutions. It could be that noise in the sample due to contamination or wetting was too large to measure the small variations in resistance. However, samples showed streaming currents and IV characteristics stable over hours.

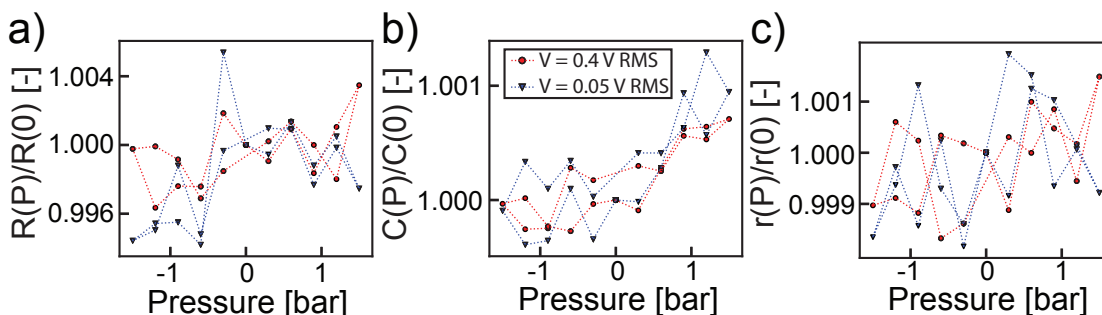


Figure 8.11 – **Pressure dependent characteristics of RTIL filled pores.** **a)** Pressure dependent resistance of an RTIL filled nanopore at 23°. An 80 nm pore is filled with bmim TFSI and protocols similar to those in the previous chapter are conducted. Here the resistance is flat within experimental error in the whole pressure range. The base resistance value was $R = 41 \text{ M}\Omega$. **b)** Capacitance measured simultaneously to the data on panel a). Capacitance also remains flat as expected since previous measurements of capacitance fluctuation have always been tied to wetting artifacts in solid state pores. **c)** Ionic current rectification as a function of pressure extracted simultaneously to data on panels a) and b). Rectification does not show the behaviour described above for aqueous salt solutions. This is postulated to be due to the much higher viscosity of RTIL samples that are from 30-100 times that of water and would thus inhibit any of the small flow effects discussed in previous sections.

The lack of a pressure dependence on the ionic current rectification is explained by the fact that the mechanism behind both the creation, and reduction of ICR described previously is flow dependent (i.e. Péclet number dependent as shown on figure (8.8)). The Péclet number depends on the viscosity η of the solution via the fluid velocity u [386]. Considering that ionic liquids are 30-100 times more viscous than aqueous solutions the pressure needed to induce the same level of ICR modulation as presented for aqueous solutions far exceeds the capabilities of the setup. However, by changing the pore size and length (shorter wider pore), and by increasing the temperature where RTIL become less viscous, this regime may be attainable with the pressure magnitude available. This is of course in the assumption that the ionic liquid system is comparable to the low Dukhin length condition of high salt concentration and large pore as previously described. If large surface effects were to be present an effect in the rectification factor under pressure is expected to be seen (f.ex ten fold increase for 1 mM KCl).

8.6.3 Zeta potential of room-temperature ionic liquids in nanopore confinement

Following the confirmation that the silicon nitride system is equivalent to the glass nanocapillary system previously described zeta potential measurements can be performed. As previously described RTIL do not conform to standard Debye-Hückel models of the screening length. This in conjuncture with their propensity to show ordering at surfaces makes the description of their zeta potential interesting. The flat rectification response shown above does give some qualitative insight into the surface behaviour of RTIL. However, thanks to the pressure nanopore setup it is possible to directly measure streaming currents in the nanopore system allowing for quantitative measurements of the zeta potential in confinement.

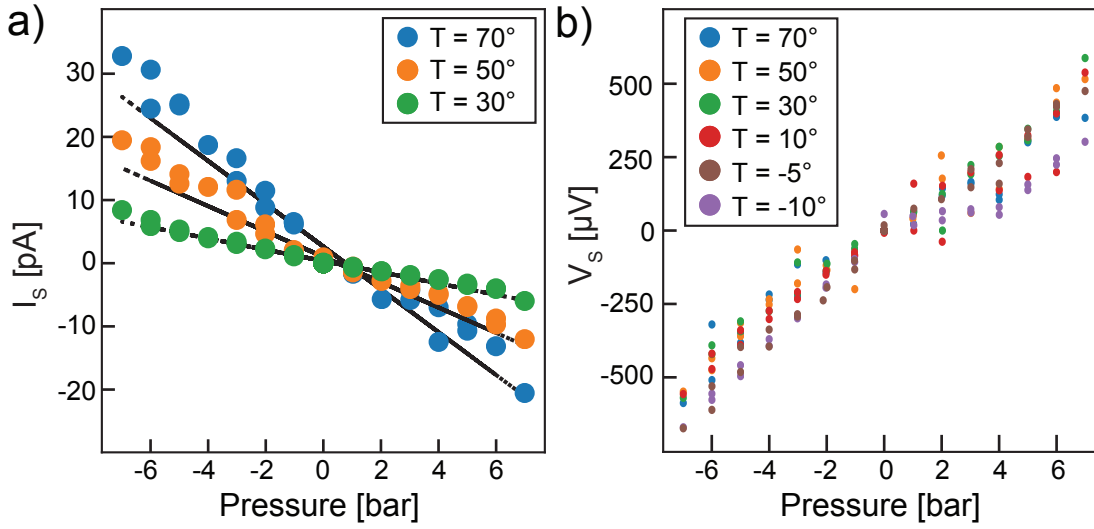


Figure 8.12 – **Streaming measurements of RTIL confined in single pores.** **a)** Streaming current for an 80 nm pore filled with bmim PF6 at different temperatures (same pore as figure (8.10)). Even at the relatively high temperature of 30°C the streaming current level at 7 bar is less than 10 pA. This shows the difficulty of measuring streaming current at large pores at low temperatures due to the increased viscosity of RTIL. **b)** Streaming potential measured with a electrometer grade pre-amplifier (input impedance $\approx 30 \text{ T}\Omega$) for the same pore as in panel a). When measuring streaming potential the signal level is almost independent of temperature due to the Walden rule for bmim PF6. This is confirmed as very little variation in streaming potential is seen, within the experimental error, over the whole temperature range.

The streaming current and potential are shown to be linear within the error in the whole range of pressure studied. This means that within the error of the experiment no corrections are necessary to equations (1.5) to consider the short length of the nanopore as compared to the modelled long circular capillary. The temperature behaviour of the streaming current depends on the viscosity of the solution η . Considering the large changes in the viscosity of RTIL with temperature the streaming current is therefore expected to dramatically decrease with lower temperatures. This is clearly seen on of figure (8.12a). However, the temperature dependence of the streaming potential is more conducive to measurements. Indeed, it only depends on the bulk viscosity and conductivity. This can be simplified by the Walden rule established in a previous chapter of the form $\sigma \propto \eta^{0.9}$. Considering that the viscosity and conductivity of RTIL will depend inversely on temperature (i.e. more conductive at high temperature but less viscous) this entails that the streaming potential should be quasi independent of temperature. This is confirmed within experimental error on panel b) of the same figure.

Despite the first measurements of RTIL streaming described in this section the precision of the streaming current measurement is low when going to low temperatures where the higher resistivity of the sample prohibits measurements. Considering this is a large factor despite the relatively large size of pores $d = 80 \text{ nm}$, it will negate any possible measurements in the range where a transition to a frozen state is expected $d \approx 20 \text{ nm}$. While streaming potential is quasi independent on the temperature a high level of accuracy is required to measure any changes in the zeta potential due to structural effects of smaller confining pores. In order to remedy these issues and retain an accurate comparison of both streaming current and potential in small pores square arrays of nanopores are used. The following section describes the first results obtained with such samples.

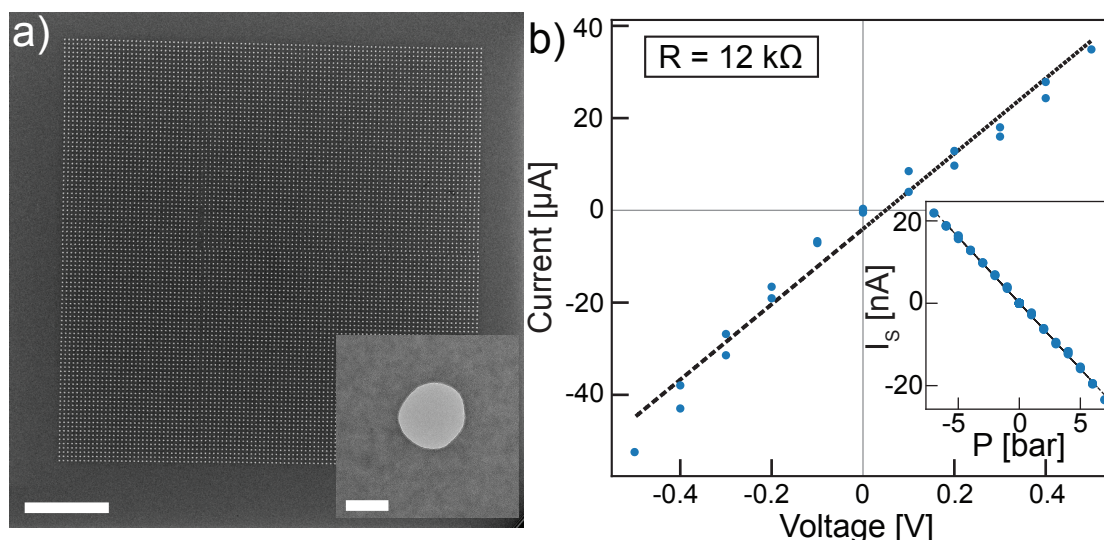


Figure 8.13 – **Signal increase in square nanopore arrays.** **a)** TEM micrographs of square nanopore arrays. Large field view shows the 100x100 array of pores on usual 20 nm thick silicon nitride membrane of side length $a = 30 \mu\text{m}$. Inset shows a close up view of one of the pores showing good shapes. Scale bar on the main image is $5 \mu\text{m}$ and for the inset is 50 nm. TEM micrographs and array fabrication courtesy of A. Chernev. **b)** DC IV curve of an array such as on panel a) in 1 M KCl. The resistance extracted from a linear fit is $R = 12 \text{ k}\Omega$ which is ≈ 100 times smaller than a single RIE hole resistance (1.2 M Ω). Inset shows the streaming current for the same sample as the main image. In this case the streaming current is also enhanced by a factor of ≈ 100 . Both the streaming current and ionic current thus confirm the \sqrt{N} scaling for square arrays of pores.[387]

8.6.4 Arrays of nanopores for signal to noise enhancement in streaming measurements

As discussed above single pore measurements while impactful and showing novel measurements of streaming potential and current, are limited by the high resistance of RTIL as well as the leakage of solid state nanopores. In this case arrays of nanopores are a possible solution. Indeed, they are easily fabricated following the usual procedure but changing the electron beam patterning process to expose an array of apertures instead of a single one. The following section describe first the confirmation that arrays of pores increase the signal to noise as expected from literature using aqueous solutions. This is followed by experiments with RTIL in nanopore arrays showing the plausibility of the approach.

The nanopore arrays are imaged via transmission electron microscopy in order to confirm uniformity in size of pores as well as the fact that all pores are opened during the etching process. Micrographs of nanopore arrays can be seen on figure (8.13a) showing a 100x100 square array of nanopores. Previous work has studied the effect of arrays on the measured conductance and found that a non-linear scaling of conductivity arises with arrays of pores. For a square array the current is seen to scale as \sqrt{N} where N is the total number of pores[387]. This sub-additive scaling is due to the access resistance term in the conductance equation (1.1). Indeed, these access terms are linked to the capacitance of the access region, assume to be a disk, and are responsible for the sub-linear response of array conductance. Panel b) of the same figure shows this scaling measured in 1 M KCl solution confirming that the majority of pores within the nanopore array are wet.

Having verified that the fabricated nanopore arrays behave as expected with aqueous solutions they are

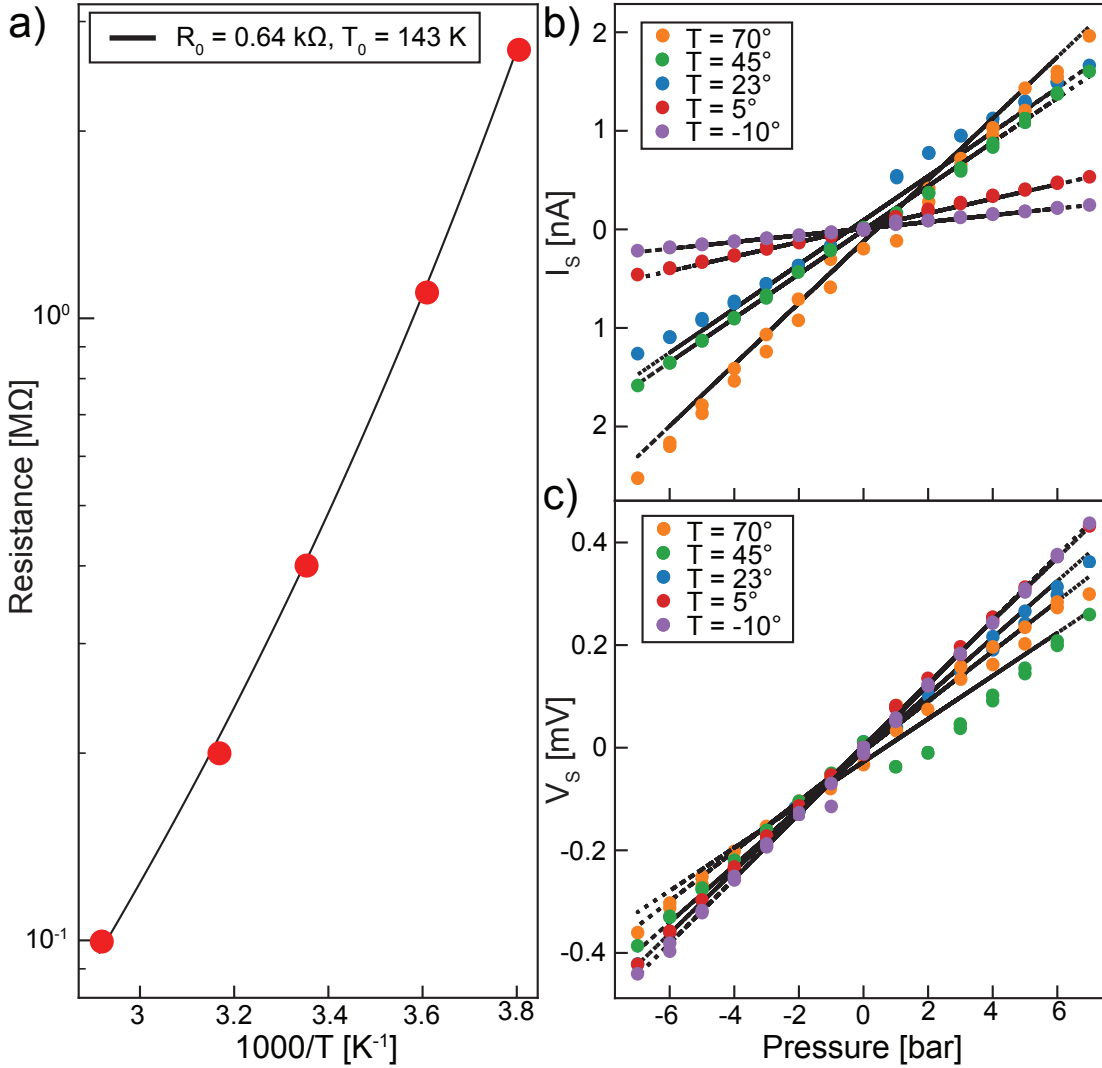


Figure 8.14 – **Nanopore arrays filled with RTIL.** **a)** Resistance as a function of temperature for a 100x100 square array of nanopores filled with bmim TFSI. Solid line shows the fit to the VFT formula (equation (6.2)) from which the values $R_0 = 0.64$ kΩ and $T_0 = 134$ K are extracted. **b)** Streaming current for different temperatures for the array of pores in panel a). While streaming current diminishes with decreasing temperature the signal level is still large enough to measure even at -10°C . **c)** Streaming potential measured at different temperatures for the same sample as on panels a) and b). The streaming potential shows a slight trend for higher streaming at lower temperatures however the error in this measurement is relatively high and no further analysis is made.

then filled with RTIL as an attempt to solve the low signal to noise for highly resistive samples. Bmim TFSI is used as the ionic liquid in this case and figure (8.14) shows the measured resistance, streaming current, and streaming potential for varying temperatures. The resistance is seen to behave with the same glassy dynamics as shown previously. However, due to the increase in conduction using an array the effective resistance R_0 is much smaller than with single pores.

Thanks to the increase in signal due to the use of an array of nanopores the streaming current is measurable down to the lower limit of the temperature control. Streaming potential in this case

does show a slight trend for lower streaming potential at higher temperatures. However, this is a measurement performed on a single chip, and the precision of these experiments is still not perfect. Taking this into account no detailed analysis of this is made. However, future measurements of ionic liquids in nanopore arrays could show effects in streaming potential and current due to their large signal to noise, even at low temperatures.

8.7 Conclusions

This section has shown how the pressure application setup can be used with RTIL to grant access to new observables such as streaming current and potential. While no freezing transitions have yet been observed in silicon nitride pores when considering the conductance alone, streaming measurements allow another angle of attack in breaking down the complex behaviour of RTIL in confinement. First studies of ionic liquid streaming characteristics will allow the quantification of zeta potential, a key variable in surface ionic structure and how this may be modulated in different conditions.

Situations of interest obviously include confinement in order to elucidate the details of a freezing transition[297] but also include how dilutions of ionic liquids behave as has been previously explored with surface force apparatus[292]. Preliminary data on pressure modulated ionic current rectification also show that RTIL due to their high viscosity seem to inhibit the coupling of flow and electrical effects. This could be used to probe their electrical behaviour which is seen to be similar to dilute electrolyte with large screening lengths.

This setup is not however limited to ionic liquids and the in depth study of aqueous solutions, mixtures, or gradients may yield additional interesting results. For example salt gradients are key to both desalination and osmotic power generation and fundamental understanding of pressure induced effects when combined with osmotic pressure could be extracted.

9 General conclusions and outlook

9.1 General conclusions

9.1.1 Conclusions: Controlled translocations

In the first part of the thesis I describe a combination of the nanopore system with optical tweezers. I show how this technique is used to allow the control of DNA translocations in different experimental configurations. First DNA-protein complexes are probed in glass nanocapillaries showing that such a combination allows both the force and current detection of proteins[66]. Taking into account the tension of DNA during the controlled translocation allows to correct for shifts in the detected protein position thus yielding a precise method for localisation of DNA-protein complexes within ± 50 nm. In addition to localisation both force and current signals are shown to allow discrimination of DNA bound proteins based on charge and size. The force signal is key as it does not depend highly on the pore size and thus offers high signal to noise where current measurements could not.

After having shown the power of the optical tweezers and nanopore experiment with DNA-protein complex I show measurements of taut DNA retraction. This is measured with the goal of further explaining the elastic behaviour of DNA during the capture event of free translocations. The optical tweezer laser detection allows a 50 fold increase in time resolution as compared to previous works[62] and thus allows the extraction of the taut DNA force-time relaxation power law behaviour. However, electroosmotic flow in glass nanocapillaries[79] is postulated to be the main barrier to further progress into more complex experiments related to DNA confirmation during translocation. To correct this I explore a method for reducing electroosmotic flow in nanocapillaries via polymer surface coating[137]. A family of PDMA based polymers are used and their coating efficiency is measured via several observables. First the amount of ionic current rectification is observed as a proxy for electroosmotic flow[226], second the time distribution of free DNA translocations is used[248; 249], and finally threading forces in optical tweezers experiments are performed[83; 140]. All these measures point to no significant reduction of electroosmotic flow in such coated pores. I hypothesise that this is due to inefficient coating of the inner walls of the capillary whose surface charge is responsible for the flow generation[214]. However, experiments with silicon nitride pores and free translocating proteins show how these same polymers are effective at reducing non-specific interactions between analytes and the pore wall[250].

Finally, I interface biological pores[252] and their lipid bilayer supports with nanocapillaries and the optical tweezers tool. This would allow not only to calibrate by direct force measurement the exact electrophoretic force on DNA within biological pores such as MspA, but would also be a geometrically

reproducible system with little flow effects that hampered the previous taut DNA studies. I show how optically available lipid bilayers over micron sized glass capillaries is possible and is confirmed by the correct insertion of MspA biological pores. However, the stability of such "painted" bilayers over time restricts the optical tweezers experiment and no DNA insertion events are seen. I attempted a strategy to increase bilayer stability, inspired by recent works in flat geometries[273], but it yields no increase in durability of lipid bilayers.

9.1.2 Conclusions: Confinement and nanofluidics

In the second part of the thesis I focus on the addition of hydrostatic pressure to the nanopore system with the long term goal of studying confinement and nanofluidic effects in both aqueous and RTIL solutions. First I use nanocapillaries identical to those used in the first part of the thesis to probe the transport properties of single room-temperature ionic liquid filled pores[67]. Such pores show the expected behaviour of glassy dynamics with variations in temperature. However, the extraction of the effective glass temperature shows no clear dependence with increasing confinement. I postulate that confinement effects are overshadowed by the large intrinsic spread in resistance of small capillaries[89], the possible presence of wetting issues modifying the conductance behaviour[48], and sample purity due to atmospheric humidity contamination[314; 315; 316; 317; 318].

Next I show how the development of a new setup of silicon nitride membrane nanopores combined with hydrostatic pressure application allows to solve the three hypothesised issues with RTIL filled glass capillaries. The application of pressure to such solid state pores is shown to reveal wetting effects with both DC and AC measurement methods[48]. The capacitance of the membrane is shown to be a good measure of chip wetting. I then show how artifacts due to improper wetting arise in a larger DC current noise spectrum, larger ionic current rectification, and in spurious pressure effects that can be measured both through DC IV curves and AC pressure sweeps.

Following the benchmarking of the pressure setup and the demonstration of necessary steps to ensure proper pore filling I show how hydrostatic pressure is able to induce strain enlargement of solid state pores[68]. The measurement and detailed theoretical explanation of the strain-induced enlargement of silicon nitride pores is the first step towards similar measurements in quasi-2D pores that have been predicted to show large mechano sensitivity in such configurations[64]. I then show the power of the chosen AC method with simultaneous measurement of ionic current rectification modulation by pressure in these symmetric nanopores. The fact that such behaviour may be completely decoupled via the AC method, as well as its unparalleled accuracy (below 1%) allows measurements of increases in ionic current rectification in the low pressure regime. This is in contrast to measurements in asymmetric pores that have only shown a reduction[230; 232]. Finally, I use the hydrostatic pressure setup on RTIL filled silicon nitride pores and I show the first measurements of streaming currents paving the way to better understanding ionic liquid surface interactions.

9.2 Outlook

This section will provide a sense of the future possibilities for the field of nanopores from the author's perspective[388]. As such it contains a subjective view[389] on the possible directions and will give paths for future research, taking into account the conclusions from both parts of this thesis focused on controlled translocations on the one hand and the addition of hydrostatic pressure control on the other.

The mechanical control of analyte translocation through nanopores is of importance to better understand the physical details of the translocation process in all nanopores, whether biological or solid-state. While nanocapillaries are of great utility due to their ease of fabrication[72] and attractive electrical properties such as low capacitance, they have been shown to be unreliable from a reproducibility standpoint[89]. The geometrical irreproducibility between capillaries coupled with their high electroosmotic flow blocks the measurements of the precise variables that are necessary to quantify the translocation process (chapter (4)). If a robust solution to negate electroosmotic flow in glass nanocapillaries reduces the variability in electrical properties, then its combination with optical tweezers may yield information on DNA tension and confirmation during translocations.

Another avenue moves away from solid state nanopores entirely and focuses on the biological pore setup discussed in chapter (5). Indeed, if a solution to the issue of bilayer stability is found then optical tweezer controlled translocations through pores such as MspA would be possible. These experiments would not only allow for calibration of the SPRNT technique[256] but lead to fundamental measurements of the translocation process. Solutions such as using giant unilamellar vesicles are a promising option to the standard bilayer formation method as they have previously been shown to work with glass capillaries[262]. SPRNT is of great utility for an exhaustive insight into motor protein function and kinetics, and can be applied even to emerging issues such as the measurement of novel Cov-SARS-2 helicase or RNA polymerase[390]. More fundamental probing of the translocation process thanks to such a setup would allow to shed light on the key fraction of capture and how DNA tension and force propagation are modulated by physical parameters such as voltage, salt concentration, DNA length, etc[182]. Insights into exact DNA confirmation during capture and translocation could then yield fundamental knowledge on how to slow down the translocation process. Such knowledge would be applicable to quasi-2D pores moving forward towards the possibility of sequencing in this geometry.

Concerning the addition of control parameters such as hydrostatic pressure or temperature control, there are many unsolved questions that will motivate future research avenues. Indeed, pressure combined with the nanopore setup is relatively recent and many interesting effects are present as has been shown in chapter (8)[68]. In particular, the use of pressure to provoke strain-induced enlargement of pores has potential in the osmotic power generation and desalination fields[36; 360]. High mechanosensitivity has been theoretically predicted[64; 375; 376; 377; 378] for pores made out of quasi-2D materials such as MoS₂, and first experimental verifications of this could lead to novel and mechanically tunable methods for the more efficient power extraction or salt rejection. The use of quasi-2D materials would also allow the additional exploration of non-linear effects with great accuracy especially using low salt concentrations where Debye or Dukhin length overlap is present for such small pores[24].

Applications of pressure also allow the measurement of streaming potentials that probe surface ordering[56]. In systems such as ionic liquids, these surface properties are still not well known[297; 305] and streaming measurements could be a key link in their understanding. However, signal level with these measurements is an issue due to the large resistance of ionic liquid filled pores, especially once pore size is reduced below 50 nm[67]. In this case, one solution using nanopore arrays has been attempted in this thesis. However, it is not the most satisfactory outcome. Indeed, the motivation behind the use of single pores is to eliminate any variability present with the use of porous media such as alumina porous membranes that have previously been used with these liquids[296].

Another option for solving the signal to noise ratio in streaming currents is to take inspiration from the precise AC lock-in acquisition presented for conductivity measurements. Indeed, it is possible to drive a microfluidic pump via an AC signal provided by the lock-in amplifier resulting in a sinusoidal pressure wave. This would allow the measurement of AC streaming currents. Due to the same principles that

Chapter 9. General conclusions and outlook

allow low signal detection in conduction (i.e. frequency isolation and time averaging of the signal) it would be possible to extract streaming currents below the noise level of DC measurements. This could open a whole new range of effects since it would be possible to measure with great accuracy the purely linear streaming current as well as any non-linearities present, similarly to what is done for conduction in chapter (8).

Bibliography

- [1] D Upper. The unsuccessful self-treatment of a case of "writer's block". *Journal of applied behavior analysis*, 7(3):497, 1974.
- [2] Erika N Carlson, Simine Vazire, and Thomas F Oltmanns. You probably think this paper's about you: Narcissists' perceptions of their personality and reputation., 2011.
- [3] Stephan A. Bolliger, Steffen Ross, Lars Oesterhelweg, Michael J. Thali, and Beat P. Kneubuehl. Are full or empty beer bottles sturdier and does their fracture-threshold suffice to break the human skull? *Journal of Forensic and Legal Medicine*, 16(3):138 – 142, 2009.
- [4] Thomas Purnell, William Idsardi, and John Baugh. Perceptual and phonetic experiments on american english dialect identification. *Journal of Language and Social Psychology*, 18(1):10–30, 1999.
- [5] Richard Stephens and Olly Robertson. Swearing as a response to pain: Assessing hypoalgesic effects of novel "swear" words. *Frontiers in Psychology*, 11:723, 2020.
- [6] Andrej Bauer. Five stages of accepting constructive mathematics. *Bulletin of the American Mathematical Society*, 54:481–498, 01 2017.
- [7] Garth A. Hargreaves, Lauren Monds, Nathan Gunasekaran, Bronwyn Dawson, and Iain S. McGregor. Intermittent access to beer promotes binge-like drinking in adolescent but not adult wistar rats. *Alcohol*, 43(4):305 – 314, 2009.
- [8] Manuel S. Barbeito, Charles Thompson Mathews, and Lawrence A. Taylor. Microbiological laboratory hazard of bearded men. *Applied microbiology*, 15 4:899–906, 1967.
- [9] Laura Chaddock, Mark B. Neider, Aubrey Lutz, Charles H. Hillman, and Arthur F Kramer. Role of Childhood Aerobic Fitness in Successful Street Crossing. *Medicine & Science in Sports & Exercise*, 44(4), 2012.
- [10] Gabrielle F. Principe and Eric Smith. The tooth, the whole tooth and nothing but the tooth: how belief in the tooth fairy can engender false memories. *Applied Cognitive Psychology*, 22(5):625–642, 2008.
- [11] Susan Hatters Friedman and Ryan CW Hall. Using star wars' supporting characters to teach about psychopathology. *Australasian Psychiatry*, 23(4):432–434, 2015.
- [12] Gregor W. Smith. Japan's phillips curve looks like japan. *Journal of Money, Credit and Banking*, 40(6):1325–1326, 2008.
- [13] Andrew A. Skolnick. Is It Ig Nobler for Science to Suffer the Slings and Arrows of Outrageous Foolery? *JAMA*, 279(13):979–981, 1998.
- [14] Erle Lim, Poppy Pomfrey, Amy Quek, and Raymond Seet. Interesting in- and outpatient attendances at hogwarts infirmary and st mungo's hospital for magical maladies. *Annals of the Academy of Medicine, Singapore*, 35:127–9, 2006.
- [15] R. Feynman. There's plenty of room at the bottom. *Engineering and Science*, 23:22–36, 1960.

Bibliography

- [16] G. Binnig, H. Rohrer, Ch. Gerber, and E. Weibel. Tunneling through a controllable vacuum gap. *Applied Physics Letters*, 40(2):178–180, 1982.
- [17] Sander J Tans, Alwin R M Verschueren, and Cees Dekker. Room-temperature transistor based on a single carbon nanotube. *Nature*, 393(6680):49–52, 1998.
- [18] A. Ashkin, J. M. Dziedzic, J. E. Bjorkholm, and Steven Chu. Observation of a single-beam gradient force optical trap for dielectric particles. *Opt. Lett.*, 11(5):288–290, 1986.
- [19] G. Binnig, C. F. Quate, and Ch. Gerber. Atomic force microscope. *Phys. Rev. Lett.*, 56:930–933, 1986.
- [20] D M Eigler and E K Schweizer. Positioning single atoms with a scanning tunnelling microscope. *Nature*, 344(6266):524–526, 1990.
- [21] Xiaoyou Xu, Robert Ray, Yunlong Gu, Harry J. Ploehn, Latha Gearheart, Kyle Raker, and Walter A. Scrivens. Electrophoretic analysis and purification of fluorescent single-walled carbon nanotube fragments. *Journal of the American Chemical Society*, 126(40):12736–12737, 2004.
- [22] K. S. Novoselov, A. K. Geim, S. V. Morozov, D. Jiang, Y. Zhang, S. V. Dubonos, I. V. Grigorieva, and A. A. Firsov. Electric field effect in atomically thin carbon films. *Science*, 306(5696):666–669, 2004.
- [23] Klaus D. Sattler, editor. *1 Handbook of Nanophysics*. CRC Press, 2010.
- [24] Lydéric Bocquet and Elisabeth Charlaix. Nanofluidics, from bulk to interfaces. *Chem. Soc. Rev.*, 39:1073–1095, 2010.
- [25] Royce W. Murray. Nanoelectrochemistry: Metal nanoparticles, nanoelectrodes, and nanopores. *Chemical Reviews*, 108(7):2688–2720, 2008.
- [26] A.A. Shanenko, M.D. Croitoru, and F.M. Peeters. Nanoscale superconductivity: Nanowires and nanofilms. *Physica C: Superconductivity and its Applications*, 468(7):593 – 598, 2008. Proceedings of the Fifth International Conference on Vortex Matter in Nanostructured Superconductors.
- [27] Volkmar Weissig, Tracy K Pettinger, and Nicole Murdock. Nanopharmaceuticals (part 1): products on the market. *International journal of nanomedicine*, 9:4357–4373, 2014.
- [28] Calum Kinnear, Thomas L. Moore, Laura Rodriguez-Lorenzo, Barbara Rothen-Rutishauser, and Alke Petri-Fink. Form follows function: Nanoparticle shape and its implications for nanomedicine. *Chemical Reviews*, 117(17):11476–11521, 2017.
- [29] Silvia Pujals and Lorenzo Albertazzi. Super-resolution microscopy for nanomedicine research. *ACS Nano*, 13(9):9707–9712, 2019.
- [30] Vinit Kumar, Stefano Palazzolo, Samer Bayda, Giuseppe Corona, Giuseppe Toffoli, and Flavio Rizzolio. DNA Nanotechnology for Cancer Therapy. *Theranostics*, 6(5):710–725, 2016.
- [31] Margaret Morash, Hannah Mitchell, Himisha Beltran, Olivier Elemento, and Jyotishman Pathak. The Role of Next-Generation Sequencing in Precision Medicine: A Review of Outcomes in Oncology. *Journal of personalized medicine*, 8(3):30, 2018.
- [32] Elizabeth A Manrao, Ian M Derrington, Andrew H Laszlo, Kyle W Langford, Matthew K Hopper, Nathaniel Gillgren, Mikhail Pavlenok, Michael Niederweis, and Jens H Gundlach. Reading DNA at single-nucleotide resolution with a mutant MspA nanopore and phi29 DNA polymerase. *Nature Biotechnology*, 30(4):349–353, 2012.
- [33] L J Steinbock, S Krishnan, R D Bulushev, S Borgeaud, M Blokesch, L Feletti, and A Radenovic. Probing the size of proteins with glass nanopores. *Nanoscale*, 6(23):14380–14387, 2014.
- [34] Jay R. Werber, Chinedum O. Osuji, and Menachem Elimelech. Materials for next-generation desalination and water purification membranes. *Nature Reviews Materials*, 1(5):16018, 2016.
- [35] Z. Siwy and A. Fuliński. Fabrication of a synthetic nanopore ion pump. *Phys. Rev. Lett.*, 89:198103, 2002.
- [36] Michal Macha, Sanjin Marion, Vishal V R Nandigana, and Aleksandra Radenovic. 2D materials

- as an emerging platform for nanopore-based power generation. *Nature Reviews Materials*, 4(9):588–605, 2019.
- [37] W. H. Coulter. Means for counting particles suspended in a fluid, 1953. US Patent 2,656,508.
- [38] Michael Graf, Martina Lihter, Mukeshchand Thakur, Vasileia Georgiou, Juraj Topolancik, B Robert Ilic, Ke Liu, Jiandong Feng, Yann Astier, and Aleksandra Radenovic. Fabrication and practical applications of molybdenum disulfide nanopores. *Nature Protocols*, 14(4):1130–1168, 2019.
- [39] Tom Z. Butler, Mikhail Pavlenok, Ian M. Derrington, Michael Niederweis, and Jens H. Gundlach. Single-molecule dna detection with an engineered mspa protein nanopore. *Proceedings of the National Academy of Sciences*, 105(52):20647–20652, 2008.
- [40] Ryan C Rollings, Aaron T Kuan, and Jene A Golovchenko. Ion selectivity of graphene nanopores. *Nature Communications*, 7(1):11408, 2016.
- [41] Lorenz J. Steinbock, Roman D. Bulushev, Swati Krishnan, Camille Raillon, and Aleksandra Radenovic. Dna translocation through low-noise glass nanopores. *ACS Nano*, 7(12):11255–11262, 2013.
- [42] Nicholas A.W. Bell and Ulrich F. Keyser. Nanopores formed by dna origami: A review. *FEBS Letters*, 588(19):3564 – 3570, 2014.
- [43] Yong-An Ren, Han Gao, and Xiangyuan Ouyang. Advances in dna origami nanopores: Fabrication, characterization and applications. *Chinese Journal of Chemistry*, 36(9):875–885, 2018.
- [44] J E Hall. Access resistance of a small circular pore. *Journal of General Physiology*, 66(4):531–532, 1975.
- [45] Stefan W Kowalczyk, Alexander Y Grosberg, Yitzhak Rabin, and Cees Dekker. Modeling the conductance and DNA blockade of solid-state nanopores. *Nanotechnology*, 22(31):315101, 2011.
- [46] Trang Vu, Julia Borgesi, Joanna Soyering, Melissa D’Alia, Shanna-Leigh Davidson, and Jiwook Shim. Employing licl salt gradient in the wild-type α hemolysin nanopore to slow down dna translocation and detect methylated cytosine. *Nanoscale*, 11:10536–10545, 2019.
- [47] Michael Graf, Martina Lihter, Dmitrii Unuchek, Aditya Sarathy, Jean-Pierre Leburton, Andras Kis, and Aleksandra Radenovic. Light-enhanced blue energy generation using mos2 nanopores. *Joule*, 3(6):1549 – 1564, 2019.
- [48] Sanjin Marion, Michal Macha, Sebastian J. Davis, Andrey Chernev, and Aleksandra Radenovic. Wetting of nanopores probed with pressure. arXiv:1911.05229v2, 2019.
- [49] Roman D. Bulushev, Sanjin Marion, and Aleksandra Radenovic. Relevance of the drag force during controlled translocation of a DNA-Protein complex through a glass nanocapillary. *Nano Lett.*, 15(10):7118–7125, 2015.
- [50] David Andelman. Introduction to electrostatics in soft and biological matter. 01 2006.
- [51] D. Andelman. Chapter 12 - electrostatic properties of membranes: The poisson-boltzmann theory. In R. Lipowsky and E. Sackmann, editors, *Structure and Dynamics of Membranes*, volume 1 of *Handbook of Biological Physics*, pages 603 – 642. North-Holland, 1995.
- [52] Reto B. Schoch, Jongyoon Han, and Philippe Renaud. Transport phenomena in nanofluidics. *Rev. Mod. Phys.*, 80:839–883, 2008.
- [53] Yang Liu, David E. Huber, Vincent Tabard-Cossa, and Robert W. Dutton. Descreening of field effect in electrically gated nanopores. *Applied Physics Letters*, 97(14):143109, 2010.
- [54] Choongyeop Lee, Laurent Joly, Alessandro Siria, Anne-Laure Biance, Rémy Fulcrand, and Lydéric Bocquet. Large apparent electric size of solid-state nanopores due to spatially extended surface conduction. *Nano Letters*, 12(8):4037–4044, 2012.
- [55] Robert J. Hunter, editor. *Foundations of colloid science*. Oxford University Press, 2001.
- [56] Brian J. Kirby and Ernest F. Hasselbrink Jr. Zeta potential of microfluidic substrates: 1. theory, experimental techniques, and effects on separations. *Electrophoresis*, 25(2):187–202, 2004.

- [57] Arnold J. Storm, Cornelis Storm, Jianghua Chen, Henny Zandbergen, Jean-François Joanny, and Cees Dekker. Fast dna translocation through a solid-state nanopore. *Nano Letters*, 5(7):1193–1197, 2005.
- [58] Roman D. Bulushev, Lorenz J. Steinbock, Sergey Khlybov, Julian F. Steinbock, Ulrich F. Keyser, and Aleksandra Radenovic. Measurement of the Position-Dependent Electrophoretic Force on DNA in a Glass Capillary. *Nano Lett.*, 14(11):6606, 2014.
- [59] U. F. Keyser, J. van der Does, C. Dekker, and N. H. Dekker. Optical tweezers for force measurements on dna in nanopores. *Review of Scientific Instruments*, 77(10):105105, 2006.
- [60] Andy Sischka, Andre Spiering, Maryam Khaksar, Miriam Laxa, Janine König, Karl-Josef Dietz, and Dario Anselmetti. Dynamic translocation of ligand-complexed DNA through solid-state nanopores with optical tweezers. *Journal of Physics: Condensed Matter*, 22(45):454121, 2010.
- [61] Andre Spiering, Sebastian Getfert, Andy Sischka, Peter Reimann, and Dario Anselmetti. Nanopore translocation dynamics of a single DNA-bound protein. *Nano Lett.*, 11(7):2978–82, 2011.
- [62] Oliver Otto, Sebastian Sturm, Nadanai Laohakunakorn, Ulrich F Keyser, and Klaus Kroy. Rapid internal contraction boosts DNA friction. *Nature communications*, 4:1780, 2013.
- [63] Douwe Jan Bonthuis and Ramin Golestanian. Mechanosensitive channel activation by diffusio-osmotic force. *Phys. Rev. Lett.*, 113:148101, 2014.
- [64] A. Smolyanitsky, A. Fang, A. F. Kazakov, and E. Paulechka. Ion transport across solid-state ion channels perturbed by directed strain. *Nanoscale*, 12:10328–10334, 2020.
- [65] Jiandong Feng, Ke Liu, Roman D Bulushev, Sergey Khlybov, Dumitru Dumcenco, Andras Kis, and Aleksandra Radenovic. Identification of single nucleotides in MoS₂ nanopores. *Nature Nanotechnology*, 10(12):1070–1076, 2015.
- [66] Roman D. Bulushev, Sanjin Marion, Ekaterina Petrova, Sebastian J. Davis, Sebastian J. Maerkl, and Aleksandra Radenovic. Single molecule localization and discrimination of dna–protein complexes by controlled translocation through nanocapillaries. *Nano Letters*, 16(12):7882–7890, 2016.
- [67] Sanjin Marion, Sebastian J. Davis, Zeng-Qiang Wu, and Aleksandra Radenovic. Nanocapillary confinement of imidazolium based ionic liquids. *Nanoscale*, 12:8867–8874, 2020.
- [68] Sebastian James Davis, Michal Macha, Andrey Chernev, David M. Huang, Aleksandra Radenovic, and Sanjin Marion. Hydrostatic pressure induced enlargement and ionic current rectification in symmetric nanopores. *Nano Letters*, 2020.
- [69] B Sakmann and E Neher. Patch clamp techniques for studying ionic channels in excitable membranes. *Annual Review of Physiology*, 46(1):455–472, 1984.
- [70] Andrew G. Ewing, Ross A. Wallingford, and Teresa M. Olefirowicz. Capillary electrophoresis. *Analytical Chemistry*, 61(4):292A–303A, 1989.
- [71] Po-Ling Chang, Michael Graf, Chao-Hsuan Hung, and Aleksandra Radenovic. Orthogonal tip-to-tip nanocapillary alignment allows for easy detection of fluorescent emitters in femtomolar concentrations. *Nano Letters*, 18(5):3165–3171, 2018.
- [72] L. J. Steinbock, J. F. Steinbock, A. Radenovic, Steinbock L., Steinbock J., and Radenovic A. Controllable shrinking and shaping of glass nanocapillaries under electron irradiation. *Nano Lett.*, 13(4):1717–1723, 2013.
- [73] Lorenz J. Steinbock, Oliver Otto, Catalin Chimerel, Joanne Gornall, and Ulrich F Keyser. Detecting dna folding with nanocapillaries. *Nano Letters*, 10(7):2493–2497, 2010.
- [74] Nicholas A. W. Bell and Ulrich F. Keyser. Specific Protein Detection Using Designed DNA Carriers and Nanopores. *J. Am. Chem. Soc.*, 137(5):2035–2041, 2015.
- [75] Péter Terejányi, István Makra, Péter Furjes, and Róbert E. Gyurcsányi. Calibration-less sizing

- and quantitation of polymeric nanoparticles and viruses with quartz nanopipets. *Analytical Chemistry*, 86(10):4688–4697, 2014.
- [76] Lizhen Chen, Haili He, and Yongdong Jin. Counting and dynamic studies of the small unilamellar phospholipid vesicle translocation with single conical glass nanopores. *Analytical Chemistry*, 87(1):522–529, 2015.
- [77] Ru-Jia Yu, Yi-Lun Ying, Yong-Xu Hu, Rui Gao, and Yi-Tao Long. Label-free monitoring of single molecule immunoreaction with a nanopipette. *Analytical Chemistry*, 89(16):8203–8206, 2017.
- [78] Ludovit P. Zweifel, Ivan Shorubalko, and Roderick Y.H. Lim. Helium scanning transmission ion microscopy and electrical characterization of glass nanocapillaries with reproducible tip geometries. *ACS Nano*, 10(2):1918–1925, 2016.
- [79] Nadanai Laohakunakorn, Benjamin Gollnick, Fernando Moreno-Herrero, Dirk G. A. L. Aarts, Roel P. A. Dullens, Sandip Ghosal, and Ulrich F. Keyser. A landau-squire nanojet. *Nano Letters*, 13(11):5141–5146, 2013.
- [80] Jayesh A. Bafna and Gautam V. Soni. Fabrication of low noise borosilicate glass nanopores for single molecule sensing. *PLOS ONE*, 11(6):1–15, 2016.
- [81] Jasmine Y. Y. Sze, Shailabh Kumar, Aleksandar P. Ivanov, Sang-Hyun Oh, and Joshua B. Edel. Fine tuning of nanopipettes using atomic layer deposition for single molecule sensing. *Analyst*, 140:4828–4834, 2015.
- [82] Xiaolong Xu, Chuanping Li, Ya Zhou, and Yongdong Jin. Controllable shrinking of glass capillary nanopores down to sub-10 nm by wet-chemical silanization for signal-enhanced dna translocation. *ACS Sensors*, 2(10):1452–1457, 2017.
- [83] Silvia Hernández-Ainsa, Christoph Muus, Nicholas A. W. Bell, Lorenz J. Steinbock, Vivek V. Thacker, and Ulrich F. Keyser. Lipid-coated nanocapillaries for DNA sensing. *Analyst*, 138(1):104–106, 2013.
- [84] Dana Al Sulaiman, Paolo Cadinu, Aleksandar P. Ivanov, Joshua B. Edel, and Sylvain Ladame. Chemically modified hydrogel-filled nanopores: A tunable platform for single-molecule sensing. *Nano Letters*, 18(9):6084–6093, 2018.
- [85] Yeon Youn, Choongman Lee, Joo Hyoung Kim, Young Wook Chang, Dug Young Kim, and Kyung-Hwa Yoo. Selective detection of single-stranded dna molecules using a glass nanocapillary functionalized with dna. *Analytical Chemistry*, 88(1):688–694, 2016.
- [86] Sumei Cao, Shushu Ding, Yingzi Liu, Anwei Zhu, and Guoyue Shi. Biomimetic mineralization of gold nanoclusters as multifunctional thin films for glass nanopore modification, characterization, and sensing. *Analytical Chemistry*, 89(15):7886–7892, 2017.
- [87] Nadanai Laohakunakorn, Vivek V. Thacker, Murugappan Muthukumar, and Ulrich F. Keyser. Electroosmotic flow reversal outside glass nanopores. *Nano Letters*, 15(1):695–702, 2015.
- [88] Oliver Otto, Lorenz J. Steinbock, and Ulrich F. Keyser. Nanocapillaries and optical tweezers for studies on DNA in confinement. In Kishan Dholakia and Gabriel C. Spalding, editors, *Optical Trapping and Optical Micromanipulation VIII*, volume 8097, pages 68 – 76. International Society for Optics and Photonics, SPIE, 2011.
- [89] Vytautas Navikas, Samuel Mendes Leitao, Sanjin Marion, Sebastian James Davis, Barney Drake, Georg E. Fantner, and Aleksandra Radenovic. High-throughput, nanocapillary filling method based on microwave radiation. *ACS Applied Nano Materials*, 0(ja):null, 2020.
- [90] Evelyne Salançon and Bernard Tinland. Filling nanopipettes with apertures smaller than 50 nm: dynamic microdistillation. *Beilstein J. Nanotechnol.*, 9:2181–2187, 2018.
- [91] Linhao Sun, Kazuki Shigyou, Toshio Ando, and Shinji Watanabe. Thermally Driven Approach To Fill Sub-10-nm Pipettes with Batch Production. *Anal. Chem.*, 91(21):14080–14084, 2019.

Bibliography

- [92] Keir C. Neuman, Edmund H. Chadd, Grace F. Liou, Keren Bergman, and Steven M. Block. Characterization of photodamage to *Escherichia coli* in optical traps. *Biophysical Journal*, 77(5):2856–2863, 1999.
- [93] Hu Zhang and Kuo-Kang Liu. Optical tweezers for single cells. *Journal of the Royal Society, Interface*, 5(24):671–690, 2008.
- [94] Pradeep Barak, Ashim Rai, Priyanka Rai, and Roop Mallik. Quantitative optical trapping on single organelles in cell extract. *Nature Methods*, 10(1):68–70, 2013.
- [95] A. M. Kaufman, B. J. Lester, and C. A. Regal. Cooling a single atom in an optical tweezer to its quantum ground state. *Phys. Rev. X*, 2:041014, 2012.
- [96] Iddo Heller, Tjalle P. Hoekstra, Graeme A. King, Erwin J. G. Peterman, and Gijs J. L. Wuite. Optical Tweezers Analysis of DNA-Protein Complexes. *Chemical Reviews*, 114(6):3087–3119, 2014.
- [97] Maurizio Righini, Antony Lee, Cristhian Cañari-Chumpitaz, Troy Lionberger, Ronen Gabizon, Yves Coello, Ignacio Tinoco, and Carlos Bustamante. Full molecular trajectories of RNA polymerase at single base-pair resolution. *Proceedings of the National Academy of Sciences*, 115(6):1286–1291, 2018.
- [98] MD Wang, Hong Yin, Robert Landick, Jeff Gelles, and SM Block. Stretching DNA with optical tweezers. *Biophys. J.*, 72(March), 1997.
- [99] Wei Cheng, Srikanth G. Arunajadai, Jeffrey R. Moffitt, Ignacio Tinoco, and Carlos Bustamante. Single-base pair unwinding and asynchronous RNA release by the hepatitis C virus NS3 helicase. *Science*, 333(6050):1746–1749, 2011.
- [100] Brent D. Brower-Toland, Corey L. Smith, Richard C. Yeh, John T. Lis, Craig L. Peterson, and Michelle D. Wang. Mechanical disruption of individual nucleosomes reveals a reversible multi-stage release of DNA. *Proceedings of the National Academy of Sciences*, 99(4):1960–1965, 2002.
- [101] Jan Liphardt, Bibiana Onoa, Steven B. Smith, Ignacio Tinoco, and Carlos Bustamante. Reversible unfolding of single RNA molecules by mechanical force. *Science*, 292(5517):733–737, 2001.
- [102] Miklós S. Z. Kellermayer, Steven B. Smith, Henk L. Granzier, and Carlos Bustamante. Folding-unfolding transitions in single titin molecules characterized with laser tweezers. *Science*, 276(5315):1112–1116, 1997.
- [103] Shixin Liu, Gheorghe Chistol, Craig L. Hetherington, Sara Tafoya, K. Aathavan, Joerg Schnitzbauer, Shelley Grimes, Paula J. Jardine, and Carlos Bustamante. A viral packaging motor varies its DNA rotation and step size to preserve subunit coordination as the capsid fills. *Cell*, 157(3):702–713, 2014.
- [104] Neuman K., Block S., Keir C. Neuman, and Steven M. Block. Optical Trapping. *Rev. Sci. Instrum.*, 75(9):2787–2809, 2004.
- [105] Joshua Shaevitz. A practical guide to optical trapping. 2006.
- [106] Arthur Ashkin. Optical trapping and manipulation of neutral particles using lasers. *Proceedings of the National Academy of Sciences*, 94(10):4853–4860, 1997.
- [107] Anna Alemany. Dynamic force spectroscopy and folding kinetics in molecular systems. 2014.
- [108] Jeffrey T. Finer, Robert M. Simmons, and James A. Spudis. Single myosin molecule mechanics: piconewton forces and nanometre steps. *Nature*, 368(6467):113–119, 1994.
- [109] SC Kuo and MP Sheetz. Force of single kinesin molecules measured with optical tweezers. *Science*, 260(5105):232–234, 1993.
- [110] Steven M. Block. Fifty Ways to Love Your Lever: Myosin Motors. *Cell*, 87(2):151–157, 1996.
- [111] Hong Yin, Michelle D. Wang, Karel Svoboda, Robert Landick, Steven M. Block, and Jeff Gelles. Transcription against an applied force. *Science*, 270(5242):1653–1657, 1995.
- [112] Steven B. Smith, Yujia Cui, and Carlos Bustamante. [7] optical-trap force transducer that operates

- by direct measurement of light momentum. In *Biophotonics, Part B*, volume 361 of *Methods in Enzymology*, pages 134 – 162. Academic Press, 2003.
- [113] Roman Bulushev. Nanocapillaries combined with optical tweezers as a single molecule technique for studying dna-protein complexes. EPFL, 2017.
 - [114] J D McGhee and P H von Hippel. Theoretical aspects of DNA-protein interactions: co-operative and non-co-operative binding of large ligands to a one-dimensional homogeneous lattice. *J. Mol. Biol.*, 86(2):469–89, 1974.
 - [115] Marcel Geertz and Sebastian J. Maerkl. Experimental strategies for studying transcription factor-dna binding specificities. *Briefings in Functional Genomics*, 9(5), 2010.
 - [116] Stephen E. Halford and John F. Marko. How do site-specific DNA-binding proteins find their targets? *Nucleic Acids Research*, 32(10):3040–3052, 2004.
 - [117] P H von Hippel and O G Berg. On the specificity of dna-protein interactions. *Proceedings of the National Academy of Sciences*, 83(6):1608–1612, 1986.
 - [118] M. M Garner and A. Revzin. A gel electrophoresis method for quantifying the binding of proteins to specific DNA regions: application to components of the Escherichia coli lactose operon regulatory system. *Nucleic acids research*, 9(13), 1981.
 - [119] DJ Galas and Schmitz A. DNase footprinting: a simple method for the detection of protein-DNA binding specificity. *Nucleic acids research*, 9(5), 1978.
 - [120] Sebastian J. Maerkl and Stephen R. Quake. A systems approach to measuring the binding energy landscapes of transcription factors. *Science*, 315(5809), 2007.
 - [121] Razvan Nutiu, Robin C. Friedman, Shunjun Luo, Irina Khrebtukova, Silva David, Robin Li, Lu Zhang, Gary P. Schroth, and Christopher B. Burge. Direct measurement of DNA affinity landscapes on a high-throughput sequencing instrument. *Nature Biotechnology*, 29(7), 2011.
 - [122] DS Johnson, A Mortazavi, RM Myers, and B Wold. Genome-wide mapping of in vivo protein-DNA interactions. *Science*, 316(5830), 2007.
 - [123] Marcel Geertz, Marcel Shore, and Sebastian J. Maerkl. Massively parallel measurements of molecular interaction kinetics on a microfluidic platform. *PNAS*, 109(41), 2012.
 - [124] Marc-André Laniel, Alain Béliveau, and Sylvain L. Guérin. *Electrophoretic Mobility Shift Assays for the Analysis of DNA-Protein Interactions*, pages 13–30. Humana Press, 2001.
 - [125] Iddo Heller, Gerrit Sitters, Onno D Broekmans, Géraldine Farge, Carolin Menges, Wolfgang Wende, Stefan W Hell, Erwin J G Peterman, and Gijs J L Wuite. STED nanoscopy combined with optical tweezers reveals protein dynamics on densely covered DNA. *Nature Methods*, 10(9):910–916, 2013.
 - [126] Andrey Ivankin, Spencer Carson, Shannon R. M. Kinney, and Meni Wanunu. Fast, label-free force spectroscopy of histone dna interactions in individual nucleosomes using nanopores. *Journal of the American Chemical Society*, 135(41):15350–15352, 2013.
 - [127] Sandor Kasas, Neil H. Thomson, Bettye L. Smith, Helen G. Hansma, Xingshu Zhu, Martin Guthold, Carlos Bustamante, Eric T. Kool, Mikhail Kashlev, and Paul K. Hansma. Escherichia coli RNA Polymerase Activity Observed Using Atomic Force Microscopy. *Biochemistry*, 36(3):461–468, 1997.
 - [128] A Hillisch, M Lorenz, and S Diekmann. Recent advances in FRET: distance determination in protein-DNA complexes. *Curr. Opin. Struct. Biol.*, 11(2):201–7, 2001.
 - [129] Benjamin Gollnick, Carolina Carrasco, Francesca Zuttion, Neville S. Gilhooly, Mark S. Dillingham, and Fernando Moreno-Herrero. Probing dna helicase kinetics with temperature-controlled magnetic tweezers. *Small*, 11(11):1273–1284, 2015.
 - [130] Gautam V. Soni and Cees Dekker. Detection of Nucleosomal Substructures using Solid-State Nanopores. *Nano Lett.*, 12(6):3180–3186, 2012.

Bibliography

- [131] C. Raillon, P. Cousin, F. Traversi, E. Garcia-Cordero, N. Hernandez, and A. Radenovic. Nanopore detection of single molecule RNAP-DNA transcription complex. *Nano Lett.*, 12:1157–1164, 2012.
- [132] Calin Plesa, Justus W. Ruitenbergh, Menno J. Witteveen, and Cees Dekker. Detection of Individual Proteins Bound along DNA Using Solid-State Nanopores. *Nano Lett.*, 15(5):3153–3158, 2015.
- [133] Breton Hornblower, Amy Coombs, Richard D Whitaker, Anatoly Kolomeisky, Stephen J Picone, Amit Meller, and Mark Akeson. Single-molecule analysis of DNA-protein complexes using nanopores. *Nat. Methods*, 2007.
- [134] M. Jinek, F. Jiang, D. W. Taylor, S. H. Sternberg, E. Kaya, E. Ma, C. Anders, M. Hauer, K. Zhou, S. Lin, M. Kaplan, A. T. Iavarone, E. Charpentier, E. Nogales, and J. A. Doudna. Structures of Cas9 Endonucleases Reveal RNA-Mediated Conformational Activation. *Science (80-.)*, 343(6176):1247997–1247997, 2014.
- [135] Allison Squires, Evrim Atas, and Amit Meller. Nanopore sensing of individual transcription factors bound to DNA. *Sci. Rep.*, 5:11643, 2015.
- [136] Olivia M. Eggenberger, Cuifeng Ying, and Michael Mayer. Surface coatings for solid-state nanopores. *Nanoscale*, 11:19636–19657, 2019.
- [137] Laura Sola and Marcella Chiari. Modulation of electroosmotic flow in capillary electrophoresis using functional polymer coatings. *J. Chromatogr. A*, 1270:324–329, 2012.
- [138] Li-Xiang Zhang, Sheng-Lin Cai, Yu-Bin Zheng, Xiao-Hong Cao, and Yao-Qun Li. Smart homopolymer modification to single glass conical nanopore channels: Dual-stimuli-actuated highly efficient ion gating. *Advanced Functional Materials*, 21(11):2103–2107, 2011.
- [139] Olivia M Eggenberger, Geoffray Leriche, Takaaki Koyanagi, Cuifeng Ying, Jared Houghtaling, Thomas B H Schroeder, Jerry Yang, Jiali Li, Adam Hall, and Michael Mayer. Fluid surface coatings for solid-state nanopores: comparison of phospholipid bilayers and archaea-inspired lipid monolayers. *Nanotechnology*, 30(32):325504, 2019.
- [140] Lukas Galla, Andreas J. Meyer, Andre Spiering, Andy Sischka, Michael Mayer, Adam R. Hall, Peter Reimann, and Dario Anselmetti. Hydrodynamic slip on dna observed by optical tweezers-controlled translocation experiments with solid-state and lipid-coated nanopores. *Nano Letters*, 14(7):4176–4182, 2014.
- [141] Erik C Yusko, Jay M Johnson, Sheereen Majd, Panchika Prangkio, Ryan C Rollings, Jiali Li, Jerry Yang, and Michael Mayer. Controlling protein translocation through nanopores with bio-inspired fluid walls. *Nature Nanotechnology*, 6(4):253–260, 2011.
- [142] Matthew Waugh, Autumn Carlsen, David Sean, Gary W. Slater, Kyle Briggs, Harold Kwok, and Vincent Tabard-Cossa. Interfacing solid-state nanopores with gel media to slow dna translocations. *ELECTROPHORESIS*, 36(15):1759–1767, 2015.
- [143] Haili He, Xiaolong Xu, and Yongdong Jin. Wet-Chemical Enzymatic Preparation and Characterization of Ultrathin Gold-Decorated Single Glass Nanopore. *Anal. Chem.*, 86(10):4815–4821, 2014.
- [144] Vincent Tabard-Cossa, Matthew Wiggin, Dhruvi Trivedi, Nahid N. Jetha, Jason R. Dwyer, and Andre Marziali. Single-molecule bonds characterized by solid-state nanopore force spectroscopy. *ACS Nano*, 3(10):3009–3014, 2009.
- [145] Jae-Seok Yu, Min-Cheol Lim, Duyen Thi Ngoc Huynh, Hyung-Jun Kim, Hyun-Mi Kim, Young-Rok Kim, and Ki-Bum Kim. Identifying the Location of a Single Protein along the DNA Strand Using Solid-State Nanopores. *ACS Nano*, 9(5):5289–5298, 2015.
- [146] Hiranmay Maity, Aswathy N. Muttathukattil, and Govardhan Reddy. Salt effects on protein folding thermodynamics. *The Journal of Physical Chemistry Letters*, 9(17):5063–5070, 2018.
- [147] Kouhei Tsumoto, Daisuke Ejima, Anna M. Senczuk, Yoshiko Kita, and Tsutomu Arakawa. Effects

- of salts on protein–surface interactions: applications for column chromatography. *Journal of Pharmaceutical Sciences*, 96(7):1677–1690, 2007.
- [148] Lu Bai, Thomas J. Santangelo, and Michelle D. Wang. Single-molecule analysis of rna polymerase transcription. *Annual Review of Biophysics and Biomolecular Structure*, 35(1):343–360, 2006.
- [149] Kiran Musunuru. The Hope and Hype of CRISPR-Cas9 Genome Editing: A Review. *JAMA Cardiology*, 2(8):914–919, 2017.
- [150] Cem Kuscu, Sevki Arslan, Ritambhara Singh, Jeremy Thorpe, and Mazhar Adli. Genome-wide analysis reveals characteristics of off-target sites bound by the Cas9 endonuclease. *Nat. Biotechnol.*, 32(7):677–683, 2014.
- [151] Xuebing Wu, David A Scott, Andrea J Kriz, Anthony C Chiu, Patrick D Hsu, Daniel B Dadon, Albert W Cheng, Alexandro E Trevino, Silvana Konermann, Sidi Chen, Rudolf Jaenisch, Feng Zhang, and Phillip A Sharp. Genome-wide binding of the CRISPR endonuclease Cas9 in mammalian cells. *Nat. Biotechnol.*, 32(7):670–676, 2014.
- [152] Samuel H. Sternberg, Sy Redding, Martin Jinek, Eric C. Greene, and Jennifer A. Doudna. DNA interrogation by the CRISPR RNA-guided endonuclease Cas9. *Nature*, 507(7490), 2014.
- [153] H. O’Geen, I. M. Henry, M. S. Bhakta, J. F. Meckler, and D. J. Segal. A genome-wide analysis of Cas9 binding specificity using ChIP-seq and targeted sequence capture. *Nucleic Acids Res.*, 43(6):3389–3404, 2015.
- [154] H Yoo, H Lim, I Yang, S Kim, and S Park. Flow cytometric investigation on degradation of macro-DNA by common laboratory manipulations. *J. Biophys. Chem.*, 2:102–111, 2011.
- [155] B Iglewicz and D C Hoaglin. *How to Detect and Handle Outliers*. ASQC basic references in quality control. ASQC Quality Press, 1993.
- [156] John F Marko and Eric D Siggia. Stretching DNA. *Macromolecules*, 28:8759–8770, 1995.
- [157] Anna Alemany, Blanca Rey-Serra, Silvia Frutos, Ciro Cecconi, and Felix Ritort. Mechanical folding and unfolding of protein barnase at the single-molecule level. *Biophysical Journal*, 110(1):63 – 74, 2016.
- [158] C. Jarzynski. Nonequilibrium Equality for Free Energy Differences. *Phys. Rev. Lett.*, 78:2690, 1996.
- [159] Gavin E. Crooks. Entropy production fluctuation theorem and the nonequilibrium work relation for free energy differences. *Phys. Rev. E*, 60:2721–2726, 1999.
- [160] Jeff Gore, Felix Ritort, and Carlos Bustamante. Bias and error in estimates of equilibrium free-energy differences from nonequilibrium measurements. *Proceedings of the National Academy of Sciences*, 100(22):12564–12569, 2003.
- [161] Claudio Rivetti, Martin Guthold, and Carlos Bustamante. Wrapping of DNA around the E.coli RNA polymerase open promoter complex. *EMBO J.*, 18(16):4464–4475, 1999.
- [162] Sung Cheol Kim, Sridhar Kumar Kannam, Stefan Harrer, Matthew T. Downton, Stephen Moore, and John M. Wagner. Geometric dependence of the conductance drop in a nanopore due to a particle. *Phys. Rev. E - Stat. Nonlinear, Soft Matter Phys.*, 89:1–9, 2014.
- [163] Stefan Kesselheim, Wojciech Müller, and Christian Holm. Origin of Current Blockades in Nanopore Translocation Experiments. *Phys. Rev. Lett.*, 112(1):018101, 2014.
- [164] R M M Smeets. Salt-dependence of ion transport and DNA translocation through solid-state nanopores. *Nano Lett.*, 6:89–95, 2006.
- [165] Ying-Hui Fu, Derek PA Kuhl, Antonio Pizzuti, Maura Pieretti, James S Sutcliffe, Stephen Richards, Annemieke JMH Verkert, Jeanette JA Holden, Raymond G Fenwick Jr, Stephen T Warren, et al. Variation of the cgg repeat at the fragile x site results in genetic instability: resolution of the sherman paradox. *Cell*, 67(6):1047–1058, 1991.
- [166] PK Hansma, B Drake, O Marti, SA Gould, and CB Prater. The scanning ion-conductance microscope. *Science*, 243(4891):641–643, 1989.

Bibliography

- [167] Nicholas A W Bell and Ulrich F Keyser. Digitally encoded DNA nanostructures for multiplexed, single-molecule protein sensing with nanopores. *Nature Nanotechnology*, 11(7):645–651, 2016.
- [168] Paul Flory. *Principles of Polymer Chemistry*. Cornell University Press, 1953.
- [169] P.G. De Gennes. Towards a scaling theory of drag reduction. *Physica A: Statistical Mechanics and its Applications*, 140(1):9 – 25, 1986.
- [170] P.G. De Gennes. Kinetics of collapse for a flexible coil. *Journal de Physique Lettres*, 46(14):639–642, 1985.
- [171] P. Pincus. Excluded volume effects and stretched polymer chains. *Macromolecules*, 9(3):386–388, 1976.
- [172] P. Pincus. Dynamics of stretched polymer chains. *Macromolecules*, 10(1):210–213, 1977.
- [173] F Brochard-Wyart. Deformations of one tethered chain in strong flows. *Europhysics Letters (EPL)*, 23(2):105–111, 1993.
- [174] Y. Marciano and F Brochard-Wyart. Normal modes of stretched polymer chains. *Macromolecules*, 28(4):985–990, 1995.
- [175] F Brochard-Wyart, H Hervet, and P Pincus. Unwinding of polymer chains under forces or flows. *Europhysics Letters (EPL)*, 26(7):511–516, 1994.
- [176] F Brochard-Wyart. Polymer chains under strong flows: Stems and flowers. *Europhysics Letters (EPL)*, 30(7):387–392, 1995.
- [177] F Brochard-Wyart, A Buguin, and P. G. de Gennes. Dynamics of taut DNA chains. *Europhysics Letters (EPL)*, 47(2):171–174, 1999.
- [178] Ludger Harnau and Peter Reineker. Relaxation dynamics of partially extended single DNA molecules. *New Journal of Physics*, 1:3–3, 1999.
- [179] Takahiro Sakaue. Nonequilibrium dynamics of a manipulated polymer: Stretching and relaxation. *AIP Conference Proceedings*, 982(1):508–511, 2008.
- [180] Oskar Hallatschek, Erwin Frey, and Klaus Kroy. Tension dynamics in semiflexible polymers. i. coarse-grained equations of motion. *Phys. Rev. E*, 75:031905, 2007.
- [181] Oskar Hallatschek, Erwin Frey, and Klaus Kroy. Tension dynamics in semiflexible polymers. ii. scaling solutions and applications. *Phys. Rev. E*, 75:031906, 2007.
- [182] T Saito and T Sakaue. Dynamical diagram and scaling in polymer driven translocation. *The European Physical Journal E*, 34(12):135, 2011.
- [183] D. Bensimon, A. J. Simon, V. Croquette, and A. Bensimon. Stretching dna with a receding meniscus: Experiments and models. *Phys. Rev. Lett.*, 74:4754–4757, 1995.
- [184] S Manneville, Ph Cluzel, J.-L Viovy, D Chatenay, and F Caron. Evidence for the universal scaling behaviour of a freely relaxing DNA molecule. *Europhysics Letters (EPL)*, 36(6):413–418, 1996.
- [185] Carlos Bustamante, Jed C Macosko, and Gijs J L Wuite. Grabbing the cat by the tail: manipulating molecules one by one. *Nature Reviews Molecular Cell Biology*, 1(2):130–136, 2000.
- [186] TT Perkins, DE Smith, and S Chu. Direct observation of tube-like motion of a single polymer chain. *Science*, 264(5160):819–822, 1994.
- [187] Thomas T. Perkins, Douglas E. Smith, and Steven Chu. Single polymer dynamics in an elongational flow. *Science*, 276(5321):2016–2021, 1997.
- [188] Stephen R Quake, Hazen Babcock, and Steven Chu. The dynamics of partially extended single molecules of DNA. *Nature*, 388(6638):151–154, 1997.
- [189] C Bustamante, JF Marko, ED Siggia, and S Smith. Entropic elasticity of lambda-phage dna. *Science*, 265(5178):1599–1600, 1994.
- [190] TT Perkins, SR Quake, DE Smith, and S Chu. Relaxation of a single dna molecule observed by optical microscopy. *Science*, 264(5160):822–826, 1994.

- [191] E. Goshen, W. Z. Zhao, G. Carmon, S. Rosen, R. Granek, and M. Feingold. Relaxation dynamics of a single dna molecule. *Phys. Rev. E*, 71:061920, 2005.
- [192] TT Perkins, DE Smith, RG Larson, and S Chu. Stretching of a single tethered polymer in a uniform flow. *Science*, 268(5207):83–87, 1995.
- [193] SB Smith, L Finzi, and C Bustamante. Direct mechanical measurements of the elasticity of single dna molecules by using magnetic beads. *Science*, 258(5085):1122–1126, 1992.
- [194] Denis Wirtz. Direct measurement of the transport properties of a single dna molecule. *Phys. Rev. Lett.*, 75:2436–2439, 1995.
- [195] Helen G. Hansma, Kenneth A. Browne, Magdalena Bezanilla, and Thomas C. Bruice. Bending and straightening of dna induced by the same ligand: Characterization with the atomic force microscope. *Biochemistry*, 33(28):8436–8441, 1994.
- [196] H G Hansma, D E Laney, M Bezanilla, R L Sinsheimer, and P K Hansma. Applications for atomic force microscopy of DNA. *Biophysical journal*, 68(5):1672–1677, 1995.
- [197] Matthias Rief, Mathias Gautel, Filipp Oesterhelt, Julio M. Fernandez, and Hermann E. Gaub. Reversible unfolding of individual titin immunoglobulin domains by afm. *Science*, 276(5315):1109–1112, 1997.
- [198] Carlos Bustamante, Steven B Smith, Jan Liphardt, and Doug Smith. Single-molecule studies of dna mechanics. *Current Opinion in Structural Biology*, 10(3):279 – 285, 2000.
- [199] Carlos Bustamante, Zev Bryant, and Steven B Smith. Ten years of tension: single-molecule DNA mechanics. *Nature*, 421(6921):423–427, 2003.
- [200] Steven B. Smith, Yujia Cui, and Carlos Bustamante. Overstretching b-dna: The elastic response of individual double-stranded and single-stranded dna molecules. *Science*, 271(5250):795–799, 1996.
- [201] Kyle Briggs, Harold Kwok, and Vincent Tabard-Cossa. Automated fabrication of 2-nm solid-state nanopores for nucleic acid analysis. *Small*, 10(10):2077–2086, 2014.
- [202] Jeff Gore, Zev Bryant, Marcelo Nöllmann, Mai U Le, Nicholas R Cozzarelli, and Carlos Bustamante. DNA overwinds when stretched. *Nature*, 442(7104):836–839, 2006.
- [203] Alessandro Bosco, Joan Camunas-Soler, and Felix Ritort. Elastic properties and secondary structure formation of single-stranded DNA at monovalent and divalent salt conditions. *Nucleic acids research*, 42(3):2064–2074, 2014.
- [204] Anna Alemany and Felix Ritort. Determination of the elastic properties of short ssdna molecules by mechanically folding and unfolding dna hairpins. *Biopolymers*, 101(12):1193–1199, 2014.
- [205] Takahiro Sakaue and Elie Raphaël. Polymer chains in confined spaces and flow-injection problems: Some remarks. *Macromolecules*, 39(7):2621–2628, 2006.
- [206] Takahiro Sakaue. Semiflexible polymer confined in closed spaces. *Macromolecules*, 40(14):5206–5211, 2007.
- [207] Takahiro Sakaue. Nonequilibrium dynamics of polymer translocation and straightening. *Phys. Rev. E*, 76:021803, 2007.
- [208] Takahiro Sakaue. Sucking genes into pores: Insight into driven translocation. *Phys. Rev. E*, 81:041808, 2010.
- [209] Takuya Saito and Takahiro Sakaue. Process time distribution of driven polymer transport. *Phys. Rev. E*, 85:061803, 2012.
- [210] Takuya Saito and Takahiro Sakaue. Cis-trans dynamical asymmetry in driven polymer translocation. *Phys. Rev. E*, 88:042606, 2013.
- [211] Kyle Briggs, Gregory Madejski, Martin Magill, Konstantinos Kastitis, Hendrick W. de Haan, James L. McGrath, and Vincent Tabard-Cossa. Dna translocations through nanopores under nanoscale preconfinement. *Nano Letters*, 18(2):660–668, 2018.

Bibliography

- [122] Michelle H. Lam, Kyle Briggs, Konstantinos Kastitis, Martin Magill, Gregory R. Madejski, James L. McGrath, Hendrick W. de Haan, and Vincent Tabard-Cossa. Entropic trapping of dna with a nanofiltered nanopore. *ACS Applied Nano Materials*, 2(8):4773–4781, 2019.
- [123] Daniel Fologea, James Uplinger, Brian Thomas, David S. McNabb, and Jiali Li. Slowing dna translocation in a solid-state nanopore. *Nano Letters*, 5(9):1734–1737, 2005.
- [124] Mao Mao, Sandip Ghosal, and Guohui Hu. Hydrodynamic flow in the vicinity of a nanopore induced by an applied voltage. *Nanotechnology*, 24(24):245202, 2013.
- [125] Mao Mao, John Sherwood, and Sandip Ghosal. Electro-osmotic flow through a nanopore. *Journal of Fluid Mechanics*, 749:167–183, 2014.
- [126] R. J. Messinger and T. M. Squires. Suppression of electro-osmotic flow by surface roughness. *Phys. Rev. Lett.*, 105:144503, 2010.
- [127] Nadanai Laohakunakorn and Ulrich F Keyser. Electroosmotic flow rectification in conical nanopores. *Nanotechnology*, 26(27):275202, 2015.
- [128] Z.S. Siwy. Ion-current rectification in nanopores and nanotubes with broken symmetry. *Advanced Functional Materials*, 16(6):735–746, 2006.
- [129] Erik C. Yusko, Ran An, and Michael Mayer. Electroosmotic flow can generate ion current rectification in nano- and micropores. *ACS Nano*, 4(1):477–487, 2010.
- [120] Ivan Vlassiuk and Zuzanna S. Siwy. Nanofluidic diode. *Nano Letters*, 7(3):552–556, 2007.
- [121] Rohit Karnik, Chuanhua Duan, Kenneth Castelino, Hirofumi Daiguji, and Arun Majumdar. Rectification of ionic current in a nanofluidic diode. *Nano Letters*, 7(3):547–551, 2007.
- [122] C. Kittel. Introduction to solid state physics. 1976.
- [123] Yinghua Qiu, Zuzanna S. Siwy, and Meni Wanunu. Abnormal ionic-current rectification caused by reversed electroosmotic flow under viscosity gradients across thin nanopores. *Analytical Chemistry*, 91(1):996–1004, 2019.
- [124] L. Wang, W. Guo, Y.B. Xie, X.W. Wang, J.M. Xue, and Y.G. Wang. Nanofluidic diode generated by ph gradient inside track-etched conical nanopore. *Radiation Measurements*, 44(9):1119 – 1122, 2009. Proceedings of the 24th International Conference on Nuclear Tracks in Solids.
- [125] Jake Rabinowitz, Martin A. Edwards, Elizabeth Whittier, Krishna Jayant, and Kenneth L. Shepard. Nanoscale fluid vortices and nonlinear electroosmotic flow drive ion current rectification in the presence of concentration gradients. *The Journal of Physical Chemistry A*, 123(38):8285–8293, 2019.
- [126] Ye Ai, Mingkan Zhang, Sang W. Joo, Marcos A. Cheney, and Shizhi Qian. Effects of electroosmotic flow on ionic current rectification in conical nanopores. *The Journal of Physical Chemistry C*, 114(9):3883–3890, 2010.
- [127] Dmitriy V. Melnikov, Zachery K. Hulings, and Maria E. Gracheva. Electro-osmotic flow through nanopores in thin and ultrathin membranes. *Phys. Rev. E*, 95:063105, 2017.
- [128] Dong-Huei Lin, Chih-Yuan Lin, Shiojenn Tseng, and Jyh-Ping Hsu. Influence of electroosmotic flow on the ionic current rectification in a ph-regulated, conical nanopore. *Nanoscale*, 7:14023–14031, 2015.
- [129] Michelle L. Kovarik, Kaimeng Zhou, and Stephen C. Jacobson. Effect of conical nanopore diameter on ion current rectification. *The Journal of Physical Chemistry B*, 113(49):15960–15966, 2009.
- [130] Wen-Jie Lan, Deric A. Holden, and Henry S. White. Pressure-dependent ion current rectification in conical-shaped glass nanopores. *Journal of the American Chemical Society*, 133(34):13300–13303, 2011.
- [131] Wen-Jie Lan, Martin A. Edwards, Long Luo, Rukshan T. Perera, Xiaojian Wu, Charles R. Martin,

- and Henry S. White. Voltage-rectified current and fluid flow in conical nanopores. *Accounts of Chemical Research*, 49(11):2605–2613, 2016.
- [232] Laetitia Jubin, Anthony Poggioli, Alessandro Siria, and Lydéric Bocquet. Dramatic pressure-sensitive ion conduction in conical nanopores. *Proceedings of the National Academy of Sciences*, 115(16):4063–4068, 2018.
- [233] Caterina Zilio, Laura Sola, Francesco Damin, Lucia Faggioni, and Marcella Chiari. Universal hydrophilic coating of thermoplastic polymers currently used in microfluidics. *Biomedical Microdevices*, 16(1):107–114, 2014.
- [234] J. P. Brunelle. Preparation of catalysts by metallic complex adsorption on mineral oxides. *Pure and Applied Chemistry*, 50(9-10):1211 – 1229, 1978.
- [235] Peter Greil, Ralf Nitzsche, Hannelore Friedrich, and Waldemar Hermel. Evaluation of oxygen content on silicon nitride powder surface from the measurement of the isoelectric point. *Journal of the European Ceramic Society*, 7(6):353 – 359, 1991.
- [236] René Thomas. The denaturation of dna. *Gene*, 135(1):77 – 79, 1993.
- [237] Jyh-Ping Hsu, Shu-Tuan Yang, Chih-Yuan Lin, and Shiojenn Tseng. Ionic current rectification in a conical nanopore: Influences of electroosmotic flow and type of salt. *The Journal of Physical Chemistry C*, 121(8):4576–4582, 2017.
- [238] Jeffrey Mc Hugh, Kurt Andresen, and Ulrich F Keyser. Cation dependent electroosmotic flow in glass nanopores. *Applied Physics Letters*, 115(11):113702, 2019.
- [239] Judit Horvath and Vladislav Dolník. Polymer wall coatings for capillary electrophoresis. *Electrophoresis*, 22(4):644–655, 2001.
- [240] Erik C Yusko, Brandon R Bruhn, Olivia M Eggenberger, Jared Houghtaling, Ryan C Rollings, Nathan C Walsh, Santoshi Nandivada, Mariya Pindrus, Adam R Hall, David Sept, Jiali Li, Devendra S Kalonia, and Michael Mayer. Real-time shape approximation and fingerprinting of single proteins using a nanopore. *Nature Nanotechnology*, 12(4):360–367, 2017.
- [241] Senkei Umehara, Nader Pourmand, Chris D. Webb, Ronald W. Davis, Kenji Yasuda, and Miloslav Karhanek. Current rectification with poly-l-lysine-coated quartz nanopipettes. *Nano Letters*, 6(11):2486–2492, 2006.
- [242] Rui Qiao and Ping He. Modulation of electroosmotic flow by neutral polymers. *Langmuir*, 23(10):5810–5816, 2007.
- [243] Michele Monteferrante, Simone Melchionna, Umberto Marini Bettolo Marconi, Marina Cretich, Marcella Chiari, and Laura Sola. Electroosmotic flow in polymer-coated slits: a joint experimental/simulation study. *Microfluidics and Nanofluidics*, 18(3):475–482, 2015.
- [244] Erin A.S. Doherty, K. Derek Berglund, Brett A. Buchholz, Igor V. Kourkine, Todd M. Przybycien, Robert D. Tilton, and Annelise E. Barron. Critical factors for high-performance physically adsorbed (dynamic) polymeric wall coatings for capillary electrophoresis of dna. *Electrophoresis*, 23(16):2766–2776, 2002.
- [245] Qianqian Cao, Chuncheng Zuo, Lujuan Li, Yanhong Ma, and Nan Li. Electroosmotic flow in a nanofluidic channel coated with neutral polymers. *Microfluidics and Nanofluidics*, 9(6):1051–1062, 2010.
- [246] Abhijeet Kshirsagar, Pradeep Nyaupane, Dhananjay Bodas, S.P. Duttagupta, and S.A. Gangal. Deposition and characterization of low temperature silicon nitride films deposited by inductively coupled plasma cvd. *Applied Surface Science*, 257(11):5052 – 5058, 2011.
- [247] Marcella Chiari, Marina Cretich, Francesco Damin, Laura Ceriotti, and Roberto Consonni. New adsorbed coatings for capillary electrophoresis. *Electrophoresis*, 21(5):909–916, 2000.
- [248] Nicholas A W Bell, Kaikai Chen, Sandip Ghosal, Maria Ricci, and Ulrich F Keyser. Asymmetric

- dynamics of DNA entering and exiting a strongly confining nanopore. *Nature Communications*, 8(1):380, 2017.
- [249] Kaikai Chen, Nicholas A.W. Bell, Jinglin Kong, Yu Tian, and Ulrich F. Keyser. Direction- and salt-dependent ionic current signatures for dna sensing with asymmetric nanopores. *Biophysical Journal*, 112(4):674 – 682, 2017.
- [250] Saurabh Awasthi, Pongsatorn Sriboonpeng, Cuifeng Ying, Jared Houghtaling, Ivan Shorubalko, Sanjin Marion, Sebastian James Davis, Laura Sola, Marcella Chiari, Aleksandra Radenovic, and Michael Mayer. Polymer coatings to minimize protein adsorption in solid-state nanopores. *Accepted for publication in Small Methods*, 0(ja):null, 2020.
- [251] Raj D. Maitra, Jungsuk Kim, and William B. Dunbar. Recent advances in nanopore sequencing. *Electrophoresis*, 33(23):3418–3428, 2012.
- [252] Yanxiao Feng, Yuechuan Zhang, Cuifeng Ying, Deqiang Wang, and Chunlei Du. Nanopore-based fourth-generation dna sequencing technology. *Genomics, Proteomics & Bioinformatics*, 13(1):4 – 16, 2015.
- [253] Christina G Siontorou, Georgia-Paraskevi Nikoleli, Dimitrios P Nikolelis, and Stefanos K Karapetis. Artificial Lipid Membranes: Past, Present, and Future. *Membranes*, 7(3):38, 2017.
- [254] David Wendell, Peng Jing, Jia Geng, Varuni Subramaniam, Tae Jin Lee, Carlo Montemagno, and Peixuan Guo. Translocation of double-stranded DNA through membrane-adapted phi29 motor protein nanopores. *Nature nanotechnology*, 4(11):765–772, 2009.
- [255] Langzhou Song, Michael R. Hobaugh, Christopher Shustak, Stephen Cheley, Hagan Bayley, and J. Eric Gouaux. Structure of staphylococcal α -hemolysin, a heptameric transmembrane pore. *Science*, 274(5294):1859–1865, 1996.
- [256] Andrew H. Laszlo, Ian M. Derrington, and Jens H. Gundlach. Mspa nanopore as a single-molecule tool: From sequencing to sprnt. *Methods*, 105:75 – 89, 2016.
- [257] Ian M Derrington, Jonathan M Craig, Eric Stava, Andrew H Laszlo, Brian C Ross, Henry Brinkerhoff, Ian C Nova, Kenji Doering, Benjamin I Tickman, Mostafa Ronaghi, Jeffrey G Mandell, Kevin L Gunderson, and Jens H Gundlach. Subangstrom single-molecule measurements of motor proteins using a nanopore. *Nature Biotechnology*, 33(10):1073–1075, 2015.
- [258] Christian Heinz, Harald Engelhardt, and Michael Niederweis. The core of the tetrameric mycobacterial porin mspsa is an extremely stable β -sheet domain. *Journal of Biological Chemistry*, 278(10):8678–8685, 2003.
- [259] Jonathan M. Craig, Andrew H. Laszlo, Henry Brinkerhoff, Ian M. Derrington, Matthew T. Noakes, Ian C. Nova, Benjamin I. Tickman, Kenji Doering, Noah F. de Leeuw, and Jens H. Gundlach. Revealing dynamics of helicase translocation on single-stranded dna using high-resolution nanopore tweezers. *Proceedings of the National Academy of Sciences*, 114(45):11932–11937, 2017.
- [260] Jonathan M Craig, Andrew H Laszlo, Ian C Nova, Henry Brinkerhoff, Matthew T Noakes, Katherine S Baker, Jasmine L Bowman, Hugh R Higinbotham, Jonathan W Mount, and Jens H Gundlach. Determining the effects of DNA sequence on Hel308 helicase translocation along single-stranded DNA using nanopore tweezers. *Nucleic Acids Research*, 47(5):2506–2513, 2019.
- [261] Irina O. Vvedenskaya, Hanif Vahedian-Movahed, Jeremy G. Bird, Jared G. Knoblauch, Seth R. Goldman, Yu Zhang, Richard H. Ebright, and Bryce E. Nickels. Interactions between rna polymerase and the “core recognition element” counteract pausing. *Science*, 344(6189):1285–1289, 2014.
- [262] Thomas Gutsmann, Thomas Heimburg, Ulrich Keyser, Kozhinjampara R Mahendran, and Mathias Winterhalter. Protein reconstitution into freestanding planar lipid membranes for electrophysiological characterization. *Nature Protocols*, 10(1):188–198, 2015.

- [263] Paul Mueller, Donald O. Rudin, H. Ti Tien, and William C. Wescott. Reconstitution of Cell Membrane Structure in vitro and its Transformation into an Excitable System. *Nature*, 194(4832):979–980, 1962.
- [264] M Montal and P Mueller. Formation of bimolecular membranes from lipid monolayers and a study of their electrical properties. *Proceedings of the National Academy of Sciences of the United States of America*, 69(12):3561–3566, 1972.
- [265] W. Hanke, C. Methfessel, U. Wilmsen, and G. Boheim. Ion channel reconstitution into lipid bilayer membranes on glass patch pipettes. *Bioelectrochemistry and Bioenergetics*, 12(3):329 – 339, 1984.
- [266] Victor Marin, Roland Kieffer, Raymond Padmos, and Marie-Eve Aubin-Tam. Stable free-standing lipid bilayer membranes in norland optical adhesive 81 microchannels. *Analytical Chemistry*, 88(15):7466–7470, 2016.
- [267] van Uitert Iris, Le Gac Séverine, and van den Berg Albert. The influence of different membrane components on the electrical stability of bilayer lipid membranes. *Biochimica et Biophysica Acta (BBA) - Biomembranes*, 1798(1):21 – 31, 2010.
- [268] Mikhail Pavlenok and Michael Niederweis. Hetero-oligomeric MspA pores in Mycobacterium smegmatis. *FEMS Microbiology Letters*, 363(7), 2016.
- [269] David R. Nelson. Statistical physics of unzipping dna. arXiv:cond-mat/0309559v1, 2003.
- [270] Claudia Danilowicz, Vincent W Coljee, Cedric Bouzigues, David K Lubensky, David R Nelson, and Mara Prentiss. DNA unzipped under a constant force exhibits multiple metastable intermediates. *Proceedings of the National Academy of Sciences of the United States of America*, 100(4):1694–1699, 2003.
- [271] Meni Wanunu, Will Morrison, Yitzhak Rabin, Alexander Y Grosberg, and Amit Meller. Electrostatic focusing of unlabelled DNA into nanoscale pores using a salt gradient. *Nature Nanotechnology*, 5(2):160–165, 2010.
- [272] Annael Brunet, Catherine Tardin, Laurence Salomé, Philippe Rousseau, Nicolas Destainville, and Manoel Manghi. Dependence of dna persistence length on ionic strength of solutions with monovalent and divalent salts: A joint theory and experiment study. *Macromolecules*, 48(11):3641–3652, 2015.
- [273] Xinqi Kang, Mohammad Amin Alibakhshi, and Meni Wanunu. One-pot species release and nanopore detection in a voltage-stable lipid bilayer platform. *Nano Letters*, 19(12):9145–9153, 2019.
- [274] Bruce J. Humphrey. The application of parylene conformal coating technology to archival and artifact conservation. *Studies in Conservation*, 29(3):117–123, 1984.
- [275] Edward M. Schmidt, Martin J. Bak, and Paul Christensen. Laser exposure of parylene-c insulated microelectrodes. *Journal of Neuroscience Methods*, 62(1):89 – 92, 1995.
- [276] Sophie Raffy and Justin Teissié. Control of lipid membrane stability by cholesterol content. *Biophysical Journal*, 76(4):2072 – 2080, 1999.
- [277] Suk Kyu Han, Young Ill Ko, Soo Jung Park, In Jung Jin, and Young Mi Kim. Oleanolic acid and ursolic acid stabilize liposomal membranes. *Lipids*, 32(7):769–773, 1997.
- [278] Michael Halter, Yoichi Nogata, Oliver Dannenberger, Tomikazu Sasaki, and Viola Vogel. Engineered lipids that cross-link the inner and outer leaflets of lipid bilayers. *Langmuir*, 20(6):2416–2423, 2004.
- [279] Hengbin Zhang, Qing Zhao, Zhipeng Tang, Song Liu, Qingtao Li, Zhongchao Fan, Fuhua Yang, Liping You, Xuemei Li, Jingmin Zhang, and Dapeng Yu. Slowing down dna translocation through solid-state nanopores by pressure. *Small*, 9(24):4112–4117, 2013.
- [280] M.A. Fardin. On the Rheology of Cats. *Rheology Bulletin*, 2(83), 2014.

Bibliography

- [281] Seda Keskin, Defne Kayrak-Talay, Uğur Akman, and Öner Hortaçsu. A review of ionic liquids towards supercritical fluid applications. *J. Supercrit. Fluids*, 43(1):150–180, 2007.
- [282] Cinzia Chiappe and Daniela Pieraccini. Ionic liquids: solvent properties and organic reactivity. *J. Phys. Org. Chem.*, 18(4):275–297, 2005.
- [283] Michel Armand, Frank Endres, Douglas R MacFarlane, Hiroyuki Ohno, and Bruno Scrosati. Ionic-liquid materials for the electrochemical challenges of the future. *Nat. Mater.*, 8(8):621–9, 2009.
- [284] Maxim V. Fedorov and Alexei A. Kornyshev. Ionic Liquids at Electrified Interfaces. *Chem. Rev.*, 114(5):2978–3036, 2014.
- [285] Feng Zhou, Yongmin Liang, and Weimin Liu. Ionic liquid lubricants: Designed chemistry for engineering applications. *Chem. Soc. Rev.*, 38(9):2590–2599, 2009.
- [286] Maciej Galiński, Andrzej Lewandowski, and Izabela Stepniak. Ionic liquids as electrolytes. *Electrochim. Acta*, 51(26):5567–5580, 2006.
- [287] Mark N. Kobrak and Hualin Li. Electrostatic interactions in ionic liquids: the dangers of dipole and dielectric descriptions. *Phys. Chem. Chem. Phys.*, 12(8):1922, 2010.
- [288] Roland Kjellander. Decay behavior of screened electrostatic surface forces in ionic liquids: the vital role of non-local electrostatics. *Phys. Chem. Chem. Phys.*, 18(28):18985–19000, 2016.
- [289] Matthew A Gebbie, Howard A Dobbs, Markus Valtiner, and Jacob N Israelachvili. Long-range electrostatic screening in ionic liquids. *Proc. Natl. Acad. Sci.*, 112(24):7432–7437, 2015.
- [290] Karel Goossens, Kathleen Lava, Christopher W. Bielawski, and Koen Binnemans. Ionic Liquid Crystals: Versatile Materials. *Chem. Rev.*, 116(8):4643–4807, 2016.
- [291] Martin Z. Bazant, Brian D. Storey, and Alexei a. Kornyshev. Double Layer in Ionic Liquids: Overscreening versus Crowding. *Phys. Rev. Lett.*, 106(4):046102, 2011.
- [292] Vahid Adibnia, Marziye Mirbagheri, Pierre-Luc Latreille, Gregory De Crescenzo, Dominic Rochefort, and Xavier Banquy. Interfacial forces across ionic liquid solutions: Effects of ion concentration and water domains. *Langmuir*, 35(48):15585–15591, 2019.
- [293] Alexander M. Smith, Alpha A. Lee, and Susan Perkin. The Electrostatic Screening Length in Concentrated Electrolytes Increases with Concentration. *J. Phys. Chem. Lett.*, 7(12):2157–2163, 2016.
- [294] Alpha A. Lee, Carla S. Perez-Martinez, Alexander M. Smith, and Susan Perkin. Scaling Analysis of the Screening Length in Concentrated Electrolytes. *Phys. Rev. Lett.*, 119(2):026002, 2017.
- [295] Juan C. Araque, Sharad K. Yadav, Michael Shadeck, Mark Maroncelli, and Claudio J. Margulis. How Is Diffusion of Neutral and Charged Tracers Related to the Structure and Dynamics of a Room-Temperature Ionic Liquid? Large Deviations from Stokes–Einstein Behavior Explained. *J. Phys. Chem. B*, 119(23):7015–7029, 2015.
- [296] Yuchen Zuo, Yuanzhong Zhang, Rundong Huang, and Younjin Min. The effect of confinement on the glass transition of ionic liquids. *Physical Chemistry Chemical Physics*, 21:22–25, 2019.
- [297] Jean Comtet, Antoine Niguès, Vojtech Kaiser, Benoît Coasne, Lydéric Bocquet, and Alessandro Siria. Nanoscale capillary freezing of ionic liquids confined between metallic interfaces and the role of electronic screening. *Nat. Mater.*, 16(6):634–639, 2017.
- [298] C. Iacob, J. R. Sangoro, W. K. Kipnusu, R. Valiullin, J. Karger, and F Kremer. Enhanced charge transport in nano-confined ionic liquids. *Soft Matter*, 8(2):289–293, 2012.
- [299] Konrad Breitsprecher, Manuel Abele, Svyatoslav Kondrat, and Christian Holm. The effect of finite pore length on ion structure and charging. *J. Chem. Phys.*, 147(10):104708, 2017.
- [300] Ryusuke Futamura, Taku Iiyama, Yuma Takasaki, Yury Gogotsi, Mark J Biggs, Mathieu Salanne, Julie Ségalini, Patrice Simon, and Katsumi Kaneko. Partial breaking of the Coulombic ordering of ionic liquids confined in carbon nanopores. *Nat. Mater.*, 16(12):1225–1232, 2017.

- [301] Radhika S Anareddy and Scott K Shaw. Long-Range Ordering of Ionic Liquid Fluid Films. *Langmuir*, 32(20):5147–5154, 2016.
- [302] Ke Ma, Romana Jarosova, Greg M Swain, and Gary J Blanchard. Charge-Induced Long-Range Order in a Room-Temperature Ionic Liquid. *Langmuir*, 32(37):9507–9512, 2016.
- [303] Diego Pontoni, Julia Haddad, Bridget M. Murphy, Sven Festersen, Oleg Konovalov, Benjamin M. Ocko, and Moshe Deutsch. Surface Phases and Surface Freezing in an Ionic Liquid. *J. Phys. Chem. C*, 123(5):3058–3066, 2019.
- [304] Vladislav Kamysbayev, Vishwas Srivastava, Nicholas Benjamin Ludwig, Olaf J. Borkiewicz, Hao Zhang, Jan Ilavsky, Byeongdu Lee, Karena W Chapman, Suriyanarayanan Vaikuntanathan, and Dmitri V. Talapin. Nanocrystals in Molten Salts and Ionic Liquids: Experimental Observation of Ionic Correlations Extending beyond the Debye Length. *ACS Nano*, 13(5):5760–5770, 2019.
- [305] Romain Lhermerout and Susan Perkin. Nanoconfined ionic liquids: Disentangling electrostatic and viscous forces. *Phys. Rev. Fluids*, 3(1):014201, 2018.
- [306] Léo Garcia, Léa Jacquot, Elisabeth Charlaix, and Benjamin Cross. Nano-mechanics of ionic liquids at dielectric and metallic interfaces. *Faraday Discuss.*, 206:443–457, 2018.
- [307] Matthew Davenport, Andrew Rodriguez, Kenneth J. Shea, and Zuzanna S. Siwy. Squeezing Ionic Liquids through Nanopores. *Nano Lett.*, 9(5):2125–2128, 2009.
- [308] Kazuyuki Fujie, Kazuya Otsubo, Ryuichi Ikeda, Teppei Yamada, and Hiroshi Kitagawa. Low temperature ionic conductor: ionic liquid incorporated within a metal–organic framework. *Chem. Sci.*, 6:4306–4310, 2015.
- [309] C Alba-Simionesco, B Coasne, G Dosseh, G Dudziak, K E Gubbins, R Radhakrishnan, and M Sliwinska-Bartkowiak. Effects of confinement on freezing and melting. *J. Phys. Condens. Matter*, 18(6):R15–R68, 2006.
- [310] Oliver Zech, Alexander Stoppa, Richard Buchner, and Werner Kunz. The conductivity of imidazolium-based ionic liquids from (248 to 468) k. b. variation of the anion. *Journal of Chemical & Engineering Data*, 55(5):1774–1778, 2010.
- [311] Alexander Stoppa, Oliver Zech, Werner Kunz, and Richard Buchner. The conductivity of imidazolium-based ionic liquids from (35 to 195) c. a. variation of cation's alkyl chain. *Journal of Chemical & Engineering Data*, 55(5):1768–1773, 2010.
- [312] Christian Schreiner, Sandra Zugmann, Robert Hartl, and Heiner J. Gores. Fractional walden rule for ionic liquids: Examples from recent measurements and a critique of the so-called ideal kcl line for the walden plot. *Journal of Chemical & Engineering Data*, 55(5):1784–1788, 2010.
- [313] C. A. Angell. Formation of Glasses from Liquids and Biopolymers. *Science (80-.)*, 267(5206):1924–1935, 1995.
- [314] Jason A. Widegren, Arno Laesecke, and Joseph W. Magee. The effect of dissolved water on the viscosities of hydrophobic room-temperature ionic liquids. *Chem. Commun.*, pages 1610–1612, 2005.
- [315] Jason A. Widegren, Eric M. Saurer, Kenneth N. Marsh, and Joseph W. Magee. Electrolytic conductivity of four imidazolium-based room-temperature ionic liquids and the effect of a water impurity. *J. Chem. Thermodyn.*, 37(6):569–575, 2005.
- [316] Chunyan Ma, Aatto Laaksonen, Chang Liu, Xiaohua Lu, and Xiaoyan Ji. The peculiar effect of water on ionic liquids and deep eutectic solvents. *Chem. Soc. Rev.*, 47:8685–8720, 2018.
- [317] Kun Liu, Cheng Lian, Douglas Henderson, and Jianzhong Wu. Impurity effects on ionic-liquid-based supercapacitors. *Molecular Physics*, 115(4):454–464, 2017.
- [318] K. Seddon, A. Stark, and M. Torres. Influence of chloride, water, and organic solvents on the physical properties of ionic liquids. *Pure and Applied Chemistry*, 72:2275–22870, 2009.

- [319] Ivan Vlassiouk, Sergei Smirnov, and Zuzanna Siwy. Ionic selectivity of single nanochannels. *Nano Letters*, 8(7):1978–1985, 2008.
- [320] Tarun Jain, Benjamin C Rasera, Ricardo Jose S Guerrero, Michael S H Boutilier, Sean C O’Hern, Juan-Carlos Idrobo, and Rohit Karnik. Heterogeneous sub-continuum ionic transport in statistically isolated graphene nanopores. *Nature Nanotechnology*, 10(12):1053–1057, 2015.
- [321] Jiandong Feng, Ke Liu, Michael Graf, Dumitru Dumcenco, Andras Kis, Massimiliano Di Ventra, and Aleksandra Radenovic. Observation of ionic Coulomb blockade in nanopores. *Nature Materials*, 15(8):850–855, 2016.
- [322] Jothi Priyanka Thiruraman, Kazunori Fujisawa, Gopinath Danda, Paul Masih Das, Tianyi Zhang, Adam Bolotsky, Néstor Perea-López, Adrien Nicolai, Patrick Senet, Mauricio Terrones, and Marija Drndić. Angstrom-size defect creation and ionic transport through pores in single-layer mos2. *Nano Letters*, 18(3):1651–1659, 2018.
- [323] R. M. M. Smeets, U. F. Keyser, M. Y. Wu, N. H. Dekker, and C. Dekker. Nanobubbles in solid-state nanopores. *Phys. Rev. Lett.*, 97:088101, 2006.
- [324] R. M. M. Smeets, U. F. Keyser, N. H. Dekker, and C. Dekker. Noise in solid-state nanopores. *Proceedings of the National Academy of Sciences*, 105(2):417–421, 2008.
- [325] Jeffrey D. Uram, Kevin Ke, and Michael Mayer. Noise and bandwidth of current recordings from submicrometer pores and nanopores. *ACS Nano*, 2(5):857–872, 2008.
- [326] Eric Beamish, Harold Kwok, Vincent Tabard-Cossa, and Michel Godin. Precise control of the size and noise of solid-state nanopores using high electric fields. *Nanotechnology*, 23(40):405301, 2012.
- [327] Gaku Nagashima, Edlyn V. Levine, David P. Hoogerheide, Michael M. Burns, and Jene A. Golovchenko. Superheating and homogeneous single bubble nucleation in a solid-state nanopore. *Phys. Rev. Lett.*, 113:024506, 2014.
- [328] Edlyn V Levine, Michael M Burns, and Jene A Golovchenko. Nanoscale dynamics of Joule heating and bubble nucleation in a solid-state nanopore. *Physical review. E*, 93(1):13124, 2016.
- [329] Yi Li, Francesca Nicoli, Chang Chen, Liesbet Lagae, Guido Groeseneken, Tim Stakenborg, Henny W. Zandbergen, Cees Dekker, Pol Van Dorpe, and Magnus P. Jonsson. Photoresistance switching of plasmonic nanopores. *Nano Letters*, 15(1):776–782, 2015.
- [330] Shi-Tao Lou, Zhen-Qian Ouyang, Yi Zhang, Xiao-Jun Li, Jun Hu, Min-Qian Li, and Fu-Jia Yang. Nanobubbles on solid surface imaged by atomic force microscopy. *Journal of Vacuum Science & Technology B: Microelectronics and Nanometer Structures Processing, Measurement, and Phenomena*, 18(5):2573–2575, 2000.
- [331] Naoyuki Ishida, Taichi Inoue, Minoru Miyahara, and Ko Higashitani. Nano bubbles on a hydrophobic surface in water observed by tapping-mode atomic force microscopy. *Langmuir*, 16(16):6377–6380, 2000.
- [332] Muidh Alheshibri, Jing Qian, Marie Jehannin, and Vincent S. J. Craig. A history of nanobubbles. *Langmuir*, 32(43):11086–11100, 2016.
- [333] Detlef Lohse and Xuehua Zhang. Surface nanobubbles and nanodroplets. *Rev. Mod. Phys.*, 87:981–1035, 2015.
- [334] Jing Qian, Vincent S. J. Craig, and Marie Jehannin. Long-term stability of surface nanobubbles in undersaturated aqueous solution. *Langmuir*, 35(3):718–728, 2019.
- [335] Kock-Yee Law. Definitions for hydrophilicity, hydrophobicity, and superhydrophobicity: Getting the basics right. *The Journal of Physical Chemistry Letters*, 5(4):686–688, 2014.
- [336] Sergei N. Smirnov, Ivan V. Vlassiouk, and Nickolay V. Lavrik. Voltage-gated hydrophobic nanopores. *ACS Nano*, 5(9):7453–7461, 2011.

- [337] Lauren Cantley, Jacob L. Swett, David Lloyd, David A. Cullen, Ke Zhou, Peter V. Bedworth, Scott Heise, Adam J. Rondinone, Zhiping Xu, Steve Sinton, and J. Scott Bunch. Voltage gated inter-cation selective ion channels from graphene nanopores. *Nanoscale*, 11:9856–9861, 2019.
- [338] Qianxiang Xiao, Yawei Liu, Zhenjiang Guo, Zhiping Liu, Detlef Lohse, and Xianren Zhang. Solvent exchange leading to nanobubble nucleation: A molecular dynamics study. *Langmuir*, 33(32):8090–8096, 2017.
- [339] Dongha Shin, Jong Bo Park, Yong-Jin Kim, Sang Jin Kim, Jin Hyoun Kang, Bora Lee, Sung-Pyo Cho, Byung Hee Hong, and Konstantin S Novoselov. Growth dynamics and gas transport mechanism of nanobubbles in graphene liquid cells. *Nature Communications*, 6(1):6068, 2015.
- [340] Fereshte Taherian, Valentina Marcon, Nico F. A. van der Vegt, and Frédéric Leroy. What is the contact angle of water on graphene? *Langmuir*, 29(5):1457–1465, 2013.
- [341] Andrew Kozbial, Zhiting Li, Caitlyn Conaway, Rebecca McGinley, Shonali Dhingra, Vahid Vahdat, Feng Zhou, Brian D’Urso, Haitao Liu, and Lei Li. Study on the surface energy of graphene by contact angle measurements. *Langmuir*, 30(28):8598–8606, 2014.
- [342] Anand P. S. Gaur, Satyaprakash Sahoo, Majid Ahmadi, Saroj P. Dash, Maxime J.-F. Guinel, and Ram S. Katiyar. Surface energy engineering for tunable wettability through controlled synthesis of mos2. *Nano Letters*, 14(8):4314–4321, 2014.
- [343] Philippe K. Chow, Eklavya Singh, Bartolomeu Cruz Viana, Jian Gao, Jian Luo, Jing Li, Zhong Lin, Ana L. Elías, Yunfeng Shi, Zuankai Wang, Mauricio Terrones, and Nikhil Koratkar. Wetting of mono and few-layered ws2 and mos2 films supported on si/sio2 substrates. *ACS Nano*, 9(3):3023–3031, 2015.
- [344] Xuemei Li, Hu Qiu, Xiaofei Liu, Jun Yin, and Wanlin Guo. Wettability of supported monolayer hexagonal boron nitride in air. *Advanced Functional Materials*, 27(19):1603181, 2017.
- [345] Pradeep Waduge, Rui Hu, Prasad Bandarkar, Hirohito Yamazaki, Benjamin Cressiot, Qing Zhao, Paul C. Whitford, and Meni Wanunu. Nanopore-based measurements of protein size, fluctuations, and conformational changes. *ACS Nano*, 11(6):5706–5716, 2017.
- [346] Matthias Firnkes, Daniel Pedone, Jelena Knezevic, Markus Döblinger, and Ulrich Rant. Electrically facilitated translocations of proteins through silicon nitride nanopores: Conjoint and competitive action of diffusion, electrophoresis, and electroosmosis. *Nano Letters*, 10(6):2162–2167, 2010.
- [347] Ji Li, Rui Hu, Xiaoqing Li, Xin Tong, Dapeng Yu, and Qing Zhao. Tiny protein detection using pressure through solid-state nanopores. *Electrophoresis*, 38(8):1130–1138, 2017.
- [348] Hengbin Zhang, Qiang Chen, Yaojun Wu, Yangyang Wang, Xiaomin Bei, and Lin Xiao. The temporal resolution and single-molecule manipulation of a solid-state nanopore by pressure and voltage. *Nanotechnology*, 29(49):495501, 2018.
- [349] Sahin Buyukdagli, Ralf Blossey, and T. Ala-Nissila. Ionic current inversion in pressure-driven polymer translocation through nanopores. *Phys. Rev. Lett.*, 114:088303, 2015.
- [350] Sergei Smirnov, Ivan Vlassiuk, Pavel Takmakov, and Fabian Rios. Water confinement in hydrophobic nanopores. pressure-induced wetting and drying. *ACS Nano*, 4(9):5069–5075, 2010.
- [351] Matthew R Powell, Leah Cleary, Matthew Davenport, Kenneth J Shea, and Zuzanna S Siwy. Electric-field-induced wetting and dewetting in single hydrophobic nanopores. *Nature Nanotechnology*, 6(12):798–802, 2011.
- [352] Simon Gravelle, Laurent Joly, Christophe Ybert, and Lydéric Bocquet. Large permeabilities of hourglass nanopores: From hydrodynamics to single file transport. *The Journal of Chemical Physics*, 141(18):18C526, 2014.
- [353] Wen-Jie Lan, Deric A. Holden, Jin Liu, and Henry S. White. Pressure-driven nanoparticle trans-

- pore across glass membranes containing a conical-shaped nanopore.
- The Journal of Physical Chemistry C*
- , 115(38):18445–18452, 2011.
- [354] Alessandro Gadaleta, Anne-Laure Biance, Alessandro Siria, and Lydéric Bocquet. Ultra-sensitive flow measurement in individual nanopores through pressure-driven particle translocation. *Nanoscale*, 7:7965–7970, 2015.
 - [355] Iago Pereiro, Anna Fomitcheva Khartchenko, Lorenzo Petrini, and Govind V. Kaigala. Nip the bubble in the bud: a guide to avoid gas nucleation in microfluidics. *Lab Chip*, 19:2296–2314, 2019.
 - [356] V Dimitrov, U Mirsaidov, D Wang, T Sorsch, W Mansfield, J Miner, F Klemens, R Cirelli, S Yemenicioglu, and G Timp. Nanopores in solid-state membranes engineered for single molecule detection. *Nanotechnology*, 21(6):065502, 2010.
 - [357] William Henry and Joseph Banks. Iii. experiments on the quantity of gases absorbed by water, at different temperatures, and under different pressures. *Philosophical Transactions of the Royal Society of London*, 93:29–274, 1803.
 - [358] Vincent Tabard-Cossa, Dhruti Trivedi, Matthew Wiggin, Nahid N Jetha, and Andre Marziali. Noise analysis and reduction in solid-state nanopores. *Nanotechnology*, 18(30):305505, 2007.
 - [359] Alessio Fragasso, Sergii Pud, and Cees Dekker. 1/f noise in solid-state nanopores is governed by access and surface regions. *Nanotechnology*, 30(39):395202, 2019.
 - [360] Razi Epsztein, Ryan M DuChanois, Cody L Ritt, Aleksandr Noy, and Menachem Elimelech. Towards single-species selectivity of membranes with subnanometre pores. *Nature Nanotechnology*, 2020.
 - [361] Anthony R. Poggioli, Alessandro Siria, and Lydéric Bocquet. Beyond the tradeoff: Dynamic selectivity in ionic transport and current rectification. *The Journal of Physical Chemistry B*, 123(5):1171–1185, 2019.
 - [362] Simon Gravelle and Christophe Ybert. Flow-induced shift of the donnan equilibrium for ultra-sensitive mass transport measurement through a single nanochannel. *The Journal of Chemical Physics*, 151(24):244503, 2019.
 - [363] Ke Liu, Martina Lihter, Aditya Sarathy, Sabina Caneva, Hu Qiu, Davide Deiana, Vasiliki Tileli, Duncan T. L. Alexander, Stephan Hofmann, Dumitru Dumcenco, Andras Kis, Jean-Pierre Leburton, and Aleksandra Radenovic. Geometrical effect in 2d nanopores. *Nano Letters*, 17(7):4223–4230, 2017.
 - [364] Bo Lu, David P. Hoogerheide, Qing Zhao, Hengbin Zhang, Zhipeng Tang, Dapeng Yu, and Jene A. Golovchenko. Pressure-controlled motion of single polymers through solid-state nanopores. *Nano Letters*, 13(7):3048–3052, 2013.
 - [365] David P. Hoogerheide, Bo Lu, and Jene A. Golovchenko. Pressure–voltage trap for dna near a solid-state nanopore. *ACS Nano*, 8(7):7384–7391, 2014.
 - [366] J. Scott Bunch, Scott S. Verbridge, Jonathan S. Alden, Arend M. van der Zande, Jeevak M. Parpia, Harold G. Craighead, and Paul L. McEuen. Impermeable atomic membranes from graphene sheets. *Nano Letters*, 8(8):2458–2462, 2008.
 - [367] Ali Najafi Sohi, Eric Beamish, Vincent Tabard-Cossa, and Michel Godin. Dna capture by nanopore sensors under flow. *Analytical Chemistry*, 92(12):8108–8116, 2020.
 - [368] J.J. Vlassak and W.D. Nix. A new bulge test technique for the determination of young’s modulus and poisson’s ratio of thin films. *Journal of Materials Research*, 7(12):3242–3249, 1992.
 - [369] Steven P Koenig, Narasimha G Boddeti, Martin L Dunn, and J Scott Bunch. Ultrastrong adhesion of graphene membranes. *Nature Nanotechnology*, 6(9):543–546, 2011.
 - [370] Narasimha G. Boddeti, Xinghui Liu, Rong Long, Jianliang Xiao, J. Scott Bunch, and Martin L.

- Dunn. Graphene blisters with switchable shapes controlled by pressure and adhesion. *Nano Letters*, 13(12):6216–6221, 2013.
- [371] Stephen P. Timoshenko and S Woinowsky-krieger. Theory of plates and shells. 1959.
- [372] H. Hencky. On the stress state in circular plates with vanishing bending stiffness. *Zeitschrift für Mathematik und Physik*, (63):311–317, 1915.
- [373] G R Willmott and P W Moore. Reversible mechanical actuation of elastomeric nanopores. *Nanotechnology*, 19(47):475504, 2008.
- [374] G. Seth Roberts, Darby Kozak, Will Anderson, Murray F. Broom, Robert Vogel, and Matt Trau. Tunable nano/micropores for particle detection and discrimination: Scanning ion occlusion spectroscopy. *Small*, 6(23):2653–2658, 2010.
- [375] Weifeng Li, Yanmei Yang, Jeffrey K. Weber, Gang Zhang, and Ruhong Zhou. Tunable, strain-controlled nanoporous mos2 filter for water desalination. *ACS Nano*, 10(2):1829–1835, 2016.
- [376] A. Fang, K. Kroenlein, and A. Smolyanitsky. Mechanosensitive ion permeation across sub-nanoporous mos2 monolayers. *The Journal of Physical Chemistry C*, 123(6):3588–3593, 2019.
- [377] Subin Sahu, Justin Elenewski, Christoph Rohmann, and Michael Zwolak. Optimal transport and colossal ionic mechano-conductance in graphene crown ethers. *Science Advances*, 5(7), 2019.
- [378] A Fang, K Kroenlein, D Riccardi, and A Smolyanitsky. Highly mechanosensitive ion channels from graphene-embedded crown ethers. *Nature Materials*, 18(1):76–81, 2019.
- [379] T Humplik, J Lee, S C O’Hern, B A Fellman, M A Baig, S F Hassan, M A Atieh, F Rahman, T Laoui, R Karnik, and E N Wang. Nanostructured materials for water desalination. *Nanotechnology*, 22(29):292001, 2011.
- [380] Natalie A. Dye, Marko Popovic, K. Venkatesan Iyer, Suzanne Eaton, and Frank Julicher. Self-organized patterning of cell morphology via mechanosensitive feedback. *bioRxiv*, 2020.
- [381] Lionel Buchaillot, Etienne Farnault, Moussa Hoummady, and Hiroyuki Fujita. Silicon nitride thin films young's modulus determination by an optical non destructive method. *Japanese Journal of Applied Physics*, 36(Part 2, No. 6B):L794–L797, 1997.
- [382] S W P van Sterkenburg. The electrostriction of silicon and diamond. *Journal of Physics D: Applied Physics*, 25(6):996–1003, 1992.
- [383] Frédéric Blaffart, Quentin Van Overmeere, Thomas Pardoën, and Joris Proost. In situ monitoring of electrostriction in anodic and thermal silicon dioxide thin films. *Journal of Solid State Electrochemistry*, 17(7):1945–1954, 2013.
- [384] P. Temple-Boyer, C. Rossi, E. Saint-Etienne, and E. Scheid. Residual stress in low pressure chemical vapor deposition sinx films deposited from silane and ammonia. *Journal of Vacuum Science & Technology A*, 16(4):2003–2007, 1998.
- [385] A.G. Noskov, E.B. Gorokhov, G.A. Sokolova, E.M. Trukhanov, and S.I. Stenin. Correlation between stress and structure in chemically vapour deposited silicon nitride films. *Thin Solid Films*, 162:129 – 143, 1988.
- [386] Harold L. Weissberg. End correction for slow viscous flow through long tubes. *Phys. Fluids*, 5(9):1033–1036, 1962.
- [387] A. Gadaleta, C. Sempere, S. Gravelle, A. Siria, R. Fulcrand, C. Ybert, and L. Bocquet. Sub-additive ionic transport across arrays of solid-state nanopores. *Physics of Fluids*, 26(1):012005, 2014.
- [388] Martin A. Schwartz. The importance of stupidity in scientific research. *Journal of Cell Science*, 121(11):1771–1771, 2008.
- [389] Gordon Pennycook, James Cheyne, Nathaniel Barr, Derek Koehler, and Jonathan Fugelsang. On the reception and detection of pseudo-profound bullshit. *Judgment and decision making*, 10:549–563, 12 2015.

Bibliography

- [390] University of Washington. *<https://www.moles.washington.edu/covid-19-research-at-moles/>*, 2020 (accessed July 8, 2020).

Sebastian Davis

davis.sebastianj@gmail.com

linkedin.com/in/sebastian-davis

+41 78 968 48 90



Strengths: I am curious and determined to learn and grow both as a person and a professional. Being a part of a high performing team at the forefront of scientific discovery and application excites and drives me. I believe that my broad set of skills will allow me to contribute to the biotech industry in order to improve the world we live in.

Education

Swiss Federal Institute of Technology at Lausanne (EPFL)

2015-2020

Doctor of Science in Physics
Focus on nanopores as fluidic sensors

Swiss Federal Institute of Technology at Lausanne (EPFL)

2010-2015

Master of Science in Physics
- Minor in Biomedical Technologies
- Master Project in collaboration with Universitat Barcelona (UB)

Gymnase du Bugnon Site de l'Ours, Lausanne

2007-2010

Maturité in Physics and Applied Mathematics
- End of study project entitled "Influences on J.R.R. Tolkien's 'The Lord of the Rings' and related works" passed with distinction
- Prix de Prestige "Pour un parcours remarquable"

Core Experience

Laboratory of Nanoscale Biology, EPFL

2015-2020

Nanopores as fluidic and biological sensors (PhD Thesis)

My objective was to characterize in detail the effect of coupled hydrostatic pressure and electrical measurements on solid-state nanopores in order to better understand their response as biological sensors (DNA, RNA, protein detection). Work such as this at the nanoscale requires precision not only in measurement but in work ethic in order to rigorously demonstrate physical trends.

I also showed diversity of knowledge by investigating other types of nanopores (glass capillaries and protein pores) and novel chemistry (room temperature ionic liquids).

During this time, I moulded my way of approaching problems and breaking down complex issues into step by step achievable goals.

Additional Professional Experiences

Small Biosystems Lab, UB

2015

Single Molecule Unfolding of Barnase at Different Temperatures

The objective of my master thesis was to study the protein Barnase as a model system to observe the temperature dependence of mechanical protein unfolding via optical tweezers. Duties included: protein expression and purification, temperature control optical tweezers, and data analysis using custom Matlab scripts. Some all atom and coarse grained molecular dynamics modelling of mechanical unfolding was also performed with the NAMD software. Collaboration among the group as well as with industry (ProteoDesign Barcelona) was encouraged.

Laboratory of the Physics of Living Matter, EPFL

2014

Lab Practical

Practical work studying the effect of microgravity on osteoblast cell topography, development, and RNA expression. Prototype cell culture chambers were designed to simulate the microgravity environment. Techniques used ranged from Atomic Force Microscopy (AFM), photolithography, and fluorescence microscopy. Close collaboration with the mechanical workshop was needed in order to draw up blueprints for a random positioning machine able to simulate microgravity.

Laboratory of Cellular Biophysics, EPFL

2013-2014

Laboratory Assistant

Two summer internships studying the elastic response of actin bundles in cell membranes. This was achieved with ultra-soft cantilevers and 3D micro-patterned substrates. I acquired experience with cell culture, PDMS micro-patterning, fluorescence/white light microscopy, protocol optimization, and data analysis.

Skills

Technical skills

Scanning Electron Microscopy (SEM), Energy Dispersive X-Ray Spectroscopy (EDX), Atomic Layer Deposition (ALD), glass nanocapillaries (Sutter P2000), silicon technologies, silicon nitride nanopores, Polydimethylsiloxane (PDMS) work, laser optics, Optical Tweezers, white light and fluorescence microscopy, plasma cleaning, biological nanopores (MspA), lipid bilayers and vesicles, protein expression and purification, work with proteins (dCas9, RNAP, Barnase), cell culture, DNA purification, Polymerase Chain Reaction (PCR), buffer preparation, agarose and acrylamide based gel assays, novel chemistry (room temperature ionic liquids), current amplifiers (ex Axopatch 200B), Faraday cage, basic soldering, temperature control systems (Peltier element, laser heating), hydrostatic pressure systems (Fluigent, Elveflow), cleanroom trained, wet lab trained.

IT skills

Python (data processing using: matplotlib, numpy, scipy, pandas, yaml, ...), Matlab (data processing, curve fitting), ImageJ (basic image analysis and processing), LabView (use for data acquisition and basic coding), C++ (basic course), LaTeX (scientific writing), Adobe Illustrator (figure preparation and basic schematic design), MS Excel, MS Word, MS Powerpoint

Soft Skills

Critical thinking, perseverance, problem solving, high organisational skills, oral and written scientific communication at different levels depending on requirement, leadership (attended workshop "Leadership for young researchers I and II"), curious, team player

Extracurricular Activities

Teaching and Supervision Duties

During my PhD as well as earlier studies at EPFL I was able to teach several introductory physics classes exercise sessions (20+ students). This allowed me to hone my skills explaining complex scientific concepts in an easy and approachable way.

I also had the opportunity to supervise two master students and several summer projects during my PhD. These experiences moulded my way of leading a project and gave me my first experiences with defining and following up on deliverables, conflict resolution, and giving/receiving feedback. Things I consider keys to success in the workplace.

Lausanne University Rugby Club

I have played rugby for 20 years and been a player at Lausanne University Rugby Club since 2010. I was awarded the best player award for the 2010-2011 season despite it being my first season out of age grade rugby. I also played for the Swiss U18 team and participated in the European championships held in Italy.

Rugby has taught me the keys of teamwork, never leaving a team-mate behind, and some fundamentals of leading by example. The tenacity and perseverance needed to perform on the rugby field as well as the camaraderie of being part of a highly performing team are things that I believe are easily transferred to a professional environment.

Swiss Civil Protection

I was part of the Atomic Biological and Chemical Unit of the Lausanne Protection Civile (PCi rank: Soldat). My time performing my civil duty allowed me to experience following orders as well as being given the opportunity to lead small groups of 6-8 people. These leadership tasks had the objective, among others, of instructing the group in chemical decontamination of personnel and vehicles, atomic activity readings, and setting up vaccination centres. Considering the military context of these tasks I learned the importance of time management, maintaining discipline, personnel management, leadership, and planning.

Other interests

Interest in Japanese language and culture, yoga, and squash. Swiss driver's license since 2011.

Personal Information

Full Name: Sebastian James Davis

DOB: 27.04.1992

Marital status: Single

Nationality: British and Swiss

Preferred contact: davis.sebastianj@gmail.com

Languages

- English (Native)
- French (Native)
- German (B1)
- Japanese (A1)